THESIS ON INFORMATICS AND SYSTEM ENGINEERING C122

Application-Oriented Performance Characterization of the Ionic Polymer Transducers (IPTs)

ANDRES HUNT

TUT
PRESS

TALLINN UNIVERSITY OF TECHNOLOGY
Faculty of Information Technology
Centre for Biorobotics

This dissertation was accepted for the defence of the degree of Doctor of Philosophy in Computer and Systems Engineering on March 15, 2017.

Supervisor: Prof. Maarja Kruusmaa
Centre for Biorobotics
Department of Information Technology
Tallinn University of Technology
Tallinn, Estonia

Opponents: Prof. John Hallam
SDU Embodied Systems for Robotics and Learning
The Maersk Mc-Kinney Moller Institute
University of Southern Denmark
Odense, Denmark

Assoc. Prof. Salvatore Graziani
Department of Electrical, Electronics and Computer Engineering
University of Catania
Catania, Italy

Defence of the thesis: April 25, 2017, Tallinn

Declaration:
Hereby I declare that this doctoral thesis, my original investigation and achievement, submitted for the doctoral degree at Tallinn University of Technology has not been submitted for doctoral or equivalent academic degree.

European Union
European Social Fund

Investing in your future

ISSN 1406-4731
ISBN 978-9949-83-090-9 (publication)
ISBN 978-9949-83-091-6 (PDF)

INFORMAATIKA JA SÜSTEEMITEHNIKA C122

Ioonpolümeeridest täiturite võimekuse karakteriseerimine rakendusteks

ANDRES HUNT

TTÜ KIRJASTUS

To my family and friends.

TABLE OF CONTENTS

LIST OF PUBLICATIONS

A Hunt, A., Chen, Z., Tan, X., and Kruusmaa, M. (2010). Control of an inverted pendulum using an Ionic Polymer-Metal Composite actuator. In 2010 IEEE/ASME International Conference on Advanced Intelligent Mechatronics Proceedings, pp. 163–168;

B Hunt, A., Chen, Z., Tan, X., and Kruusmaa, M. (2009). Feedback Control of a Coupled IPMC (Ionic Polymer-Metal Composite) Sensor-Actuator. In ASME 2009 Dynamic Systems and Control Conference Proceedings, Volume 1, pp. 485–491;

C Hunt, A., Chen, Z., Tan, X., and Kruusmaa, M. (2016). An integrated electroactive polymer sensor–actuator: design, model-based control, and performance characterization. Smart Materials and Structures, 25(3), pp. 035016;

D Hunt, A., Ristolainen, A., Ross, P., Öpik, R., Krumme, A., and Kruusmaa, M. (2013). Low cost anatomically realistic renal biopsy phantoms for interventional radiology trainees. European Journal of Radiology, 82(4), pp. 594–600.

OTHER RELATED PUBLICATIONS

E Kruusmaa, M., Hunt, A., Punning, A., Anton, M., and Aabloo, A. (2008). A linked manipulator with ion-polymer metal composite (IPMC) joints for soft- and micromanipulation. In 2008 IEEE International Conference on Robotics and Automation Proceedings, pp. 3588–3593;

F Opik, R., Hunt, A., Ristolainen, A., Aubin, P. M., and Kruusmaa, M. (2012). Development of high fidelity liver and kidney phantom organs for use with robotic surgical systems. In 2012 4th IEEE RAS&EMBS International Conference on Biomedical Robotics and Biomechatronics (BioRob) Proceedings, pp. 425–430.

AUTHOR'S CONTRIBUTIONS TO THE PUBLICATIONS

A Realization of the idea (design, building, modelling, control design), experiments, data processing, producing the figures and writing most of the manuscript;

B Realization of the idea (design, building, modelling, control design), experiments, data processing, producing the figures and writing most of the manuscript;

C Realization of the idea (design, building, modelling, control design), experiments, data processing, producing the figures and writing most of the manuscript;

D Material manufacturing and property calibration methodology, supervising the experimental work, processing the material calibration and phantom evaluation results, producing the figures, writing most of the paper and executing corrections according to reviews;

E Realization, experimental work and data processing related to the manipulator arm, and writing the respective sections;

F Gelatin gel manufacturing techniques, methodology and experimental set-up for measuring ultrasound properties.

ABBREVIATIONS

CAD – computer-aided design

CPC – carbon-polymer composite

CT – computed tomography

DAP – direct assembly process

DOF – degree of freedom

EAP – electroactive polymer

ICPF – ionic conducting polymer gel film

IEAP – ionic electroactive polymer

IL – ionic liquid

IPCC – ionic polymer-conductor composite

IPCMC – ionic polymer-carbon-metal composite

IPMC – ionic polymer-metal composite

IPT – ionic polymer transducer

PI – proportional-integral

PID – proportional-integral-derivative

RMS – root mean square

1. INTRODUCTION

Ionic polymer-metal composites (IPMCs) and ionic polymer-carbon-metal composites (IPCMCs) are ionic polymer transducers (IPTs) that bend when voltage is applied between their electrodes (shown in Figures 1.1 and 1.2), and reciprocally generate voltage when they are bent. They consist of an ion-conductive polymer backbone (typically in a form of a thin sheet), mobile (i. e. loosely coupled) ions that can move within the polymer, and conductive electrodes that are applied on the facets of the ionic polymer backbone. Such construction allows ion migration within the material sample when it is mechanically or electrically stimulated, resulting in voltage generation or observable bending respectively. The basic working principles and construction of the IPMC and IPCMC materials are discussed in Section 3.1 in more detail. Potential processes that dominate the actuation and sensing phenomena are illustrated respectively in Figures 1.3 and 1.4.

Features that make IPTs an attractive alternative to conventional sensors and actuators include large bending strains, low activation voltages, simple construction, and ease of shaping and miniaturization. Small maximum output force is considered an advantage or a drawback depending on the specific application. In terms of limitations the performance variations (degradation usually) and non-linearities limit their use or make their application a challenging. Properties of the IPTs are reviewed in more depth in Section 3.1.2.

The appealing properties of the IPTs have sparked numerous papers that report possible applications for these ”smart” materials. Locomotion and manipulation mechanisms for various ground and underwater robots, energy harvesting elements, actuation or sensing in surgical tools and prosthesis are only some examples, and a more in-depth review is provided in Section 3.2. Most of these studies focus on presenting their idea and providing a proof-of-concept demonstration of its feasibility, but exclude reliability and performance evaluation in terms of actual requirements. Furthermore, to the best of the author’s knowledge none of them have been adapted into use. Clearly the authors have been counting on advances in materials science to improve the IPTs, but developments have not been as fast as expected. A characterization of currently available IPT materials in terms of their sensing and actuation performances and potential limitations would significantly facilitate evaluating their present suitability for different implementations.

(a) *(b)* *(c)*

Figure 1.1. Actuating an IPMC sample. Resting position (b), and 2 V with opposite polarities applied for 2 s (a,c).

Since IPTs exhibit both sensing and actuation functionalities, several research groups have been developing methodologies to achieve a self-sensing actuator, described in more detail in Section 3.3.3. Unfortunately so far this concept has not been demonstrated to function in the presence of external disturbances. Currently, a much more realistic alternative is to combine multiple material samples into a single device for simultaneous actuation and sensing. This would allow to exploit their novel properties with minimum impact on actuation capabilities. To date, only few preliminary studies reviewed in Section 3.3.2 have considered this concept, and a more thorough investigation would be necessary to explore its potential.

The aims of the work presented in this thesis are the following:

- to study the performance and limitations of the IPT actuators in a real-time application (approaching the limits of their actuation capabilities), by realizing an IPT-actuated inverted pendulum;
- to study the feasibility of the coupled IPT sensor-actuator concept, for achieving an extended functionality with an existing material technology;
- to thoroughly characterize the design and closed-loop performance of an IPT sensor-actuator prototype using three common IPT materials in order to provide qualitative and quantitative information on the feasibility of the IPTs and the sensor-actuator concept in applications;
- to provide a realistic test-bed for studying the feasibility of IPTs in invasive medical applications.

Balancing an inverted pendulum system is a real-time critical task with clear validation criteria, and it is expected to provide information on the behaviour,

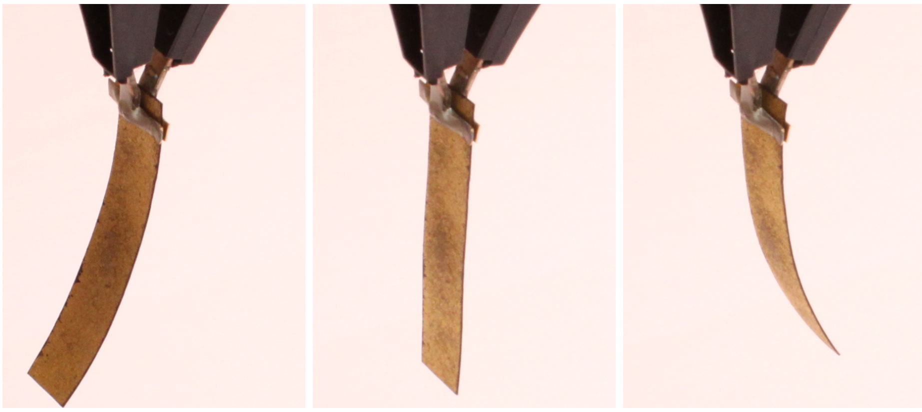

(a) *(b)* *(c)*

Figure 1.2. Actuating an IPCMC sample. Resting position (b), and with 2 V applied for 2 s at opposite polarities (a,c).

performance and limitations of the IPT actuators when functioning at high actuation voltages near their limitations. The experimental set-up consists of an IPMC-actuated lever that is coupled to a lightweight cart supporting the inverted pendulum while the entire assembly is submerged in a water tank. Dynamics of the system is captured using a 5th order state-space model that is further used to design a full-state linear quadratic optimal controller and a state observer. In order to be able to balance the system, the unexpectedly strong back-relaxation in IPMC actuation dynamics is effectively treated as an uncertainty by substituting the actual cart position with a simulated estimation. Stabilizing the inverted pendulum is achieved for up to 30 minute long experiments, demonstrating the feasibility of the IPT actuators in a real-time performance critical task, and indicating the low actuation moment and unexpectedly strong back-relaxation effect as significant limitations.

In order to investigate feasibility of the integrated IPT sensor-actuator concept and provide information on its performance, a sensor-actuator prototype is constructed. Two short IPCMC samples (side-by-side configuration) are mechanically coupled together and fixed to the Earth frame in one end using a spring-loaded clamp with electrical terminals. In the other end, a plastic clamp couples them together and attaches to a rigid extension rod. Empirical models are used to capture the actuation and sensing dynamics, and a PI (proportional-integral) controller is designed. The behaviour of the prototype is studied in closed-loop experiments of sinusoidal reference following, and its performance in IPT feedback configuration is validated against an external feedback. Results show that the IPT sensor-actuator prototype works well in short term (few seconds), but longer experiments (up to a minute) fail due to low-frequency noise in IPCMC sensing signal that causes significant error accumulation in position estimation.

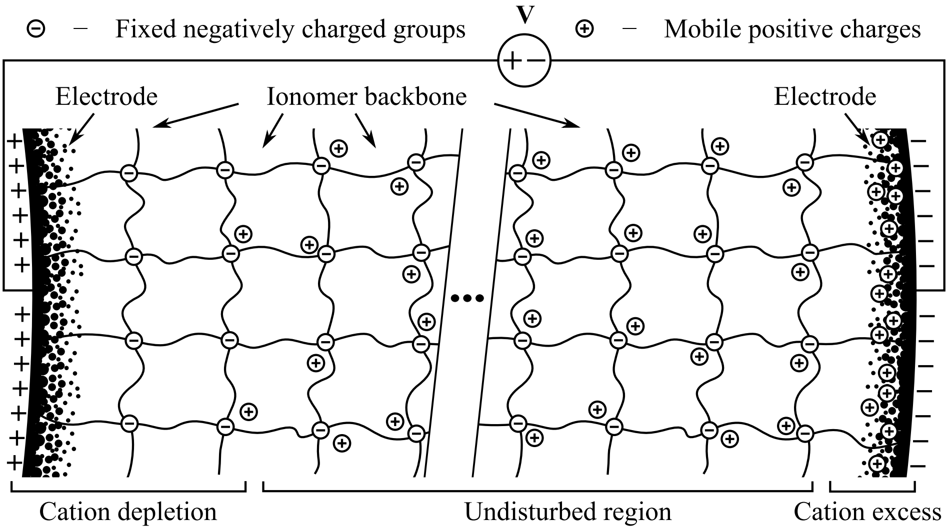

Figure 1.3. A simplified explanation to the initial fast actuation phenomenon in IPMC and IPCMC materials in response to applied voltage. When voltage is applied, the mobile cations start migrating within the material, carrying along some solvent (if present). Very high cation concentration forms in the narrow proximity of the cathode electrode, and a wider cation-depleted region forms in the proximity of the anode electrode. The region in-between remains electrically neutral as the aforementioned charge imbalances shield it from the applied electric field. Repulsive electrostatic forces between the branches of the dendritic electrode in the cation-rich region cause deformations in the material structure, observable as bending. Refer to Section 3.4.3 for more information.

Next, an improved design of the integrated IPT sensor-actuator concept is proposed, and a more systematic approach is taken in order to qualitatively and quantitatively characterize the performance and limitations of both the design concept and three different IPT materials. A prototype is constructed using two IPT samples for actuation and one for sensing, positioned in a symmetrical side-by-side configuration, fixed to the Earth frame by a spring-loaded clamp (with electrical terminals) in one end, and mechanically coupled together (and to a rigid extension rod) in the other end. The IPT materials and the sensor-actuator design is thoroughly characterized using physics-based models. A series of closed-loop experiments are conducted on the prototype using the three different IPT materials, PI and H_∞ controllers, and both the IPT and the laser distance meter feedback. This allows to provide qualitative and quantitative performance characterization, and compare the results material-wise, controller-wise, and against external feedback baseline. Significantly longer experiments with IPT sensor feedback are achieved than ever before, but the low-frequency noise in IPT sensor signal remains the major performance limitation.

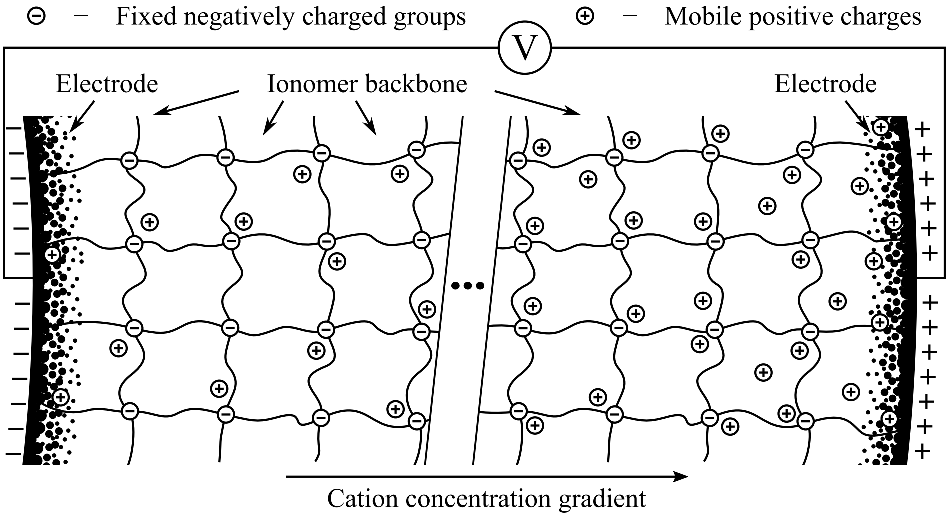

Figure 1.4. A simplified explanation of possible processes dominating the sensing phenomenon. Bending the transducer produces the solvent and ion distribution gradients across the material thickness, resulting in a potential difference between the material electrodes. More information is provided in Section 3.4.3.

Mechanical compliance and limited actuation capabilities of the IPT materials can be considered as intrinsic safety measures when using them in invasive medical equipment, and therefore such applications deserve more thorough consideration. In order to establish a realistic test-bed for evaluating feasibility of IPTs in invasive medical applications, a phantom manufacturing process is reported and validated. Gelatin gels are identified as the best suited soft tissue mimicking materials for such purpose, and their properties are experimentally related to their composition. Phantoms are obtained by segmenting the organ models in patient CT scans, producing mould models in CAD software, making physical mould parts using rapid prototyping, and casting the phantoms (in multiple steps). For proper elasticity and ultrasound appearance the respective soft tissue properties are obtained from the literature and required gel compositions are looked up from material characterization results. Following these techniques a set of ultrasound guided renal biopsy phantoms are produced and validated by radiology residents, confirming realistic anatomy and appearance in ultrasound imaging. Basing on the reported and validated soft tissue phantom manufacturing technique a test-bed design is proposed for validating IPTs in an invasive medical application, particularly as an active guidewire in a catheter system, but validating the application itself remains future work.

The rest of this thesis is organized as follows. First, the contributions of the thesis are presented in Chapter 2. Next, the literature overview in Chapter 3 discusses the background and properties of the IPMC and IPCMC materials, reviews proposed applications, various control reports and modelling approaches.

Chapter 4 presents the work related to the IPT-actuated inverted pendulum system, and Chapters 5 and 6 report the studies on the initial and improved designs of the integrated IPT sensor-actuator concept respectively. Developing a realistic test-bed for evaluating the feasibility of IPTs in medical applications is presented in Chapter 7. Finally, the conclusions summarize the work presented in this thesis.

2. CONTRIBUTIONS OF THE THESIS

Contributions of this thesis are:

- Implementation of the IPT materials in the first real-time performance-critical application with clear validation criteria, i. e. balancing an inverted pendulum system. Results provide information about the behaviour of IPT materials (particularly IPMCs), and about the implementation limitations, in particular, actuation limits, long-term stability and back-relaxation at elevated operational voltages.
- The concept development and realization of an integrated sensing and actuation system using IPTs, i. e. achieving extended functionality with the existing material technology. The first reported IPT sensor-actuator prototype (using IPCMCs), capable of precise reference position tracking. Validation of this concept and qualitative characterization of its performance in closed-loop configuration. Identification of low-frequency noise in the sensing signal as potential limitation for applications.
- Improved IPT sensor-actuator design. Three IPTs characterized in terms of fundamental material parameters (physics-based models). Performance of the IPT sensor-actuator prototype qualitatively and quantitatively characterized in the closed-loop configuration. Performance comparison for the sensor-actuator is provided material-wise, controller-wise and with respect to the external feedback. Up to 30 min long experiments are achieved in IPT feedback configuration, 90 times longer than ever reported before. The identified potential limitations vary material-wise, and include back-relaxation of the actuator and low-frequency noise in the sensing signal.
- Ultrasound-compatible soft tissue substitute phantom design and manufacturing techniques providing a realistic test-bed for studying IPTs in medical applications (as an active guidewire in catheter design). Phantom material properties are related to their composition. Test phantoms are produced and validated in renal biopsy training procedure by interventional radiology residents. Evaluation results confirm that the phantoms and included pathologies appear realistic in ultrasound imaging.

3. LITERATURE OVERVIEW

This section explores the literature related to this thesis, introducing the IPMCs and IPCMCs, and summarizing various studies on applications, closed-loop control and modelling of these materials, as well as phantom material technologies for evaluating the IPTs in medical applications. First, IPMC and IPCMC materials are addressed in Section 3.1, briefly covering their categorization, manufacturing, construction and properties. Then, the potential exploitation of these materials is demonstrated trough the multitude of proposed applications in biomedical engineering, different aspects of robotics, energy harvesting and other fields in Section 3.2. Next, Section 3.3 examines the reported feedback configurations and control methods that have been used for closed-loop control of IPTs. Black-box, grey-box and white-box approaches for modelling the materials are covered in Section 3.4, also reviewing some mechanisms that have been hypothesized to be responsible for actuation and sensing phenomena. An overview of currently available phantom material technologies that can be used for evaluating medical applications of the IPTs is provided in Section 3.5. Literature overview is concluded in Section 3.6.

For more details on topics related to IPTs interested readers are referred to numerous review papers, e. g. Shahinpoor [1, 2], Bhandari *et al.* [3], Jo *et al.* [4].

3.1. IPMCs and IPCMCs

This thesis studies ionic polymer transducers (ITPs) [5, 6], that are also classified as ionic electroactive polymer (IEAP) transducers [7], ionic polymer-conductor composites (IPCCs) [2], or ionic conducting polymer gel film (ICPF) transducers [8]. The particular materials under investigation are ionic polymer metal composites (IPMCs) and equivalent IPCCs that have nanoporous carbon electrodes instead of noble metal ones (described by the provider as IPMCs with nanoporous carbon electrodes [9]). Nanoporous carbon electrodes perform similarly to the dendritic electrodes of the IPMCs, and thin gold film on their surfaces only serves to enhance surface conductivity, rendering these materials functionally and by construction roughly equivalent. While IPCCs with carbon electrodes are addressed as carbon-polymer composites (CPC) in Paper C, this term is not used in this thesis to avoid confusion with actuators that are produced by applying ionic liquid (IL) and porous carbon electrodes on a thin ion-permeable polymer film e. g. in [10]. For simplicity, the term ionic polymer-carbon-metal composite, i. e. IPCMC, is used further on. Due to abovementioned similarities to IPMCs, IPCMCs are occasionally also addressed as IPMCs and many of the studies focusing on IPMCs are also qualitatively valid for IPCMC materials [9, 11, 12, 13].

IPMCs and IPCMCs are high strain and low elastic modulus electromechanical transducers that exhibit two-way coupling, i. e. they produce electric signals when bent, and bend when voltage is applied. They are 'smart' materials produced by plating ionic polymers with conductive metal or carbon electrodes. Essentially, 'smart' materials (also known as 'intelligent', 'adaptive' and 'structronic' materials) are materials designed to conduct significant energy conversion between physical domains (mechanical, electrical, thermal, magnetic, chemical), displaying a remarkable change in a state variable in one domain upon a change in a state variable in another [7]. Ionic polymers are a type of (electromechanical) electroactive polymers, that accordingly provide coupling between electrical and mechanical domains, expressed in a change in their shape or dimensions when subjected to electric field, and vice versa. Electronic electroactive polymers (e. g. piezoelectric polymers, dielectric elastomers) and ionic electroactive polymers (e. g. hydrogels and aforementioned ionic polymers) can be distinguished, the latter functioning trough diffusion or conduction of charged species within the polymer. Due to large deformations in response to low activation voltages (usually less than 10 V), ionic electroactive polymers are often used in sensor and actuator applications. Thus, by compositing ionic polymers with conductive electrodes, one type or smart materials have been used to achieve new smart materials with novel properties. A brief overview of available EAP materials and their history has been described by Bar-Cohen and Zhang in [14].

The first study describing the bending of an IPMC transducer under low-voltage electric stimuli was reported in 1992 by Oguro et al. [15] (patentented in [16]). In the same year an equivalent design was proposed for propelling a fish-like swimming robot by Shahinpoor [17]. Using a platinized Nafion™membrane as a vibration dampener and an accelerometer for detecting disturbances normal to the polymer membrane surface were also reported in 1992 by Sadeghipour *et al.* [18]. The sensing phenomenon, i. e. voltage generation upon bending was first reported in 1995 by Shahinpoor [19, 20]. These novel properties of a metallized ionic polymer membrane have motivated many studies ever since.

IPCMC materials emerged as Akle *et al.* developed a direct assembly process (DAP) as an alternative to chemical deposition of metal electrodes on the polymer membrane [21] allowing to obtain electrodes with controlled dimensions and morphology [22, 6]. They produced ionic polymer trasnducers (IPT) with single wall carbon nanotube (SWNT), RuO2 and polyaniline electrodes covered with gold foil to enhance the surface conductivity. Later, Palmre *et al.* used this technique (DAP) to produce IPTs with nanoporous carbon-based electrodes, based on carbide-derived-carbon (CDC), coconut-shell-based activated carbon, and TiC-based carbon [9, 23].

3.1.1. Material construction

IPT properties are significantly influenced by the details of the manufacturing process [24], but in brief, the materials used in this work are manufactured as follows. A thin ($100\mu m - 300\mu m$) ion-conductive polymer membrane (e. g. Nafion, Flemion) [21] is either purchased or manufactured in-house [25], [26]. These materials consist of a mesh of long polymer molecules with short side-chains that are terminated with ionic groups and respective loosely coupled counter-ions [21]. In order to produce IPMC transducers, noble metal (e. g. platinum, gold) electrodes are deposited on both faces of the polymer membrane using the electroless plating technique [27]. Correspondingly, IPCMC transducers are obtained using the direct assembly process (DAP) [6] to deposit carbon electrodes that are further covered with gold foil and hot-pressed in order to enhance surface conductivity [9]. Loosely coupled counter-ions are exchanged for larger ones (e.g. Na^{+}, Li^{+} in place of protons in Nafion) as required [28], and the most common solvent medium is water [21]. Ionic liquids (ILs) function both as counter-ions and solvent, and are often used as a non-volatile and more stable alternative to abovementioned ion-water mixture, allowing to utilize the materials also in dry environments and at higher voltages [29] [9] [30].

Various combinations of counter-ion species and polymer backbones result in materials with diverse properties [31, 32]. A more extensive investigation of different ions in combination with both Nafion and Flemion membranes has been reported by Nemat-Nasser [28]. Regarding the surface electrodes, their purpose is not only producing electric field within ionic polymers, but their structure also dictates material preformance to a large extent. In fact, Doi *et al.* demonstrated that, in the presence of electric field, ionic polymer gels that are in contact with electrodes behave differently from the ones that are not in contact with electrodes [33]. The dendritic structure of the electrodes greatly contributes to the actuation phenomenon. For example, Okazaki *et al.* manufactured an IPMC sample by vacuum plating gold electrodes on an ionic polymer sheet, but the resulting material exhibited almost no actuation [34]. Analogously to the dendritic structure of the IPMC electrodes, it is the total porosity of the IPCMC surface electrodes that influences their actuation. Torop *et al.* showed that the displacement response of the IPCMCs increases with the increase of the mesopore size, and the induced strain is proportional to the total porosity of the used carbon-derived carbon [35]. Depending on the material and the structure of the electrodes, the performance of the IPTs may be significantly influenced also by the presence and variation in surface resistance. This phenomenon has been studied for example by Shahinpoor *et al.* [36] and Punning *et al.* [37]. Interestingly Johanson *et al.* achieved reversion in the surface resistance effects (using Pt and Cu electrodes and Cu^{2+} counter-ions) by active re-deposition of copper during actuation, but undesirable growth of copper dendrites inside the polymer backbone severely limited their usability [38].

While the typical IPT samples are manufactured as thin sheets, also thicker materials and unusual geometries have been reported. In order to achieve materials that are capable to output larger forces Kim and Shahinpoor made over 2 mm thick IPMC samples using the solution recasting technique [25], and Kim *et al.* were able to achieve up to 1 mm thick Nafion membranes in search for an alternative for commercially available materials with a limited thickness range [26]. Some examples of IPTs with unconventional geometry include helical IPMCs reported by Moenkhah *et al.* [39], hollow tube-shaped IPMCs with sectored electrodes and resistive strain sensors [40], and cylindrical (not hollow) IPMCs with sectored electrodes [41]. The latter two are able to bend in 2 degrees of freedom.

3.1.2. Material properties

Actuation of IPMCs and IPCMCs is observable in response to low voltage signals, usually up to 5 V [42]. Higher voltages are avoided to protect the material from electrolysis (if the solvent includes water) or from heat damage. The voltages that are generated on the material electrodes upon mechanical excitation are approximately two orders of magnitudes smaller than the voltages needed to produce equivalent deformation when the same sample is used as an actuator [43, 44]. Besides voltage also current and surface resistance have been measured for sensing purposes (Section 3.3.2). In addition to the abovementioned actuation phenomenon, some IPMCs have also been reported to be capable of electrochemical self-oscillations [45, 46].

Appealing properties of IPTs include softness, flexibility, light weight, ease of scalability, mechanical simplicity, mechanical compliance and very high strains. Some IPMCs have been reported to achieve even bending beyond a complete loop [47]. Properties limiting their application include the low maximum output force, sensitivity towards the environment, and non-linear and varying material behaviour. The so-called back-relaxation effect is so strong for some polymer-cation combinations that under constant DC voltage after the initial actuation the materials bend back beyond their initial rest position [28, 48]. In quasi-static operation, short IPMCs with a rigid extension have been shown to behave more linearly at large deformations than long material samples [49].

Over the years, modelling studies have considered different processes to dominate the sensing and actuation phenomena. These include ion motions and subsequent electrostatic interactions [50], formation of pressure gradient by solvent flux due to ion flux [51, 52, 50], and internal stresses and interactions between ion pairs inside hydrophilic clusters [44, 53]. These processes are further discussed later, in Section 3.4.3 on physics-based modelling of IPTs.

The IPT's operating conditions and configuration may also affect the way they behave. According to Moeinkhah *et al.*, IPMC performance varies with clamping pressure, and optimum is a trade-off between electrical and mechanical effects of clamping [54]. When water serves as the ion transport medium in IPTs the materials need to be kept hydrated to maintain their actuation performance [1]. Sensing behaviour has also been reported to differ between fully and partially hydrated samples [55] (Flemion membrane, Au electrodes), but wet environment was found not essential [56] (Nafion 117, Na^+ cations, electrode material not reported). According to Chen *et al.*, the sensing signal amplitude of the IPMCs (provided by Environmental Robots Inc.) increases for approximately 5 minutes after taking it out of the water, and then starts to decrease [57]. Investigation of the impact of the ambient humidity on the electrical properties of the IPMCs with ionic liquids indicated that the membrane resistance decreases exponentially with increase in the humidity [58]. Furthermore, Must *et al.* demonstrated that IPCMCs could be used as ambient relative humidity sensors [59]. Brunetto *et al.* investigated the impact of temperature and humidity on IPMCs and reported a strong increase in actuation with increase the of humidity [60] (Nafion 115, Na^+ cations, Pt electrodes and water solvent), as well as the increase in the sensing signal amplitude and noise with the increase of humidity [61] (Nafion 117, Na^+ cations, Pt electrodes and water solvent), but no significant dependences on temperature. An empirical model of the temperature impact on IPMC sensing has been reported by Ganley *et al.* [62]. Material degradation due to electrode oxidation has been reported by Kim and Kim [63], and a thorough methodology for studying material durability, self-degradation and degradation was proposed by Punning *et al.*, but the results of this study are still underway [64].

3.2. Proposed applications

Since the introduction of the IPMC transducers a wide variety of reports have been published on their potential application. Many of them are summarized in review papers, e. g. [1, 65, 66, 3, 67], but in this section it is intended to provide a broader overview on the scope of the applications proposed for IEAP transducers. In the following, biomedical, robotics, energy harvesting and other applications are introduced.

3.2.1. Biomedical engineering

The novel properties of IEAP transducers have been found to be potentially useful in a variety of applications in the field of biomedical engineering.

Multiple aspects of potential exploitation of the IPTs in limb prosthesis have been studied. Lee *et al.* stacked 5 Nafion films to manufacture stronger material samples for their three-joint IPMC-actuated artificial finger prototype [68]. In the same year Biddiss and Chau investigated the usage of the IPMCs for sensing in hand prosthesis [69]. An IPMC-actuated hand prosthesis prototype was built by Aravinthan *et al.*, and they further used EMG signals from skin electrodes on human limbs to actuate the device [70]. Using EMG signals to actuate IPMCs was also investigated by Jain *et al.* [71]. The major limitation in most of the prosthesis applications was the low achievable actuation force.

While some of the proposed IPT applications in medical equipment are non-invasive, e. g. blood pressure and heart rate monitoring system of Keshavarzi *et al.* [72] (IPTs used on the inner surface of a cuff), most of the applications qualify as interventional medicine equipment. Using IPMCs as active guidewires in microcatheters was first proposed by Guo *et al.* [73]. Over a decade later, Fang *et al.* studied manufacturing of IPMC actuators specifically for using them in a low-cost disposable active cardiac catheter [74], and in [75] they further produced and tested three different IPMCs for the same purpose. Also, using IPMC actuators as bending tips in scanning fibre endoscopes and catheteroscopes has been studied by Yoon *et al.* [76]. Ferrara *et al.* suggested using IPMCs for pressure transducer in human spine [77].

Various surgical instruments have been proposed utilizing IPTs for sensing or actuation purposes. McDaid *et al.* proposed a 2-DOF IPMC-actuated surgical tool and investigated the performance of one of its joints in the closed-loop configuration [78]. Fu *et al.* built an IPMC-actuated surgical tool prototype and added a strain gauge on its surface for feedback [79]. Surgical tactile probes with IPMCs for sensing and actuation have been proposed by Bonomo *et al.*, who present a prototype for contact registration and tissue stiffness estimation [80], and Brunetto *et al.* who used vibrations in a different prototype to distinguish between tissue materials [81]. Chen *et al.* used an IPMC actuator with an attached PVDF sensor for embryo injection and demonstrated the procedure on a fruit fly embryo [82].

3.2.2. Robotics

Many other robotics applications, reaching beyond medical robotics, have been proposed for IPTs. They include robot designs that are capable of carrying their own bodyweight. Yamakita *et al.* simulated a biped walking robot [83], and later also performed a preliminary walking experiment reporting a 5 or 6 step sequence [84]. Arena *et al.* used a four-segment 105 mm long IPMC actuator in their externally powered worm-like robot, that carried its own weight and achieved 0.14 mm/s locomotion speed [85]. Hou *et al.* reported preliminary experimental results with an IPMC-actuated amoeba robot [86]. Simulations of another amoeba robot design have been reported by Chen *et al.* [87]. Stasik *et al.* proposed and modelled a self-rolling wheel that uses IPMCs for shifting its center of gravity for locomotion [88].

Flapping wing designs using IPTs have been explored by Lee and Park [89], and Kim *et al.* [90]. The first study used an IPMC-actuated rack-pinion system in their design resembling an insect wing, and achieved 15 degree flapping amplitude at 15 Hz frequency [89]. In the second study, the bending deformation of the actuator was directly transmitted to the attached wings [90]. Unfortunately neither of the devices became airborne.

Some applications have been proposed for robot manipulation. Using elliptic friction drive actuator elements Tadokoro *et al.* proposed and tested a 3-DOF and a 6-DOF IPMC micromanipulator, and reported 2 mm and 0.4 mm maximum displacements respectively [91]. Nakabo *et al.* demonstrated a realization of a multi-DOF manipulator achieved by patterning a single IPMC sample [92]. Kruusmaa *et al.* used short IPMC actuators as joints in a 2-link micromanipulator design [93]. A 2-DOF IPMC-actuated manipulator was also proposed by Mcdaid *et al.*, using a model-free iterative feedback tuning controller in the testing of the prototype [94].

Similarly to the catheter tip and catheteroscope designs introduced in Section 3.2.1, IPTs have been proposed for building end-effectors. Lumia and Shahinpoor built a two- and a four-finger IPMC microgripper, and demonstrated lifting a 10.3 g rock with the latter prototype [95]. Another simple microgripper with 2 parallel actuators was reported by Jain *et al.* [96]. Feng and Tsai reported IPMC micro-tweezers with multiple electrodes on the polymer membrane to achieve clamping functionality and motion in multiple degrees of freedom [97].

A wide range of applications that have been proposed in underwater robotics are overviewed in the next subsection.

3.2.3. Underwater robotics

This subsection explores the numerous studies that have reported utilizing IPTs to provide their biomimetic underwater robot designs with sensing or actuation capabilities. A comparison between some of these designs as well as other solutions utilizing different 'smart' materials has been provided by Chu *et al.*, and it was concluded that IPTs are slower than shape memory alloys (SMAs), but easier to miniaturize, and produce larger strains than lead zirconate titanates (PZTs) and SMAs [67].

Since Shahinpoor proposed to use ionic gel fibers with numerous printed electrodes for a propulsion mechanism of a fish-like robot [17], many similar propulsion techniques exploiting IPTs have been reported. One distinctive design category includes robots consisting of a boat-like buoyant body and an IPT sample to actuate the tail fin(s) for propulsion. Mojarrad and Shahinpoor modelled and experimentally studied the propulsion of a fish-like IPMC caudal fin attached to a styrofoam boat, and reported speeds up to 19 mm/s [98, 99]. Guo et al. used two separately controlled IPMC-actuated tail fins attached to a wooden boat-shaped body in their underwater microrobot design, and reportedly achieved up to 5.35 mm/s speed (dimensions 40 mm by 10 mm) [100]. Later, Guo et al. improved the design with a solenoid-actuated center of mass adjuster and a buoyancy control unit driven by IPMC electrolysis, achieving the speed of 5.21 mm/s (45 mm long, 20 mm wide, 4mm thick) [101]. Laurent and Piat used similar design with two beating IPMC-actuated polyethylene fins attached to a boat-like polyethylene body, and reported the maximum speed of 1.8 mm/s (dimensions 50 mm by 10 mm by 10 mm) [102].

Most common designs of (biomimetic) robotic fish consist of a fish-like body and an IPT-actuated fin(s). This kind of a prototype with a foam body and a trapezoidal IPMC caudal fin has been reported by Paquette *et al.* to experimentally measure its thrust force in a vertically suspended configuration [103]. Later, Kim *et al.* performed a similar study in 3.5 % NaCl solution to demonstrate feasibility of operation in a salt water environment [104]. Another robotic fish prototype was reported by Shen *et al.* [105]. It has a dolphin-like rigid body and an IPMC-actuated flexible caudal fin, and was used to validate their thrust performance model. The tethered 47.5 mm long prototype weighed 5.05 g and achieved the top speed of 46 mm/s.

Several untethered IPT-actuated biomimetic underwater robot prototypes have also been reported. Jung *et al.* and Kim *et al.* studied the motion of their wirelessly controlled tadpole robot prototype consisting of a rigid head and an IPMC-actuated thin polymer film caudal fin, and the 96 mm long robot reportedly achieved the maximum speed of 23.6 mm/s [106, 107]. Tan *et al.* used an IPMC-propelled caudal fin to build a mobile untethered fish-like underwater sensing platform for educational use [108]. The 235 gram 230 mm long prototype achieved 6.3 mm/s peak speed. In an upgraded design a passive plastic caudal fin was used in the tip of the IPMC actuator to improve the swimming efficiency, and the 140 gram 148 mm long robot achieved approximately 22 mm/s maximum speed [109]. A similar robotic fish prototype was modelled also by Chen *et al.* [110]. Hu *et al.* used the model of [109] to simulate their idea of petroleum exploration platform supervision using a swarm of IPMC-propelled robotic fish [111]. Kopman *et al.* modelled the planar locomotion of a remotely controlled IPMC-propelled robotic fish using rigid-body dynamics and validated the results experimentally on a prototype consisting of a stiff body, an IPMC actuator and a passive silicon fin [112]. The 130 mm long prototype weighed 85 g and achieved 7.8 mm/s surge speed. Later, Aureli *et al.* extended the modelling using modal analysis and achieved approximately 12 mm/s maximum surge speed [113, 114].

Not all the biomimetic designs use caudal fin(s) to propel the prototype. Kamamichi *et al.* built a snake-like robot that floats on the surface and consists of three rigid links and two IPMC-actuated joints [115]. The robot weighs 0.6 g and the 120 mm long prototype achieved 8 mm/s speed. Anton *et al.* proposed a ray-like underwater robot with a buoyant body and two pectoral fins, each actuated by two IPMC samples, and reported up to 9 mm/s propulsion speed [116]. Punning *et al.* realized a more complex ray-like underwater robot design using 8 IPMC samples in each pectoral fin, and reported an average speed of 5 mm/s [117]. Later, Chen *et al.* built a robotic manta ray prototype with IPMCs actuating only the leading edges of its polydimethylsiloxane fins and reported 7.4 mm/s swimming speed for the 55 gram and 110 mm long prototype [118]. Yeom and Oh used curved IPMC actuators to build a jellyfish-mimicking robot and reported the maximum vertical speed of 0.057 mm/s [119].

Several reports study the usage of IPTs in underwater robotics without actually building a prototype. Anton *et al.* proposed the usage of short IPMC actuators in a multilink caudal fin design, and demonstrated with analytical modelling and CFD simulations that a two-link tail fin achieves better swimming efficiency than a one-link version [120]. Shen *et al.* used simulations based on the IPMC actuation model of Chen *et al.* [121] to study using PID and fuzzy control on an IPMC-propelled robotic fish [122]. Palmre *et al.* investigated moulding multiple IPMC actuators into a silicone fin in order to produce more complex biomimetic deformations [123].

Besides the fish-like designs, also walking IPT-enabled underwater robots have been reported. Kim *et al.* used custom-made 1.15 mm thick IPMCs to construct a walking ciliary 8-legged microrobot, that was 65 mm long, weighed 4.4 g and achieved speeds up to 17 mm/min [124]. Another design of an 8-legged walking IPMC microrobot was reported by Guo *et al.* in [125], and the 33 mm long prototype achieved 8.3 mm/s walking speed. A fully IPMC-bodied quadruped robot constructed from patterned and shaped IPMC samples by Tomita *et al.* (maximum length 53 mm) was demonstrated to walk like a turtle with maximum velocity of 0.936 mm/s [126]. Shi *et al.* used 10 IPMC samples in their two different designs of underwater microrobots capable of various types of locomotion and grasping. Their 60 mm long prototype and 33 mm long prototype achieved walking speeds of 10.5 mm/s and 1.54 mm/s respectively [127, 128]. Chang and Kim made an aquatic walking robot with six 2-DOF IPMC-actuated legs and the 102 mm long robot weighing 39 g achieved 0.5 mm/s speed [129].

3.2.4. Energy harvesting

Since IPTs are capable of converting mechanical energy into electrical, it is natural to explore their feasibility for energy harvesting. Dogruer *et al.* investigated charging a battery from the mechanical stimulation of IPMC materials, compared the performance of the samples with different dimensions and concluded that narrow thick samples charge faster [130]. Tiwari and Kim studied the impact of electrodes and cation species on the charging rate and concluded that larger cations result in a higher charging rate [131]. Later they proposed a disc-shaped energy-harvesting tool for exploiting uncontrolled or multi-directional vibrations [132]. Brufau-Penella *et al.* used a grey-box model to describe IPMC energy harvesting capabilities, and predicted that a $400\mu m$ thick material's maximum power density is $0.25\mu W cm^{-2}$ at the resonance frequency of 24 Hz [133]. Aureli *et al.* modelled IPMC energy harvesting in fluids, and reported that an approximately $1.5cm^2$ material sample generates 1 nW power when vibrating in its second structural mode with 1 mm amplitude [134]. Cha *et al.* modelled and demonstrated underwater energy harvesting from torsional vibrations of a patterned IPMC sample, and reported the maximum power density of $10^{-7} - 10^{-6}\mu W mm^{-3}$ [135]. Jamshidi *et al.* modelled IPTs as energy harvesters in low subsonic flow and reported that a $300\mu m$ thick square sample with 38 mm side length can produce 1.75 mW power [13].

3.2.5. Applications for sensing

While there are numerous applications proposed for IPTs that exploit their actuation capability, benefitting from sensing functionality is much less explored. IPTs have been used as sensors for estimating the velocity in a tactile sensor design by Konyo *et al.* [136]. Paola *et al.* proposed and demonstrated an IPMC-based vibration sensor [137]. Fang and Chen reported preliminary experiments on using IPMCs as impact sensors, e. g. in a shoe [138]. Chew *et al.* proposed using IPMCs for position sensing in the joints of robotic fingers [139]. Ando *et al.* presented a seismic sensor design using IPMCs [140]. Abdulsadda and Tan constructed an artificial lateral line sensor using on IPMCs, and demonstrated its underwater localization capabilities [141, 142]. Zhong *et al.* investigated using IPMC materials for measuring cycle-to-cycle characteristics of pulsating flow [143], and Che *et al.* studied detecting the start and end of the flow [144].

3.2.6. Other applications

All IPT applications cannot be categorized into the previously discussed larger groups, therefore some of them are reviewed in this subsection. These include an IPMC-driven loop-shaped actuator element proposed by Tadokoro *et al.* that produces elliptic motion and is able to drive objects with friction in various designs [145]. Using the actuator element, they constructed a rotary motor prototype that floats in water and achieved the maximum speed of 6 rpm. Similar actuator elements were also used in realizing a distributed drive conveyor belt design and their prototype consisting of 40 elements achieved 0.62 mm/s speed in translating objects [146]. Using another concept Mcdaid *et al.* reported an IPMC-driven stepper motor prototype [147].

In terms of space applications, IPTs have been proposed for dust-wipers in space by Bar-Cohen *et al.* [148, 47], and for actuating inflatable space structures by Tung *et al.* [149]. IPTs could also be used to produce mirrors with controllable focal length. Bao *et al.* proposed and simulated their concept of a parabolic mirror with IPMC-controlled focal length [150]. Kothera and Leo studied using feedback control of a square-plate IPMC actuator for utilizing it in a membrane mirror application [151]. Later, Wei and Su simulated an IPMC-focusable parabolic mirror design and also presented preliminary experimental results obtained on their prototype without a mirror finish [152].

For pumping fluids, Lee *et al*, and Lee and Kim proposed and simulated a micropump design that uses an IPMC as an active membrane [153, 154]. A micropump prototype for drug delivery was built by Mcdaid *et al.*, and online iterative feedback was used to improve its reliability [155]. Further, in terms of fluids, a viscometer design that uses one IPMC sample for generating vibrations and another one for measurements, was proposed by Brunetto *et al.*, and it was validated on sucrose solution to estimate the density and viscosity of the fluid [156].

Some authors have reported studies that are not a potential application, but aim to overcome some limitations or facilitate using IPTs in applications. For example Punning *et al.* demonstrated that using modulated input signal on IPMC actuators reduces their power consumption and peak current consumption [157]. Lee *et al.* designed a microstrip patch antenna into the IPMC electrodes for wireless actuation [158], and Abdelnour *et al.* proposed and experimentally characterized a wireless powering system, and demonstrated it in a flow visualization experiment [159]. Fleming *et al.* proposed to use controlled activation of different segments on a patterned IEAP actuator in order to alleviate back-relaxation effects [160].

Many of the potential applications for IPTs have not been discussed in this overview. Nevertheless, this non-exhaustive overview demonstrated multitude of applications that have been proposed for IPT materials in different fields so far.

3.3. Closed-loop control of IPTs

Open-loop control of IPT actuators frequently does not result in satisfactory performance due to large overshoots and long setting times, while closed-loop configuration offers significantly better results [161, 162], etc. This section reviews the control methods that have been applied on IPTs to improve their performance, various methods that have been used to provide a feedback signal for closed-loop control, studies that have investigated using IPTs both for actuation and sensing, and the efforts to achieve self-sensing IPTs.

3.3.1. Reported control methods

Many closed-loop control methods with various complexities have been applied on IPT actuators. The more conventional methods include using a linear quadratic regulator (LQR) and a state observer to achieve full state feedback [48, 163], lead-lag control [164, 161], PID control [162], PID with integrator anti-windup scheme [165], purely integral gain [166], and combination of (curve-fitted) feedforward and PI feedback control [167]. An adaptive fuzzy control algorithm has been reported by Oh and Kim [168], and Song *et al.* used a repetitive control concept for error reduction in periodic signal tracking [169].

More complex control methods usually aim to compensate for material nonlinearities, and these include robust adaptive control with leakage modification (only simulations reported) [170], quantitative feedback theory robust control [171], operator-based robust nonlinear control [172], integral periodic output feedback control [173], PI control combined with a simplified adaptive inverse control method [174], model reference adaptive control [175, 176, 177], active disturbance rejection control [178], and time-delay control with noise filtering and anti-windup scheme [179]. Sliding mode controllers have been reported by Hao *et al.* [180], and Sun *et al.* [181] (similar to sliding mode control).

3.3.2. Combined sensing and actuation

Some studies have reported utilizing other materials in combination with IPT actuators to achieve compact realization for their closed-loop system. Chen *et al.* bonded a PVDF sample on an IPMC actuator and demonstrated its usability in embryo injection application [82, 182] (patented in [183]), and Leang *et al.* bonded resistive strain gauges on IPMC actuators to achieve integrated sensing for feedback control experiments [184]. As a logical alternative, some works actually utilize IPMC materials in the closed-loop configuration both for sensing and actuation. These studies can be considered as steps towards an integrated IPT sensor-actuator.

Newbury built a motor-like rotary device with 4 IPMCs for actuation and one for displacement sensing [185]. He designed a compensator for the device and reported a performance improvement over the open-loop configuration in sinusoidal reference tracking, but in a very narrow frequency range. Bonomo *et al.* proposed to use IPMCs for vibration control, and demonstrated the idea on an experimental device consisting of two IPMC samples with identical dimensions fastened side-by-side to a thin plastic sheet [186]. The output voltage of the sensor sample was amplified and applied to the actuator, resulting in sustained or damped oscillations upon an external mechanical stimulus, depending on the polarity of the feedback. The sheet deformation during vibrations was not measured and the concept was concluded feasible based on a qualitative evaluation. Gonzalez and Lumia proposed a two-finger microgripper design utilizing one IPMC sample for sensing and another for actuation [187]. Material dynamics was described using empirical models, and the actuator displacement was estimated from the sensor voltage reading. Using a PID controller, they performed closed-loop step response measurements for validating the design concept, but on a different set-up from the proposed design.

A preliminary study on an integrated IPMC actuator/sensor for precision feedback control was presented by Yamakita *et al* [188]. In their experimental work they focused on validating the sensing scheme based on an LTI (linear time-invariant) sensor model in combination with an observer to estimate the bending angle from the sensor voltage reading. A sensing model for the 2 mm by 20 mm material sample was identified from input-output data, and in validation experiments they connected an IPMC sensor and an actuator in parallel, and closed the loop using a PID controller. They reported a 10 s long 0.2 rad amplitude step response and 10 s long 0.2 rad amplitude sinusoidal reference following with approximately 0.2 Hz frequency. In experiments, they used 200 $\mu\mathtt{m}$ thick Au-plated Nafion 117 membrane doped with $\mathtt{Na}^+$ (actuator) and $\mathtt{TEA}^+$ cations. The report is very brief on experimental details and results, and does not disclose implementation details or any further description of the set-up.

3.3.3. Self-sensing IPTs

In self-sensing IPTs, both the actuation and sensing are accomplished using the same material sample. This concept is particularly interesting because it would allow to push the design miniaturization of closed-loop applications to the limits as the need for the challenging sensor integration disappears. Several possible solutions to achieve self-sensing have been proposed.

Punning *et al.* proposed a self-sensing IPMC actuator concept based on the observation that the surface resistance change correlates with IPMC bending, but asymmetrically for stretching and compression [189, 37]. The same design was later used also by Nam and Ahn to conduct preliminary closed-loop experiments [190].

Park *et al.* proposed a self-sensing technique basing on signal conditioning in order to estimate bending deformation from the change in electrical impedance, but presented no experimental validation [191]. A similar approach was hypothesized to be feasible also by Kruusamäe *et al.*, reporting correlation between the bending deformation and impedance of both the whole actuator and its individual electrodes [192].

Nakaido *et al.* proposed to use multiple parallel electrodes on the same polymer membrane to achieve both sensing and actuation functionality within the single material sample [193]. Major limitation of such a design appeared to be electrical interference between sensor and actuator electrodes through the polymer backbone. In order to reduce these interferences Kruusamäe *et al.* added a grounded electrode segment between the sensing and actuating electrodes in their experimental study [194, 195], and presented a preliminary report on modelling their self-sensing patterned IPMC concept in [196].

Ko *et al.* proposed to estimate IPMC bending curvature from the actuator's charge [197]. This was obtained by instantaneously disconnecting the circuit and measuring voltage between the actuator's electrodes. Experimental results confirmed the existence of correlation between the open circuit voltage and the material curvature. Linear relationship between actuator's charge and deformation at extremely low humidity levels was later reported by Sasaki *et al.*, who also demonstrated its usability for control [198]. Unfortunately, these approaches have not been shown to function in the presence of external mechanical disturbances.

3.4. Modelling the materials

This section introduces various models from different modelling approaches that have been used to describe the IPTs. Most of them are derived to capture the sensing and actuation behaviour of IPMCs, but many of them also apply for IPCMCs. This overview includes black-box, grey-box and white-box approaches, and aims to provide context and rationale for the models used in this thesis. The section covering the white-box models also discusses different comprehensions of the processes behind the sensing and actuation phenomena of IPTs.

3.4.1. Black-box models

Black-box linear transfer functions are a simple mean to describe the actuation dynamics of IEAP transducers and many studies have taken advantage of this. Mallavarapu and Leo, and Mallavarapu *et al.* used empirical models identified from step response to describe IPMC actuation dynamics for control design purposes [48, 163]. Bhat and Kim fitted empirical transfer function (fourth order) models to experimentally measured step responses in order to design lead-lag controllers for precision control of IPMC force and displacement [164, 161]. Kothera and Leo used a linear empirical model for IPMC actuation dynamics and reported simulation and experimental results of integral feedback control [166]. Kang *et al.* used experimentally identified empirical models to design and compare the performance of a PID controller and three robust controllers in simulations [199]. Another study that used curve-fitted models to describe IPMC actuation dynamics for control was reported by Shan *et al.* [167].

Some authors have used neural networks to model IEAP transducers. Yanmei *et al.* used them to capture the hysteresis of IPMC [200]. Truong *et al.* constructed an IPMC actuation model based on recurrent multilayer perceptron neural network and self-adjustible learning mechanism, validated it experimentally and further proposed using it as a self-sensing method for position estimation [201, 202]. Later, Truong and Ahn used a general multilayer perceptron neural network model in combination with smart learning mechanism to identify IPMC actuation dynamics [203].

Other black-box modelling techniques have also been used to describe IPTs. Chen *et al.* used Preisach operator to model the quasi-static actuation hysteresis in IPMCs and applied its inverse to improve the open-loop positioning precision [204]. Ahn used a fuzzy model to capture IPMC actuation dynamics that also well accommodated the material's non-linear properties [205]. Caponetto *et al.* identified a fractional order transfer function model from experimental data to describe the IPMC actuation dynamics [206].

3.4.2. Grey-box models

Grey-box models combine the knowledge about materials with experimental data, i. e. the final models are formulated by adding empirical portions to the existing white-box components. Usually they are less laborious to identify and implement than white-box models and possess some advantages over (the least laborious) black-box models, e. g. predict the behaviour of a geometrically scaled material sample, allow to validate some hypothesis, etc. Equivalent circuit models are frequently used for describing either the electrical impedance of the IPTs, or as a component of electromechanical transduction models.

Equivalent circuit electrical impedance models usually describe the current-voltage relationship on the material electrodes. Bonomo *et al.* used nonlinear lumped parameter equivalent circuit models to describe electrical behaviour of IPMC materials [207, 208]. Takagi *et al.* used a distributed parameter equivalent circuit model with irrational transfer function representation to capture the electrical impedance of the IPMC materials [209]. Cha *et al.* used Poisson-Nernst-Planck modelling framework and introduced the electron transportation term to the charge dynamics in the proximity of electrodes in order to derive an electrical impedance model for IPMCs [210]. Based on the analytical model, an equivalent circuit model with lumped elements was proposed (as a resistor in series with a parallel connection of a capacitor and a Warburg impedance element), and experimentally validated.

Many authors have used equivalent circuit models as a part of their sensing or actuation dynamics models. Bao *et al.* used a lumped and a distributed RC line model to describe electrical behaviour of IPMC actuators, and established a simple actuation model using the lumped equivalent circuit model [211]. Kanno *et al.* modelled the dynamics of an IPMC actuator by dividing it into 3 stages: a lumped 10-element electrical equivalent circuit, a mechanical stage with each element divided into 3 layers, and a second order model for current-generated stress [8, 212, 213]. Newbury and Leo used a black-box two-port representation of a linear system to capture both sensing and actuation dynamics of IPMC materials [185], further extended their framework into a grey-box model by including physically meaningful portions to it in [214], and provided in-depth validation in [215]. Akle and Leo modified this model to describe sensing and actuation of their stacked IPMC transducers, both in series and in parallel configurations [216]. Paquette *et al.* combined their equivalent circuit model with an electromechanical coupling model of De Gennes *et al.* [52] to describe the force behaviour of multilayer IPMCs [217]. Bonomo *et al.* modelled IPMC actuation [218], cascading a lumped equivalent circuit model with a mechanical reaction model adapted from [219]. Punning *et al.* proposed an equivalent circuit for IPMCs that accounts varying surface resistance [220], and later modelled the material as a one-dimensional distributed RC transmission line, expressed its non-uniform bending from its current distribution, and demonstrated a delayed and distorted sensing output [221, 222, 223]. Mcdaid *et al.* constructed and validated a three-stage model for IPMC actuation consisting of a non-linear equivalent circuit, an electromechanical coupling transfer function from [218], and a segmented mechanical beam model [224]. Caponetto *et al.* described IPMC actuation by combining an equivalent circuit model from [218] with their electromechanical coupling model [225].

Other grey-box approaches do not explicitly include an equivalent circuit model. Bonomo *et al.* based on the work of Newbury [185], to establish their linear model for IPMC sensing [56]. Brunetto *et al.* used a model for voltage-induced bending from [185] in combination with Euler-Bernoulli beam theory and hydrodynamic function concept, achieving a model of IPMC actuators immersed in viscous fluids [226]. Must *et al.* derived and verified a scalable linear dynamic model of IPMC actuation, linking the actuation voltage to the bending moment and material deformation [227]. Bandopadhya used pseudo-rigid modelling technique to obtain a linear transfer function model for IPMC actuators [228]. Vunder *et al.* modelled IEAP back-relaxation by combining a lumped equivalent circuit model with spring-damper elements [229].

3.4.3. White-box models

White-box models describe the macroscopic behaviour of IPTs trough modelling the physical processes that (are assumed to) occur within the material upon excitation. This section gives a brief overview of reported white-box models and introduces different mechanisms that have been hypothesized to govern the sensing and actuation phenomena in IPMC and IPCMC materials. The summarized reports provide a chronological overview about the derivation of models that are used in this thesis, the studies that provided the basis for their derivation, alternative explanations for sensing and actuation phenomena, the studies that explain the shortcomings of the models used in this thesis, and also the early modelling efforts.

An early study from Shahinpoor reported a phenomenological continuum microelectromechanics model describing the polymer gel strips in electric field, but did not include electrodes yet [230, 231]. Later, Shahinpoor described IPMC actuation using a modification of the classical Euler-Bernoulli beam theory, and modelled the stress generation through Coulombic interactions between charged electrodes (with dendritic structure), mobile cations, hydroxyl anions and immobile cations [232]. A different idea was presented by Asaka and Oguro, explaining the actuation phenomenon through electrokinetically induced pressure gradient and presenting a solution for a step response of an IPMC actuator [51].

A model for IPMC actuation that explains both the fast bending and the slow back-relaxation was proposed by Tadokoro *et al.* [50]. Beam dynamics is omitted and the model explains the initial bending phase by water concentration gradient resulting from ion migration. In the subsequent back-relaxation phase the electrostatic forces acting between fixed sulfonic acid groups on the anode side become dominant, while the excess cation charge on the cathode side is balanced by the negative charge.

Gennes *et al.* presented a linear irreversible thermodynamics model for IPMC actuation and sensing based on Onsager's relations for charge and solvent transportation [52]. According to this static model the actuation phenomenon results from ion migration across the material thickness upon application of voltage, causing water molecules to drag along and thus building a water pressure gradient. Reversely, when the material is bent, mechanical stress creates a water pressure gradient across the material thickness and the migrating water drags along cations, resulting in a voltage between the electrodes. The models express the bending moment in IPMCs due to applied voltage, and the electric field due to the applied moment, both in the undeformed shape of the material.

Nemat-Nasser and Li studied electrostatically induced fast actuation and sensing response of the IPMC transducers [44]. Model development relied on the significance of the clustered morphology within the material, where hydrophilic sulfonate groups form tight clusters (20 - 50 Å diameter) with water inside, and anion-cation pairs are located on their spherical surfaces. Applied voltage results in almost instantaneous cation redistribution, that further causes polymer chain relaxation in the anion-rich region clusters, and extensions in the cation-rich region clusters, resulting in material bending. The sensing phenomenon upon bending of the material is explained through the difference in the deformed shapes of the cluster surfaces and the cation-water medium within the clusters that causes formation of effective electric dipoles, resulting in a measurable voltage between the surface electrodes. Actuation and sensing models are validated based on experimental results from [1] and [43], and the theory accurately predicts that the sensing voltage is two orders of magnitude smaller than the voltage required to produce the same deformation. In the following, some relations established in [44] are brought out, that later became the basis for several other studies. Governing equations for charge distribution were given as:

$$\nabla \cdot \mathbf{D} = \rho; \quad \mathbf{D} = \kappa_e \mathbf{E}; \quad \mathbf{E} = -\nabla \phi, \tag{3.1}$$

where the parameters are: $\mathbf{E}$ – electric field, $\mathbf{D}$ – electric displacement, κ_e - effective dielectric constant of the polymer, ϕ – electric potential, and ρ – charge density. Continuity equation for cation distribution C^+ is given as:

$$\frac{\partial C^+}{\partial t} + \nabla \cdot \mathbf{J} = 0, \tag{3.2}$$

where $\mathbf{J}$ is the ion flux vector that can be expressed as:

$$\mathbf{J} = -d(\nabla C^+ + \frac{C^+ F}{RT} \nabla \phi + \frac{C^+ \Delta V}{RT} \nabla p) + C^+ \mathbf{v}, \tag{3.3}$$

and its parameters are as follows: d – ionic diffusivity, F – Faraday's constant, R – universal gas constant, T – absolute temperature, ΔV – volumetric change, p – fluid pressure, and $\mathbf{v}$ – free solvent velocity. The latter is described by Darcy's law:

$$\mathbf{v} = d_h(-C^- F \nabla \phi - \nabla p), \tag{3.4}$$

where d_h is the hydraulic permeability coefficient, and C^- is the anion concentration.

In further investigation of the micromechanisms dominating the functioning of IPMCs, Nemat-Nasser studied the materials with different polymer backbone and counter-ion combinations [53]. The established actuation model explains the back-relaxation to be caused by extensive restructuring of the sulfonate groups and redistribution of the cations in the cathode boundary layers, that causes pressure reduction. The model was validated against the experimentally measured IPMC response to a 1 V step signal followed by short-circuit at the 31st second.

Farinholt and Leo derived a model describing the charge produced when bending an IPMC sample under short-circuit conditions [233]. In the model derivation, it was hypothesized that the charge accumulation on the polymer surfaces is responsible for the sensing phenomenon. Mechanical deformation and the resulting charge density were related by a proportionality constant. Derivation relied on the field equations 3.1 – 3.4 from the abovementioned studies ([44] and [53]). The following governing PDE describing the charge density was established:

$$\frac{\partial \rho}{\partial t} - d\nabla^2 \rho + \frac{F^2 dC^-}{\kappa_e RT}(1 - C^- \Delta V)\rho = 0. \tag{3.5}$$

It was solved by the separation of variables, and analytical expressions were established for charge density, electric field and electric potential for IPMC sensor in a cantilevered configuration. The model was experimentally validated for geometric scalability on IPMCs doped with four different cation species. Farinholt further elaborates the modelling approach in his thesis in [5] and extends the study by considering the impact of electrical impedance on actuation and sensing.

Weiland and Leo built a computational model to investigate the role of polarization effect in actuation and sensing of IPMCs [234]. A clustered morphology was assumed (as in [44, 53]), polarization effects were hypothesized to be responsible for both actuation and sensing phenomena, and the transport mechanism was hypothesized to dominate the back-relaxation. Results showed that polarization is a feasible explanation for the initial fast bending in actuation, but the same cannot be concluded for sensing.

Based on the abovementioned studies (particularly [44, 52]), Costa Branco and Dente developed a continuum electromechanical model for IPMCs on a macroscale level [235]. According to the model, the forces within the polymer appear due to electrostatic interactions between negatively charged fixed ion groups while the role of the solvent was considered negligible. Within the regions where the cation concentration is higher than anion concentration (near cathode electrode), the net electrostatic forces only act between the cations causing their redistribution while the polymer experiences no forces. In regions with higher anion concentration there exist electrostatic forces that are transmitted to the polymer backbone, causing the membrane to deform. An equivalent circuit model was used to relate the current and voltage. For model validation, the simulation results for quasi-static operation were compared against the experiment results for IPMC sensing current in response to the applied surface pressure, and actuator tip displacement in response to applied current (or voltage). This work was extended by Costa Branco *et al.* in [236], establishing a model for non-uniformly charged IPMC actuators, incorporating the effects of gravity.

The effects of various cation and solvent combinations (in Nafion 117 polymer gel) on the fast bending and the subsequent back-relaxation of IPMC actuators was studied by Nemat-nasser and Zamani [237]. Relying on the earlier modelling work of Nemat-Nasser in [53], the comparison against experimental results showed that the theory correctly predicts the roles of cations and solvents role in actuation, especially on the extent of back-relaxation.

Chen *et al.* presented a transfer function model for IPMC sensing, relating the displacement of the tip of the material beam to the corresponding short-circuit current [57]. The derivation based the governing PDE for charge distribution in equation 3.5 (presented by Farinholt and Leo in [233]), that was solved in Laplace domain. The charge density at the electrode boundaries was considered to be proportional to the mechanical stress, and distributed surface resistance was considered. For implementation purposes the resulting infinite-dimensional transfer function model was approximated to a fourth-order rational transfer function, usable for arbitrary input deformations. In the experimental work, they conducted the model identification, validated its geometric scalability and the significance of the surface resistance effects, and demonstrated the functionality of the model in estimating the applied bending displacement.

Following the sensing model Chen *et al.* published a control-oriented transfer function model for IPMC actuation relating the out-of-plane displacement of the tip of the material beam in response to applied voltage [121]. Its derivation follows similar steps as the sensing model derivation in [57], relying on the same PDE for charge distribution (equation 3.5 [5]). The resulting non-linear analytical actuation model accounting for the distributed surface resistance is reduced to a finite-order rational transfer function for implementation purposes, and cascaded with a second order model describing the beam dynamics. Again, the significance of considering the surface resistance and the geometric scalability were experimentally validated, and the model was demonstrated to be beneficial for H_∞ and PI control design in subsequent closed-loop reference tracking experiments. In their following study, Chen *et al.* reported advances in the derivation of a non-linear control-oriented model for IPMC actuation [238]. It was based on a non-linear circuit model (that was experimentally validated), and on a non-linear PDE governing the charge distribution.

Bufalo *et al.* used the theory of mixtures to achieve a three-dimensional modelling framework describing the static deformations of IPMC actuators [239]. According to the model, hydrophilic cations that migrate towards the cathode in the electric field, also transport the solvent, causing the hydrophobic polymer to expand nearby the cathode, and further resulting in actuation. Using Euler-Bernoulli beam theory and parallel-plate approximation, a one-dimensional model for beam-like IPMCs was obtained from the general framework, and was experimentally validated.

Wallmersperger *et al.* studied the electrical response of a proton-based Nafion ™117 membrane between flat plate electrodes (gold, silver and copper) to identify the impact of material's dielectric permittivity and ion diffusion constant on the behaviour of current and charge density [240]. Electrochemical model simulations were validated against experiments. Comparing the results to actual IPMC samples showed that IPMCs exhibit significantly higher current and charge densities. This is due to the dendritic structure of IPMC electrodes, that results in much higher effective surface areas than flat plates with identical external dimensions. Studies that use external electrode dimensions to calculate electrode surface areas thus reach erroneous values, and in order to match the model with the experimental measurements they report unreasonably high values for the dielectric permittivity and the diffusion constant.

Porfiri used the multiphase mixture theory to establish an electromechanical model for sensing and actuation of thin flat IPMCs at small static deformations [241]. The study aimed to improve the understanding about IPMC behaviour and the role of capacitance in it. According to the calculations using Hashin-Shtrikman bounds, the relative dielectric permittivity of IPMCs should remain between 6.4 and 20, but unrealistically high values are often reported due to erroneously considering the material as a flat-plate capacitor. Processes considered to dominate the actuation and sensing were the chemical-expansion stress and the internal polarization respectively. The study showed that IPMC sensing and actuation efficiencies strongly correlate to the material's capacitance (as experimentally shown by Akle *et al.* [242]), and that the capacitance of an IPMC depends on its dielectric permittivity and boundary layer thickness, and does not depend on material thickness.

3.4.4. Finite element models

Often analytical solutions to material models are too complex or laborious to establish, or are not desiable for other reasons. In this case finite element methods (FEM) become handy in producing computational solutions to existing sets of equations. Using finite element methods to obtain the mechanical response of IPMC actuators to step or sinusoidal inputs has been reported e. g. by Tadokoro *et al.* [243], Leo *et al.* [244], and Wallmersperger *et al.* [245]. Pugal *et al.* used FEM to describe IPMC actuation and self-oscillations due to electrochemical reactions [246, 247], and surface resistance effects were added to their base model in [248, 249]. Three-dimensional transduction of IPMCs was studied by Pugal *et al.* using FEM to estimate both the bending and twisting motions of an actuator with patterned electrodes [250]. Using higher order finite element methods with adaptive multi-meshing has been reported by Pugal [251] and Pugal *et al.* [252]. Caponetto *et al.* added thermal effects to their finite element study of IPMC actuation [253], and investigated the effect of environment relative humidity on the resonant frequency of IPMC actuation [254].

3.5. Phantom materials for validating IPT medical applications

While the limited actuation capabilities of the IPT materials restrict their implementation in many fields, in some applications they may be in fact desirable, e. g. providing intrinsic safety barrier in medical procedures. The preliminary studies on using IPTs in medical applications, reviewed in Section 3.2.1 include multiple works that propose IPTs for invasive medical procedure equipment such as a catheter with IPT guidewire, originally proposed by Guo *et al.* [73]. Testing novel medical equipment and procedures directly on humans is unthinkable for various reasons (safety, ethics, legislation, cost, etc.), and in order to test the aforementioned device and other medicine-related IPT applications in realistic conditions the best solution is to use phantoms. Phantoms are artificial objects that are designed to realistically mimic some specific properties of the living tissues of interest. In order to validate diverse medical procedures that are performed with ultrasound guidance, including catheterization, the necessary phantoms should imitate the mechanical and ultrasound properties of human tissues. The properties that the phantoms need to imitate, and more common phantom material technologies are reviewed in the following.

Young's modulus of different soft tissues has been estimated to vary from 1 kPa to over 1 MPa [255]. Mean elasticities for some tissues obtained using share-wave ultrasound elastography include 2.9 kPa for pancreas, 10.38 kPa for parotid gland, 10.97 kPa for thyroid tissue, 10.4 kPa for masseter muscle, 31.2 kPa for supraspinatus muscle and 51.5 kPa for the Achilles tendon [256]. Depending on the region and presence of pathologies, elasticities in different regions of human kidney remain roughly between 5 to 50 kPa [257]. Requirements for ultrasound properties of tissue-mimicking phantoms have been established by ICRU (International Commission on Radiation Units & Measurements) and AIUM (American Institute of Ultrasound medicine), and ultrasound broadband attenuation should remain between 0.3 – 0.7 dB $dBcm^{-1}MHz^{-1}$, and ultrasound propagation speed of 1540 ± 15 m s^{-1} [258, 259, 260, 261]. More specific figures for the ultrasound properties of various mammalian tissues can be found in [262, 263].

Materials that can be used for mimicking different properties of living tissues may be categorized as hydrogels, organogels and flexible elastomeric materials [264]. Gelatin gels are hydrogels that allow to achieve Young's modulus between 2.5 kPa and 500 kPa, ultrasound broadband attenuation 0.2 – 1.5 $dBcm^{-1}MHz^{-1}$ and ultrasound propagation speed between 1550 m s^{-1} and 1650 m s^{-1} [265, 266]. While simple to manufacture, gelatin gels are susceptible to bacteria and their mechanical material properties vary up to 100 days post manufacturing due to prolonged cross-linking process [266, 265, 267]. Materials similar to gelatin gels include oil-in-gelatin dispersions that have a wider range of elasticity and that to some extent display tissue-like non-linearities [268, 269], and agar gels that also behave more non-linearly and have a higher melting temperature than gelatin gels [265, 267, 270].

Polyacrylamide gels (chemical gels) have very finely adjustable and stable properties and due to their toxicity they are not susceptible to bacteria [271]. Unfortunately they are much more complex to manufacture than gelatin gels [271, 272, 273]. Polyurethane is another very stable material that allows to achieve very low Young's moduli. The swollen segmented polyurethane gels are also ultrasound-compatible, but the complex manufacturing process of such materials usually is a trade secret [264]. Other phantom materials include propylene glycol with gelatinizer [274], gelatin-filled open cell foams [275], polyvinyl alcohols (PVAs) [276, 277, 278], silicon-based rubbers [279], but they either are very complex to manufacture, or do not offer suitable range of material properties. More details on the properties of different phantom materials and how they compare to each other and living tissues can be found in [280, 274, 281].

3.6. Conclusions

This section provided an overview of studies related to different aspects of this thesis. In conclusion, IPMC and IPCMC materials possess attractive novel actuation and sensing properties, but their performance, non-linearities and sensitivity towards the environment are currently significant limitations. The multitude of proposed applications clearly indicates the demand for low-voltage bending sensors and actuators, especially in the field of robotics. However, validation of the proposed applications is usually limited to brief demonstrations, and their feasibility is not systematically analysed. To the best of author's knowledge, none of the proposed applications have been adapted into a commercial use. This indicates that most of these studies count on the advances in material development, while the materials are yet not sufficiently mature for applications. To some extent the non-linearities and sensitivities towards environment can be compensated, and performance can be improved using closed-loop control methods. Keeping the overall dimensions of a closed-loop system compact is challenging. The least performance-degrading solutions include self-sensing and using separate samples of the same material both for sensing and actuation. Precise reference tracking has not been demonstrated with self-sensing in the presence of external disturbances, while promising developments reported with an integrated sensor-actuator made of the same material require further investigation.

For describing sensing and actuation phenomena, black-box, grey-box and white-box models with various levels of complexity have been reported. Particularly interesting for this thesis are the control-oriented models. While sensing and actuation phenomena are not yet fully understood, white-box modelling studies also describe the processes that have been hypothesized to dominate sensing and actuation phenomena.

While in many applications the limited actuation capabilities pose a major limitation and softness may not be advantageous, they may be desirable properties in medical applications providing intrinsic safety measures. In order to validate the potential medical applications of the IPTs in realistic conditions there are several tissue-mimicking phantom technologies available, and the simplest one that meets the most of the potential requirements are the gelatin gels.

4. IPMC-ACTUATED INVERTED PENDULUM

4.1. Introduction

Due to the novel actuation and sensing properties, the IPMC and IPCMC materials have high technological potential for many application (see Section 3.2). Their adaptation for commercial use has so far been delayed due to material properties and the sophisticated dynamic behaviour, but while the improvements are still insufficient, many authors seek for aid in closed-loop control in order to compensate (to some extent) for the limitations, as reviewed in Section 3.3. The performance is usually compared to other control methods or the open-loop configuration, and criteria to meet some actual needs are frequently not established. In application reports the functionality of the proposed designs do not necessarily depend on the actuation performance, e. g. IPT-propelled robotic fish (Section 3.2.3), while it is of paramount importance in others, e. g. surgical robotics (Section 3.2.1). Nevertheless, practicality and feasibility are infrequently considered, virtually relying on advances in material development.

In this study, IPMC actuators are used for stabilizing an inverted pendulum system. This is a real-time critical abstract application with a performance criterion that is simple to validate – stabilizing the system for the entire duration of the experiment, i. e. at least for 5 min. While the task has no direct practical value, it demonstrates the material behaviour in application-like conditions, and to the best of author's knowledge, it is the first successful implementation of IPMC actuators in real-time critical operation. Its feasibility depends to a great extent on the material performance. The lack of or degradation of the performance results in a failure to compensate for disturbances in real time, and the pendulum falls over. Previously, this task has been studied by Anton *et al.* [282], who modelled the system using an empirical model, and were able to stabilize the system for up to 10 s.

The proposed IPMC-actuated inverted pendulum system is realized, its dynamics is modelled, and closed-loop controller is designed and applied as follows. First an empirical model is obtained to describe the IPMC moment generation stage. Next, a 2nd order model is used to relate the cart position to the IPMC's moment. Based on these models the system dynamics is established as a 5th order state-space model, and a linear quadratic regulator (LQR) and state observer are designed. Finally, inverted pendulum stabilization experiments are

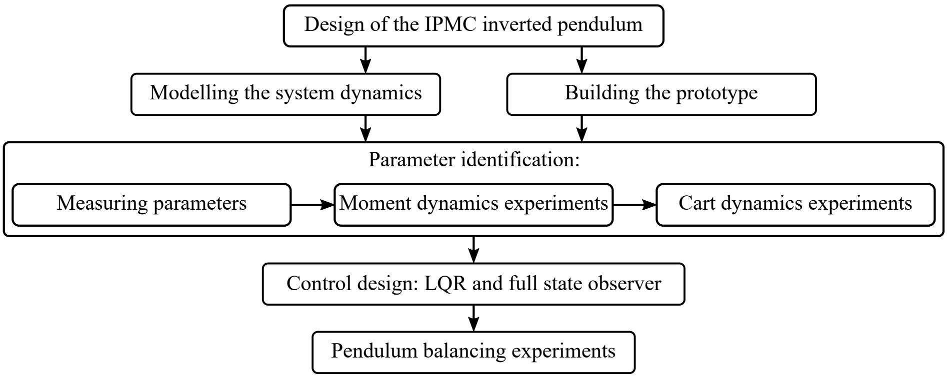

Figure 4.1. Block diagram describing the workflow in this study.

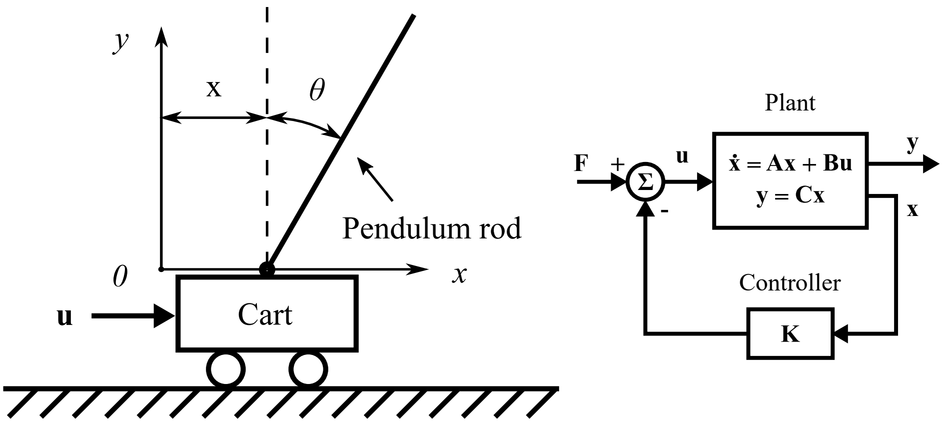

(a) Construction. *(b) Control system.*

Figure 4.2. Classical inverted pendulum problem.

performed. Block diagram describing the work process in this study is shown in Figure 4.1.

In a classical inverted pendulum problem (Figure 4.2) the two objectives are keeping the pendulum upright and maintaining the initial cart position [283]. Achieving them both appeared impossible early in this study due to significant back-relaxation effects that cause variations in the cart position that corresponds to zero input voltage (during actuation). The extent of this effect varies among materials with different ionomer and counter-ion combinations [53]. This issue is circumvented by substituting the measured cart position with the estimated position (Figure 4.3), that effectively allows the cart position to vary within the limits of unmodelled dynamics and disturbances near the initial position while keeping the pendulum upright. Furthermore, this maintains actuation voltages low, increasing material's lifespan and decreasing the power consumption.

The study presented in this chapter is based on publication A.

4.2. Materials

Balancing the inverted pendulum system is accomplished using IPMC material samples provided by Environmental Robots Inc. They are manufactured based on Nafion ™117 polymer backbone, and coated with Pt electrodes. Average thickness of the materials is 360 μm, the counter-ions are exchanged for Li^+ ions, and water is used as a solvent. Thus, they need to be kept hydrated in order to minimize variations in actuation dynamics. In this study the entire set-up is submerged in deionized water and the results reported later are achieved using a 30 mm (width) by 10 mm (height) material sample.

4.3. Design

This section describes the construction of the IPMC-actuated inverted pendulum system. The qualitative design criteria are dictated to a great extent by IPMC properties. The system has to be operated underwater in order to keep the materials uniformly hydrated. This causes undesirable damping due to water drag, while buoyancy compensates some of the mass of the inverted pendulum's rod. Mobile components need to be kept lightweight and miniature in order to maintain low inertia and damping in the IPMC-actuated portion of the inverted pendulum system. Also, the actuator needs to be wide enough to provide a sufficient actuation moment.

A short (and wide) IPMC sample with a rigid extension rod is used for actuating the cart that supports the inverted pendulum, instead of using a long IPMC beam extending from the clamping level down to the cart level. The extension rod with a small cross-section experiences much less water drag than a wide IPMC sample, and it does not bend back, allowing to reduce power consumption and energy loss into the environment. Larger cart displacements are achieved with much less IPMC material. Also, short IPMCs have been shown to work more efficiently and linearly than long ones [49, 93].

The realization of the inverted pendulum system consists of an IPMC-actuated manipulator arm and a lightweight cart-and-pendulum system, as shown in Figure 4.3a. The entire system is submerged in deionized water in a transparent tank (length 130 mm, width 290 mm, height 210 mm), as can be seen in a photo of the set-up in Figure 4.5. The design of the inverted pendulum system underwent through several modification steps, miniaturizing the cart and increasing the actuator width in order to reduce water drag and inertia, and to increase actuation moment.

The purpose of the manipulator arm is actuating the cart (and pendulum) by transforming the IPMC-generated bending moment into force acting on the cart. IPMC-actuated manipulator arm system consists of the following components (see Figures 4.3a and 4.5): (1) A massive vertically suspended clamp with gold electrodes for fixing one end of the actuator to the Earth frame, and supplying power to the actuator. The chassis of the clamp is made of aluminium and

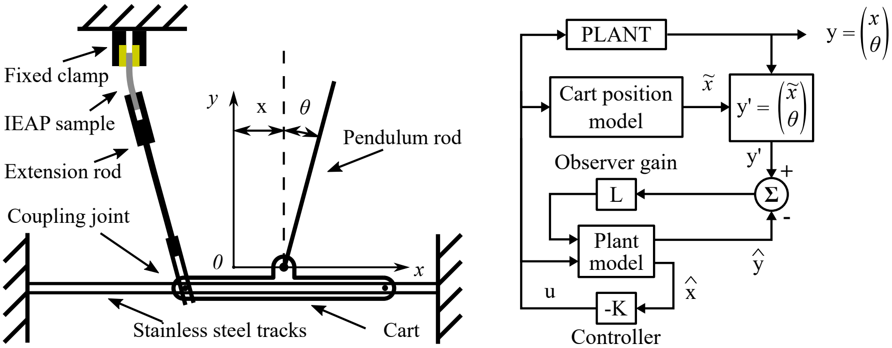

(a) Construction. *(b) Control system.*

Figure 4.3. IPMC-actuated inverted pendulum system.

plastic, and the maximum clamping width is 30 mm; (2) A wide and short IPMC sample (or multiple samples in parallel) for actuating the system, with typical unclampled dimensions of 30 mm by 5 mm; (3) A plastic clamp that mechanically couples the IPMC actuator to the rigid extension rod; (4) A rigid and lightweight carbon fibre extension rod for moving the cart; (5) A fork made of thin plastic sheet that is attached in the tip of the extension rod and couples the IPMC-actuated rod to the axle of the cart with minimum clearance. The total length of the manipulator arm is a trade-off between the achievable actuation force and displacement limits at the cart level.

The cart that supports the inverted pendulum rod is made of carbon fibre elements and two stainless steel rods, the latter acting as the axles that slide on the stainless steel rails (see Figures 4.3a and 4.5). The lightweight cart components are bonded together using a commercial super glue adhesive. The inverted pendulum rod is made of carbon fibre and it attaches to the cart via a low-friction 1-DOF rotary joint that is made of plastic and carbon fibre components. The plastic fork in the tip of the extension rod fits one of the stainless steel axles on the cart, and provides mechanical coupling with the IPMC actuator. The distance from the fixed edge of the IPMC sample to the cart level is 67 mm, and the cart weighs 0.5 g including the weight of the inverted pendulum joint. The inverted pendulum rod is 68 mm long and weighs 19 mg, while the buoyancy compensates 12 mg of it.

Kinematics of the entire system is intended to be constrained to a single plane. The cart slides on two pairs of stainless steel rails that support its axles and constrain its motion to a line. Both the inverted pendulum and the manipulator rod are coupled to the cart (roughly) in its plane of symmetry, and their motions are constrained to the same plane.

4.4. Modelling

A model for describing the dynamics of the inverted pendulum system is established by combining the models of the dynamics of the individual subsystems – the IPMC-actuated manipulator arm, the cart and the inverted pendulum. The input for the system dynamics is the voltage that is applied to the IPMC actuator.

First, the dynamics describing the moment generated by the IPMC sample due to input voltage is captured using an empirical first order transfer function, relating the moment M to input voltage U:

$$\frac{M(s)}{U(s)} = \frac{a}{s+b}, \tag{4.1}$$

where a and b are experimentally identified parameters, and s is the Laplace variable. The first order model in this study is sufficient to describe the IPMC moment generation dynamics, because short IPMCs experience negligible surface resistance effects (a cause for their non-linear behaviour), and they have been shown to perform more linearly than long samples [49]. Furthermore, when considering the actuation model proposed by Chen *et al.* [121], their moment generation model (equation (29) in [121]) also reduces to a first order model when surface resistance effects are ignored and implementation approximations are performed (equations (36) and (37) in [121]).

Next, the passive dynamics of the IPMC-actuated manipulator arm and the cart are combined into a single second order system relating the cart position X to the actuation moment M:

$$\frac{X(s)}{M(s)} = \frac{c}{Is^2+rs+k}, \tag{4.2}$$

where I is the effective moment of inertia of the combined system of the IPMC-actuated manipulator arm and the cart, k is the effective stiffness due to the flexibility of the IPMC sample and gravity acting on the vertically suspended IPMC-actuated arm, c is the gain coefficient that depends on the effective length of the manipulator arm, and r is the effective damping coefficient. Using a proportional damping coefficient is justified due to low cart speeds, and a linear relation between the manipulator angle and the cart position is justified due to small actuation angles.

The model describing the dynamics of the inverted pendulum portion is derived following [283], and after combining these results with equations (4.1) and (4.2), a state-space presentation of the final model is the following:

$$\begin{aligned} \dot{x} &= Ax + Bu, \\ y &= Cx, \end{aligned} \tag{4.3}$$

where x is the state vector with five variables (inverted pendulum angle and its time derivative, cart position and its time derivative, and one state variable from the moment generation model), y is the output vector (inverted pendulum angle and cart position), u is the input vector (applied voltage), and A, B and C are state, input and output matrices, respectively (values reported in publication A).

Hereby the model for the IPMC-actuated inverted pendulum system is established, and the following section describes the control system that is utilized for balancing the inverted pendulum.

4.5. Control system

Based on the inverted pendulum model (equation 4.3), a full state linear quadratic optimal controller (LQR) is designed following [283] and using Mathworks Matlab R2009a software. Additionally, a full state observer is designed (using pole placement technique) in order to avoid measurement noise in the velocities, and estimate the state related to the IPMC actuator moment (equation 4.1). The block diagram of the control system is shown in Figure 4.3b, and more details on the controller, including the controller and observer gains, can be found in publication A.

Hereby, the modelling and control design for IPMC-actuated inverted pendulum system is achieved, and next the experimental set-ups are described.

4.6. Experimental set-ups

Two different experimental set-ups are used in this study, one for measuring the blocked force of the IPMC-actuated arm and the other one for the system identification and closed-loop control experiments. Diagrams demonstrating their arrangements are shown in Figure 4.4.

The blocked force measuring experiments are arranged as shown in Figure 4.4a. The IPMC-actuated manipulator arm is vertically suspended by its clamped end that fixes the assembly to the Earth frame. The mobile end of the manipulator arm is coupled to a force gauge (AD Instruments Ltd MLT0202) by the fork in its tip, and the force gauge is fixed to the Earth frame. The IPMC sample is stimulated with voltage signals from a PC computer with Labview 8.6 environment through a NI data acquisition board PCI-6703 and a custom-built unity gain amplifier based on a LM675 operational amplifier integrated circuit. Simultaneously, the output force is measured using the aforementioned force gauge and digitized using a NI PCI-6034E data acquisition board. The experiment is controlled and the frequency response of the moment generated by the IPMC sample upon excitation is extracted in the NI Labview 8.6 environment.

In the rest of the experiments the inverted pendulum system described in Section 4.3 is submerged in water, and operated from a PC computer with NI Labview 8.6 environment as shown in Figure 4.4b. The actuation of the IPMC sample is controlled via NI PCI-6703 data acquisition board and LM675-based unity gain amplifier. The cart's position and inverted pendulum's angle are

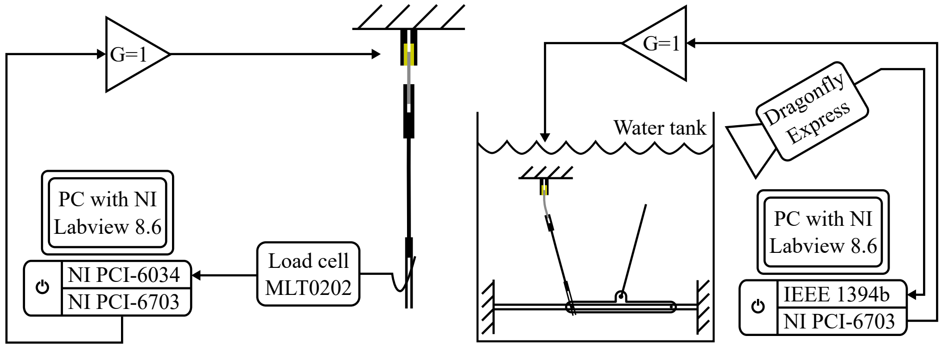

(a) Measuring force. *(b) All other experiments.*

Figure 4.4. Experimental set-ups used in this study.

measured using a high-speed camera Dragonfly Express via IEEE1394b interface at 120 Hz and 130 Hz framerates. An image of the inverted pendulum system during the operation is shown in Figure 4.5. Results are processed and saved using NI LabView 8.6 environment, and in all the experiments the actuation voltage saturation limits are set to $\pm$ 4.0 V.

These experimental set-ups are utilized in the system identification and inverted pendulum stabilization experiments, that will be described in the next two sections.

4.7. System identification

This section introduces the routines that are followed in order to identify the parameters of the inverted pendulum system model derived in Section 4.4.

First, the parameters are identified for the IPMC moment generation dynamics described in equation 4.1 in Section 4.4. This is accomplished using the blocked force measurement experimental set-up shown in Section 4.6 and Figure 4.4a. The frequency response of the IPMC-generated moment is experimentally measured by exciting the IPMC actuator with sinusoidal voltages at 10 different frequencies, logarithmically distributed between 0.1 Hz and 30 Hz at 1.5 V amplitude, and simultaneously measuring force at the tip of the extension rod. Magnitude and phase information are extracted from the measurement results using NI Labview 8.6 software. Since the load cell is not waterproof, measurements are only taken at 10 frequencies, in air. Parameters a and b (equation 4.1) are curve-fitted to experimental data using *fminsearch* function in Mathworks Matlab R2009a software, minimizing the error between the experimental data and the achieved model.

Next, the model parameters are identified for the combined system of the IPMC-actuated arm and the cart. The model is given in equation 4.2 in Section 4.4, and the identification is performed using the final experimental set-up, described in Section 4.6 and Figure 4.4b. The inverted pendulum is removed from the cart for the identification experiments, and the frequency response of the manipulator-cart system is measured by exciting the actuator with sinusoidal input voltages at 20 frequencies logarithmically distributed between 0.1 Hz and 10 Hz at 2.5 V amplitude, and simultaneously measuring the cart position. Gain coefficient c is calculated from the effective length of the manipulator arm. Cascading the previously identified moment generation model (equation 4.1) with manipulator-cart dynamics in equation 4.2 allows to obtain the unknown parameters (I, r and k) by curve-fitting (again, using Matlab function *fminsearch*) the cascaded model to the experimentally obtained magnitude and phase characteristics.

Once the system identification is complete the controller is designed according to Section 4.5 and inverted pendulum stabilization experiments are conducted as described in the following section.

4.8. Inverted pendulum stabilization experiments

After the inverted pendulum system is built, its model is identified and the controller along with the state observer is designed (see Section 4.5 for details), the inverted pendulum stabilization experiments are conducted. System construction and control configuration is shown in Figure 4.3, the experimental set-up is given in Figure 4.4b, and a photo of the completed system is shown in Figure 4.5.

In the earlier stages of this study the IPMC-actuated inverted pendulum system was provided with zero pendulum angle and zero cart position as the references, alike in a classical inverted pendulum problem [283]. However, soon after the experiment was started the actuation voltage saturated while the cart was at the reference position. The position could not be maintained, and the pendulum fell over. As described in the introduction of this chapter, this issue is circumvented by using a model-estimated cart position instead of the measured cart position, essentially allowing the cart position to vary within the limits of the unmodelled dynamics and disturbances while keeping the actuation voltage near zero. Using the model-estimated position instead of the measured position allows to successfully balance the IPMC-actuated inverted pendulum system.

The experiments are performed using a PC computer with NI Labview 8.6 software, that controls the experiments, saves the results, and performs preliminary processing. During the experiments it is possible to switch between the measured cart position and the respective model estimation, and immediate improvement in performance and reduction in actuation voltages are seen when the switching from the measurement to the model estimation is performed early during the experiment, before the pendulum falls over.

The experimental results for the IPMC-actuated inverted pendulum system are presented in the following section.

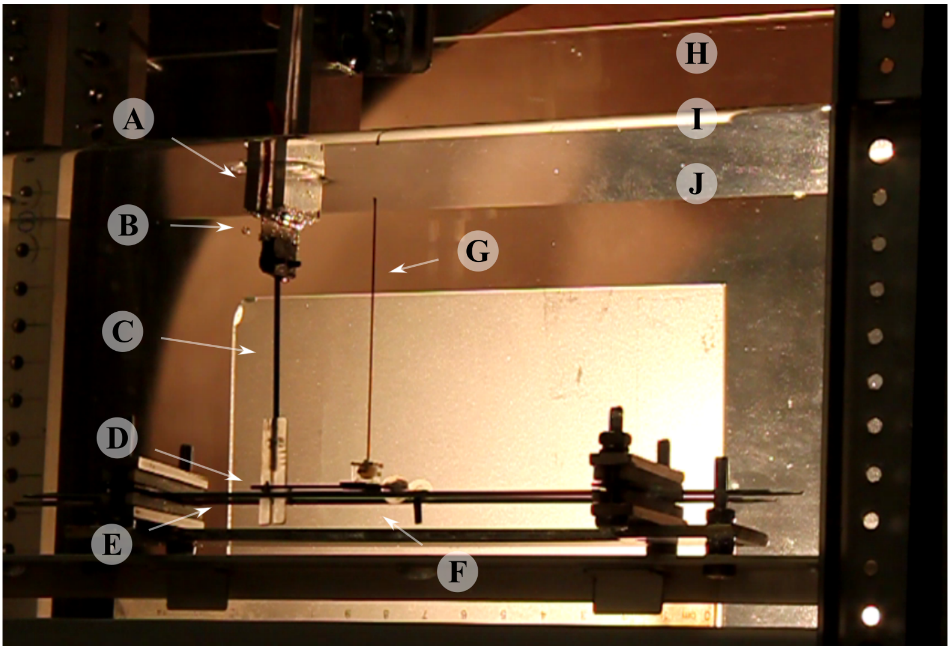

Figure 4.5. Final experimental set-up: A – fixed clamp that provides electrical contacts; B – IPMC actuator(s); C – rigid extension rod; D – groove joint coupling the extension rod and an axle of the cart; E – stainless steel rails that support the cart; F – cart; G – inverted pendulum; H – air; I – water surface; J – water.

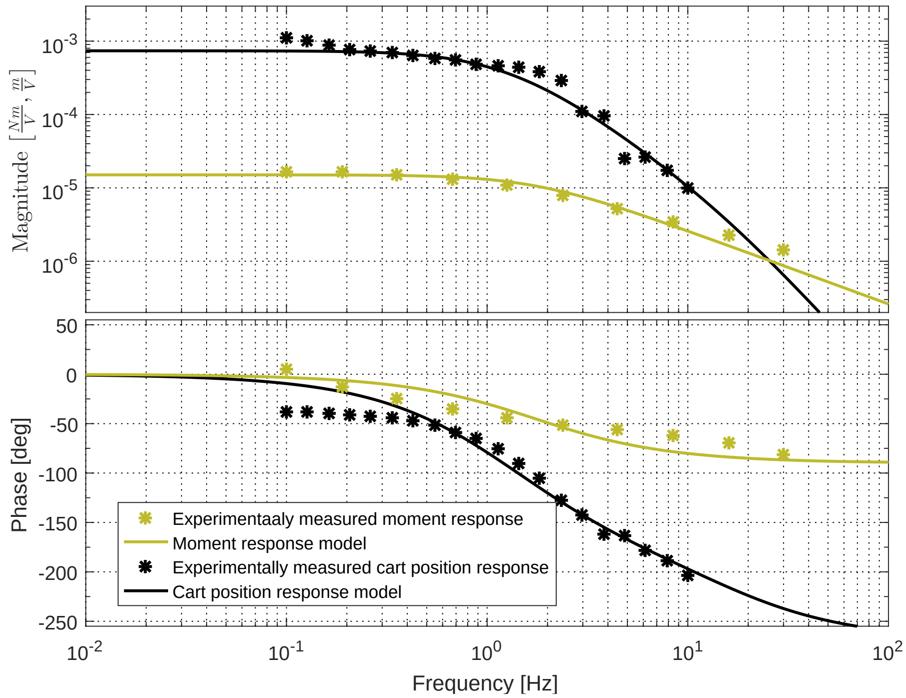

Figure 4.6. Experimentally measured frequency responses of the actuation moment and cart position in response to the input voltage, and the respective models.

4.9. Results

The results with the IPMC-actuated inverted pendulum system are obtained using a 30 mm by 10 mm IPMC sample, described in more detail in Section 4.2. System identification results, i. e. the experimentally measured frequency responses and respective curve-fitted models for moment generation dynamics and cart actuation dynamics are shown in Figure 4.6, while the full final model for the complete system can be found in publication A.

In the preliminary experiments of stabilizing the inverted pendulum system, the reference position for both the inverted pendulum and the cart is zero. In this case, it is not possible to stabilize the system for any longer than 10 s, and similar results were also reported by Anton *et al.* [49]. Cart position corresponding to zero input voltage deviates from the initial position due to material non-linearities (back-relaxation effect), controller output voltage saturates, and the stabilization experiment fails.

When using the model estimation instead of the measured cart position (see Section 4.8) the inverted pendulum can be kept upright for the entire experiment duration of 5 min. Following a series of 5 min long experiments, also a successful 30 min long stabilization experiment is performed, but the following 30 min long experiments fail (due to material performance degradation). The

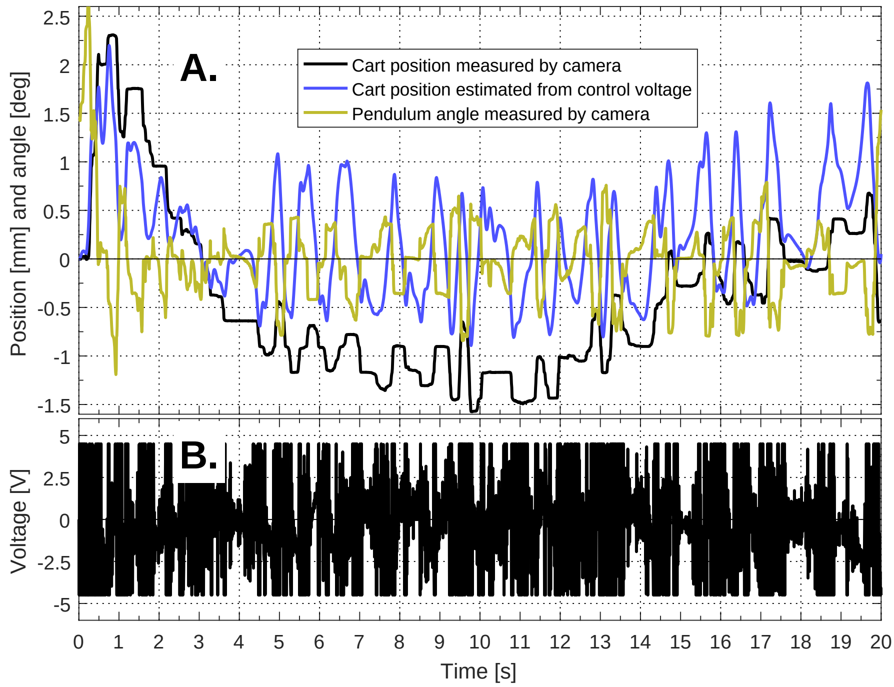

Figure 4.7. Experimental results of balancing the IPMC-actuated inverted pendulum system. Measured and estimated cart positions, pendulum angle and control voltage are plotted for the first 20 s of the experiment.

typical behaviour of the cart position, its model estimation, pendulum angle and control voltage can be seen in Figure 4.7, showing a fragment of the first 10 s of a stabilization experiment. A video of another such experiment is available online [284].

During the experiments, the cart position and the pendulum angle do not remain stationary, but exhibit visible fluctuations that are also seen in Figure 4.7. It is also observed that throughout the experiments the materials gradually lose their actuation performance, initially requiring increasingly higher voltage to stabilize the system, gradually reaching voltage saturation limits more often, and eventually failing to stabilize the system. Formation and separation of bubbles is also observable on the surface of the IPMC sample, indicating the occurrence of electrolysis at higher actuation voltages.

4.10. Discussion

The IPMC-actuated inverted pendulum system presented in this study demonstrates the capabilities of the IPMC materials in more complex application-like conditions in closed-loop real-time tasks operating near the material's performance limits, and is not intended to solve any particular practical problem. While the design provides relatively little quantitative information about the IPMC performance, and has been improved on several occasions before successful experiments were accomplished, these results offer qualitative information on IPMC behaviour when operating at high voltages near the limits of the material capabilities. Validating whether the IPMCs are capable of balancing the inverted pendulum system is straight-forward (pass or fail).

As can be seen in the system identification results in Figure 4.6, the moment dynamics and cart position dynamics models well approximate the respective experimental measurement results. The designed controller, the state observer and the control system allowed to successfully stabilize the IPMC-actuated inverted pendulum system for the entire experiment duration.

Slow fluctuation in the cart position is caused by material unmodelled non-linearities. Fast fluctuations in the cart position and pendulum angle (Figure 4.7) can be explained as a combination of multiple factors, including external disturbances, a slight deviation in camera alignment, relatively low angle and position reading resolution and speed, voltage saturation limits, deviation in IPMC properties due to high actuation voltages, unmodelled system dynamics and respective control design deviations from the optimum, etc.

In order to produce sufficient actuation moments and deformations it is necessary to use high actuation voltages on the IPMC sample. This causes the occurrence of electrolysis within the material, presumably further causing loss of counter-ions and subsequent performance degradation to the point where the IPMC cannot stabilize the inverted pendulum any more. This hypothesis is supported by that the actuation capability is re-established after performing an ion doping process.

In this study the real-time task of stabilizing an inverted pendulum system is successfully achieved using IPMC transducers. The back-relaxation effect that causes significant change in the cart position that corresponds to zero input voltage is too strong to compensate it only with a closed-loop controller, and this issue is circumvented by using a different control strategy that sacrifices the cart positioning accuracy in order to keep the inverted pendulum upright. This phenomenon may pose a significant limitation in applications requiring accurate positioning. The inverted pendulum system is repeatedly balanced for the entire 5 min experiment durations, and also for a 30 min experiment duration, that is much longer than anticipated. However, the gradual performance degradation that speeds up at higher operational voltages makes it challenging to realize the applications that require long-term operation from the materials.

4.11. Conclusions

This study aims to qualitatively investigate the behaviour of the IPMC materials in application-like conditions by operating a real-time-critical closed-loop system close to the material performance limits. The suitability of IPMCs to solve the task of balancing the inverted pendulum system is simple to validate,

i. e. pass or fail. It is not intended to solve any particular real-life problem or quantitatively characterize the material performance. The IPMC-actuated inverted pendulum design is proposed and implemented, a fifth order state-space model is established to describe the dynamics of the system, model parameters that are not defined by the design are obtained from system identification experiments using curve-fitting, a linear quadratic optimal controller and state observer are designed for the system, and the inverted pendulum is successfully stabilized in the final experiments. Maintaining the inverted pendulum upright by an IPMC actuator is achieved repeatedly for the entire duration of the 5 min long experiments, and once for the entire duration of a 30 min long experiment. Due to the non-linear behaviour of the IPMCs it is necessary to allow the cart position to vary within the limits of unmodelled dynamics in order to be able to stabilize the system for any longer than 10 s.

In addition to low actuation moment the primary limitations that are encountered in this work are material degradation and back-relaxation. IPMC performance degrades rapidly when actuation voltages are beyond electrolysis threshold, most probably due to loss of counter-ions. The back-relaxation is known to vary for different materials [53], and its unexpectedly significant extent is probably also due to high operation voltages.

Closed-loop control studies that consider IPMC and IPCMC transducers usually concentrate on controlling the force or displacement of the actuator itself, but in this work a more complex system is controlled using IPMCs, requiring continuous real-time intervention. Using closed-loop control is not sufficient to overcome the material non-linearities, but the main goal of stabilizing the inverted pendulum is achieved by modifying the control system. Performance of the IPMC actuator can be characterized by experiment durations. Stabilizing the system is demonstrated for up to 30 min long experiments, and repeatedly in 5 min long experiments. Considering the material properties these results are better than anticipated.

5. INTEGRATED IPT SENSOR-ACTUATOR

5.1. Introduction

This study focuses on realizing an integrated sensor-actuator design using IPCMC materials. Using external devices for providing IPT actuator systems' position feedback is cumbersome (see Section 3.3.1), and integrating other materials with IPTs significantly limits their actuation capabilities (see Section 3.3.2). At the same time, progress toward a functioning IPT self-sensing solution is slow (Section 3.3.3). Therefore, it is reasonable to use IPTs for both sensors and actuators in designs that aim to benefit from the novel properties of the IPTs and require both actuation and sensing functionalities. However, the only report that proposes an integrated IPMC actuator/sensor concept and investigates its closed-loop control [188] is very laconic on results and does not disclose any details of the design (see Section 3.3.2). Self-sensing on the other hand has not so far been demonstrated to function in the presence of external disturbances (Section 3.3.3).

This work intends to design and realize a functional IPCMC-actuated closed-loop system that can accurately follow the reference position using feedback from an IPCMC sensor. Such an integrated sensor-actuator serves to validate the feasibility of using IPTs for sensing and actuation within the same device, and in closed-loop applications requiring accurate positioning. The validation would result in a preliminary (qualitative) characterization of such a design concept in terms of reference following (for sinusoidal inputs at multiple frequencies) as well as the design's potential limitations.

The work in this chapter is performed as follows. The design of the integrated IPCMC sensor-actuator prototype is realized using two mechanically coupled and electrically isolated IPCMC samples. It resembles a 1-DOF rotational joint with a rigid link attached. The sensor-actuator's actuation and sensing dynamics are captured using empirical models identified from experimental frequency response measurements. A PI controller is designed and closed-loop experiments are performed to validate and evaluate the design. Results show that the device works well in short experiments, but in longer runs its reference following is disturbed due to low-frequency noise in the sensing signal. A block diagram illustrating how different parts of this work are linked is shown in Figure 5.1.

This chapter is based on the work reported in publication B, which is also partially based on the author's master thesis in [285].

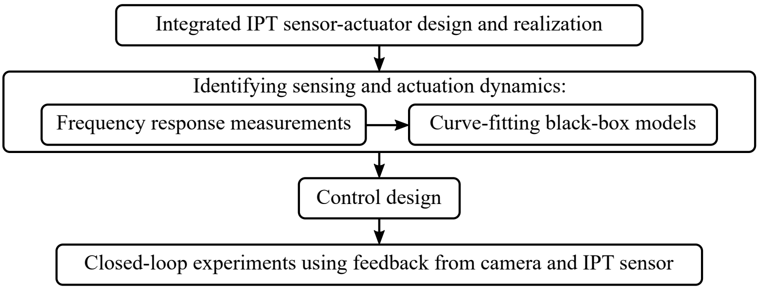

Figure 5.1. Workflow of this chapter.

5.2. Materials

The IPT sensor-actuator prototype is built using IPCMC materials provided by Intelligent Materials and Systems Laboratory, University of Tartu. These materials are manufactured basing on Nafion™117 polymer membrane that is treated with $LiClO_4$, coated with coconut shell derived active carbon electrodes, and further coated with a thin gold foil [9]. Carbon electrodes are applied using the direct assembly process (DAP), and thin gold foils are added on top of them by hot-pressing in order to reduce surface resistance. Emi-Tf ionic liquid fills the purpose of both the counter-ions and the solvent. These materials have a very low surface resistance and they can work in dry environments due to the low vapour pressure of the ionic liquid. More information on the background, construction, manufacturing and properties for these materials can be found in Section 3.1.

5.3. Design

The IPCMC-driven integrated sensor-actuator is intended to achieve simultaneous sensing and actuation using only IPCMC materials and to work as a 1-DOF rotational joint. The design of a device that meets these requirements is given in Figure 5.2 and a photo of the completed prototype is shown in Figure 5.3.

The prototype consists of: (1) two IPCMC samples with equal lengths (10 mm), a narrow one for sensing (width 2 mm) and a wide one for actuation (width 10 mm); (2) a spring-loaded clamp (maximum clamping width 16 mm) that fixes the samples to the Earth frame by one end, provides electrical connections to both samples, and allows quick assembly; (3) a lightweight plastic clamp that couples the free ends of the IPCMC samples mechanically together while keeping them electrically isolated (face dimensions 16 mm by 9 mm); and (4) a lightweight rigid rod (length 55 mm) that is attached to the mechanical coupler, and serves as a rigid extension that is actuated by the IPCMC actuator and whose tip position can be measured. Such a sensor-actuator design with short IPCMC samples positioned side-by-side on the same plane allows the sensor to closely

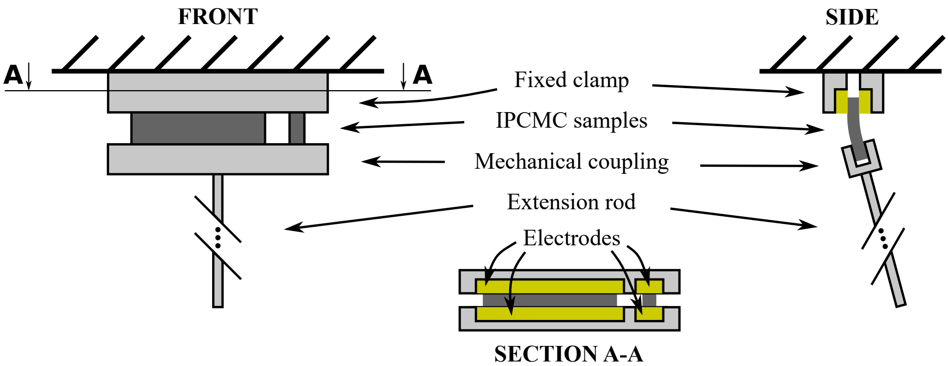

Figure 5.2. Design of the IPCMC integrated sensor-actuator prototype.

follow the shape of the actuator, resulting in an accurate feedback signal. Using a narrow sensor sample keeps its mechanical impact on the actuation small. The operational length of the IPCMCs, i. e. length of the unclamped portion varies between 3 mm and 7 mm, allowing to achieve a good electrical contact between the clamp and the material surface (the gold foil easily wears off on these samples).

5.4. Experimental setup

Model identification and closed-loop control experiments in this study are performed using a single experimental set-up shown in Figure 5.4. All experiments are controlled from a PC computer with NI Labview 8.5 environment, NI PCI-6703 and PCI-6034E data acquisition boards, and an IEEE 1394b port. The IPCMC sensor-actuator assembly is suspended vertically in air by the spring-loaded clamp, and the position of its tip is measured using an IEEE 1394b camera (Dragonfly Express, Point Grey Research Inc.), such that one pixel size corresponds to 0.19 mm on the sensor-actuator plane. In order to actuate the system, a controlled voltage input, directed through a unity gain amplifier (based on LM675T operational amplifier), is applied to the wider IPCMC sample using the NI PCI-6703 data acquisition board. Short-circuit current of the IPCMC sensor is converted to voltage and amplified by 120 000 using an amplifier circuit based on OP275G operational amplifier, before it is digitized using the NI PCI-6034E data acquisition board.

5.5. Identification of actuation and sensing dynamics

Due to their low complexity and quick parameter identification process, linear empirical transfer function models are used to capture the sensing and actuation dynamics of the device. Short material samples have been shown to behave more linearly than long ones [49], and disregarding material non-linearities

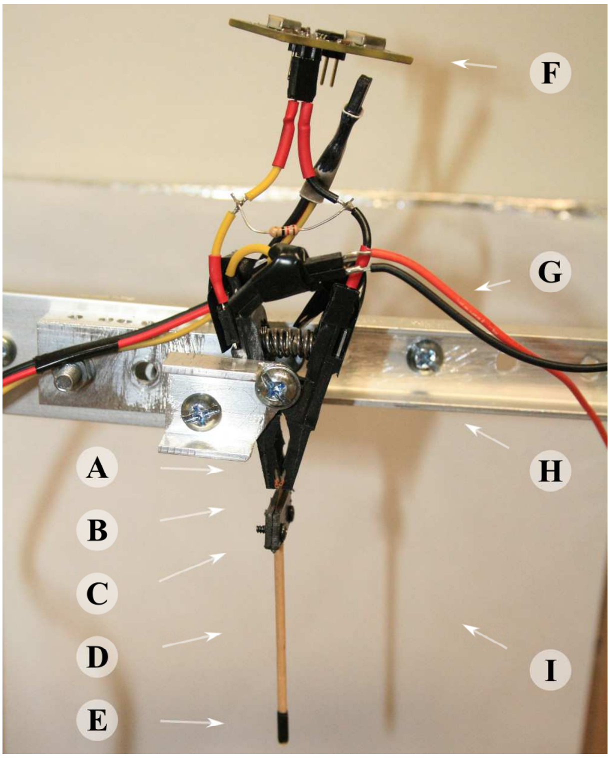

Figure 5.3. Side view of the integrated IPCMC sensor-actuator prototype. A – spring-loaded clamp with electrical terminals; B – IPCMC samples (side-by-side); C – clamp that couples free ends of the IPCMC samples mechanically together; D – rigid extension rod; E – tip of the rod is black for camera tracking; F – IPCMC sensing amplifier board; G – wires for powering the actuator; H – supporting structure fixed to the Earth frame; I – uniform white background that is backlit during experiments.

also simplifies the modelling. Experimental work for model identification is performed using the set-up described in Section 5.4, first identifying the actuation and then sensing dynamics model.

Identification of the actuation dynamics starts with measuring the respective frequency response. This is performed by applying sinusoidal voltages with 2 V amplitude and 30 s duration at 20 different frequencies, logarithmically distributed between 0.1 Hz and 15 Hz. Simultaneously, the position of the tip of the rigid extension rod is measured. Magnitude and phase information for the relation between the voltage and the position is extracted from these measurement results using NI Labview 8.5 software. A finite-dimensional rational transfer model is fitted to the obtained frequency response using *invfreqs* function in Matlab R2008a software.

Measuring the frequency response for the sensing dynamics is performed similarly to the actuation. Short-circuit current of the IPCMC sensor and the position of the rigid extension are simultaneously measured while the

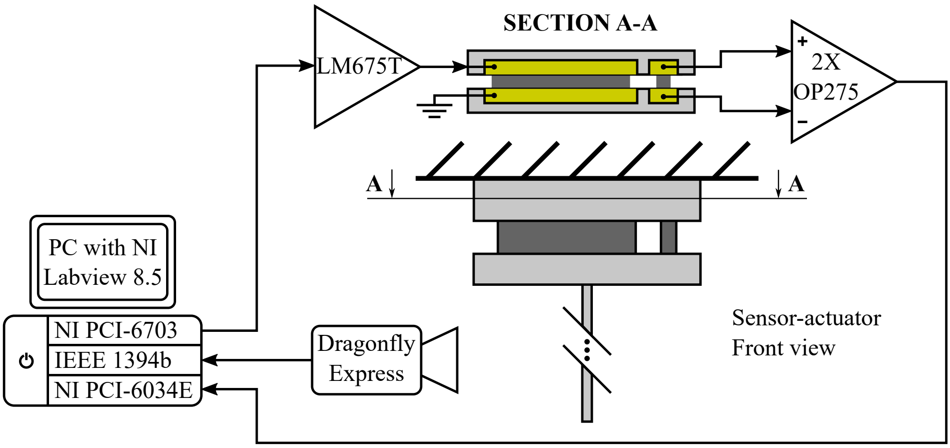

Figure 5.4. Experimental set-up.

sensor-actuator prototype is actuated at 20 different frequencies logarithmically distributed between 0.1 Hz and 8 Hz, at 2 V amplitude. A wider interval is not used because the measurements become excessively noisy at higher frequencies, as the actuation amplitude and the sensing signal respectively approach the camera's resolution limit (0.19 mm per pixel) and the measurement noise level. Nevertheless, such a frequency interval is sufficient to capture the important characteristics of sensing dynamics. An empirical transfer function model is obtained for the inverse of the sensing dynamics using Matlab R2008a function *invfreqs*.

5.6. Control

A manually tuned PI controller is used in closed-loop experiments with the integrated IPCMC sensor-actuator. It is easy to design and simple to implement, and well meets the needs of this preliminary study. Control design is performed in NI Labview 8.5 simulation loop, where the actuation model, cascaded with the controller, is running in unity feedback configuration. Controller parameters are manually tuned while observing the system's response to reference signals. In the experimental part of the work the unity gain feedback is obtained using a camera and an IPCMC sensor. The block diagrams of the respective control systems are shown in Figure 5.5.

5.7. Closed-loop experiments

Closed-loop experiments on the IPCMC sensor-actuator prototype (described in Section 5.3) are performed with experimental set-up described in Section 5.4. System responses are measured for sinusoidal reference signals with 0.1 Hz, 0.5 Hz and 1 Hz frequencies using feedback signals both from the IPCMC actuator

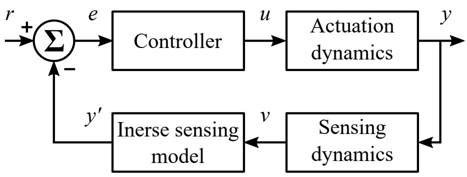

(a) IPCMC feedback.

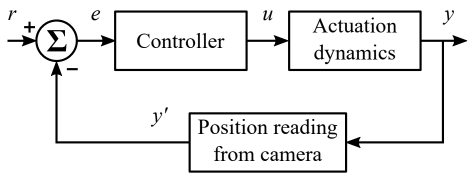

(b) Camera feedback.

Figure 5.5. Closed-loop configurations in the experiments.

and camera in order to establish basis for comparison. Respective control system block diagrams are shown in Figure 5.5.

In the first set of closed-loop experiments the position feedback signal (i. e. the position of the tip of the sensor-actuator) is obtained from the camera image (block diagram of the control system is given in Figure 5.5b). This allows to validate the designed controller, fine-tune its gains if necessary, and establish a reference to which the closed-loop results with IPCMC feedback can be compared to. In these experiments the position estimation from the IPCMC signal is also recorded for comparison.

Finally, the integrated IPCMC sensor-actuator feedback control experiments are performed, using the position estimated from the IPCMC sensing signal for feedback (control system diagram in Figure 5.5a). This is accomplished by passing the IPCMC short-circuit current measurement through a real-time simulation of the inverse of the sensing dynamics model (model described in Section 5.5). Position readings obtained from the camera are also recorded and used for comparison.

5.8. Results

The results reported in this study are obtained using the IPCMC materials described in Section 5.2. The same experiment series have also been performed using other IPCMC materials, i. e. with TiC derived carbon, anhydrous RuO_2 and hydrous RuO2 $_2$ electrodes [9] instead of the coconut shell derived activated carbon electrodes, but due to the very noisy sensing signal of these materials the experiments were unsuccessful and therefore these results are not reported here.

Experimentally measured actuation and sensing dynamics (process described in Section 5.5) are given along with the respective empirical models in Figure 5.6. After designing the controller (see Section 5.6), the closed-loop system (i. e. a cascade of the PI controller and the actuation model in unity feedback configuration) is simulated using sinusoidal input signals with the same frequencies that are used in the experiments (0.1 Hz, 0.5 Hz and 1 Hz). The results of these simulations are shown in Figure 5.7. Next, the experiments are conducted on the actual IPCMC sensor-actuator prototype, as described in Section 5.7. Results of the experiments using the camera for feedback (block

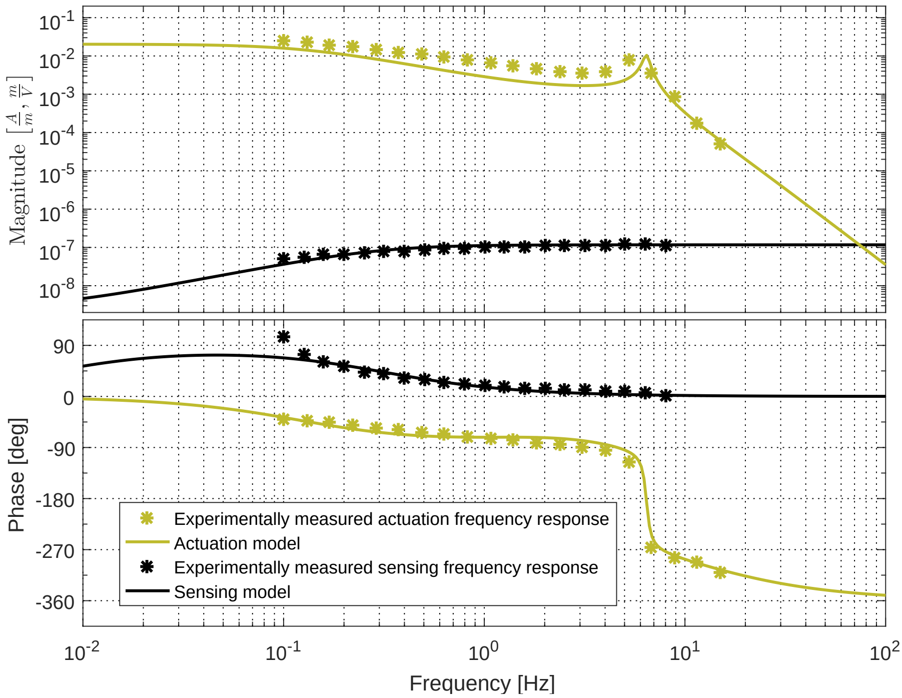

Figure 5.6. Experimentally measured frequency responses of the sensing and actuation dynamics of the integrated IPCMC sensor-actuator prototype, and the respective curve-fitted models.

diagram in Figure 5.5b) are given in Figure 5.8, and results for IPCMC sensor feedback experiments are presented in Figure 5.9. In the closed-loop experiments with IPCMC feedback a low-frequency drift in the estimated position signal is observable. It causes the actual position to slowly deviate from the reference, eventually saturating the actuator voltage and causing the experiments to fail. Experiment durations of 45 s at 0.1 Hz, 2 min at 0.5 Hz, and 60 s at 1 Hz respectively are achieved before the control signal saturates and experiments are halted to prevent material damage.

5.9. Discussion

As can be seen in Figure 5.6, the models for sensing and actuation dynamics have discrepancies with respect to the measurements, but for this study they approximate the experimental results sufficiently well. Discrepancies in actuation magnitude are compensated by controller fine-tuning in experiments with camera feedback, and the error in sensing dynamics phase is considered insignificant. The simulations (Figure 5.7) are performed using the fine-tuned controller gains, and discrepancies in the reference tracking are caused by modelling errors, voltage saturation limits and consequent relatively low gains. The latter allows

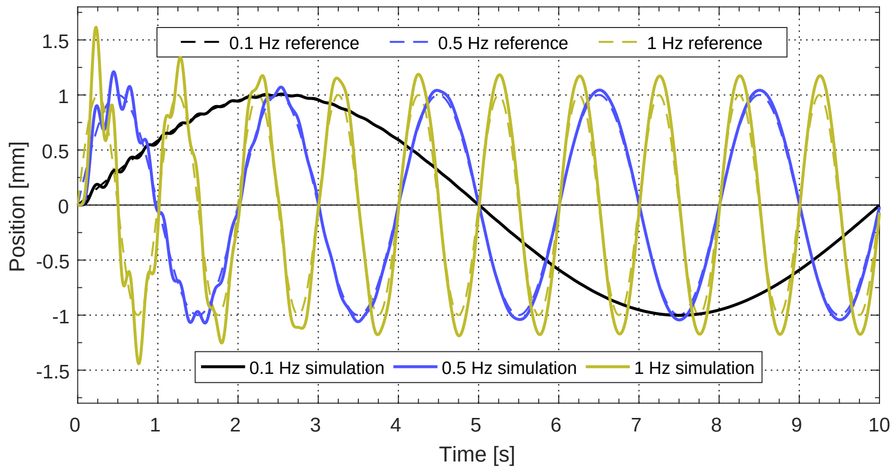

Figure 5.7. Simulated response of the IPCMC sensor-actuator prototype actuation dynamics with the PI controller for three sinusoidal reference signals with different frequencies.

to prevent material deterioration in the experiments. Frequencies below 0.1 Hz are avoided in the experiments because the material non-linearities (e. g. back-relaxation [28]) manifest themselves stronger in the lower frequency range.

In the closed-loop experiments with feedback from the camera (Figure 5.8) it can be seen that the modelling error in the sensing dynamics model at 0.1 Hz frequency (frequency response in Figure 5.6) has a noticeable effect on position estimation while at other frequencies the estimation is reasonably accurate. The controller is seen to perform well, and the tracking errors are insignificant considering the properties of IPTs (Section 3.1), generally remaining within the distance corresponding to a single pixel (0.19 mm).

Results for the closed-loop experiments with IPCMC sensor feedback (5.5a) show that the errors between the IPCMC position estimation and the reference signal are similar to the errors between the camera-estimated position and the reference signal, indicating that the control performs equivalently in both experiments. Also, an IPCMC sensor offers better position resolution than the camera. Discrepancies between the camera measurements and the IPCMC estimation are observable, and they are the reason for the IPCMC feedback to perform inferior to the camera feedback. Tracking results at 0.1 Hz and 0.5 Hz indicate that the sensing dynamics of the IPCMC sensor changes, as the camera measurements have become larger than the IPCMC estimation. Considering that all experimental work is performed within 5 h, this change is unexpectedly large.

While in short experiments the integrated IPCMC sensor-actuator prototype with IPCMC feedback functions as described above, in longer experiments the performance is degraded by low-frequency noise in the sensor's short-circuit current. This causes error accumulation in position estimation, and the

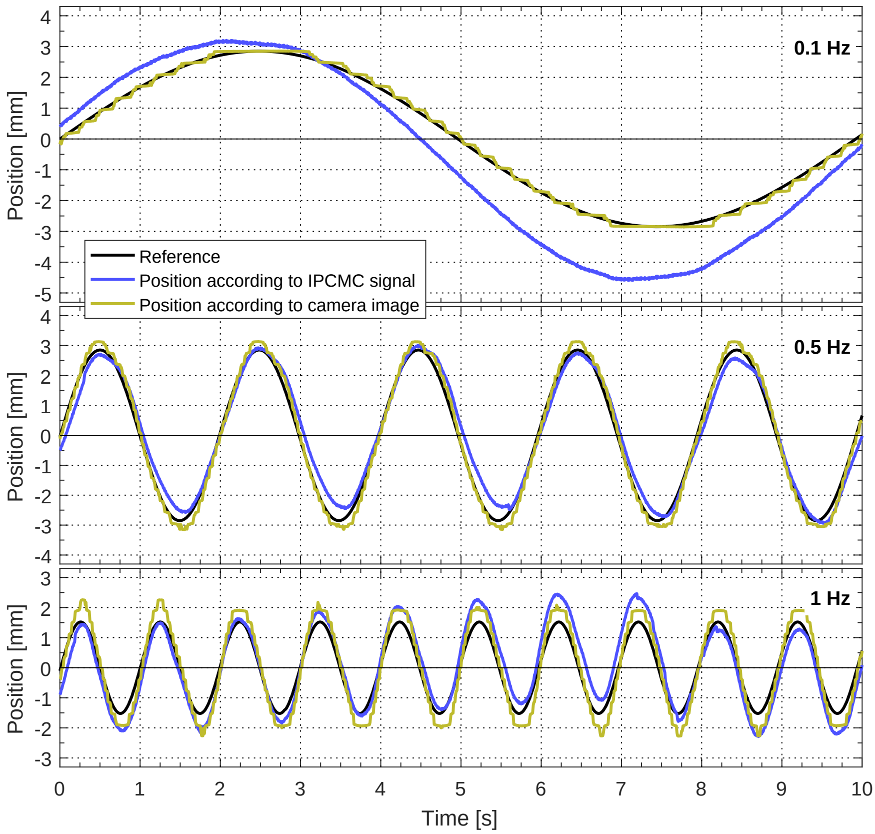

Figure 5.8. Results of the closed-loop control experiments with the integrated IPCMC sensor-actuator prototype, feedback from camera image.

experiments are aborted when the control voltage remains saturated. It is seen that periodically removing the error allows to achieve a fair tracking performance also in longer experiments, but this would require an external position measuring circuit, beating the purpose of the integrated sensor-actuator design. The reason behind the error accumulation is not clear, but the too simplistic design of the current sensing amplifier is suspected.

All in all, the integrated IPCMC sensor-actuator prototype is demonstrated to function, and a qualitative characterization is provided for its performance and limitations.

5.10. Conclusions

In this study a proof-of-concept design of an integrated IPT sensor-actuator device is proposed and a prototype is built. Closed-loop control experiments are performed using the IPT sensor signal as the feedback source and compared

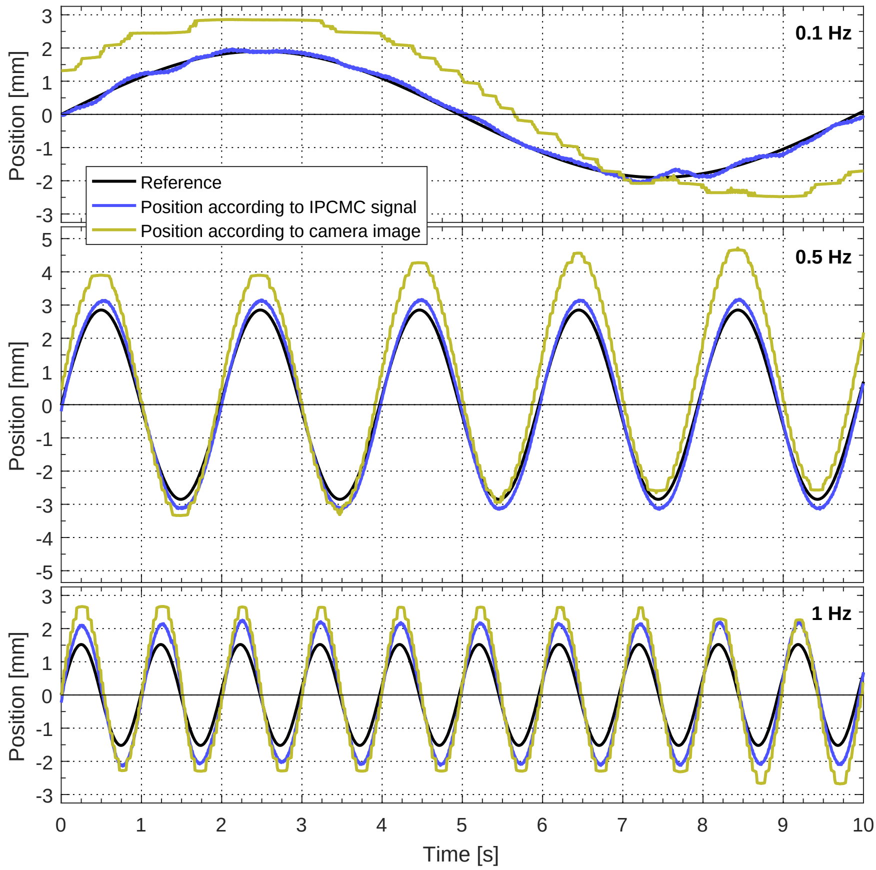

Figure 5.9. Results of the closed-loop control experiments with the integrated IPCMC sensor-actuator prototype, feedback from IPCMC sensing.

against the results of a system using external feedback, the latter establishing a basis for qualitative evaluation of the design concept. By design, the prototype resembles a 1-DOF rotational joint composing of two short IPCMC samples in side-by-side configuration, one for actuation and the other for sensing, mechanically coupled together in both ends and electrically isolated. By one end the joint is fixed to the Earth frame and a rigid extension link is attached to the other end for position tracking. Actuation and sensing dynamics are described using empirical models, and a proportional-integral (PI) controller is designed by manually adjusting the gains. Closed-loop control experiments are performed using sinusoidal reference signals of 0.1 Hz, 0.5 Hz and 1 Hz.

In the experimental set-up used in this study, the position estimation resolution of the IPCMC sensor is superior to that of the camera. Comparing the experimental results with position feedback from the IPCMC sensor against the results with camera feedback shows that in short term (up to a minute) the inferior performance of the IPCMCs is caused by modelling errors in the sensing transfer function model's magnitude. This shortcoming is easy to overcome with putting more effort in model fitting. More significant shortcomings include changes in sensing dynamics within very short time intervals causing an error in position estimation amplitude, and low-frequency noise in the short-circuit sensing current causing error accumulation in position estimation. Processes responsible for these phenomena remained unclear, but the low-frequency noise in the sensing signal is suspected to origin from the design of the sensing amplifier.

The results of this study demonstrate that an integrated IPT sensor-actuator concept is in fact feasible, but in order to make use of it in applications the causes for above-mentioned limitations need to be identified and resolved. Results that are reported in this work provide a preliminary, qualitative evaluation for the integrated sensor-actuator concept, using only IPCMC materials, black-box models, PI control and a small selection of sinusoidal reference signals. For systematic evaluation of using IPTs in an integrated sensor-actuator design, a more thorough study is needed, involving different types of IPT materials, characterization of these materials in terms of their fundamental parameters (using physics-based models for describing their dynamics), quantitative performance evaluation with a wider set of closed-loop experiments and more complex (model-based) control methods, which would reduce the material-independent effects to minimum. This kind of systematic evaluation is the topic of the next chapter.

6. INTEGRATED IPT SENSOR-ACTUATOR: EXTENDED STUDY

6.1. Introduction

Integrating sensing and actuation functionality of the IPTs into a single design allows to exploit the full potential of these novel materials (Section 3.3.2), but very few studies have explored this concept. Yamakita *et al.* [188] reported a 10 s long closed-loop 0.2 Hz sinusoidal reference following using IPMCs for actuation and sensing, but did not disclose any details on how these results were obtained (design, experimental set-up). Other studies utilize simultaneous sensing and actuation to control the angle of a rotary device in oscillations [185], sustain or damper vibrations of a thin plastic sheet [186], and for positioning the contacting sensor and actuator (a conceptual microgripper) [187] (Section 3.3.2). So far, self-sensing has not been demonstrated to function in the presence of external disturbances (Section 3.3.3). This study continues to investigate the integrated IPT sensor-actuator concept introduced in Chapter 5, that provided preliminary evaluation for the concept using black-box models to describe the dynamics, and performed closed-loop sinusoidal reference following experiments using PI control. In this study, the mostly qualitative results of Chapter 5 are extended by a more systematic quantitative evaluation of the improved design, thoroughly characterizing the sensor-actuator design and materials in terms of their fundamental parameters using physics-based models. The closed-loop performance is characterized using PI and H_∞ control and three different IPT materials for several different reference signals.

This study aims to further investigate feasibility of the IPTs for integrated sensing and actuation on an improved sensor-actuator design. It is intended to provide full characterization of the design and materials in terms of physically meaningful parameters, and achieve quantitative closed-loop performance characterization for a wide variety of reference signals. This would provide a quantitative reference, allowing to compare between different materials and IPT sensing against an external feedback source, indicate the significance of the choice of the control method and modelling, and aid to identify the application limitations of the IPT materials.

First the variety of materials used in the experimental work are described, and the improved design of the integrated IPT sensor-actuator is introduced. It uses

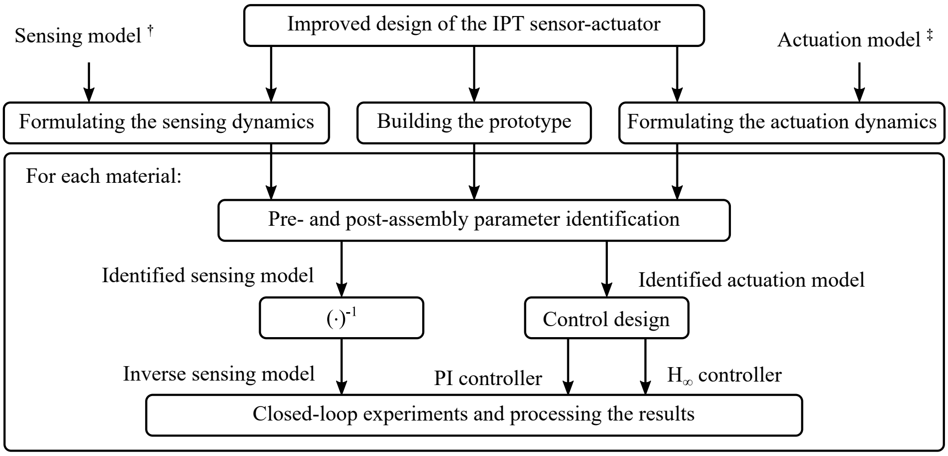

Figure 6.1. Workflow of this study. †Sensing model in [57], ‡actuation model in [121].

three short IPT samples that are placed symmetrically side-by-side and clamped together in both ends, functionally resembling a 1-DOF rotational joint. Next the adapted physics-based models describing the actuation and sensing dynamics of the system are presented, and control design (PI and H_∞) is introduced. In experimental work the system identification is performed, controllers are designed, and performance of the sensor-actuator is characterized in closed-loop experiments. The results allow to compare the performance material-wise, control-wise, and against an external feedback source, thus providing information about the feasibility of the concept for applications. Structure of the work in this study is illustrated in Figure 6.1.

Work presented in this chapter is based on publication C.

6.2. Materials

This section gives a brief overview on the three IPT materials that are used in the integrated IPT sensor-actuator study. These include one IPCMC and two IPMCs that are referred to as material # 1, # 2 and #3 in accordance with publication C, as follows:

The first material (# 1) is an IPCMC provided by the Intelligent Materials and Systems Laboratory (University of Tartu) that is manufactured from Nafion™117 ionomer backbone [9]. Nafion is coated with coconut shell derived active carbon electrodes using DAP (direct assembly process), and covered with gold foil and hot-pressed. This allows to achieve very low surface resistance that only varies insignificantly with bending. The IPCMC is immersed in EMI-Tf ionic liquid that serves both as counter-ions and a solvent, and has very low vapour pressure making the materials usable in dry environments. The same type of material is also used in the previous study (Section 5.2).

Material #2 is a typical IPMC that is made by depositing Pt electrodes on Nafion™117 membrane, and exchanging the loosely coupled H^+ ions for Li^+. Since water acts as a solvent in these materials, their performance depends on the hydration level. In order to maintain (roughly) consistent operation they need to be kept hydrated. These IPMCs are provided by Environmental Robots Inc. [286] and very similar materials are also used in the IPMC-actuated inverted pendulum study (Section 4.2).

The third material (# 3) is again an IPMC, this time provided by the Intelligent Materials and Systems Laboratory. It is very similar to material # 2, but the electrode material is gold instead of Pt, and the manufacturing time is 5 years earlier. Again, water is used as a solvent and the samples need to be kept hydrated for consistent operation.

Thus, the IPCMCs used in this study are well suited for operation in dry environments while the particular IPMCs need water environment for consistent results. More information on the IPT materials and their background is provided in Section 3.1. Next section describes the construction of the improved design of the integrated IPT sensor-actuator.

6.3. Design

This section introduces the design and realization of the improved integrated IPT sensor-actuator. Conceptually it is very similar to the preliminary design described in Section 5.3. Short IPT samples are used in side-by-side configuration to achieve simultaneous actuation and sensing in a device that is functionally similar to a 1-DOF rotational joint. A rigid link is attached to its mobile end, as shown in Figure 6.2. The main difference between this prototype and the former one lies in using two IPT actuators (on both sides of the narrow sensor sample) instead of one. Symmetrically arranged two wide actuator samples prevent unwanted twisting, and provide a larger moment for actuating the rigid extension rod. Although in principle the design modification is not significant, the entire prototype is rebuilt, and all the components are made such that the device is usable both in water and in air with both wet and dry IPTs.

The improved IPT sensor-actuator design is shown in Figure 6.3, and a photo of the assembled device is given in Figure 6.8. The prototype consists of the following components: (1) one narrow IPT sample for sensing and two wide ones for actuation on both sides of the sensor, all cut from the same material, and placed symmetrically in the same plane side-by-side; (2) a spring-loaded clamp with gold-plated silver electrodes, that provides electrical connections to each of the material samples, mechanically fixes them by one end to the Earth frame, and allows to quickly assemble and disassemble the set-up; (3) a plastic screw clamp that attaches to the free ends of the IPT samples and mechanically couples them together; (4) a rigid extension rod made of carbon fibre that attaches by one end to the above-mentioned (mobile) screw clamp, and accommodates a rectangular measurement target for the laser distance meter in the other end.

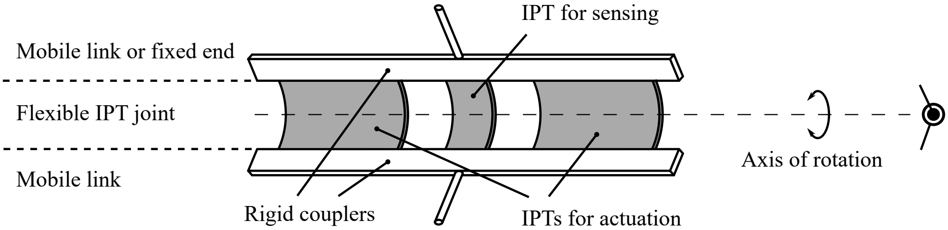

Figure 6.2. Working principle of the integrated IPT sensor-actuator.

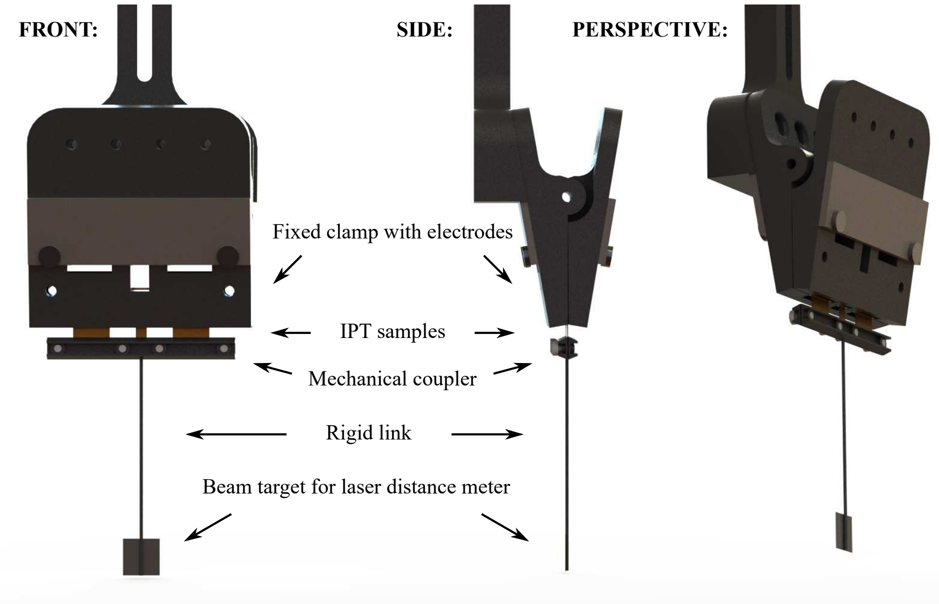

Figure 6.3. Design of the integrated IPT sensor-actuator.

Both the spring-loaded clamp and the screw clamp in the ends of the IPT samples are made of ABS plastic using 3D Touch rapid prototyping machine from 3D Systems Inc.

Sensing and actuation dynamics models for this design are established in the next section.

6.4. Modelling

This section describes the models for capturing the sensing and actuation dynamics of the integrated IPT sensor-actuator. The actuation model is necessary for designing the controllers. The inverse of the sensing dynamics is used for real-time extraction of position information from the sensor output signal. To capture the complex response of the IPT materials to arbitrary stimuli (either electrical or mechanical) as accurately as possible, and describe the sensor and actuators in terms of (mutual) physically meaningful parameters (within the accuracy of the model and its linearisation), the physics-based models for both sensing and actuation dynamics from Chen *et al.* [57, 121] are adapted. These models are derived based on the same governing PDEs for charge redistribution dynamics as presented in [44] and [233]. The models are geometrically scalable, account surface resistance effects, and for application purposes the authors have reduced them to finite order rational transfer functions. More information on these models, related studies and rationale behind choosing them is provided in Sections 3.4.3 and 3.6.

The models that are used in this study are originally developed to describe IPMC materials, but are also valid for IPCMCs. This is because of the similarities in the construction of these materials, and validity of the model derivation assumptions for both materials. First, the IPCMCs and IPMCs that are used in this work are based on the same Nafion ™117 polymer backbone. Second, the nanoporous carbon electrodes on the IPCMCs have very high effective surface area [9], similar to the dendritic structure of the Pt or Au electrodes in case of IPMC materials. In the model derivation process, the sensing and actuation phenomena are explained by (not clearly defined) electrostatic interactions, that are represented in the models through constant coupling coefficients relating the mechanical stress and the accumulated charge on the material surface. This can be considered valid for both materials. Since the models consider solvent effects on actuation and sensing negligible, and as the ionic liquid in IPCMCs serves as an equivalent to counter-ions and solvent in IPMCs, the materials may be considered equivalent in this modelling approach.

The original reports [57, 121] model actuation and sensing dynamics of long cantilever-beam-like IPMC samples. Alterations that are needed to adapt these models to describe the integrated IPT sensor-actuator (introduced in Section 6.3) are described in the following subsections, maintaining as much of the original notation as possible.

6.4.1. Sensing dynamics

This section establishes the sensing dynamics for the integrated IPT sensor-actuator prototype. Since the sensing model in [57] related the short-circuit current of an IPMC sample to the out-of-plane displacement in the tip of the material beam, the out-of-plane displacement of the short sensor sample used in the sensor-actuator prototype needs to be identified from the position of the tip of the extension rod. Assuming small deformations and that the IPT samples are bending in the first cantilever mode, the coefficient relating the sensor sample's out-of-plane displacement to the (measurable) position of the tip of the extension rod can be given:

$$C = \frac{L}{1.3765 L_e + L}, \tag{6.1}$$

where L is the length of the bending portion of the IPT sensor, and L_e is the distance from the fixing clamp to the tip of the extension (measuring level).

Now the sensing model can be adapted from [57] as follows:

$$\hat{H}(s) = \frac{i(s)}{x(s)} = C \cdot f(s) \cdot g(s), \tag{6.2}$$

where $i(s)$ is the short-circuit sensing current, $x(s)$ is position of the tip of the rigid extension at the laser distance meter measuring level, and functions $f(s)$ and $g(s)$ describe sensing dynamics and surface resistance effects respectively, and can be written as:

$$f(s) = \frac{\lambda_1 s^3 + \lambda_2 s^2 + \lambda_3 s}{s + K}, \tag{6.3}$$

$$g(s) = \frac{\mu_1 s^2 + \mu_2 s + \mu_3}{s^2 + \mu_4 s + \mu_5}, \tag{6.4}$$

$$K \approx \frac{F^2 d C^-}{\kappa_e R T}, \tag{6.5}$$

where the terms are F – Faraday constant, d – ion diffusivity, C^- – anion concentration, κ_e – (effective) dielectric permittivity, R – universal gas constant, T – absolute temperature, and the coefficients λ and μ are given as:

$$\lambda_1 = -\frac{3YW_s h\sqrt{Kd}}{8\alpha_0 L^3 K^2}, \quad \lambda_2 = -4K\lambda_1, \quad \lambda_3 = 8K^2\left(\sqrt{\frac{d}{h^2K}} - 1\right)\lambda_1, \tag{6.6}$$

$$\begin{aligned} \mu_1 = \frac{L^2}{6}, \quad \mu_2 = \frac{3h}{\kappa_e r_0}, \quad \mu_3 = \frac{12h^2}{\kappa_e^2 r_0^2 L^2}, \\ \mu_4 = \frac{12h}{\kappa_e r_0 L^2}, \quad \mu_5 = \frac{24h^2}{\kappa_e^2 r_0^2 L^4}, \end{aligned} \tag{6.7}$$

and the rest of the undefined terms are Y – Young's modulus, W_s – width of the sensor sample, h – material's semi-thickness, α_0 – charge-stress coupling constant, and r_0 – surface resistance per material length and width.

In the experiments the inverse of this model is utilized in order to obtain the position of the tip of the sensor-actuator device from the measured short-circuit current. The next subsection establishes the model for actuation dynamics, expressed in terms of the same parameters as the sensing model.

6.4.2. Actuation dynamics

This section establishes the actuation model for the integrated IPT sensor-actuator device, that is used in this study for control design and simulations. In model derivation, the IPT portion of the sensor-actuator is considered as a 1-DOF rotational joint that is fixed in the Earth frame by one end, and a rigid link (the

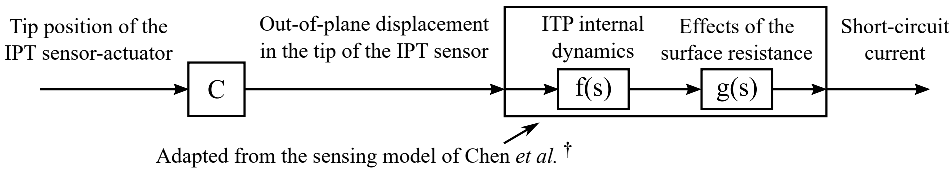

Figure 6.4. Composition of the model describing the sensing dynamics. †Sensing model in [57].

extension rod) is attached to its other end. The axis of rotation of this joint coincides with the outer edge of the spring-loaded clamp, it possesses torsional stiffness due to IPT properties and gravity, damping due to the environment and internal friction of the IPTs, and it is actuated by the moment supplied by the IPT actuators. The overall model for actuation dynamics of the integrated IPT sensor-actuator is a cascade of the voltage-induced moment (IPT actuators) and passive dynamics of the mobile portion of the device. The latter can be considered as a spring-mass-damper system.

The actuation model in [121] relates the out-of-plane displacement of the tip of a long IPMC beam to the voltage that is applied on the material electrodes. The final form of this model is a cascade of a voltage-induced bending displacement (due to charge redistribution dynamics), and a second order dynamics model describing the passive vibration of the material beam. In this study their intermediate results are used in order to establish an expression for the voltage-induced moment in IPT actuators.

Model $G(s)$ that describes actuation dynamics of the integrated IPT sensor-actuator, relates its tip displacement $X(s)$ to the input voltage $V(s)$, and can be written as:

$$G(s) = \frac{X(s)}{V(s)} = p(s) \cdot q(s), \tag{6.8}$$

where $p(s)$ is the model for voltage-induced moment produced by IPT actuators, $q(s)$ is the passive dynamics of the mobile portion of the device, and s is Laplace variable. As previously mentioned, the model for voltage-induced moment $p(s)$ is obtained from the intermediate results in [121] (equations (20), (29) and (46)). Since the active portions of the material samples are very small, the surface resistance effects can be neglected, and the model relating the moment $M(s)$ produced by voltage $V(s)$ can be expressed:

$$p(s) = \frac{M(s)}{V(s)} = \frac{\alpha_0 \kappa_e K W_a h(1-\gamma)}{\gamma \kappa_e r_2' s^2 + \gamma(h + \kappa_e K r_2')s + Kh}, \tag{6.9}$$

where W_a is the total width of the actuator samples, r_2' is the trough-material resistance per length, and γ is defined as

$$\gamma = h\sqrt{\frac{K}{d}}. \tag{6.10}$$

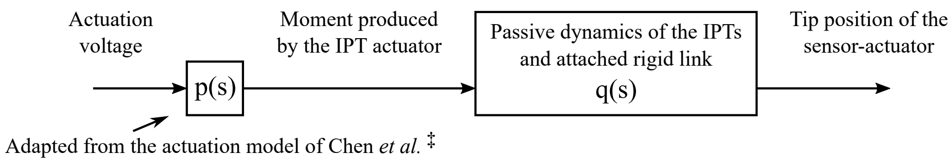

Figure 6.5. Composition of the actuation model. ‡Actuation model in [121].

Other parameters' definitions are in agreement with the previous subsection. Due to omitting the surface resistance effects the actuation moment does not depend on the length of the IPT sample.

Passive dynamics of the mobile portion of the device is described using a second order mass-spring-damper model relating the position of the tip of the sensor-actuator $X(s)$ to applied moment $M(s)$ as follows:

$$q(s) = \frac{X(s)}{M(s)} = \frac{\mathcal{L}}{I} \cdot \frac{1}{s^2 + 2\xi\omega_n s + \omega_n^2}, \tag{6.11}$$

where $\mathcal{L}$ is the distance from the IPT clamping level to the position measuring level in the tip of the sensor-actuator, I is the moment of inertia of the mobile portion of the sensor-actuator with respect to the clamping axis, ω_n is the natural frequency, and ξ is the damping coefficient. Such a model captures the passive dynamics of the IPT sensor-actuator sufficiently well for the purposes of this study. The actuation model that is established in this subsection is necessary for designing the controllers, as described in the next section.

6.5. Control

This section describes the two controllers that are used in this study, i. e. PI and $\mathtt{H}_\infty$. Controllers are designed based on the actuation model described in detail in Section 6.4.2.

PI (proportional-integral) controller is designed analogously to the previous study described in Section 5.6. NI Labview 2010 software is used to constantly re-calculate the step response for the actuation model in closed-loop configuration with a PI controller, while the controller gains are manually tuned. The resulting response is constantly observed, aiming to achieve the shortest settling time for 5% error margin. PI control is later used to establish the reference for evaluating the significance the control methods on the performance of the sensor-actuator.

$\mathtt{H}_\infty$ controller is designed using Matlab software, again based on the actuation model. Selecting the weights on output error W_e and control effort W_u is based on the instructions in [287] and [288]. First and second order weights are used, depending on the closed-loop performance. The resulting controllers are usually of very high order, and they are reduced to the 5th order to facilitate implementation.

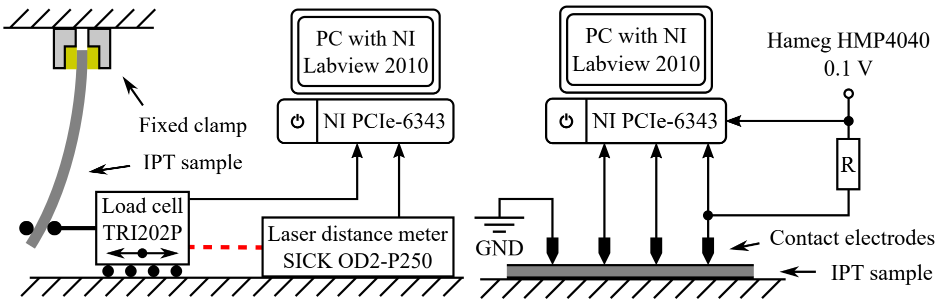

(a) Young's modulus identification. *(b) Measuring surface resistance.*

Figure 6.6. Experimental set-ups used in parameter identification prior to assembling the sensor-actuator prototype.

Now the modelling and control of the integrated IPT sensor-actuator design are introduced, and the next section concentrates on describing the experimental set-ups.

6.6. Experimental set-ups

Experimental set-ups that are used in this study include one for measuring the Young's modulus of the materials, one for measuring their surface resistance, and the final fully assembled device with the respective set-up used for the system identification and closed-loop control experiments. The set-ups are described in more detail in the following subsections.

6.6.1. Measuring Young's modulus

Young's modulus is experimentally measured as a part of the model parameter identification process. The respective experimental set-up is shown in Figure 6.6a. One end of a larger IPT sample is fixed to the Earth frame using a massive aluminium clamp with plastic-coated clamping surfaces (non-conductive), and the free end is inserted between a stainless steel fork-like coupler that attaches to a force gauge (Panlab TRI202P). During the experiments the force gauge is manually moved on the horizontal surface, and its position is measured using a laser distance meter (SICK OD2-P250W150U0). Using a NI PCIe-6343 data acquisition board the position and force readings are digitized, and further stored and processed in a PC in NI Labview 2010 environment.

6.6.2. Measuring surface resistance

IPT surface resistance per unit length and width is obtained experimentally using a four-point resistance measuring scheme. This allows to avoid erroneous results due to contact resistances between the material and electrodes. The diagram of the experimental set-up is given in Figure 6.6b. The width of the material sample is measured, and the sample is pressed against electrodes that are attached on a flat surface. A resistor with known resistance is connected in series with this set-up, and 0.1 V is applied (Hameg HMP4040 power supply) as shown in Figure 6.6b. Current through the IPT sample can be calculated from the voltage on the resistor, and further the material's surface resistance can be calculated from the voltage reading between the inner electrodes that are in contact with the IPT sample. Measurements are controlled from a PC with NI Labview 2010 environment via a NI PCIe-6343 data acquisition board, and dimension-normed surface resistance r_0 is calculated.

6.6.3. Final experimental set-up

The rest of the experiments are performed using the final set-up shown in Figures 6.7 and 6.8. The IPT sensor-actuator device is assembled as described in Section 6.3 and it is vertically suspended by the spring-loaded clamp fixed in the Earth frame. Actuation takes place in a vertical plane, that is perpendicular to the axis of the device's rotational joint.

IPT actuators are electrically connected in parallel and they are powered via a bipolar power supply Kepco BOP 20-10MC (optimized for capacitive loads) that serves to protect the data acquisition board and provide sufficient current at all actuation voltages. Short-circuit current between the IPT sensor's electrodes is measured using a 2-step amplifier circuit that operates from a battery pack. It is based on OPA111BM operational amplifiers and functions as a current to voltage converter and amplifier with the gain of 100 000. Position of the tip of the sensor-actuator is measured using a laser distance meter Z4M-S40 from Omron with maximum resolution of 40 $\mu\mathrm{m}$. Again, a PC running NI Labview 2010 and NI PCIe-6343 data acquisition board controls the experiments, processes the measurements and stores the results. Experiments are conducted at 10 kHz sampling rate and saturation limit in all experiments is set to 3.5 V.

The experimental set-ups described in these subsection are used in parameter identification that is discussed in the next section, and later also in the subsequent closed-loop experiments to characterize the performance of the device.

6.7. Parameter identification

This section focuses on identifying the parameters of the sensing and actuation models presented above in Sections 6.4.1 and 6.4.2 respectively. Physical constants contained in these models are known from literature but the design- and material-specific parameters need to be measured or experimentally identified.

Parameter identification is performed in steps and are combined with assembling the integrated IPT sensor-actuator prototype. It starts with measuring the raw material samples, and the whole identification process is performed as follows:

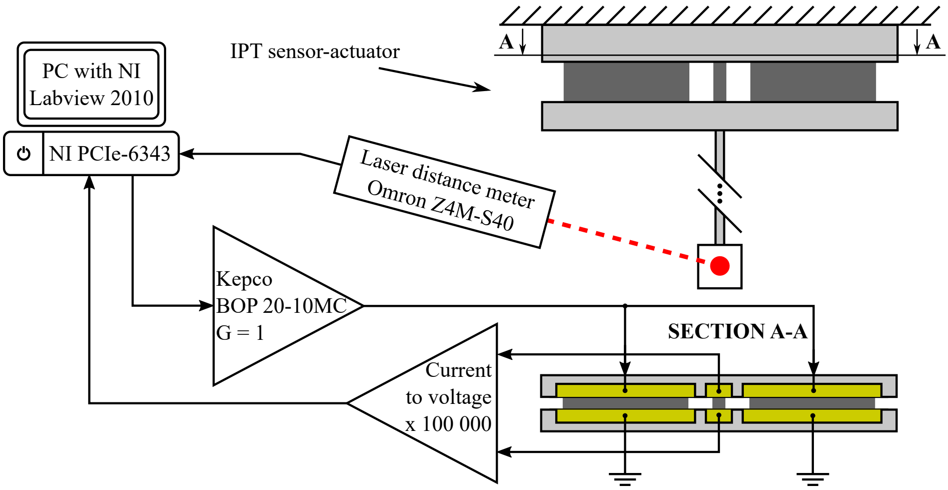

Figure 6.7. Final experimental set-up.

- Prior to cutting a material sample into pieces with appropriate dimensions for the sensor-actuator, it is placed into a plastic bag for protection and its thickness is measured in multiple locations using a micrometer screw gauge. Thickness of the bag in these locations is subtracted, and an average material thickness $2h$ is calculated.

- Young's modulus of the material sample is measured using the experimental set-up described in Section 6.6.1. Deformations are applied by moving the load cell manually, and it is stopped instantaneously to take (simultaneous) force and deformation readings. Proportionality coefficient between the measured force P and applied deformation σ is obtained from these results using linear regression, and further Young's modulus can be calculated:

$$Y = \frac{Pl^3}{3\sigma I_y}, \tag{6.12}$$

  where l is the free length of the IPT sample and I_y is the area moment of inertia for the material sample (rectangular cross-section).

- Measuring the normalized surface resistance r_0 is performed using the four-point set-up described in Section 6.6.2. Readings are taken over several seconds at 100 S/s sampling rate and averaged for a more precise result.

- The large material sample used in aforementioned experiments is then cut into a set of small samples for sensor and actuators in the IPT sensor-actuator prototype described in Section 6.3, and the device is assembled. Then the length of the free portion of the IPT samples L and the widths of the actuators W_a and the sensor W_s are measured.

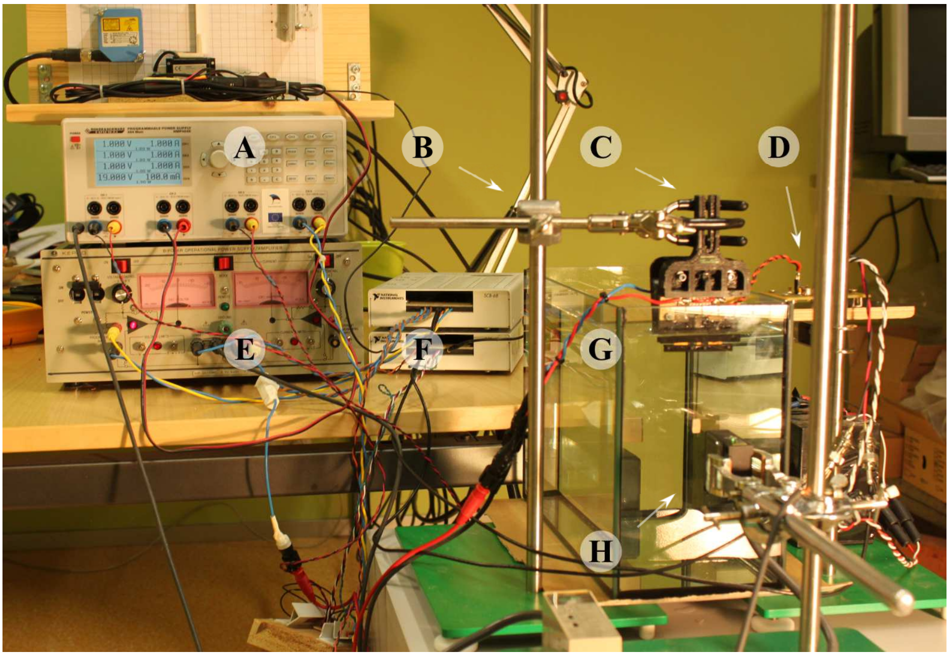

Figure 6.8. Fully assembled integrated IPT sensor-actuator system in the final experiments: A – power supply for sub-systems in different experimental set-ups (here used to power the laser distance meter); B – stand that fixes the sensor-actuator to the Earth frame; C – fixed end of the integrated IPT sensor-actuator prototype; D – short-circuit current sensing circuit (battery-powered); E – unity gain amplifier for powering the IPT actuators; F – terminal boxes of the data acquisition board; G – water tank; H – laser distance meter.

- From geometry and mass distribution of the device the moment of inertia of the mobile portion of the IPT sensor-actuator is calculated with respect to the edge of the spring-loaded clamp (i. e. equivalent axis). Inertial properties of the mobile clamp and rigid extension are obtained from a CAD model in Solidworks 2015 software.

- Next the natural frequency ω_n and the damping ratio ξ are experimentally determined using the set-up described in Section 6.6.3. The device is mechanically excited and the parameters are extracted from measuring the free oscillations either in air (IPCMC) or in water (IPMCs).

- Frequency responses for actuation and sensing dynamics are experimentally measured using the set-up described in Section 6.6.3 in order to identify the remaining parameters. In the experiments, the IPT actuators are excited with sinusoidal input signals (2 V amplitude) logarithmically distributed between 0.2 Hz to 15 Hz or wider frequency intervals aiming to capture their essential characteristics. Signals are applied for at least 30 s, but for no less than 2 full periods. Simultaneously, the position of the tip of the integrated IPT sensor-actuator and short-circuit current of the sensor sample are measured. Phase and magnitude information for both sensing and actuation dynamics are extracted for each frequency in the end of the experiments using NI Labview 2010 software.

- Based on the aforementioned frequency response measurements the remaining parameters, i. e. d, α_0, κ_e, C^- and r_2' are curve-fitted to the experimental data using unconstrained non-linear optimization function *fminsearch* in Matlab R2015a software. It must be noted that these parameters cannot be uniquely defined based on the experimentally measured frequency responses. In order to obtain realistic results, the initial values for these parameters are selected according to the original papers on modelling the sensing and actuation dynamics in [57, 121].

When parameter identification process is complete the controllers are designed for the closed-loop system (Section 5.6) and performance of the IPT sensor-actuator device is characterized as described in the following section.

6.8. Performance characterization

This section describes how the performance of the integrated IPT sensor-actuator is characterized in the closed-loop experiments. Once the models for actuation and sensing are identified (Section 6.7) and controllers are designed (Section 6.5), the closed-loop experiments are conducted on the sensor-actuator prototype (Section 6.3) using the final experimental set-up described in Section 6.6.3.

In order to provide a systematic characterization, the following reference signals are used in the closed-loop experiments:

- unit step $u(t) = 1\,mm \cdot U(t - 0.5s)$, where $U(\cdot)$ is the Heaviside function;
- four sinusoids with 0.5 Hz, 1 Hz, 2 Hz and 3 Hz frequencies at 1 mm amplitude;
- three random signals that are generated using Matlab R2015a software by applying 4th order Bessel bandpass filter to randomly generated signals (10 kHz sampling rate) and further normalized not to exceed 1 mm actuation amplitude. The lower passband limit for all signals is 0.1 Hz and the higher limits are 2 Hz, 3 Hz and 4 Hz;
- 1 Hz sinusoidal reference with 1 mm actuation amplitude and duration of either 30 min (IPT feedback) or 2 hours (laser feedback).

All these closed-loop experiments with the integrated IPT sensor-actuator (except the long-term sine wave following) are conducted using three different materials (see Section 6.2), PI and $\mathtt{H}_\infty$ controllers, and feedback from both the IPT sensor and the laser distance meter. Thus 34 experiments are conducted on

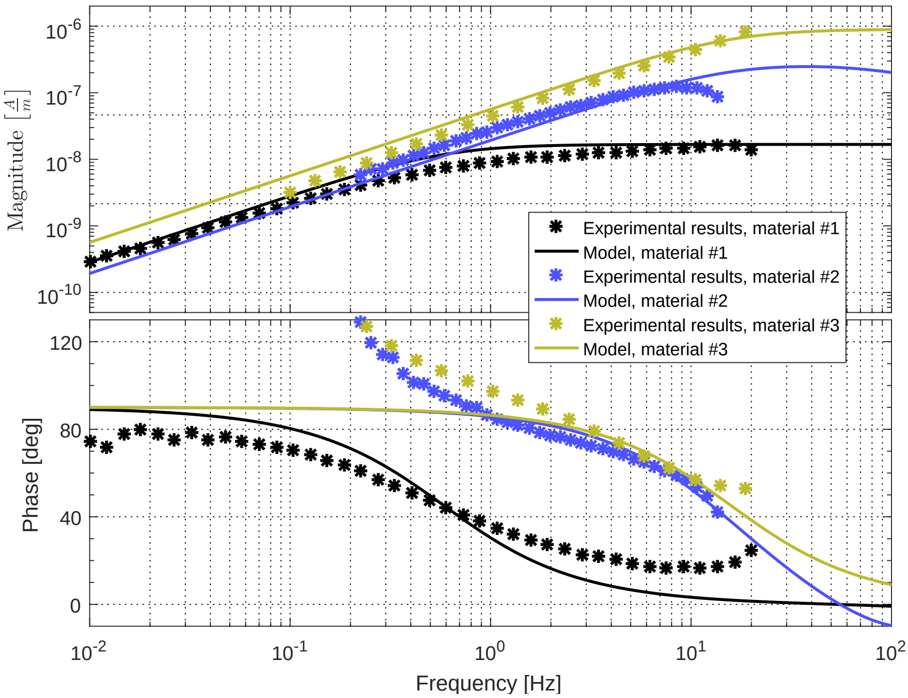

Figure 6.9. Sensing dynamics of the integrated IPT sensor-actuator. Experimentally measured frequency responses and respective models for all three materials.

each material, resulting in 102 experiments in total. This allows to establish a sufficient basis for comparison between different materials, controllers and against an external feedback source. The experimental results are presented in the following section.

6.9. Results

This section presents the experimental results of this study. Parameter identification is performed according to Section 6.7, and the resulting values for the model parameters are presented in Table 6.1. Frequency responses of the identified models and experimentally measured sensing and actuation dynamics are shown in Figures 6.9 and 6.10, respectively. After designing the controllers according to Section 6.5 the work continues with characterization of the performance of the sensor-actuator prototype.

Closed-loop step response is measured for 15 s in all the material, controller and feedback configurations (step is shifted to 0.5 s from the beginning of the experiments). First 3 s of all experiments are plotted in Figure 6.11. A full quantitative characterization of these results are given in publication C (Table 2), including delay time, rise time, peak time, percent overshoot and settling time. Due to a strong high-frequency noise in the position reading of the IPCMC sensor

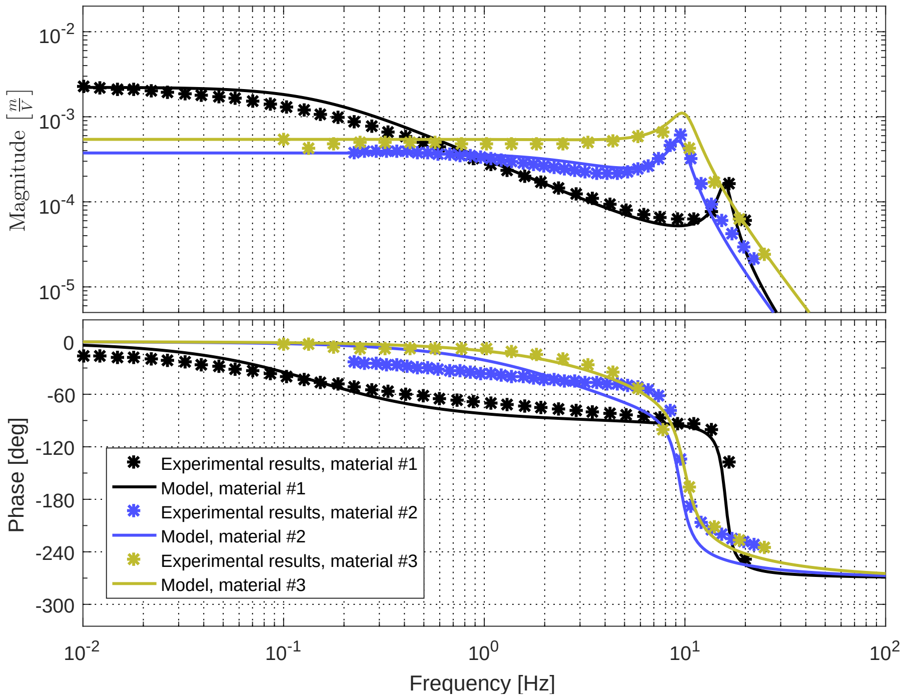

Figure 6.10. Actuation dynamics of the integrated IPT sensor-actuator. Experimentally measured and respective identified model frequency responses are plotted for each material.

(material # 1) its signal is down-sampled by 10 prior to characterization. The poor performance of the material #3 is caused by a strong low-frequency drift in its short-circuit current reading, and strongly non-linear actuation behaviour. Similar to the phenomenon described in the inverted pendulum study in Chapter 4 and in literature overview in Section 3.1.2, the material bends back beyond its initial position during actuation causing even the experiments in laser feedback configuration to fail.

For comparison, the simulated step responses for the respective actuation models in closed-loop configuration with the designed controllers are plotted in Figure 6.12 and a quantitative characterization can be found in publication C (Table 3).

The sinusoidal reference tracking experiments are 30 s long, unless they need to be aborted earlier due to saturation of the actuation voltage for any longer than 1 period of the reference signal. In Figure 6.13 the results of these experiments are presented through the sequences of the RMS tracking errors calculated over each period of the reference signal. Due to a large amount of experimental data and for the purpose of readability, only a single period of these experiments (starting at 2 s) is shown in Figure 6.14. For quantitative characterization of the results, the errors in magnitude and phase are given for each experiment (with respect to the reference signals) in publication C (Table 4) along with the RMS tracking errors.

Durations of the random reference following experiments are also 30 s unless they need to be aborted earlier to prevent damage to the materials. RMS errors over each 0.5 s intervals of the experiment durations are plotted in Figure 6.15, and first 2 seconds of all experiments are plotted in Figure 6.16. For quantitative characterization the RMS errors over the entire experiment durations are presented in publication C (Table 5).

Since comparing the PI and $\mathtt{H}_\infty$ controllers is already possible in the previous experiments, the long duration sinusoidal reference tracking experiments are only performed using $\mathtt{H}_\infty$ controller. Experiment durations are set to 2 hours in the laser feedback configuration and 30 min for IPT feedback, unless the actuation voltage saturates for longer than 1 s. Experimental results in terms of RMS errors over each 1 s interval are shown in Figure 6.17, total durations of these experiments are given in Table 6.2, and additionally the power consumption during these experiments is shown in Figure 6.18. The experiment with material #2 in laser distance meter feedback configuration is halted before its intended end (2 h) for technical reasons.

6.10. Discussion

In applications that exploit the novel properties of IPT materials it is advantageous to use IPTs for both sensing and actuation when a compact source of feedback with minimal impact on actuation is required. In order to investigate such concept an improved design of the integrated IPT sensor-actuator is built and its performance is characterized in this study, continuing the work started in the preliminary study in Chapter 5. In this section these results are analyzed and the comparison of the performance is provided material-wise, controller-wise and against the external feedback.

In the course of parameter identification it appeared that it is not possible to achieve consistent values for all of the physically meaningful parameters used to describe both the sensing and actuation dynamics of the same IPT material samples. Thus, charge-stress coupling constant α_0 and dielectric permittivity κ_e are split into two distinct values, as can be seen in parameter identification results in Table 6.1. Different values for charge-stress coupling constant α_0 in fact appear logical when looking into the meaning of this parameter. It provides a proportional relation between the charge and stress on the surface of the material (Section 6.4.2 and 6.4.1), bypassing laborious modelling of the essentially different complex processes that actually dominate the sensing and actuation phenomena (reviewed in Section 3.4.3).

Values for dielectric permittivity κ_e appear significantly different and very unrealistic already in the original reports of Chen *et al.* [57, 121]. Also in this study, the model identification results in unrealistic values and does not converge at all unless separate values for sensing and actuation are used. This suggests

Table 6.1. Parameter identification results.

Measured or calculated parameter	Symbol	# 1	# 2	# 3	Unit
Material thickness	$2h$	277	353	282	µm
Young's modulus	Y	140	154	658	MPa
Surface resistance	r_0	0.543	64.0	0.144	Ω
Total width of the actuators	W_a	18.9	20.8	20.8	mm
Sensor width	W_s	1.95	3.72	2.96	mm
Operational material length	L	3.03	2.53	2.22	mm
Effective length of elongation	L_e	61.0	59.64	58.60	mm
Moment of inertia about clamp	I_{xx}	$1.79 \cdot 10^{-7}$	$1.71 \cdot 10^{-7}$	$1.66 \cdot 10^{-7}$	kg m^2
Material surface density	ρ	0.460	0.650	0.570	kg m^{-2}
Natural frequency	ω_0	15.9	8.70	10.0	Hz
Damping ratio	ξ	0.0611	0.100	0.135	–
Room temperature	t	22.4	22.9	21.6	°C

Fitted parameter	Symbol	# 1	# 2	# 3	Unit
Ionic diffusivity	d	$3.44 \cdot 10^{-12}$	$3.48 \cdot 10^{-11}$	$3.32 \cdot 10^{-11}$	m^2 s^{-1}
Anion concentration	C^-	1064	1068	1089	mol m^{-3}
Resistance trough material	r'_2	$9.98 \cdot 10^{-6}$	$9.99 \cdot 10^{-6}$	$1.00 \cdot 10^{-5}$	Ωm
Dielectric permittivity for sensor	κ_{e_s}	$3.76 \cdot 10^{-3}$	$1.52 \cdot 10^{-3}$	$1.38 \cdot 10^{-3}$	F m^{-1}
Dielectric permittivity for actuator	κ_{e_a}	$2.99 \cdot 10^{-6}$	$5.07 \cdot 10^{-7}$	$1.41 \cdot 10^{-7}$	F m^{-1}
Charge-stress coupling constant for sensor	α_{0_s}	$1.39 \cdot 10^{5}$	$3.35 \cdot 10^{5}$	$3.18 \cdot 10^{5}$	J C^{-1}
Charge-stress coupling constant for actuator	α_{0_a}	-0.213	-0.0220	-0.0828	J C^{-1}

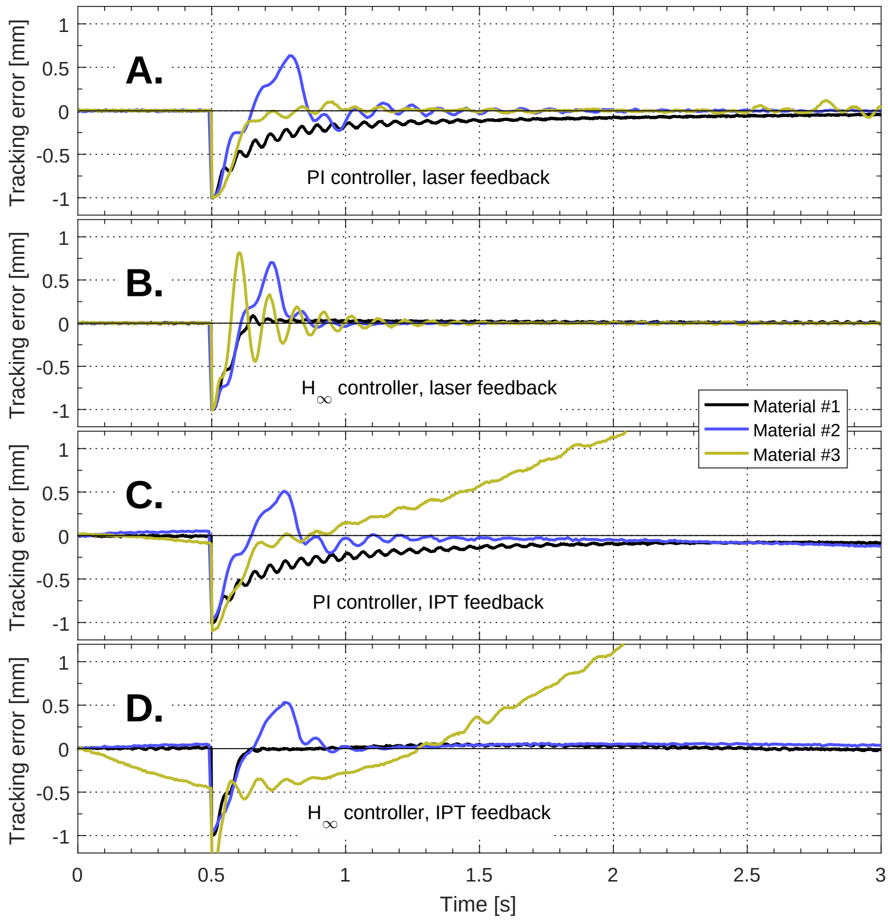

Figure 6.11. Tracking errors during the first 3 s of the step response measurements for each of the three materials, laser (A, B) and IPT (C, D) feedback, and PI (A, C) and $\mathtt{H}_\infty$ *(B, D) control.*

that some false assumptions have been made in model derivation in [57, 121]. Indeed, as was later clarified by Porfiri [241] it is not correct to consider the IPTs as parallel-plate capacitors whose entire thickness is a dielectric medium. The polymer backbone in fact conducts counter-ions, and the high capacitance of the IPTs is actually caused by the high effective surface area of the electrodes and the thin boundary layers in their proximity. Unrealistic values for κ_e are a result of this false-assumption. Values for the rest of the parameters in the sensing and actuation models agree.

Discrepancies between the identified models and experimentally measured frequency responses are mainly caused by unmodelled dynamics. Considering the non-linear behaviour of the materials (such as the back-relaxation discussed in Section 3.1.2) is out of the scope of this work. Errors in the actuation

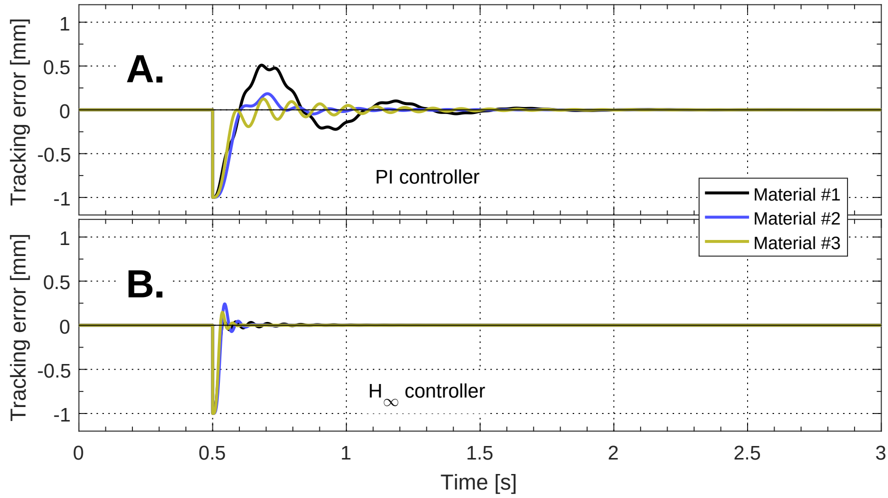

Figure 6.12. Tracking errors in simulated step responses for each actuation model in closed-loop configuration with respective PI (A) and H_∞ (B) controller.

Table 6.2. Durations of the extended 1 Hz sinusoidal reference following experiments.

Feedback		Laser			IPMC	
Material	#1	#2	#3	#1	#2	#3
Duration	7200 s	4513.3 s	76.82 s	300 s	1800 s	4.295 s

models are minor (Figure 6.10) and therefore they do not significantly affect the control design and the consequent closed-loop performance. Inaccuracies in the sensing model (Figure 6.9) result in additional phase and magnitude errors in the closed-loop experiments, but considering the material properties they are sufficiently small. These models are chosen in this study because they are suitable for control and allow to describe the IPT materials in terms of physically meaningful parameters. Numerous other modelling reports are reviewed in Section 3.4, and choosing which model to use depends the application in hand.

As it can be seen in Figures 6.12, 6.11 and in publication C (Tables 2 and 3), the simulation and experimental results in step response measurements clearly differ. These discrepancies result from the voltage saturation limits, external disturbances and model perturbations that are not accounted in the simulations due to their laboriousness and low significance in terms of the aims of this study.

Experimental results indicate that the most significant weakness of the IPT materials that limits using them in integrated sensing and actuation applications is the low-frequency noise in the short-circuit sensing current that is also reported in the results of the preliminary study in Chapter 5. Strength of this noise varies across materials and it causes error accumulation in the position estimation. Initially it is hypothesized that the poor design of the sensing signal measuring

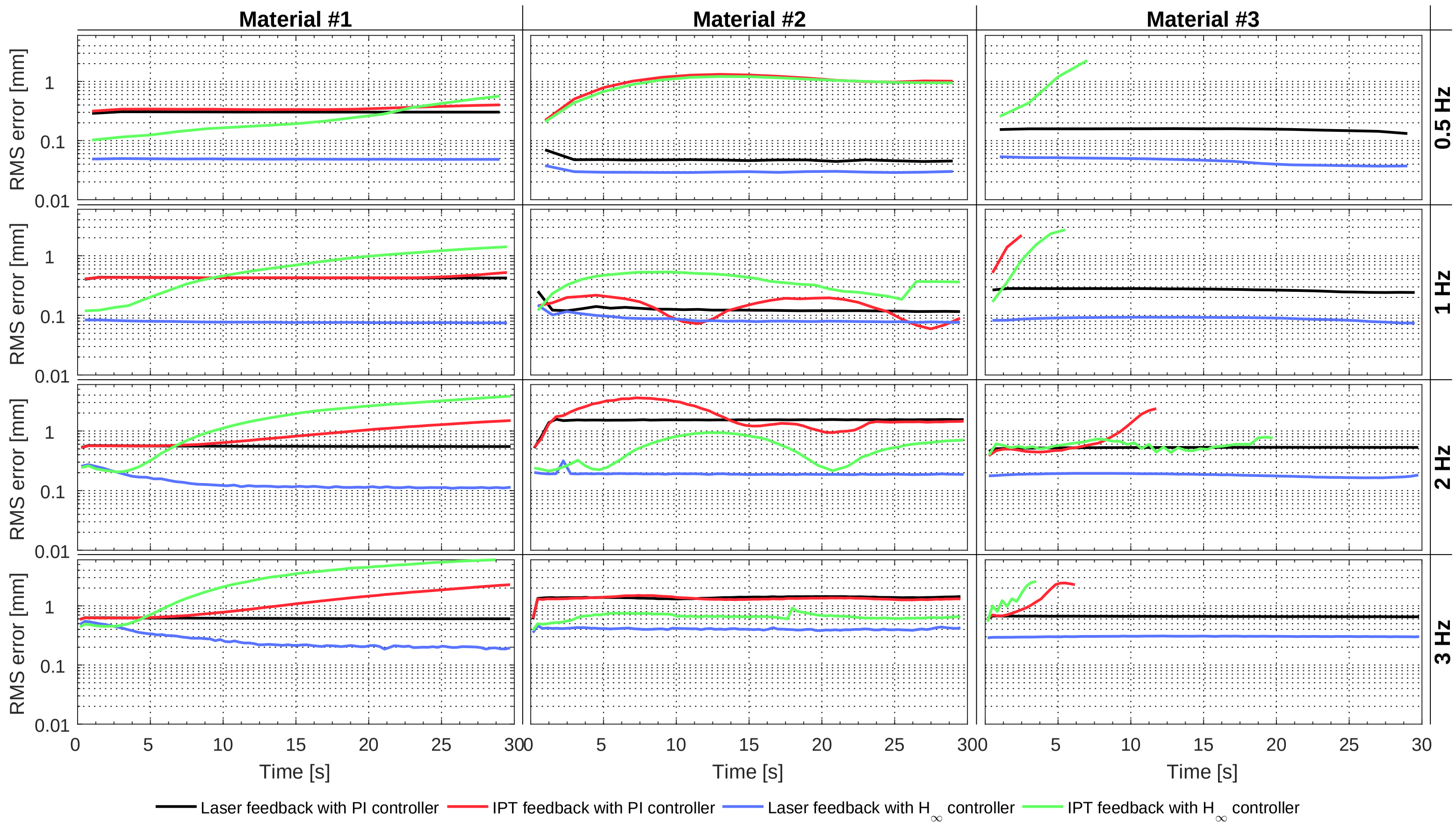

Figure 6.13. RMS tracking errors in the sinusoidal reference following experiments, calculated over each period of the reference signal.

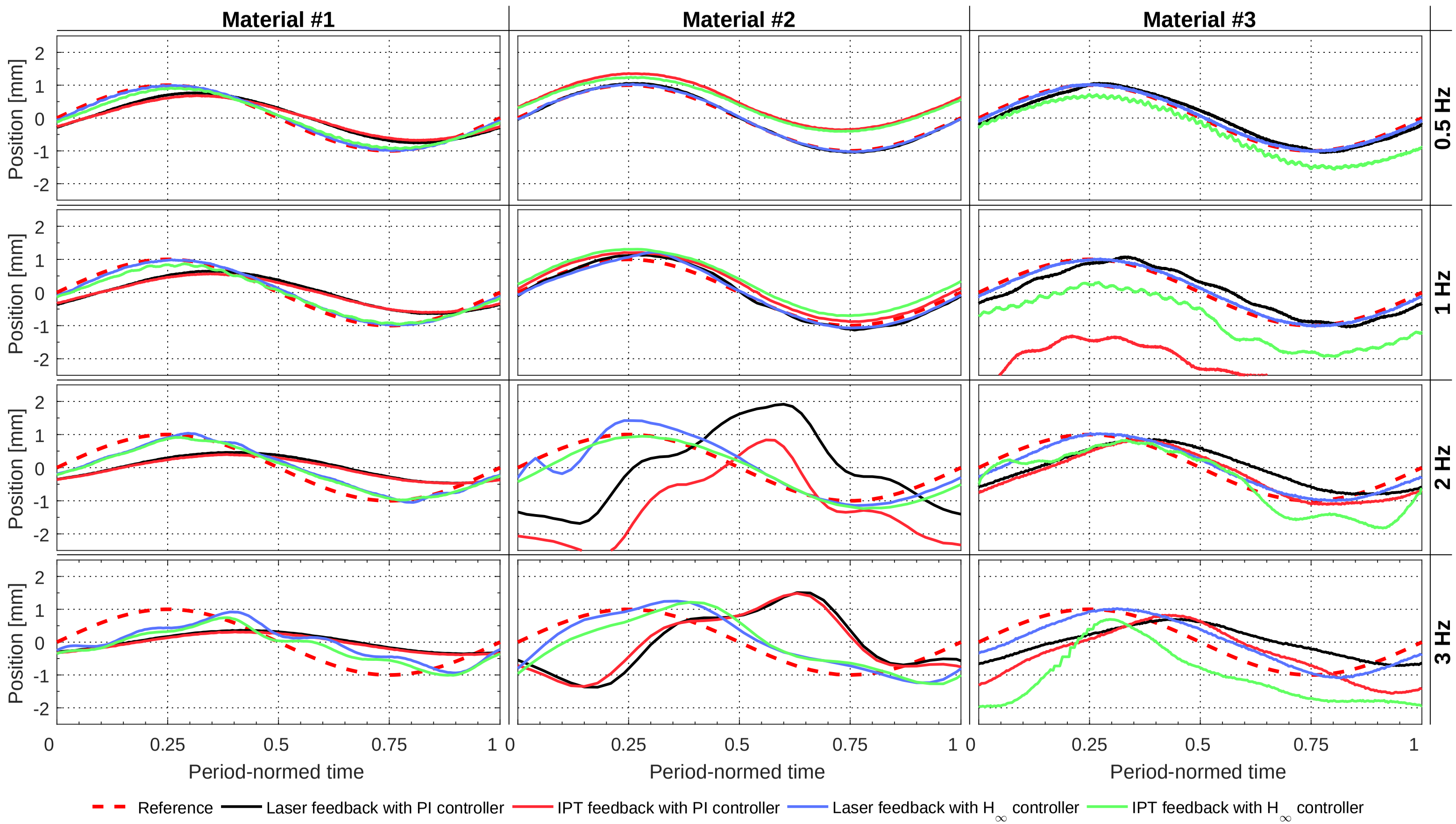

Figure 6.14. Sinusoidal reference following results over a single period of the reference signals, starting at 2 s from the beginning of the experiments.

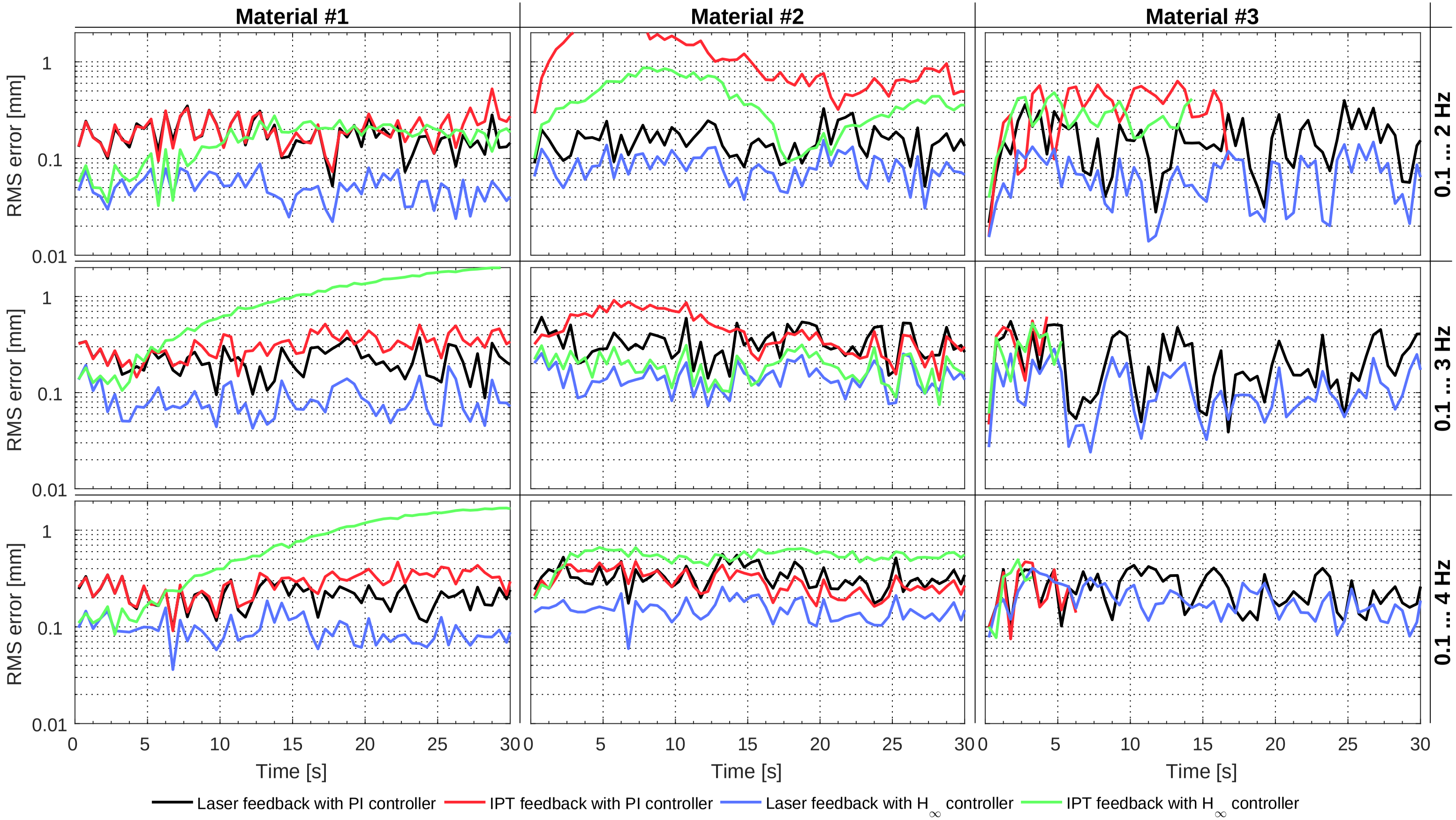

Figure 6.15. RMS tracking errors in the random reference following experiments, calculated over each 0.5 s interval.

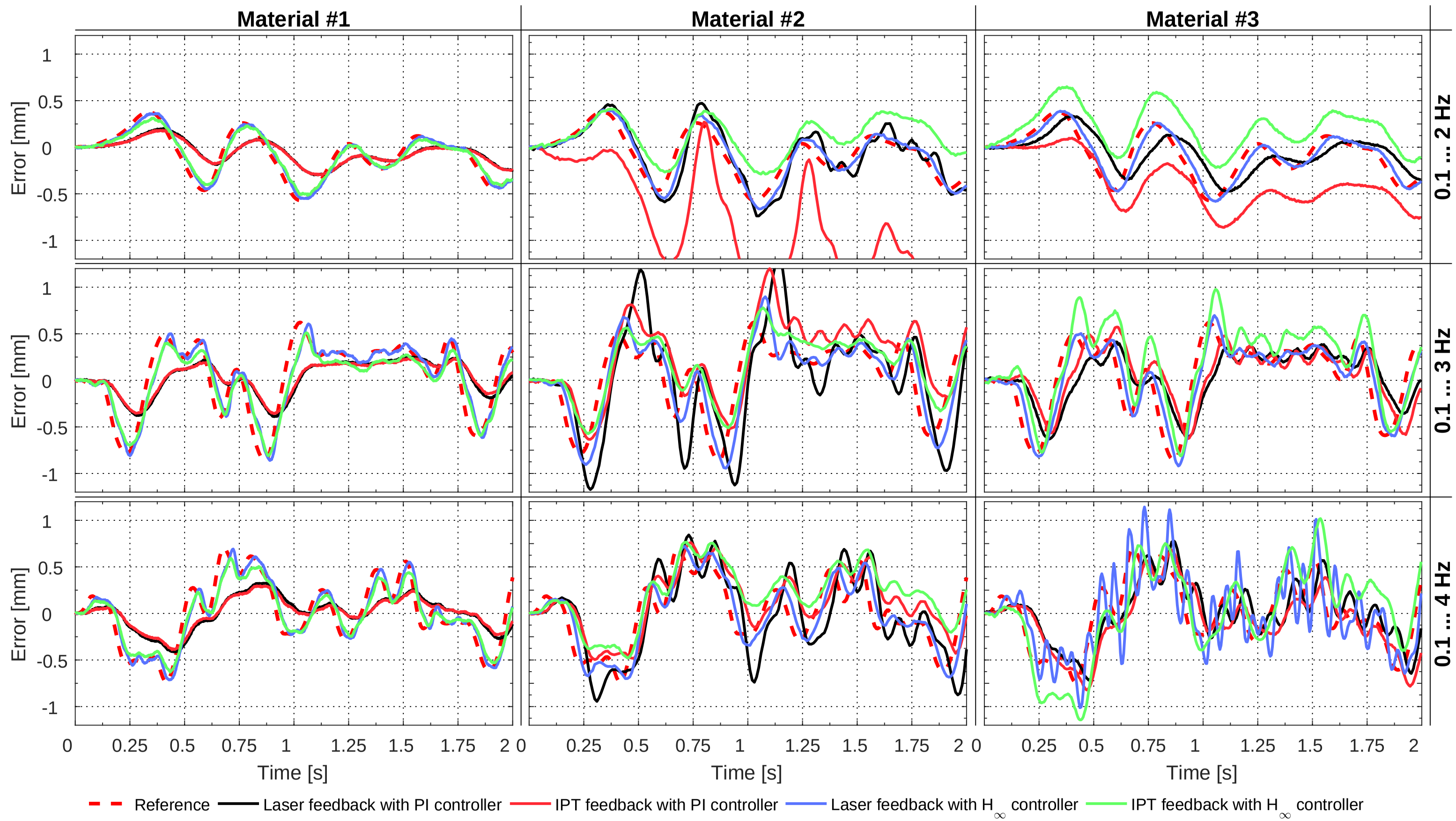

Figure 6.16. Random reference following for the first 2 s of each experiment.

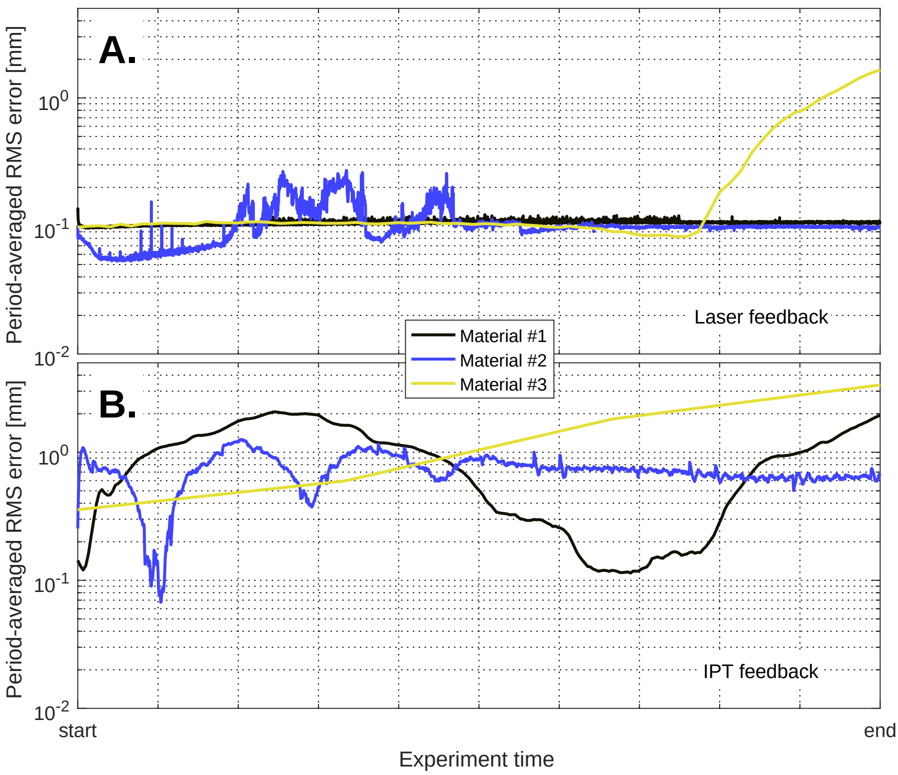

Figure 6.17. RMS tracking error in long duration sinusoidal reference following experiments with laser (A) and IPT (B) feedback. The error is calculated over each 1 s period and time is normalized to the total duration of each experiment.

circuit is the source of this noise since the original paper on sensing dynamics [57] does not report such a noise. After testing several amplifier designs, including an equivalent of what is used in [57] the noise reduces, but does not disappear. While the exact reason of this low-frequency noise remains unknown in this study the potential reasons include: (1) interactions between the IPT sensor and the amplifier circuit; (2) environmental impact (factors influencing the performance of the IPTs are reviewed in Section 3.1.2); and (3) unmodelled internal dynamics of the materials.

The performance of the integrated IPT sensor-actuator device in IPT sensor feedback configuration is throughout all experiments clearly inferior to the results with laser distance meter feedback. While in short run (few seconds up to a minute, depending on the material) their behaviour is similar, in longer experiments the aforementioned low frequency noise in sensing signal renders IPTs inferior or even unusable as the main source of the feedback.

Throughout the results it is seen that $\mathtt{H}_\infty$ controllers perform remarkably better than respective PI controllers. This is an anticipated finding since more complex model-based controllers are usually able to shape the closed-loop performance

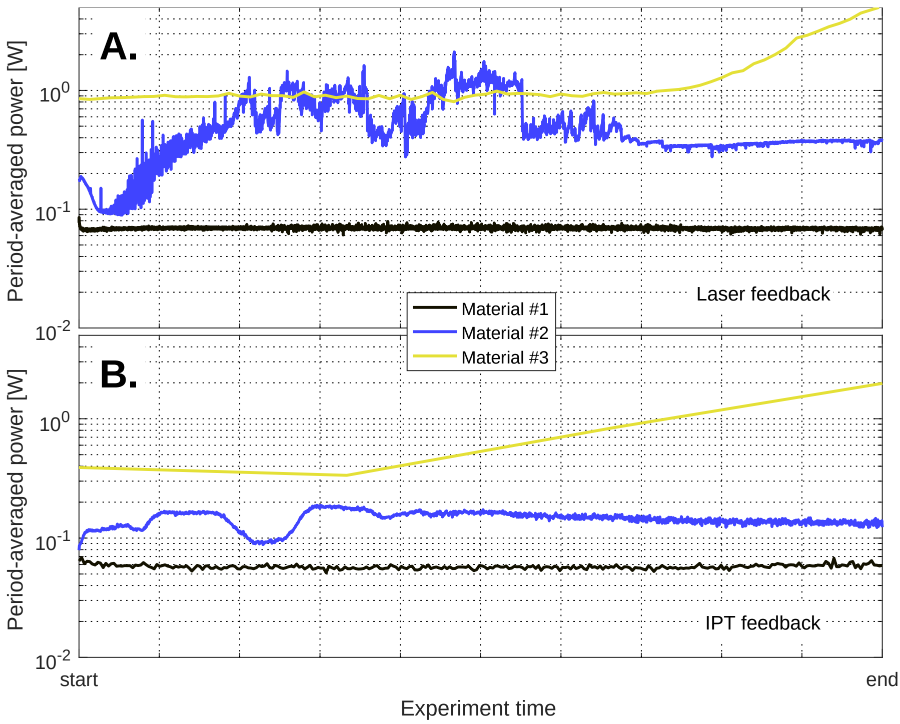

Figure 6.18. Power consumption in long-term 1 Hz sinusoidal reference following experiments with laser (A) and IPT (B) feedback. Time is normalized to experiment durations.

to greater extent. Considering the improvement with respect to the PI controller, $\mathtt{H}_\infty$ or other advanced control methods should be preferred over PI control when possible.

Comparing to the other IPTs, the material #3 exhibits significantly stronger non-linear behaviour in actuation and higher low-frequency noise in the sensing signal. The position of the tip of the sensor-actuator corresponding to zero actuation voltage varies significantly even in the sinusoidal reference following experiments (Figure 6.13), eventually saturating the control voltage and forcing the experiments to be halted. Previously, similar observations also motivated the task modification in the inverted pendulum study in Chapter 4.

A potential explanation to different behaviour of the material # 3 lies in its very high stiffness. As Nemat-Nasser hypothesized in [53] high pressure in the cathode boundary layer causes extensive cation restructuring and redistribution that is responsible for material back-relaxation and possibly for the drift in the position corresponding to zero actuation voltage, also observed in this study. It also needs to be pointed out that while material #3 is shorter than the other IPT samples, its shorter length does not have significant impact on its actuation capability (see magnitude in Figure 6.10), and its short-circuit current is actually stronger than in case of the other materials (see Figure 6.9 and parameters L and α_{0_s} in Table 6.1). Possibly the stronger low-frequency noise in sensing signal is also related to higher material stiffness.

Performances of the materials # 1 and #2 are very similar, but due to different environments (air versus water with added mass effects and higher damping ratio) they cannot be compared in detail. In long-duration sinusoidal reference following experiments in IPT feedback configuration, the sensing signal of material # 1 is less stable than that of material # 2, resulting in termination of the experiments at 300 s. It is also noticed that material #2 has higher power consumption than # 1, most probably caused by the environment. Other experiments do not reveal further remarkable differences in performance and when selecting which material to prefer the decision should be taken according to application environment.

To the author's best knowledge the aforementioned closed-loop experiment durations using IPT feedback signal are much longer than reported ever before.

In this study the materials # 1 and # 2 perform at least 7500 and 4500 work cycles respectively while material #3 executes less than 450. Despite the large number of cycles, no noticeable performance degradation is observed. The relatively small actuation amplitudes achieved in this work are to some extent caused by the weight of the mobile portion of the prototype assembly.

In general, it is demonstrated that it is possible to use IPTs for both sensing and actuation in closed-loop configuration, but the primary factor that limits the performance of such a design is the low-frequency noise in short-circuit sensing current. Further investigation is necessary to identify its origin. Actuation-wise, the back-relaxation effect may also limit the performance of the sensor-actuator, and its extent varies significantly among materials.

The results provided in this study are hopefully valuable when choosing IPT materials for applications.

6.11. Conclusions

This study explores the feasibility of a device that achieves both actuation and sensing functionalities using IPT materials. Based on the integrated IPT sensor-actuator concept previously introduced in Chapter 5, an improved sensor-actuator design is proposed that consists of three short IPT samples and a rigid extension, functioning similarly to a 1-DOF rotational joint with a rigid extension. Sensing and actuation dynamics of the device and the materials is captured using physics-based models that fully characterize the set-up and IPT samples in terms of physically meaningful parameters. Proportional-integral (PI) and H_∞ controllers are designed and closed-loop experiments are conducted with the device. In experimental work the response of the system is measured for step input, four sinusoidal reference signals, three random reference signals and one long-duration sinusoidal reference signal, using three different IPT materials and feedback both from an IPT sensor and a laser distance meter. All the experimental results are quantitatively characterized providing full description of the design and its performance, allowing to compare the performance of the device material-wise and against external feedback, and evaluate the significance of the control method (PI against model-based H_∞) on the results.

The improved design of the integrated IPT sensor-actuator performs better than the one in the previous study in Chapter 5, but still the limitations to potential applications are set by the material properties. Position sensing from IPT signal is stable for a limited timespan resulting in good short-term performance (few seconds up to few minutes), but in longer experiments the low-frequency noise in short-circuit sensing current causes it to significantly deteriorate. Potential reasons for this noise include interactions between the sensor sample and the current measuring circuit, unmodelled processes within the material, and environment influence, but the cause remains unclear and needs further investigation. In terms of actuation capabilities, the potential limitations lie in the non-linearities such as the material-dependent back-relaxation (strongest in case of material # 3) and low strain in response to input voltage, but compared to sensing limitations they are insignificant. While these limitations manifest throughout this work, no additional performance degradation is observed.

While in this study the physics-based models serve both the control and material characterization purposes, less laborious grey-box or black-box models allow to achieve similar performance with much less effort. A controller-wise comparison shows that H_∞ control results in much better performance than PI control, suggesting thst advanced control methods should be preferred over the simplistic ones when possible. When comparing the results that are obtained using IPT feedback to those of the laser distance meter, the latter are clearly superior due to the aforementioned limitations of the IPT feedback. Material-wise comparison shows that materials # 1 and # 2 perform similarly, the former suits well for operation in air and the latter in water. Material #3 performs significantly worse than the others displaying strong non-linearities in actuation performance and strong low-frequency noise in sensing signal. Preferring material #1 or #2 for an application should depend on what kind of environment it will be operating in.

Some of the more important results of this study include a 30 min long successful closed-loop sinusoidal reference following experiment (material # 2), 90 times longer than reported before (Section 3.3.2). In this study materials #1 and #2 perform over 7500 and 4900 work cycles respectively and material #3 performs a little less than 450 cycles, whereas no performance degradation is observable.

Using IPT materials for both actuation and sensing within the same design allows to exploit the attractive novel properties of these ”smart” materials while keeping the system compact and impact on the actuation performance minimal. Very few preliminary reports have explored such a configuration so far. This study investigates the integrated IPT sensor-actuator concept in detail and thoroughly characterizes its performance, providing qualitative and quantitative reference basis for using them in applications.

7. TESTBED FOR IPT MEDICAL APPLICATIONS

7.1. Introduction

Limited actuation capabilities of the IPT materials are a major restriction in many of the proposed applications (see Section 3.2), but provide an integrated safety measure in their potential medical applications, reviewed in Section 3.2.1. Limited actuation moment, mechanical compliance, ease of shaping and miniaturizability are some of the IPT properties that raise interest for using them in medical applications such as a catheter system with an active IPT guidewire [73]. While the reports covered in Section 3.2.1 work with conventional flat IPTs, also other geometries have been reported (Section 3.1.1), including a more suitable cylindrical [41] design capable of bending in any direction. However, feasibility of the IPTs for medical applications (including the active guidewire concept) has not been thoroughly studied and deserves further investigation. Such techniques cannot be validated on human patients, and this study focuses on providing a suitable test-bed for investigating IPTs in invasive medical procedures, particularly the active IPT guidewire in a catheter system.

This study continues to investigate feasibility and behaviour of the IPT materials in applications, aiming to provide a test-bed for medical applications, and further study the concept of a catheter with an active IPT guidewire.

Characterizing the gelatin gel properties with respect to their composition allows to obtain materials with desired mechanical and ultrasound properties. Following the phantom[1] manufacturing procedure allows to produce realistic testing and validation environment for IPT applications with no safety, legal or ethical issues. Renal biopsy training phantoms are manufactured on this study in order to qualitatively validate suitability of the obtained phantoms for human soft tissue substitutes in ultrasound guided interventions. A phantom design is proposed for studying the IPTs as an active guidewire in catheter systems under ultrasound guidance, and validation experiments are intended to be performed in the future.

The work in this study is organized as follows. Comparing different phantom material technologies (Section 3.5) indicates that with using gelatin

[1]Phantoms are specially designed objects that substitute humans or animals in experiments, training etc., realistically mimicking some relevant aspects of their tissue properties and/or anatomy.

gels it is possible to produce inexpensive phantoms with realistic elasticity and ultrasound properties with the least effort. Multiple sets of test samples are manufactured and their Young's moduli, ultrasound broadband attenuations, ultrasound propagation speeds and radiodensities are characterized, relating the material properties to their composition. Phantom materials replicating various human soft tissues can be produced by first seeking up the respective reference values from literature, and selecting required material compositions from the material characterization results. Phantoms with desired anatomy or construction are produced by segmenting organ models from patient CT scans (optional), creating respective mould models using CAD software, materializing them using rapid prototyping, and finally casting the phantoms from gelatin gels (possibly in multiple casting steps). For validating the results of such phantom manufacturing technique, a set of renal biopsy phantoms with realistic properties (mechanical, ultrasound and CT-compatible) and anatomy (patient-specific, with cysts) are produced and evaluated in the training of radiology residents. Basing on the same manufacturing procedure, a phantom design is proposed for evaluating the medical applications of IPTs, particularly the concept of a catheter with an active IPT guidewire. Validating feasibility of the IPT materials as an active guidewire in a catheter system currently remains future work due time restrictions.

This chapter is based on the work reported in publication D.

7.2. Material manufacturing

This section describes the manufacturing process of the gelatin gel phantom materials. These materials will be used to produce a realistic soft tissue substitute test-bed for evaluating IPTs in medical applications. Commercial phantoms (e. g. abdominal and renal phantoms reviewed in D) are expensive and offer only limited anatomical variations to work with. Gelatin gels are selected for soft tissue substitute materials in this study since they are simple to manufacture, non-toxic, inexpensive and allow to well mimic the soft tissue properties, as discussed in Section 3.5.

As described previously in different studies [266, 265, 267] the purposes of the components in the gelatin gel tissue substitutes are as follows. Gelatin and distilled water form the self-supportive gel, and their component ratio sets the lower bound to the achievable elasticity. Formaldehyde cross-links the protein molecules rising the material's melting temperature, but also causes additional stiffening for 100 days post manufacturing at a decelerating rate. Alcohol, such as 1-propanol (preferred for its high boiling point), increases the ultrasound propagation speed within the material and is used when very fine tuning is necessary. Graphite flakes and glass beads allow adjusting the ultrasound attenuation and back-scattering properties, and (food) preservatives may be added in order to increase the lifespan of the materials.

The manufacturing process of gelatin gels in this study has the following steps:

- gelatin gel and graphite flakes are mixed together, poured into a beaker containing distilled water, and allowed to hydrate for approximately 10 min;
- the beaker is placed into a hot water bath and the mixture is constantly stirred until it clears between 32 °C and 40 °C (varies with material composition). Temperatures are kept low and heating durations short in order to prevent protein denaturation and to obtain consistent results;
- the mixture is degassed in a vacuum chamber for 10 min;
- formaldehyde is added and slowly stirred into the mixture;
- mixture is cast into a mould that is then fastened on a slowly rotating frame in order to prevent the graphite from settling while the gel congeals, and afterwards placed in a fridge for further hardening.

More details on the particular components and manufacturing details are provided in publication D.

7.3. Material composition and properties

Since gelatin gel soft tissue substitute properties vary with ingredient specifications and even manufacturers [265] it is necessary to relate the available material compositions to the resulting mechanical and ultrasound properties. This is achieved by producing a set of test samples with different gelatin, graphite powder and formaldehyde concentrations, and measuring the respective parameters. Materials are manufactured following the procedure described in Section 7.2, and at each material composition two samples (cylindrical, 46 mm diameter) with different thicknesses (12 mm and 17 mm) are cast in order to be able to measure their ultrasound properties.

Young's modulus of the material samples is measured using a custom-built dynamic mechanical analysis (DMA) device described in more detail in [289]. Ultrasound propagation speed and broadband attenuation are measured using the experimental set-up shown in Figure 7.1. Material samples are placed in a water tank on top of a solid metal plate, under a fixed 5 MHz dual element ultrasound transducer (Sauter Gmbh) that is attached to an ultrasound pulser-receiver (JSR Ultrasonics DPR 300). Experiments are controlled from a PC in NI Labview 2010 environment and waveforms are captured using a 100 MSs^{-1} digitizer NI USB-5133. Ultrasound broadband attenuation is calculated from the difference in attenuation of two samples of the same material with different thickness.

In addition to the mechanical and ultrasound properties also the radiodensities of the test samples are measured using a multidetector CT scanner (Brilliance 64, Philips Healthcare) in order to investigate the CT-compatibility of the material. All material properties are measured 1 day post manufacturing the respective samples.

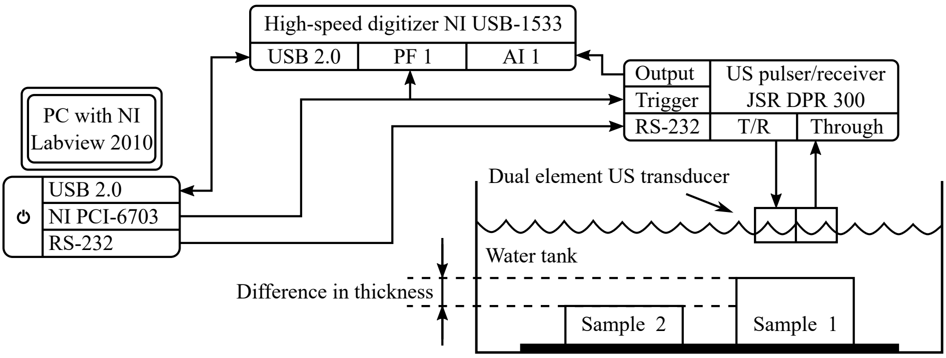

Figure 7.1. Experimental set-up for measuring ultrasound properties.

7.4. Phantoms

This section describes the phantom manufacturing methodology that allows to produce soft tissue substitutes with various complexities, tailored for specific tests of interest. Once the required tissue properties are determined from the literature (Section 3.5), respective material compositions are looked up from the results of the mapping procedure described in Section 7.3, and phantoms are manufactured as follows:

- when patient-specific or realistic anatomy is required the organs of interest are segmented from the CT scans using 3D Slicer software, and the resulting model is transformed into a CAD format;
- using CAD software, the (multi-component) moulds are created for casting the phantom components;
- physical moulds are created using rapid prototyping;
- parts of phantoms are cast and assembled according to the manufacturing procedure described in Section 7.2.

According to the aforementioned phantom manufacturing procedure renal biopsy phantoms are manufactured and further tested in the training curricula of the second year radiology residents, qualitatively validating the phantom manufacturing procedures and gelatin gel property identification results. The patient-specific test phantoms mimic cysts for biopsy targets, and during the training they are covered with opaque plastic as the biopsies are performed under ultrasound imaging. More detailed information on their properties and manufacturing are provided in publication D.

Design of the test-bed for validating the feasibility of the potential IPT applications in medicine, particularly as an active guidewire in a catheter system (see Section 3.2.1), is depicted in Figure 7.2. Such phantom is intended for testing the catheter prototype in passing through bifurcations of different diameters at

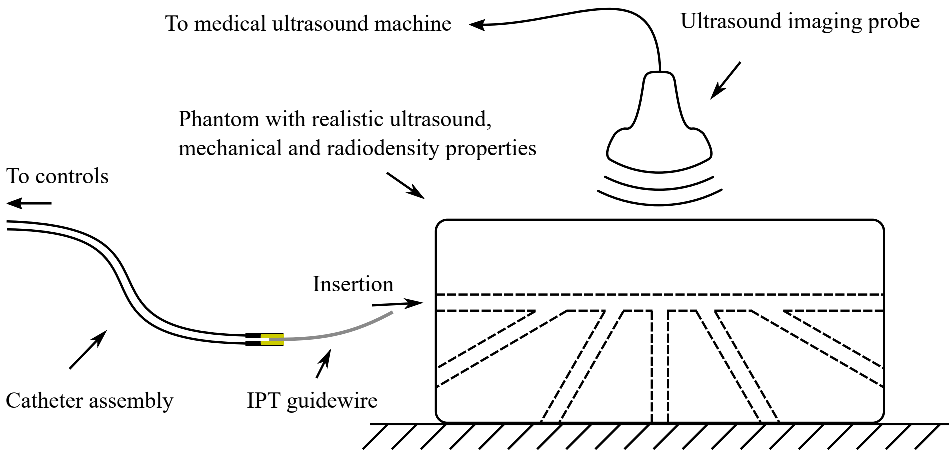

Figure 7.2. Experimental test-bed for studying the IPT active guidewire concept.

various angles under ultrasound guidance, and the respective phantom needs to mimic the elasticity and ultrasound properties of the blood vessels and surrounding soft tissues in order to establish a realistic test medium.

7.5. Results

Relating the phantom material properties to their composition is performed by manufacturing material samples described in Section 7.3 according to techniques described in Section 7.2, and measuring the properties of these samples as described in Section 7.3. For measuring Young's modulus a set of material samples is manufactured with gelatin concentrations varying from 100 g/l to 130 g/l in 10 g/l increments, and formaldehyde concentrations varying from 0.05 wt% to 0.2 wt% in 0.05 wt% increments. Results in Figure 7.3 show that both the component concentrations have significant impact on the Young's modulus that may be considered linear in the region of interest. Graphite concentration also has linear impact on the Young's modulus, but at concentrations up to 1 wt% it may be considered negligible compared to the effects of formaldehyde and gelatin.

For measuring the ultrasound broadband attenuation and propagation speed another set of material samples is manufactured, with gelatin concentrations varying from 100 g/l to 140 g/l in 10 g/l increments (0.1 wt% of formaldehyde, no graphite). Results show that the gelatin concentration has very insignificant impact on material's ultrasound broadband attenuation (Figure 4 in publication D), that may be considered linear. Further experiments are conducted on an extended set of material samples with gelatin concentrations of 95 g/l, 105 g/l and 115 g/l, and graphite concentrations varying from 0 wt% to 0.75 wt% in 0.25 wt% increments. Respective results are plotted in Figure 7.4, and they show that the graphite concentration has quite linear impact on the attenuation while

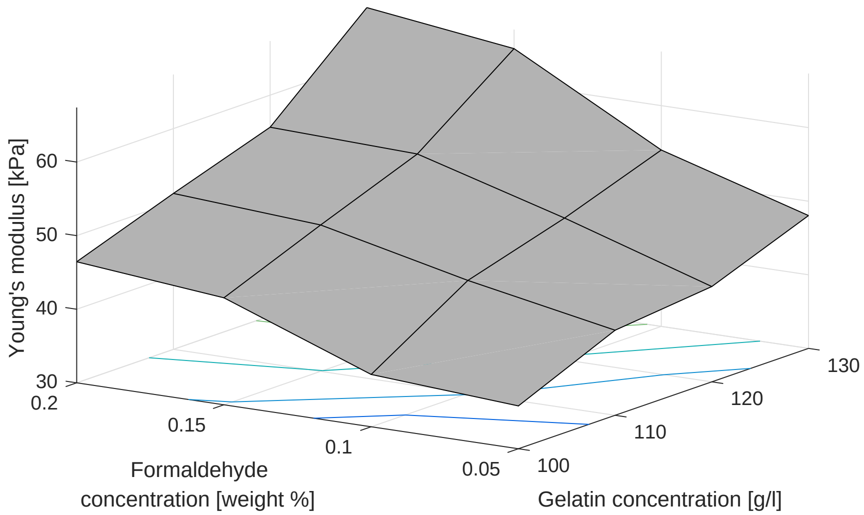

Figure 7.3. Experimentally measured Young's modulus at different formaldehyde and gelatin concentrations.

the effect of gelatin is negligible. Results of the ultrasound propagation speed measurements did not show significant correlation to gelatin, formaldehyde and graphite concentration, and over all the measured samples an average speed of 1450 m/s is calculated with 32.7 m/s standard deviation.

Radiodensity measurements are performed on larger material samples (250 ml). In the first set of test samples the formaldehyde concentrations vary from 0 wt% to 2 wt% (100 g/l gelatin concentration, no graphite) and have no observable impact on radiodensity of the material. In the second set of test samples the graphite concentrations vary between 0 wt % and 1 wt% (100 g/l gelatin, 0.1 wt% formaldehyde) and increase in graphite concentration only increases the standard deviation in the measured radiodensities from 3 HU to 8 HU. In the third set of test samples the gelatin concentration is varied from 60 g/l to 140 g/l (0.1 wt% of formaldehyde, no graphite), and as can be seen in Figure 7.5 its impact on the material's radiodensity is quite linear.

An example of a renal biopsy training phantom that is produced for validating the mapping of material properties and phantom manufacturing process is shown in Figure 7.6. The evaluation is performed by second year radiology residents as a part of their ultrasound-assisted biopsy training, and the procedure is described in greater detail in publication D. Phantom kidney and pathologies are anatomically realistic in ultrasound imaging, and manufacturing costs are estimated to be below 60 $ per phantom.

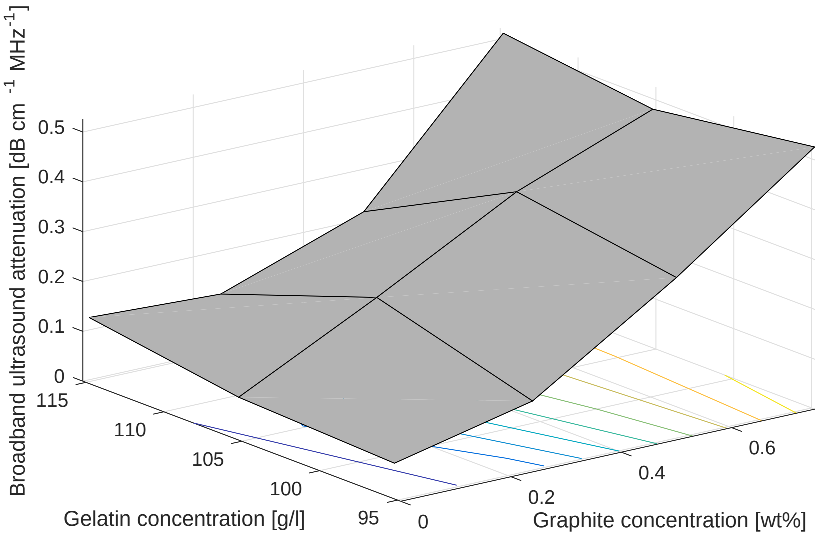

Figure 7.4. Experimentally measured ultrasound broadband attenuation at different gelatin and graphite concentrations.

7.6. Discussion and future work

Measuring the Young's modulus, ultrasound attenuation, ultrasound propagation speed and additionally the radiodensity of the gelatin gel samples results in characterization of the material properties in terms of their composition. Based on these results it is possible to manufacture mechanically realistic soft tissue phantom that are medical ultrasound-compatible. First the properties of the respective tissues are determined from the literature, then the required material compositions are looked up from the results of material characterization, and finally the phantoms are cast, possibly in parts. Since each gel's component's concentration significantly influences only one or two of its properties, it is possible to tune the phantom properties remarkably well.

Since the ultrasound propagation speed within the materials is very realistic (actual and targeted mean values differ by less than 7%) there is no alcohol added to the materials. Also, the phantoms are used within few days to few weeks post manufacturing, and no additional preservatives are needed to expand the material lifespan, allowing to maintain a simple manufacturing process.

The methodology for achieving anatomically realistic soft tissue substitute phantoms is further validated by manufacturing a set of renal biopsy phantoms and evaluating them in the training process of the second year radiology residents. Cost of manufacturing of these phantoms is below 60 $ per phantom, including labour. Evaluation results show that the phantoms and included pathologies look realistic, they suit well for training, but fail to mimic the complex internal

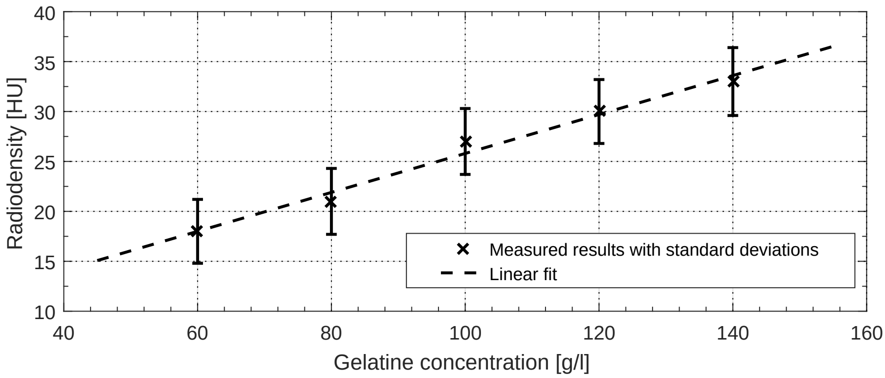

Figure 7.5. Impact of the gelatin concentration on the radiodensity of the gelatin gel.

structure of actual human kidneys. More information on the evaluation procedure and respective results are available in publication D.

In future work it is intended to use the established material characterization and validated phantom manufacturing technology in order to produce phantoms for testing the medical applications of IPTs, particularly as an active guidewire in a catheter system. Design of such a phantom is proposed in Figure 7.2 in Section 7.4, and it provides a realistic test-bed without arising any safety, legal or ethical issues. The intended validation procedure on the IPT active guidewire in a catheter device involves testing its penetration capability in blood vessel bifurcations with various anatomies, diameters and angles. Such a phantom would also allow to validate various other surgical tool concepts proposed in Section 3.2.1, and potentially combine the self-sensing concept studied in Chapters 5 and 6 in order to facilitate guiding the catheter during the operation.

7.7. Conclusions

Mechanical compliance and limited maximum forces exerted by the IPTs are limitations in many potential applications, but provide intrinsic safety measures that could be very beneficial in medical applications. Ultrasound-compatible phantoms with realistic anatomy and mechanical properties allow to validate many different types of novel medical instruments and techniques in realistic conditions. This study focuses on producing soft tissue substitute phantoms with such properties in order to validate medical applications of the IPT materials, specifically as an active guidewire in a catheter system.

After identifying gelatin gels as suitable phantom materials, the relations between their composition and properties are identified in terms of Young's modulus, ultrasound propagation speed, ultrasound broadband attenuation and material radiodensity. Next, a phantom manufacturing procedure is introduced that allows to achieve mechanically realistic soft tissue substitutes with patient-

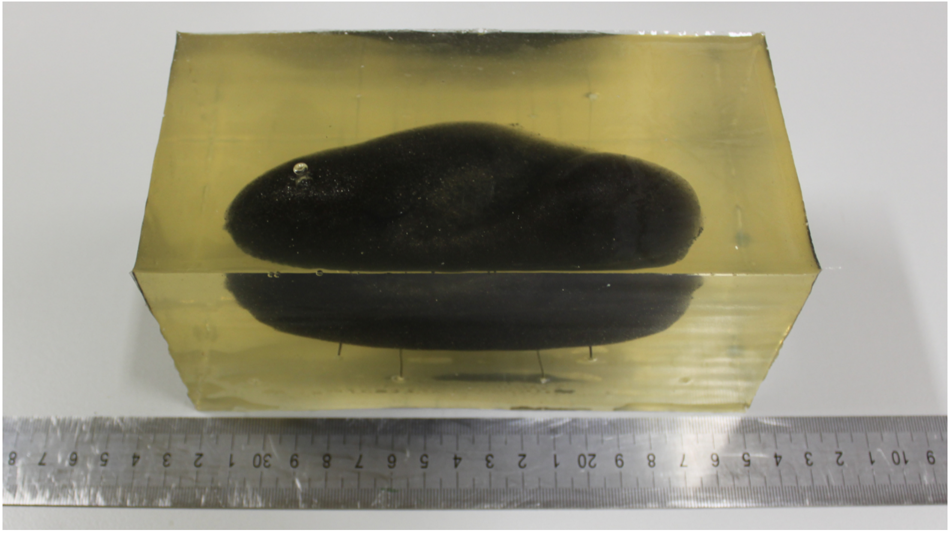

Figure 7.6. A renal biopsy phantom validated by the radiology residents.

specific anatomy and realistic appearance in ultrasound imaging. Anatomically realistic renal biopsy phantoms are produced from human CT scans and validated in an ultrasound-guided biopsy procedure as a part of radiology residents' training curricula. Based on the material characterization results and successful validation of the phantom manufacturing techniques, a phantom design is proposed for validation of a potential medical application of the IPT materials as an active guidewire in catheter systems.

As a result of this study the phantom material properties are related to their composition, manufacturing techniques producing realistic tissue mimicking phantoms are established, and resulting anatomically realistic patient-specific phantoms are validated in the training of radiology residents. The phantom manufacturing technique introduced in this work allows to produce economically affordable soft tissue substitutes that are suitable for many applications.

In order to validate the usability of the IPT materials in medical applications, particularly as an active guidewire in a catheter device, a phantom design is proposed that allows to test such devices in passing blood vessel bifurcations at different angles and diameters under ultrasound guidance. In continuation of this work it is intended to realize a compact design of a catheter system with an active IPT guidewire and validate the design feasibility on the aforementioned phantom under ultrasound guidance. Initially it is intended to control the IPT actuation manually, and further by integrating an IPT sensor with the actuator, establishing closed-loop control similarly to Chapters 5 and 6.

Thus, the softness and limited actuation capabilities of the IPTs provide them with intrinsic safety measures, and their feasibility for medical applications, such as an active guidewire in a catheter, deserves a more systematic evaluation. In this study the soft tissue phantom manufacturing process is introduced and validated, and a phantom design is proposed aiming to provide a test-bed for evaluating IPTs in medical applications. Since the validation experiments exceed the scope of this thesis, they must remain the future work.

CONCLUSIONS

Due to attractive properties including the sensing and actuation capabilities, the IPT materials have been forecast to trigger advances in robotics, biomedical engineering, energetics, etc., and enable integrated designs exploiting the potential of the material to full extent. Despite the multitude of reports on potential implementations their adaptation to practical use has been delayed, most probably due to insufficient performance and reliability. The few studies reporting integrating the actuation and sensing functionalities only offer very preliminary results. This thesis looks into the state-of-the-art of the performance of the IPT materials and their feasibility in applications. Behaviour of the IPT materials at their performance limits and respective limitations are studied by utilizing them for the first time in a real-time critical application, balancing an inverted pendulum system. Next, the feasibility of an integrated IPT sensor-actuator concept, and performance and limitations of the materials in closed-loop configuration with IPT feedback are investigated. Studying the performance of the materials and the sensor-actuator concept is resumed on an improved design, thoroughly characterizing its set-up, materials and closed-loop performance. The limited performance of the IPTs can be considered as an intrinsic safety measure in medicine, and therefore a test-bed is provided for investigating the invasive medical applications of the IPTs in realistic conditions with no safety, legal or ethical issues.

It is demonstrated that when using IPT materials as actuators it is possible to stabilize an inverted pendulum system for maximum of 30 min, and repeatedly for 5 min long experiments. While the proof-of-concept real-time task is successfully completed using IPMC materials, the inertia of the system is reduced in multiple steps before the successful experiments can be performed. Additional damping and added mass effects in water on the one hand simplify the stabilization task as they slow down the motion of the inverted pendulum rod, and on the other hand provide additional load on the actuator. Besides the limited actuation moment, the IPMCs used in this study exhibit a strong back-relaxation effect (stronger at higher actuation voltages) that causes the cart position corresponding to zero input voltage to vary. This limitation is overcome by allowing the cart position to vary within the limits of external disturbances and (unmodelled) non-linear dynamics, otherwise it is not possible to stabilize the system for any longer than 10 s. Such phenomenon restricts the exploitation of these particular materials in applications requiring precise position control. After several successful 5 min long experiments the actuation capability degrades and pendulum balancing attempts fail subsequently earlier. This is believed to be caused by the loss of counter-ions due to high actuation voltages ($\pm$ 4 V saturation limits), since electrolysis is observable and since the actuation capabilities of the same materials can be fully restored by repeating the ion-exchange process. Thus, it is possible to use IPTs in real-time tasks, but limiting factors that must be taken into consideration include limited actuation, back-relaxation effects and performance degradation at high actuation voltages.

Results of the close-loop sinusoidal reference following (0.1 Hz, 0.5 Hz and 1 Hz) experiments on the integrated IPT sensor-actuator prototype (using IPCMCs) provide a qualitative demonstration of the feasibility of such a concept. Unexpectedly strong low-frequency noise in the sensor's short-circuit current causes a gradual error accumulation in the position estimation, further causing an error in reference tracking. In short term (few seconds) the closed-loop reference tracking error of the prototype in IPT feedback configuration remains within the limits of modelling errors in the sensing model, whereas IPTs provide a better precision than the camera resolution achieves in this experimental set-up. In the long run (up to 1 min) the position estimation gradually deteriorates (due to the aforementioned low-frequency noise), eventually saturating the actuation voltage, and the experiment must be aborted to prevent damaging the actuator. The source of the low-frequency noise in the sensing signal is not identified, but interactions between the primitive current sensing circuit and the sensor sample are suspected. Therefore, the primarily qualitative results of this study indicate that the integrated IPT sensor-actuator concept is feasible for implementation for very limited time periods, but the noise in sensing signal needs to be resolved in order to use them for longer intervals than just a few seconds.

To characterize the materials and the improved IPT sensor-actuator design, the actuation and sensing dynamics are described in terms of fundamental material properties and prototype parameters. Closed-loop experiments of the step response (1 mm amplitude), sinusoidal reference following (1 mm amplitude at 0.5 Hz, 1 Hz, 2 Hz and 3 Hz frequencies), random reference following (3 spectra from 0.1 Hz to 2 Hz, 3 Hz and 4 Hz) and long-duration sinusoidal reference following (up to 30 min and 2 h with IPT and laser distance meter feedback respectively) are performed on the prototype using three different materials (an IPCMC with coconut shell derived active carbon electrodes, one IPMC with Pt and one with Au electrodes), two different controllers (PI and $\mathtt{H}_\infty$) and both IPT and laser distance meter feedback. Based on these results, the performance of the design and materials is qualitatively and quantitatively characterized. In this study, up to 30 min long closed-loop experiments are successfully conducted in IPT feedback configuration (extended 1 Hz sinusoidal reference following), 90 times longer than reported before. Low-frequency noise in the IPT short-circuit current reading reduces with the improved amplifier design, but is also observed to vary across materials. It causes an error accumulation in the position estimation, limiting the typical closed-loop experiment durations to last between few seconds up to several minutes before the control voltage saturates. In terms of actuation performance, the back-relaxation effects significantly vary among the materials from unobservable to very strong, but performance degradation in the course of the experiments is not observed. In this work the physics-based models are used for material characterization, and due to their very laborious nature are not recommended for applications. H_∞ controllers allow to achieve much smaller tracking errors than the PI controllers indicating that advanced control methods should be preferred over simple ones. Thus, this study provides thorough qualitative and quantitative characterization of the sensor-actuator design, materials and their closed-loop performance. The primary limitations, i. e. the back-relaxation effect in actuation and low-frequency noise in sensing, are observed to vary across materials.

In order to provide a test-bed for investigating the potential medical applications of IPTs in realistic conditions, manufacturing techniques are presented that allow to produce soft tissue substitute phantoms with desired (potentially patient-specific) anatomy and realistic mechanical and ultrasound properties. Gelatin gel properties are experimentally related to their composition, allowing to seek up recipes for desired material properties. Phantoms are manufactured by segmenting organs of interest from CT scans, creating moulds using CAD software and rapid prototyping, and casting the final phantom from gelatin gels with a specified composition. Ultrasound compatible renal biopsy training phantoms are produced for qualitatively validating the manufacturing methodology by radiology residents, and evaluation results confirm that the anatomy and appearance in ultrasound imaging are realistic. Next, a test-bed is proposed for validating invasive IPT medical applications (particularly a catheter design with active IPT guidewire) in realistic conditions under ultrasound imaging. In future work it is intended to build a catheter prototype with active IPT guidewire, and validate its performance on the aforementioned test-bed, by passing it through blood vessel bifurcations of various geometries and diameters under ultrasound imaging guidance. In the initial tests the IPT guidewire is planned to be operated manually by switching the voltage on and off, and in the following experiments an integrated IPT sensor is added to the guidewire, allowing to operate it in closed-loop configuration simply by setting the reference position.

REFERENCES

[1] M. Shahinpoor, Y. Bar-Cohen, J. O. Simpson, and J. Smith, "Ionic polymer-metal composites (IPMCs) as biomimetic sensors, actuators and artificial muscles - a review," *Smart Materials and Structures*, vol. 7, no. 6, pp. R15–R30, Dec. 1998.

[2] M. Shahinpoor, "Ionic polymer–conductor composites as biomimetic sensors, robotic actuators and artificial muscles—a review," *Electrochimica Acta*, vol. 48, no. 14-16, pp. 2343–2353, Jun. 2003.

[3] B. Bhandari, G. Y. Lee, and S. H. Ahn, "A review on IPMC material as actuators and sensors: Fabrications, characteristics and applications," *International Journal of Precision Engineering and Manufacturing*, vol. 13, no. 1, pp. 141–163, 2012.

[4] C. Jo, D. Pugal, I. K. Oh, K. J. Kim, and K. Asaka, "Recent advances in ionic polymer-metal composite actuators and their modeling and applications," *Progress in Polymer Science*, vol. 38, no. 7, pp. 1037–1066, 2013.

[5] K. Farinholt, "Modeling and characterization of ionic polymer transducers for sensing and actuation," Ph.D. dissertation, Virginia Polytechnic Institute and State University, 2005.

[6] B. J. Akle, M. D. Bennett, D. J. Leo, K. B. Wiles, and J. E. McGrath, "Direct assembly process: A novel fabrication technique for large strain ionic polymer transducers," *Journal of Materials Science*, vol. 42, no. 16, pp. 7031–7041, 2007.

[7] D. J. Leo, *Engineering Analysis of Smart Material Systems*. Hoboken, NJ, USA: John Wiley & Sons, Inc., Aug 2007.

[8] R. Kanno, S. Tadokoro, M. Hattori, T. Takamori, M. Costaftis, and K. Oguro, "Dynamic model of ICPF (ionic conducting polymer film) actuator," in *1995 IEEE International Conference on Systems, Man and Cybernetics. Intelligent Systems for the 21st Century*. IEEE, 1995, pp. 177–182.

[9] V. Palmre, D. Brandell, U. Mäeorg, J. Torop, O. Volobujeva, A. Punning, U. Johanson, M. Kruusmaa, and A. Aabloo, "Nanoporous carbon-based electrodes for high strain ionomeric bending actuators," *Smart Materials and Structures*, vol. 18, no. 9, p. 095028, 2009.

[10] K. Kruusamäe, A. Punning, and A. Aabloo, "Self-sensing properties of carbon-polymer composite (CPC) actuators," in *Proceedings of SPIE, Electroactive Polymer Actuators and Devices (EAPAD) 2011*, Y. Bar-Cohen and F. Carpi, Eds., vol. 7976, Mar 2011, p. 79760Q.

[11] W. Yang, H. Choi, S. Choi, M. Jeon, and S.-Y. Lee, "Carbon nanotube–graphene composite for ionic polymer actuators," *Smart Materials and Structures*, vol. 21, no. 5, p. 055012, May 2012.

[12] V. Vunder, M. Itik, I. Põldsalu, A. Punning, and A. Aabloo, "Inversion-based control of ionic polymer–metal composite actuators with nanoporous carbon-based electrodes," *Smart Materials and Structures*, vol. 23, no. 2, p. 025010, Feb 2014.

[13] S. Jamshidi, M. Dardel, M. H. Pashaei, and R. a. Alashti, "Energy harvesting from limit cycle oscillation of a cantilever plate in low subsonic flow by ionic polymer metal composite," *Proceedings of the Institution of Mechanical Engineers, Part G: Journal of Aerospace Engineering*, vol. 229, no. 5, pp. 814–836, 2015.

[14] Y. Bar-Cohen and Q. Zhang, "Electroactive Polymer Actuators and Sensors," *MRS Bulletin*, vol. 33, no. 03, pp. 173–181, 2008.

[15] K. Oguro, Y. Kawami, and H. Takenaka, "Bending of an ion-conducting polymer film-electrode composite by an electric stimulus at low voltage," *Journal of Micromachine Society*, vol. 5, no. 1, pp. 27–30, 1992.

[16] K. Oguro, H. Takenaka, and Y. Kawami, "Actuator element," Patent US 5,268,082, 1993.

[17] M. Shahinpoor, "Conceptual design, kinematics and dynamics of swimming robotic structures using ionic polymeric gel muscles," *Smart Materials and Structures*, vol. 1, no. 1, pp. 91–94, Mar. 1992.

[18] K. Sadeghipour, R. Salomon, and S. Neogi, "Development of a novel electrochemically active membrane and 'smart' material based vibration sensor/damper," *Smart Materials and Structures*, vol. 1, no. 2, pp. 172–179, Jun. 1992.

[19] M. Shahinpoor, "Micro-Electro-Mechanics of Ionic Polymeric Gels As Electrically Controllable Artificial Muscles," *Journal of Intelligent Material Systems and Structures*, vol. 6, no. 3, pp. 307–314, May 1995.

[20] M. Shahinpoor, “New effect in ionic polymeric gels: the ionic flexogelectric effect,” in *Proc. SPIE, Smart Structures & Materials’ 95*, vol. 2441, San Diego, CA, 1995, pp. 42–53.

[21] K. J. Kim and M. Shahinpoor, “Ionic polymer metal composites: II. Manufacturing techniques,” *Smart Materials and Structures*, vol. 12, no. 1, pp. 65–79, Feb. 2003.

[22] B. J. Akle, M. D. Bennett, and D. J. Leo, “Ionic electroactive hybrid transducers,” in *Smart Structures and Materials 2005: Electroactive Polymer Actuators and Devices (EAPAD)*, vol. 5759. SPIE, 2005, pp. 153–164.

[23] V. Palmre, D. Brandell, U. Mäeorg, J. Torop, O. Volobujeva, A. Punning, U. Johanson, and A. Aabloo, “Ionic polymer metal composites with nanoporous carbon electrodes,” in *Proc. SPIE, Electroactive Polymer Actuators and Devices (EAPAD) 2010*, vol. 7642, Mar. 2010, pp. 76 421D–1–76 421D–9.

[24] T. Nakamura, T. Ihara, T. Horiuchi, T. Mukai, and K. Asaka, “Measurement and Modeling of Electro-Chemical Properties of Ion Polymer Metal Composite by Complex Impedance Analysis,” *SICE Journal of Control, Measurement, and System Integration*, vol. 2, no. 6, pp. 373–378, 2009.

[25] K. Kim and M. Shahinpoor, “A novel method of manufacturing three-dimensional ionic polymer–metal composites (IPMCs) biomimetic sensors, actuators and artificial muscles,” *Polymer*, vol. 43, no. 3, pp. 797–802, Feb. 2002.

[26] S. J. Kim, Y. Jung, K. K. Leang, and K. J. Kim, “Development of dimensionally scalable IPMC materials,” in *2010 IEEE/ASME International Conference on Advanced Intelligent Mechatronics*, vol. 9, no. 17 2. IEEE, Jul. 2010, pp. 145–150.

[27] M. Shahinpoor and K. J. Kim, “Ionic polymer-metal composites: I. Fundamentals,” *Smart Materials and Structures*, vol. 10, no. 4, pp. 819–833, Aug. 2001.

[28] S. Nemat-Nasser and Y. Wu, “Comparative experimental study of ionic polymer-metal composites with different backbone ionomers and in various cation forms,” *Journal of Applied Physics*, vol. 93, no. 9, p. 5255, 2003.

[29] M. D. Bennett and D. J. Leo, “Ionic liquids as stable solvents for ionic polymer transducers,” *Sensors and Actuators, A: Physical*, vol. 115, no. 1, pp. 79–90, 2004.

[30] M. Okamoto, K. Kikuchi, and S. Tsuchitani, “Evaluation of operating characteristics of Flemion®-based IPMC with ionic liquids operated in water,” in *2010 IEEE/SICE International Symposium on System Integration*. IEEE, Dec. 2010, pp. 272–276.

[31] Y. Abe, A. Mochizuki, T. Kawashima, S. Yamashita, K. Asaka, and K. Oguro, “Effect on bending behavior of counter cation species in perfluorinated sulfonate membrane-platinum composite,” *Polymers for Advanced Technologies*, vol. 9, no. 8, pp. 520–526, Aug. 1998.

[32] N. Kamamichi, M. Yamakita, T. Kozuki, K. Asaka, and Z.-W. Luo, “Doping effects on robotic systems with ionic polymer–metal composite actuators,” *Advanced Robotics*, vol. 21, no. 1-2, pp. 65–85, Jan. 2007.

[33] M. Doi, M. Matsumoto, and Y. Hirose, “Deformation of ionic polymer gels by electric fields,” *Macromolecules*, vol. 25, no. 20, pp. 5504–5511, Sep. 1992.

[34] H. Okazaki, S. Sawada, M. Kimura, H. Tanaka, T. Matsumoto, T. Ohtake, and S. Inoue, “Soft Actuator Using Ionic Polymer–Metal Composite Composed of Gold Electrodes Deposited Using Vacuum Evaporation,” *IEEE Electron Device Letters*, vol. 33, no. 7, pp. 1087–1089, Jul. 2012.

[35] J. Torop, M. Arulepp, T. Sugino, K. Asaka, A. Jänes, E. Lust, and A. Aabloo, “Microporous and mesoporous carbide-derived carbons for strain modification of electromechanical actuators,” *Langmuir*, vol. 30, no. 10, pp. 2583–2587, 2014.

[36] M. Shahinpoor and K. J. Kim, “The effect of surface-electrode resistance on the performance of ionic polymer-metal composite (IPMC) artificial muscles,” *Smart Materials and Structures*, vol. 9, p. 543, 2000.

[37] A. Punning, M. Kruusmaa, and a. Aabloo, “Surface resistance experiments with IPMC sensors and actuators,” *Sensors and Actuators A: Physical*, vol. 133, no. 1, pp. 200–209, Jan. 2007.

[38] U. Johanson, U. Mäeorg, V. Sammelselg, D. Brandell, A. Punning, M. Kruusmaa, and A. Aabloo, “Electrode reactions in Cu-Pt coated ionic polymer actuators,” *Sensors and Actuators, B: Chemical*, vol. 131, no. 1, pp. 340–346, 2008.

[39] H. Moeinkhah, J. Rezaeepazhand, A. Akbarzadeh, and I.-k. Oh, “Accurate Dynamic Modeling of Helical Ionic Polymer-Metal Composite Actuator Based on Intrinsic Equations,” *IEEE/ASME Transactions on Mechatronics*, vol. 20, no. 4, pp. 1680–1688, Aug. 2015.

[40] M. A. Tsugawa, K. K. Leang, V. Palmre, and K. J. Kim, "Sectored Tube-Shaped Ionic Polymer-Metal Composite Actuator With Integrated Sensor," in *Proceedings of the ASME 2013 Conference on Smart Materials, Adaptive Structures and Intelligent Systems*, Sept 2013, p. V002T06A001.

[41] S. J. Kim, D. Pugal, J. Wong, K. J. Kim, and W. Yim, "A bio-inspired multi degree of freedom actuator based on a novel cylindrical ionic polymer-metal composite material," *2011 15th International Conference on Advanced Robotics (ICAR)*, pp. 435–440, Jun. 2011.

[42] K. Asaka, K. Oguro, Y. Nishimura, M. Mizuhata, and H. Takenaka, "Bending of Polyelectrolyte Membrane-Platinum Composites by Electric Stimuli I. Response Characteristics to Various Waveforms." *Polymer Journal*, vol. 27, no. 4, pp. 436–440, 1995.

[43] M. Mojarrad and M. Shahinpoor, "Ion-exchange-metal composite sensor films," in *Proceedings of SPIE Smart Structures and Materials' 97*, 1997, pp. 52–60.

[44] S. Nemat-Nasser and J. Y. Li, "Electromechanical response of ionic polymer-metal composites," *Journal of Applied Physics*, vol. 87, no. 7, p. 3321, 2000.

[45] D. Kim and K. J. Kim, "A theoretical and experiment study for self-oscillatory ionic polymer–metal composite actuators," *Smart Materials and Structures*, vol. 16, no. 5, pp. 1789–1795, Oct. 2007.

[46] D. Kim and K. Kim, "Ionic polymer–metal composite actuators exhibiting self-oscillation," *Sensors and Actuators A: Physical*, vol. 137, no. 1, pp. 129–133, Jun. 2007.

[47] Y. Bar-Cohen, S. P. Leary, M. Shahinpoor, J. S. Harrison, and J. G. Smith, "Electroactive polymer (EAP) actuators for planetary applications," in *Proceedings of SPIE's 6th Annual International Symposium on Smart Structures and Materials*, Y. Bar-Cohen, Ed., no. 3669, May 1999, pp. 57–63.

[48] K. Mallavarapu and D. J. Leo, "Feedback Control of the Bending Response of Ionic Polymer Actuators," *Journal of Intelligent Material Systems and Structures*, vol. 12, no. 3, pp. 143–155, 2001.

[49] M. Anton, A. Aabloo, A. Punning, and M. Kruusmaa, "A mechanical model of a non-uniform ionomeric polymer metal composite actuator," *Smart Materials and Structures*, vol. 17, no. 2, p. 025004, Apr. 2008.

[50] S. Tadokoro, S. Yamagami, T. Takamori, and K. Oguro, "Modeling of Nafion-Pt composite actuators (ICPF) by ionic motion," in *Proceedings*

of SPIE Smart Structures and Materials 2000: Electroactive Polymer Actuators and Devices (EAPAD), vol. 3987, 2000, pp. 92–102.

[51] K. Asaka and K. Oguro, “Bending of polyelectrolyte membrane platinum composites by electric stimuliPart II. Response kinetics,” *Journal of Electroanalytical Chemistry*, vol. 480, no. 1-2, pp. 186–198, Jan. 2000.

[52] P. G. D. Gennes, K. Okumura, M. Shahinpoor, and K. J. Kim, “Mechanoelectric effects in ionic gels,” *Europhysics Letters (EPL)*, vol. 50, no. 4, pp. 513–518, May 2000.

[53] S. Nemat-Nasser, “Micromechanics of actuation of ionic polymer-metal composites,” *Journal of Applied Physics*, vol. 92, no. 5, p. 2899, 2002.

[54] H. Moeinkhah, J.-Y. Jung, J.-H. Jeon, A. Akbarzadeh, J. Rezaeepazhand, K. C. Park, and I.-K. Oh, “How does clamping pressure influence actuation performance of soft ionic polymer–metal composites?” *Smart Materials and Structures*, vol. 22, no. 2, p. 025014, 2013.

[55] C. Bonomo, C. Negro, L. Fortuna, and S. Graziani, “Characterization of IPMC strip sensorial properties: preliminary results,” in *Proceedings of the 2003 International Symposium on Circuits and Systems, 2003. ISCAS ’03.*, vol. 4. IEEE, 2003, pp. IV–816–IV–819.

[56] C. Bonomo, L. Fortuna, P. Giannone, S. Graziani, and S. Strazzeri, “A model for ionic polymer metal composites as sensors,” *Smart Materials and Structures*, vol. 15, no. 3, pp. 749–758, Jun. 2006.

[57] Z. Chen, X. Tan, A. Will, and C. Ziel, “A dynamic model for ionic polymer–metal composite sensors,” *Smart Materials and Structures*, vol. 16, no. 4, pp. 1477–1488, Aug. 2007.

[58] K. Kikuchi and S. Tsuchitani, “Effects of environmental humidity on electrical properties of ionic polymer-metal composite with ionic liquid,” in *ICCAS-SICE, 2009.* IEEE, 2009, pp. 4747–4751.

[59] I. Must, V. Vunder, F. Kaasik, I. Põldsalu, U. Johanson, A. Punning, and A. Aabloo, “Ionic liquid-based actuators working in air: The effect of ambient humidity,” *Sensors and Actuators B: Chemical*, vol. 202, no. October, pp. 114–122, oct 2014.

[60] P. Brunetto, L. Fortuna, P. Giannone, S. Graziani, and S. Strazzeri, “Static and Dynamic Characterization of the Temperature and Humidity Influence on IPMC Actuators,” *IEEE Transactions on Instrumentation and Measurement*, vol. 59, no. 4, pp. 893–908, Apr. 2010.

[61] P. Brunetto, L. Fortuna, P. Giannone, S. Graziani, and S. Strazzeri, “Characterization of the Temperature and Humidity Influence on Ionic

Polymer–Metal Composites as Sensors," *IEEE Transactions on Instrumentation and Measurement*, vol. 60, no. 8, pp. 2951–2959, Aug. 2011.

[62] T. Ganley, D. L. S. Hung, G. Zhu, and X. Tan, "Temperature-dependent Ionic polymer-metal composite (IPMC) sensing dynamics: Modeling and inverse compensation," *2010 IEEE/ASME International Conference on Advanced Intelligent Mechatronics*, pp. 447–452, Jul. 2010.

[63] D. Kim and K. J. Kim, "Experimental Investigation on Electrochemical Properties of Ionic Polymer-Metal Composite," *Journal of Intelligent Material Systems and Structures*, vol. 17, no. 5, pp. 449–454, May 2006.

[64] A. Punning, I. Must, I. Poldsalu, V. Vunder, R. Temmer, K. Kruusamaee, F. Kaasik, J. Torop, P. Rinne, T. Lulla, U. Johanson, T. Tamm, and A. Aabloo, "Lifetime measurements of ionic electroactive polymer actuators," *Journal of Intelligent Material Systems and Structures*, vol. 25, no. 18, pp. 2267–2275, 2014.

[65] M. Shahinpoor and K. J. Kim, "Ionic polymer–metal composites: IV. Industrial and medical applications," *Smart Materials and Structures*, vol. 14, no. 1, pp. 197–214, Feb. 2005.

[66] D. Pugal, K. Jung, A. Aabloo, and K. J. Kim, "Ionic polymer-metal composite mechanoelectrical transduction: review and perspectives," *Polymer International*, vol. 59, no. 3, pp. 279–289, Jan. 2010.

[67] W.-S. Chu, K.-T. Lee, S.-H. Song, M.-W. Han, J.-Y. Lee, H.-S. Kim, M.-S. Kim, Y.-J. Park, K.-J. Cho, and S.-H. Ahn, "Review of biomimetic underwater robots using smart actuators," *International Journal of Precision Engineering and Manufacturing*, vol. 13, no. 7, pp. 1281–1292, Jul. 2012.

[68] S. J. Lee, M. J. Han, S. J. Kim, J. Y. Jho, H. Y. Lee, and Y. H. Kim, "A new fabrication method for IPMC actuators and application to artificial fingers," *Smart Materials and Structures*, vol. 15, no. 5, pp. 1217–1224, 2006.

[69] E. Biddiss and T. Chau, "Electroactive polymeric sensors in hand prostheses: Bending response of an ionic polymer metal composite," *Medical Engineering and Physics*, vol. 28, no. 6, pp. 568–578, 2006.

[70] P. Aravinthan, N. GopalaKrishnan, P. A. Srinivas, and N. Vigneswaran, "Design, development and implementation of neurologically controlled prosthetic limb capable of performing rotational movement," in *Emerging Trends in Robotics and Communication Technologies (INTERACT), 2010 International Conference on*. IEEE, 2010, pp. 241–244.

[71] R. Jain, S. Datta, S. Majumder, S. Mukherjee, D. Sadhu, S. Samanta, and K. Banerjee, "Bio-mimetic Behaviour of IPMC Artificial Muscle Using EMG Signal," in *2010 International Conference on Advances in Recent Technologies in Communication and Computing*. IEEE, Oct. 2010, pp. 186–190.

[72] A. Keshavarzi, M. Shahinpoor, K. J. Kim, and J. Lantz, "Blood pressure, pulse rate, and rhythm measurement using ionic polymer-metal composite sensors," in *Proceedings of SPIE*, vol. 3669. SPIE, March 1999, pp. 369–376.

[73] S. Guo, T. Fukuda, K. Kosuge, F. Arai, K. Oguro, and M. Negoro, "Micro catheter system with active guide wire," in *Proceedings of 1995 IEEE International Conference on Robotics and Automation*. IEEE, 1995, pp. 79–84.

[74] B. K. Fang, M. S. Ju, and C. C. K. Lin, "A new approach to develop ionic polymer-metal composites (IPMC) actuator: Fabrication and control for active catheter systems," *Sensors and Actuators, A: Physical*, vol. 137, no. 2, pp. 321–329, 2007.

[75] B. K. Fang, C. C. K. Lin, and M. S. Ju, "Development of sensing/actuating ionic polymer-metal composite (IPMC) for active guide-wire system," *Sensors and Actuators, A: Physical*, vol. 158, no. 1, pp. 1–9, 2010.

[76] W. Yoon, P. Reinhall, and E. Seibel, "Analysis of electro-active polymer bending: A component in a low cost ultrathin scanning endoscope," *Sensors and Actuators A: Physical*, vol. 133, no. 2, pp. 506–517, Feb. 2007.

[77] L. Ferrara, M. Shahinpoor, K. J. Kim, B. Schreyer, A. Keshavarzi, E. Benzel, and J. Lantz, "Use of ionic polymer-metal composites (IPMCs) as a pressure transducer in the human spine," in *Proceedings of SPIE*, vol. 3669. SPIE, March 1999, pp. 394–401.

[78] A. J. McDaid, S. Q. Xie, and K. C. Aw, "A compliant surgical robotic instrument with integrated IPMC sensing and actuation," *International Journal of Smart and Nano Materials*, vol. 3, no. 3, pp. 188–203, 2012.

[79] L. Fu, A. J. McDaid, and K. C. Aw, "Control of an IPMC actuated robotic surgical tool with embedded interaction sensing," *IEEE/ASME International Conference on Advanced Intelligent Mechatronics, AIM 2013*, pp. 1255–1259, 2013.

[80] C. Bonomo, P. Brunetto, L. Fortuna, P. Giannone, S. Graziani, and S. Strazzeri, "A Tactile Sensor for Biomedical Applications Based on IPMCs," *IEEE Sensors Journal*, vol. 8, no. 8, pp. 1486–1493, 2008.

[81] P. Brunetto, L. Fortuna, P. Giannone, S. Graziani, and F. Pagano, "A Resonant Vibrating Tactile Probe for Biomedical Applications Based on IPMC," *IEEE Transactions on Instrumentation and Measurement*, vol. 59, no. 5, pp. 1453–1462, May 2010.

[82] Z. Chen, Y. Shen, N. Xi, and X. Tan, "Integrated sensing for ionic polymer–metal composite actuators using PVDF thin films," *Smart Materials and Structures*, vol. 16, no. 2, pp. S262–S271, Apr. 2007.

[83] M. Yamakita, N. Kamamichi, Y. Kaneda, K. Asaka, and Z.-W. Luo, "Development of artificial muscle actuator using ionic polymer with its application to biped walking robots," in *Proceedings of SPIE*, Y. Bar-Cohen, Ed., vol. 5051, San Diego, CA, Jul. 2003, pp. 301–308.

[84] M. Yamakita, N. Kamamichi, T. Kozuki, K. Asaka, and Z.-W. Luo, "Control of Biped Walking Robot with IPMC Linear Actuator," in *Proceedings, 2005 IEEE/ASME International Conference on Advanced Intelligent Mechatronics*. IEEE, 2005, pp. 48–53.

[85] P. Arena, C. Bonomo, L. Fortuna, M. Frasca, and S. Graziani, "Design and control of an IPMC wormlike robot." *IEEE Transactions on Systems, Man, and Cybernetics*, vol. 36, no. 5, pp. 1044–52, Oct. 2006.

[86] J. Hou, M. Luo, and T. Mei, "The design and control of Amoeba-like robot," in *2010 International Conference on Computer Application and System Modeling (ICCASM 2010)*. IEEE, Oct. 2010, pp. V1–88–V1–91.

[87] L. Chen, M. Luo, and T. Mei, "A Dynamic Simulation of Force in the Movement of Ameba Based on Cosmos," in *2010 Second International Conference on Modeling, Simulation and Visualization Methods*. IEEE, May 2010, pp. 78–82.

[88] M. Stasik, M. Moore, C. Plaxico, and J. Sayre, "Electroactive polymer (EAP) mobility device," in *Proceedings of SPIE*, vol. 8687, 2013, p. 86870B.

[89] S. Lee, H. Park, S. D. Pandita, and Y. Yoo, "Performance improvement of ipmc (ionic polymer metal composites) for a flapping actuator," *International Journal of Control Automation and Systems*, vol. 4, no. 6, pp. 748–755, 2006.

[90] H.-I. Kim, D.-K. Kim, and J.-H. Han, "Study of flapping actuator modules using IPMC," in *Electroactive Polymer Actuators and Devices (EAPAD) 2007*, Y. Bar-Cohen, Ed., vol. 6524, Apr. 2007, pp. 65 241A–65 241A–12.

[91] S. Tadokoro, S. Yamagami, M. Ozawa, T. Kimura, T. Takamori, and K. Oguro, "Soft micromanipulation device with multiple degrees of freedom consisting of high polymer gel actuators," pp. 37–42, 1999.

[92] Y. Nakabo, T. Mukai, and K. Asaka, "Kinematic modeling and visual sensing of multi-DOF robot manipulator with patterned artificial muscle," *Proceedings of the 2005 IEEE International Conference on Robotics and Automation*, pp. 4315–4320, April 2005.

[93] M. Kruusmaa, A. Hunt, A. Punning, M. Anton, and A. Aabloo, "A linked manipulator with ion-polymer metal composite (IPMC) joints for soft- and micromanipulation," in *2008 IEEE International Conference on Robotics and Automation*. IEEE, May 2008, pp. 3588–3593.

[94] A. J. McDaid, K. C. Aw, S. Q. Xie, and E. Haemmerle, "Development of a 2DOF micromanipulation system with IPMC actuators," in *2011 IEEE/ASME International Conference on Advanced Intelligent Mechatronics (AIM)*. IEEE, Jul. 2011, pp. 518–523.

[95] R. Lumia and M. Shahinpoor, "Microgripper design using electroactive polymers," in *Proceedings of the SPIE*, Y. Bar-Cohen, Ed., vol. 3669, March 1999, pp. 322–329.

[96] R. K. Jain, S. Datta, and S. Majumder, "IPMC based micro gripper for miniature part handling," in *2010 IEEE International Conference on Mechatronics and Automation*. IEEE, Aug. 2010, pp. 1414–1419.

[97] G. H. Feng and J. W. Tsai, "3D omnidiectional contollable elastic IPMC tweezer with self-sensing and adjustable clamping force abilities for biomedical applications," in *16th International Solid-State Sensors, Actuators and Microsystems Conference, TRANSDUCERS'11*, vol. 3, 2011, pp. 1725–1728.

[98] M. Mojarrad and M. Shahinpoor, "Noiseless propulsion for swimming robotic structures using polyelectrolyte ion-exchange membrane," in *Proceedings of SPIE*, A. Crowson, Ed., vol. 2716, Feb 1996, pp. 183–192.

[99] M. Mojarrad and M. Shahinpoor, "Ion-exchange-metal composite sensor films," in *Proceedings of SPIE*, R. O. Claus, Ed., vol. 3042. SPIE, Jun 1997, pp. 52–60.

[100] S. Guo, T. Fukuda, N. Kato, and K. Oguro, "Development of underwater microrobot using ICPF actuator," *Proceedings of the 1998 IEEE International Conference on Robotics and Automation*, vol. 2, pp. 1829–1834, May 1998.

[101] S. Guo, T. Fukuda, and K. Asaka, "A new type of fish-like underwater microrobot," *IEEE/ASME Transactions on Mechatronics*, vol. 8, no. 1, pp. 136–141, Mar. 2003.

[102] G. Laurent and E. Piat, "Efficiency of swimming microrobots using ionic polymer metal composite actuators," in *Proceedings of the IEEE International Conference on Robotics and Automation*, vol. 4. IEEE, 2001, pp. 3914–3919.

[103] J. Paquette, K. Kim, and W. Yim, "Aquatic robotic propulsor using ionic polymer-metal composite artificial muscle," in *2004 IEEE/RSJ International Conference on Intelligent Robots and Systems (IROS)*, vol. 2. IEEE, 2004, pp. 1269–1274.

[104] K. J. Kim, W. Yim, J. W. Paquette, and D. Kim, "Ionic Polymer-metal Composites for Underwater Operation," *Journal of Intelligent Material Systems and Structures*, vol. 18, no. 2, pp. 123–131, 2007.

[105] Q. Shen, T. Wang, J. Liang, and L. Wen, "Hydrodynamic performance of a biomimetic robotic swimmer actuated by ionic polymer–metal composite," *Smart Materials and Structures*, vol. 22, no. 7, p. 075035, 2013.

[106] J. Jung, B. Kim, and Y. Tak, "Undulatory tadpole robot (TadRob) using ionic polymer metal composite (IPMC) actuator," *Proceedings of the 2003 IEEE/RSJ International Conference on Intelligent Robots and Systems (IROS 2003)*, vol. 3, pp. 2133–2138, Oct 2003.

[107] B. Kim, D.-H. Kim, J. Jung, and J.-O. Park, "A biomimetic undulatory tadpole robot using ionic polymer–metal composite actuators," *Smart Materials and Structures*, vol. 14, no. 6, pp. 1579–1585, 2005.

[108] X. Tan, D. Kim, N. Usher, D. Laboy, J. Jackson, A. Kapetanovic, J. Rapai, B. Sabadus, and X. Zhou, "An Autonomous Robotic Fish for Mobile Sensing," in *2006 IEEE/RSJ International Conference on Intelligent Robots and Systems*. IEEE, Oct. 2006, pp. 5424–5429.

[109] E. Mbemmo, Z. Chen, S. Shatara, and X. Tan, "Modeling of biomimetic robotic fish propelled by an ionic polymer-metal composite actuator," *2008 IEEE International Conference on Robotics and Automation*, pp. 689–694, May 2008.

[110] Z. Chen, S. Shatara, and X. Tan, "Modeling of Biomimetic Robotic Fish Propelled by An Ionic Polymer–Metal Composite Caudal Fin," *IEEE/ASME Transactions on Mechatronics*, vol. 15, no. 3, pp. 448–459, Jun. 2010.

[111] Q. Hu, L. Xu, and X. Liu, "MOGA application feasibility research on ocean petroleum exploration platform seawater environment supervision," in *2010 Sixth International Conference on Natural Computation*. IEEE, Aug. 2010, pp. 3503–3507.

[112] V. Kopman, M. Aureli, and M. Porfiri, “Free-Locomotion of a Fish-Like Robotic Swimmer Propelled by a Vibrating Ionic Polymer Metal Composite,” in *ASME 2009 Dynamic Systems and Control Conference, Volume 1*. ASME, 2009, pp. 477–484.

[113] M. Aureli, V. Kopman, and M. Porfiri, “Free-Locomotion of Underwater Vehicles Actuated by Ionic Polymer Metal Composites,” *IEEE/ASME Transactions on Mechatronics*, vol. 15, no. 4, pp. 603–614, Aug. 2010.

[114] M. Aureli, V. Kopman, and M. Porfiri, “Control-oriented modeling of ionic polymer metal composites for biomimetic underwater propulsion,” in *American Control Conference (ACC), 2010*, 2010, pp. 6016–6021.

[115] N. Kamamichi, M. Yamakita, K. Asaka, and Z. W. Luo, “A snake-like swimming robot using IPMC actuator/sensor,” *Proceedings - IEEE International Conference on Robotics and Automation*, pp. 1812–1817, May 2006.

[116] M. Anton, A. Punning, A. Aabloo, M. Listak, and M. Kruusmaa, “Towards a biomimetic EAP robot,” *Proc. of TAROS*, pp. 6–8, 2004.

[117] A. Punning, M. Anton, M. Kruusmaa, and A. Aabloo, “A biologically inspired ray-like underwater robot with electroactive polymer pectoral fins,” in *IEEE International Conference on Mechatronics and Robotics*, vol. 2004, 2004, pp. 241–245.

[118] Z. Chen, T. I. Um, and H. Bart-Smith, “Bio-inspired robotic manta ray powered by ionic polymer–metal composite artificial muscles,” *International Journal of Smart and Nano Materials*, vol. 3, no. 4, pp. 296–308, Dec. 2012.

[119] S.-W. Yeom and I.-K. Oh, “A biomimetic jellyfish robot based on ionic polymer metal composite actuators,” *Smart Materials and Structures*, vol. 18, no. 8, p. 085002, 2009.

[120] M. Anton, Z. Chen, M. Kruusmaa, and X. Tan, “Analytical and computational modeling of robotic fish propelled by soft actuation material-based active joints,” *2009 IEEE/RSJ International Conference on Intelligent Robots and Systems*, pp. 2126–2131, Oct. 2009.

[121] Z. Chen and X. Tan, “A Control-Oriented and Physics-Based Model for Ionic Polymer–Metal Composite Actuators,” *IEEE/ASME Transactions on Mechatronics*, vol. 13, no. 5, pp. 519–529, Oct. 2008.

[122] Q. Shen, T. Wang, L. Wen, and J. Liang, “Modelling and Fuzzy Control of an Efficient Swimming Ionic Polymer-Metal Composite Actuated Robot,” *International Journal of Advanced Robotic Systems*, vol. 10, no. 10, p. 350, Oct. 2013.

[123] V. Palmre, J. J. Hubbard, M. Fleming, D. Pugal, S. Kim, K. J. Kim, and K. K. Leang, "An IPMC-enabled bio-inspired bending/twisting fin for underwater applications," *Smart Materials and Structures*, vol. 22, no. 1, p. 014003, Jan. 2013.

[124] B. Kim, J. Ryu, Y. Jeong, Y. Tak, B. Kim, and J.-O. Park, "A ciliary based 8-legged walking micro robot using cast IPMC actuators," in *2003 IEEE International Conference on Robotics and Automation*, vol. 3. IEEE, 2003, pp. 2940–2945.

[125] S. Guo, L. Shi, and K. Asaka, "IPMC actuator-sensor based a biomimetic underwater microrobot with 8 legs," in *IEEE International Conference on Automation and Logistics (ICAL)*, Sep. 2008, pp. 2495–2500.

[126] N. Tomita, K. Takagi, and K. Asaka, "Development of a quadruped soft robot with fully IPMC body," in *SICE Annual Conference 2011*, Sep. 2011, pp. 1687–1690.

[127] L. Shi, S. Guo, and K. Asaka, "Development of a novel underwater microrobot with proximity sensors," in *Proceedings of the 2011 IEEE/ICME International Conference on Complex Medical Engineering*. IEEE, May 2011, pp. 69–73.

[128] L. Shi, S. Guo, and K. Asaka, "A bio-inspired underwater microrobot with compact structure and multifunctional locomotion," in *2011 IEEE/ASME International Conference on Advanced Intelligent Mechatronics (AIM)*. IEEE, Jul. 2011, pp. 203–208.

[129] Y.-C. Chang and W.-J. Kim, "Aquatic ionic-polymer-metal-composite insectile robot with multi-dof legs," *IEEE/ASME Transactions on Mechatronics*, vol. 18, no. 2, pp. 547–555, 2013.

[130] D. Dogruer, R. Tiwari, and K. Kim, "Ionic polymer metal composites as energy harvesters," in *Electroactive Polymer Actuators and Devices (EAPAD)*, Y. Bar-Cohen, Ed., vol. 6524, no. 775, Apr. 2007, pp. 65 241C1–65 241C10.

[131] R. Tiwari and K. J. Kim, "Improved IPMC sensing by use of cation and through induced nano-to-micro scale surface cracks," in *Sensors and Smart Structures Technologies for Civil, Mechanical, and Aerospace Systems 2008*, M. Tomizuka, Ed., vol. 6932, San Diego, California, Mar. 2008, pp. 69 323H–69 323H–12.

[132] R. Tiwari and K. J. Kim, "Disc-shaped ionic polymer metal composites for use in mechano-electrical applications," *Smart Materials and Structures*, vol. 19, no. 6, p. 065016, 2010.

[133] J. Brufau-Penella, M. Puig-Vidal, P. Giannone, S. Graziani, and S. Strazzeri, "Characterization of the harvesting capabilities of an ionic polymer metal composite device," *Smart Materials and Structures*, vol. 17, no. 1, p. 015009, 2007.

[134] M. Aureli, C. Prince, M. Porfiri, and S. D. Peterson, "Energy harvesting from base excitation of ionic polymer metal composites in fluid environments," *Smart Materials and Structures*, vol. 19, no. 1, p. 015003, 2009.

[135] Y. Cha, L. Shen, and M. Porfiri, "Energy harvesting from underwater torsional vibrations of a patterned ionic polymer metal composite," *Smart Materials and Structures*, vol. 22, no. 5, p. 055027, May 2013.

[136] M. Konyo, Y. Konishi, S. Tadokoro, and T. Kishima, "Development of velocity sensor using ionic polymer-metal composites," in *Proceedings of SPIE*, vol. 5385, no. 1. SPIE, 2004, pp. 307–318.

[137] B. Paola, L. Fortuna, P. Giannone, S. Graziani, and S. Strazzeri, "IPMCs as vibration sensors," in *IEEE Instrumentation and Measurement Technology Conference*, May 2008, pp. 2065–2069.

[138] S. C. Fang and H. H. Chen, "Flexible impact sensor using IPMC," *The UoA Undergraduate Mechatronics Research Journal*, pp. 7–9, 2009.

[139] X. Chew, a. V. D. Hurk, and K. Aw, "Characterisation of ionic polymer metallic composites as sensors in robotic finger joints," *International Journal of Biomechatronics and Biomedical Robotics*, vol. 1, no. 1, p. 37, 2009.

[140] B. Ando, S. Baglio, A. Beninato, S. Graziani, F. Pagano, and E. Umana, "A seismic sensor based on IPMC combined with ferrofluids," in *2012 IEEE International Instrumentation and Measurement Technology Conference Proceedings*. IEEE, May 2012, pp. 1829–1832.

[141] A. T. Abdulsadda and X. Tan, "Underwater source localization using an IPMC-based artificial lateral line," *2011 IEEE International Conference on Robotics and Automation*, pp. 2719–2724, May 2011.

[142] A. T. Abdulsadda and X. Tan, "Nonlinear estimation-based dipole source localization for artificial lateral line systems." *Bioinspiration & biomimetics*, vol. 8, no. 2, p. 026005, 2013.

[143] J. Zhong, D. L. S. Hung, G. Zhu, and X. Tan, "Cycle-to-cycle response of ionic polymer-metal composite materials subject to pulsing flow-induced stimulus," in *2012 IEEE/ASME International Conference on Advanced Intelligent Mechatronics (AIM)*. IEEE, Jul. 2012, pp. 432–437.

[144] X. Chen, G. Zhu, X. Yang, D. L. S. Hung, and X. Tan, "Model-Based Estimation of Flow Characteristics Using an Ionic Polymer-Metal Composite Beam," *IEEE/ASME Transactions on Mechatronics*, vol. 18, no. 3, pp. 932–943, Jun. 2013.

[145] S. Tadokoro, T. Murakami, S. Fuji, R. Kanno, M. Hattori, T. Takamori, and K. Oguro, "An elliptic friction drive element using an ICPF actuator," *IEEE Control Systems Magazine*, vol. 17, no. 3, pp. 60–68, Jun. 1997.

[146] S. Tadokoro, S. Fuji, M. Fushimi, R. Kanno, T. Kimura, T. Takamori, and K. Oguro, "Development of a distributed actuation device consisting of soft gel actuator elements," in *Proceedings of the 1998 IEEE International Conference on Robotics and Automation*. IEEE, May 1998, pp. 2155–2160.

[147] A. J. McDaid, K. C. Aw, K. Patel, S. Q. Xie, and E. Haemmerle, "Development of an ionic polymer–metal composite stepper motor using a novel actuator model," *International Journal of Smart and Nano Materials*, vol. 1, no. 4, pp. 261–277, 2010.

[148] Y. Bar-Cohen, S. P. Leary, A. Yavrouian, K. Oguro, S. Tadokoro, J. S. Harrison, J. G. Smith, and J. Su, "Challenges to the application of IPMC as actuators of planetary mechanisms," in *Proceedings of SPIE*, Y. Bar-Cohen, Ed., vol. 3987, Newport Beach, CA, 2000, pp. 140–146.

[149] S. Tung, S. R. Witherspoon, L. a. Roe, A. Silano, D. P. Maynard, and N. Ferraro, "A MEMS-based flexible sensor and actuator system for space inflatable structures," *Smart Materials and Structures*, vol. 10, no. 6, pp. 1230–1239, Dec. 2001.

[150] X. Bao, Y. Bar-Cohen, Z. Chang, and S. Sherrit, "Numerical modeling of single-layer electroactive polymer mirrors for space," *Electroactive Polymer Actuators and Devices*, vol. 5051, pp. 381–388, 2003.

[151] C. S. Kothera and D. J. Leo, "Position Control of a Square-plate Ionic Polymer Actuator Using Output Feedback," *Journal of Intelligent Material Systems and Structures*, vol. 18, no. 3, pp. 219–234, Oct. 2007.

[152] H.-C. Wei and G.-D. J. Su, "A large-stroke deformable mirror by gear shaped IPMC design," *2011 6th IEEE International Conference on Nano/Micro Engineered and Molecular Systems*, pp. 113–116, Feb. 2011.

[153] S. Lee, K. J. Kim, and H. C. Park, "Modeling of an IPMC Actuator-driven Zero-Net-Mass-Flux Pump for Flow Control," *Journal of Intelligent Material Systems and Structures*, vol. 17, no. 6, pp. 533–541, Jun. 2006.

[154] S. Lee and K. J. Kim, “Design of IPMC actuator-driven valve-less micropump and its flow rate estimation at low Reynolds numbers,” *Smart Materials and Structures*, vol. 15, no. 4, pp. 1103–1109, Aug. 2006.

[155] A. J. McDaid, K. C. Aw, E. Haemmerle, and S. Q. Xie, “Control of IPMC Actuators for Microfluidics With Adaptive “Online” Iterative Feedback Tuning,” *IEEE/ASME Transactions on Mechatronics*, vol. 17, no. 4, pp. 789–797, Aug. 2012.

[156] P. Brunetto, L. Fortuna, P. Giannone, S. Graziani, and F. Pagano, “A small scale viscometer based on an IPMC actuator and an IPMC sensor,” in *2010 IEEE Instrumentation & Measurement Technology Conference Proceedings*. IEEE, 2010, pp. 585–589.

[157] A. Punning, M. Anton, M. Kruusmaa, and A. Aabloo, “An engineering approach to reduced power consumption of IPMC (ion-polymer metal composite) actuators,” *ICAR ’05. Proceedings., 12th International Conference on Advanced Robotics, 2005.*, pp. 856–863, 2005.

[158] J. S. Lee, S. Gutta, W. Yim, and K. J. Kim, “Preliminary study of wireless actuation and control of IPMC actuator,” in *2010 IEEE/ASME International Conference on Advanced Intelligent Mechatronics*. IEEE, Jul. 2010, pp. 157–162.

[159] K. Abdelnour, A. Stinchcombe, M. Porfiri, J. Zhang, and S. Childress, “Wireless Powering of Ionic Polymer Metal Composites Toward Hovering Microswimmers,” *IEEE/ASME Transactions on Mechatronics*, vol. 17, no. 5, pp. 924–935, Oct. 2012.

[160] M. J. Fleming, K. J. Kim, and K. K. Leang, “Mitigating IPMC back relaxation through feedforward and feedback control of patterned electrodes,” *Smart Materials and Structures*, vol. 21, no. 8, p. 085002, 2012.

[161] N. Bhat and W.-J. Kim, “Precision force and position control of an ionic polymer metal composite,” *Proceedings of the Institution of Mechanical Engineers, Part I: Journal of Systems and Control Engineering*, vol. 218, no. 6, pp. 421–432, Sep. 2004.

[162] R. Richardson, M. Levesley, M. Brown, J. Hawkes, K. Watterson, and P. Walker, “Control of ionic polymer metal composites,” *IEEE/ASME Transactions on Mechatronics*, vol. 8, no. 2, pp. 245–253, Jun. 2003.

[163] K. Mallavarapu, K. M. Newbury, and D. J. Leo, “Feedback control of the bending response of ionic polymer-metal composite actuators,” in *Proceedings of SPIE*, Y. Bar-Cohen, Ed., vol. 4329. Spie, Jul. 2001, pp. 301–310.

[164] N. D. Bhat, “Modeling and precision control of ionic polymer metal composite,” Ph.D. dissertation, Texas A&M University, 2003.

[165] K. Yun and W.-j. Kim, “Microscale position control of an electroactive polymer using an anti-windup scheme,” *Smart Materials and Structures*, vol. 15, no. 4, pp. 924–930, 2006.

[166] C. S. Kothera and D. J. Leo, “Bandwidth Characterization in the Micropositioning of Ionic Polymer Actuators,” *Journal of Intelligent Material Systems and Structures*, vol. 16, no. 1, pp. 3–13, Jan. 2005.

[167] Y. Shan and K. K. Leang, “Frequency-weighted feedforward control for dynamic compensation in ionic polymer–metal composite actuators,” *Smart Materials and Structures*, vol. 18, no. 12, p. 125016, 2009.

[168] S.-j. Oh and H. Kim, “A Study on the Control of an IPMC Actuator Using an Adaptive Fuzzy Algorithm,” *KSME International Journal*, vol. 18, no. 1, pp. 1–11, 2004.

[169] S. Song, Y. Shan, K. J. Kim, and K. K. Leang, “Tracking control of oscillatory motion in IPMC actuators for underwater applications,” *2010 IEEE/ASME International Conference on Advanced Intelligent Mechatronics*, pp. 169–174, Jul. 2010.

[170] H. M. La and W. Sheng, “Robust adaptive control with leakage modification for a nonlinear model of ionic polymer metal composites (IPMC),” *2008 IEEE International Conference on Robotics and Biomimetics, ROBIO 2008*, pp. 1783–1788, 2008.

[171] D. N. C. Nam, D. Q. Truong, Y. J. Il, and A. K. Kwan, “Precision Control for Ionic Polymer Metal Composite Actuator Based on Quantitative Feedback Theory,” in *2010 International Conference on Control, Automation and Systems*, Gyeonggi-do, Korea, 2010, pp. 443–447.

[172] T. Hanawa, A. Wang, M. Deng, and C. Jiang, “Operator-based Robust Nonlinear Control for An Ionic-Polymer Metal Composite with Hysteretic Properties Compensation,” in *Advanced Mechatronic Systems (ICAMechS), 2012 International Conference on*, 2012, pp. 12–17.

[173] Z. Sun, L. Hao, L. Liu, and J. Gao, “Improved Periodic Output Feedback control method for creep characteristic of thick IPMC plate,” in *2012 IEEE International Conference on Information and Automation*. IEEE, Jun. 2012, pp. 987–992.

[174] L. Hao, Z. Sun, Y. Xiong, and L. Liu, “An error compensator based simplified adaptive inverse control method for IPMC actuators tuning,” in *2013 IEEE International Conference on Cyber Technology in Automation, Control and Intelligent Systems*. IEEE, May 2013, pp. 291–296.

[175] X. Chen, “Robust control for ionic polymer-metal composite actuators,” in *2014 IEEE International Conference on Mechatronics and Automation*. IEEE, Aug. 2014, pp. 491–496.

[176] X. Chen and C.-Y. Su, “Control design for ionic polymer-metal composite based actuators,” in *2014 IEEE International Conference on Information and Automation (ICIA)*. IEEE, Jul. 2014, pp. 806–811.

[177] X. Chen and H. Kano, “Modelling and control for ionic polymer-metal composite actuators,” in *Proceeding of the 11th World Congress on Intelligent Control and Automation*. IEEE, Jun. 2014, pp. 1658–1663.

[178] Y. Xiong, Y. Chen, Z. Sun, L. Hao, and J. Dong, “Active disturbance rejection control for output force creep characteristics of ionic polymer metal composites,” *Smart Materials and Structures*, vol. 23, no. 7, p. 075014, 2014.

[179] J. H. Lee, B. J. Kim, J. S. Kim, D. S. Song, M. G. Lee, J. Y. Jho, D. M. Kim, K. Rhee, and S. J. Lee, “Time-delay control of ionic polymer metal composite actuator,” *Smart Materials and Structures*, vol. 24, no. 4, p. 047002, 2015.

[180] L. Hao, Y. Chen, and Z. Sun, “The sliding mode control for different shapes and dimensions of IPMC on resisting its creep characteristics,” *Smart Materials and Structures*, vol. 24, no. 4, p. 045040, 2015.

[181] Z. Sun, L. Hao, W. Chen, Z. Li, and L. Liu, “A novel discrete adaptive sliding-mode-like control method for ionic polymer–metal composite manipulators,” *Smart Materials and Structures*, vol. 22, no. 9, p. 095027, 2013.

[182] Z. Chen, K.-Y. Kwon, and X. Tan, “Integrated IPMC/PVDF sensory actuator and its validation in feedback control,” *Sensors and Actuators A: Physical*, vol. 144, no. 2, pp. 231–241, Jun. 2008.

[183] X. Tan, N. Xi, Z. Chen, and Y. Shen, “Integrated actuator sensor structure,” Patent US 7,982,375 B2, 2011.

[184] K. K. Leang, Y. Shan, S. Song, and K. J. Kim, “Integrated Sensing for IPMC Actuators Using Strain Gages for Underwater Applications,” *IEEE/ASME Transactions on Mechatronics*, vol. 17, no. 2, pp. 345–355, Apr. 2012.

[185] K. M. Newbury and D. J. Leo, “Electromechanical modeling and characterization of ionic polymer benders,” *Journal of Intelligent Material Systems and Structures*, vol. 13, no. 1, pp. 51–60, Jan. 2002.

[186] C. Bonomo, L. Fortuna, P. Giannone, and S. Graziani, "A sensor-actuator integrated system based on IPMCs," in *Proceedings of IEEE Sensors, 2004.* IEEE, 2004, pp. 489–492.

[187] C. Gonzalez and R. Lumia, "An IPMC microgripper with integrated actuator and sensing for constant finger-tip displacement," *Smart Materials and Structures*, vol. 24, no. 5, p. 055011, 2015.

[188] M. Yamakita, A. Sera, N. Kamamichi, K. Asaka, and Zhi-Wei Luo, "Integrated design of IPMC actuator/sensor," in *Proceedings of the 2006 IEEE International Conference on Robotics and Automation (ICRA 2006)*. IEEE, May 2006, pp. 1834–1839.

[189] A. Punning, M. Kruusmaa, and A. Aabloo, "A self-sensing ion conducting polymer metal composite (IPMC) actuator," *Sensors and Actuators A: Physical*, vol. 136, no. 2, pp. 656–664, May 2007.

[190] D. N. C. Nam and K. K. Ahn, "Modeling and control of a self-sensing polymer metal composite actuator," *Smart Materials and Structures*, vol. 23, no. 2, p. 025025, 2014.

[191] I.-S. Park, K. Jung, D. Kim, S.-M. Kim, and K. J. Kim, "Physical Principles of Ionic Polymer–Metal Composites as Electroactive Actuators and Sensors," *MRS Bulletin*, vol. 33, no. 03, pp. 190–195, 2008.

[192] K. Kruusamäe, A. Punning, M. Kruusmaa, and A. Aabloo, "Dynamical variation of the impedances of IPMC," in *Proceedings of SPIE*, vol. 7287. SPIE, 2009, pp. 72 870V–72 870V–9.

[193] H. Nakadoi, A. Sera, M. Yamakita, K. Asaka, Z. W. Luo, and K. Ito, "Integrated actuator-sensor system on patterned IPMC Film: Consideration of electoric interference," *Proceedings of the 2007 4th IEEE International Conference on Mechatronics, ICM 2007*, pp. 8–10, May 2007.

[194] K. Kruusamäe, P. Brunetto, S. Graziani, A. Punning, G. Di Pasquale, and A. Aabloo, "Self-sensing ionic polymer-metal composite actuating device with patterned surface electrodes," *Polymer International*, vol. 59, no. 3, pp. 300–304, Dec. 2009.

[195] K. Kruusamäe, P. Brunetto, S. Graziani, L. Fortuna, M. Kodu, R. Jaaniso, A. Punning, and A. Aabloo, "Experiments with self-sensing IPMC actuating device," in *Proceedings of SPIE*, Y. Bar-Cohen, Ed., vol. 7642, Mar. 2010, pp. 76 420V–76 420V–6.

[196] K. Kruusamäe, P. Brunetto, A. Punning, M. Kodu, R. Jaaniso, S. Graziani, L. Fortuna, and A. Aabloo, "Electromechanical model for a self-sensing ionic polymer – metal composite actuating device with patterned surface

electrodes," *Smart Materials and Structures*, vol. 20, no. 12, p. 124001, 2011.

[197] B.-G. Ko, H.-C. Kwon, and S. J. Lee, "A Self-Sensing Method for IPMC Actuator," *Advances in Science and Technology*, vol. 56, pp. 111–115, 2008.

[198] M. Sasaki, W. Lin, H. Tamagawa, S. Ito, and K. Kikuchi, "Self-Sensing Control of Nafion-Based Ionic Polymer-Metal Composite (IPMC) Actuator in the Extremely Low Humidity Environment," *Actuators*, vol. 2, no. 4, pp. 74–85, 2013.

[199] S. Kang, J. Shin, S. J. Kim, H. J. Kim, and Y. H. Kim, "Robust control of ionic polymer–metal composites," *Smart Materials and Structures*, vol. 16, no. 6, pp. 2457–2463, 2007.

[200] L. Yanmei, C. Zhen, and X. Dingyu, "Identification for Piezoelectric Smart Materials based on Neural Networks method," *2010 2nd International Conference on Advanced Computer Control*, pp. 608–611, 2010.

[201] D. Q. Truong, K. K. Ahn, D. N. C. Nam, and J. I. Yoon, "Estimation of Bending Behavior of an Ionic Polymer Metal Composite Actuator Using a Nonlinear Black-Box Model," in *2010 International Conference on Control, Automation and Systems (ICCAS)*, Gyeonggi-do, Korea, 2010, pp. 438–442.

[202] D. Q. Truong, K. K. Ahn, D. N. C. Nam, and J. I. Yoon, "Identification of a nonlinear black-box model for a self-sensing polymer metal composite actuator," *Smart Materials and Structures*, vol. 19, no. 8, p. 085015, 2010.

[203] D. Q. Truong and K. K. Ahn, "Modeling of an ionic polymer metal composite actuator based on an extended Kalman filter trained neural network," *Smart Materials and Structures*, vol. 23, no. 7, p. 074008, 2014.

[204] Z. Chen, X. Tan, and M. Shahinpoor, "Quasi-static positioning of ionic polymer-metal composite (IPMC) actuators," in *Advanced Intelligent Mechatronics. Proceedings, 2005 IEEE/ASME International Conference on*. IEEE, 2005, pp. 60–65.

[205] H. P. H. Anh, "Particle swarm optimization identification of IPMC actuator using fuzzy NARX model," *2010 IEEE Conference on Cybernetics and Intelligent Systems*, pp. 108–113, Jun. 2010.

[206] R. Caponetto, S. Graziani, F. Sapuppo, and V. Tomasello, "An enhanced fractional order model of ionic polymer-metal composites actuator," *Advances in Mathematical Physics*, vol. 2013, 2013.

[207] C. Bonomo, L. Fortuna, S. Graziani, and D. Mazza, “A circuit to model an Ionic Polymer-Metal Composite as actuator,” in *2004 IEEE International Symposium on Circuits and Systems (IEEE Cat. No.04CH37512)*. IEEE, 2004, pp. IV–864–7.

[208] C. Bonomo, L. Fortuna, P. Giannone, and S. Graziani, “A circuit to model the electrical behavior of an ionic polymer-metal composite,” *IEEE Transactions on Circuits and Systems I: Regular Papers*, vol. 53, no. 2, pp. 338–350, Feb. 2006.

[209] K. Takagi, Y. Nakabo, Z.-W. Luo, and K. Asaka, “On a distributed parameter model for electrical impedance of ionic polymer,” *Proceedings of SPIE*, vol. 6524, pp. 652 416–652 416–8, 2007.

[210] Y. Cha, M. Aureli, and M. Porfiri, “A physics-based model of the electrical impedance of ionic polymer metal composites,” *Journal of Applied Physics*, vol. 111, no. 12, p. 124901, 2012.

[211] X. Bao, Y. Bar-Cohen, and S.-S. Lih, “Measurements and macro models of ionomeric polymer-metal composites (IPMC),” in *Proceedings of the SPIE Smart Structures and Materials Symposium*, Y. Bar-Cohen, Ed., vol. 4695. SPIE, Jul. 2002, pp. 220–227.

[212] R. Kanno, S. Tadokoro, T. Takamori, and K. Oguro, “3-dimensional dynamic model of ionic conducting polymer gel film (ICPF) actuator,” *1996 IEEE International Conference on Systems, Man and Cybernetics*, pp. 2179–2184, 1996.

[213] R. Kanno, S. Tadokoro, T. Takamori, M. Hattori, and K. Oguro, “Linear approximate dynamic model of ICPF (ionic conducting polymer gel film) actuator,” in *Proceedings of IEEE International Conference on Robotics and Automation*, vol. 1. IEEE, Apr. 1996, pp. 219–225.

[214] K. M. Newbury and D. J. Leo, “Linear Electromechanical Model of Ionic Polymer Transducers -Part I: Model Development,” *Journal of Intelligent Materials Systems and Structures*, vol. 14, no. 6, pp. 333–342, Jun. 2003.

[215] K. M. Newbury and D. J. Leo, “Linear Electromechanical Model of Ionic Polymer Transducers -Part II: Experimental Validation,” *Journal of Intelligent Materials Systems and Structures*, vol. 14, no. 6, pp. 343–357, Jun. 2003.

[216] B. Akle and D. J. Leo, “Electromechanical transduction in multilayer ionic transducers,” *Smart Materials and Structures*, vol. 13, no. 5, p. 1081, 2004.

[217] J. W. Paquette, K. J. Kim, J.-D. Nam, and Y. S. Tak, "An equivalent circuit model for ionic polymer-metal composites and their performance improvement by a clay-based polymer nano-composite technique," *Journal of Intelligent Materials Systems and Structures*, vol. 14, no. 10, pp. 633–642, Oct. 2003.

[218] C. Bonomo, L. Fortuna, P. Giannone, S. Graziani, and S. Strazzeri, "A nonlinear model for ionic polymer metal composites as actuators," *Smart Materials and Structures*, vol. 16, no. 1, pp. 1–12, Feb. 2007.

[219] K. Newbury, "Characterization, modeling, and control of ionic polymer transducers," Ph.D. dissertation, Virginia Polytechnic Institute and State University, 2002.

[220] A. Punning, M. Anton, M. Kruusmaa, and A. Aabloo, "Empirical model of a bending IPMC actuator," in *Proceedings of SPIE*, Y. Bar-Cohen, Ed., vol. 6168. SPIE, Mar. 2006, p. 61681V.

[221] A. Punning, U. Johanson, M. Anton, A. Aabloo, and M. Kruusmaa, "A Distributed Model of Ionomeric Polymer Metal Composite," *Journal of Intelligent Material Systems and Structures*, vol. 20, no. 14, pp. 1711–1724, Sep. 2009.

[222] A. Punning, U. Johanson, M. Anton, M. Kruusmaa, and A. Aabloo, "A distributed model of IPMC," in *Proceedings of SPIE*, Y. Bar-Cohen, Ed., vol. 6927, San Diego, CA, Mar. 2008, pp. 69 270G–69 270G–10.

[223] A. Punning, "Electromechanical characterization of ionic polymer-metal composite sensing actuators," Ph.D. dissertation, University of Tartu, 2007.

[224] A. J. McDaid, K. C. Aw, E. Haemmerle, and S. Q. Xie, "A conclusive scalable model for the complete actuation response for IPMC transducers," *Smart Materials and Structures*, vol. 19, no. 7, p. 075011, 2010.

[225] R. Caponetto, S. Graziani, F. Pappalardo, and F. Sapuppo, "Identification of IPMC nonlinear model via single and multi-objective optimization algorithms," *ISA transactions*, vol. 53, no. 2, pp. 481–488, 2013.

[226] P. Brunetto, L. Fortuna, S. Graziani, and S. Strazzeri, "A model of ionic polymer–metal composite actuators in underwater operations," *Smart Materials and Structures*, vol. 17, no. 2, p. 025029, 2008.

[227] I. Must, M. Anton, M. Kruusmaa, and A. Aabloo, "Linear modeling of elongated bending EAP actuator at large deformations," in *Proceedings of SPIE*, vol. 7287. SPIE, 2009, pp. 728 723–728 723–12.

[228] D. Bandopadhya, “Derivation of Transfer Function of an IPMC Actuator Based on Pseudo-Rigid Body Model,” *Journal of Reinforced Plastics and Composites*, vol. 29, no. 3, pp. 372–390, 2010.

[229] V. Vunder, A. Punning, and A. Aabloo, “Mechanical interpretation of back-relaxation of ionic electroactive polymer actuators,” *Smart Materials and Structures*, vol. 21, no. 11, p. 115023, Nov. 2012.

[230] M. Shahinpoor, “Microelectromechanics of ionic polymeric gels as synthetic robotic muscles,” in *Proceedings of SPIE*, V. K. Varadan, Ed., vol. 2189. SPIE, 1994, pp. 265–274.

[231] M. Shahinpoor, “Continuum electromechanics of ionic polymeric gels as artificial muscles for robotic applications,” *Smart Materials and Structures*, vol. 3, no. 3, p. 367, sep 1994.

[232] M. Shahinpoor, “Electromechanics of ionoelastic beams as electrically controllable artificial muscles,” vol. 3669. SPIE, March 1999, pp. 109–121.

[233] K. Farinholt and D. J. Leo, “Modeling of electromechanical charge sensing in ionic polymer transducers,” *Mechanics of Materials*, vol. 36, no. 5-6, pp. 421–433, Jun. 2004.

[234] L. M. Weiland and D. J. Leo, “Electrostatic analysis of cluster response to electrical and mechanical loading in ionic polymers with cluster morphology,” *Smart Materials and Structures*, vol. 13, no. 2, pp. 323–336, Apr. 2004.

[235] P. J. Costa Branco and J. A. Dente, “Derivation of a continuum model and its electric equivalent-circuit representation for ionic polymer–metal composite (IPMC) electromechanics,” *Smart Materials and Structures*, vol. 15, no. 2, pp. 378–392, Apr. 2006.

[236] P. J. Costa Branco, B. Lopes, and J. A. Dente, “Nonuniformly Charged Ionic Polymer–Metal Composite Actuators: Electromechanical Modeling and Experimental Validation,” *IEEE Transactions on Industrial Electronics*, vol. 59, no. 2, pp. 1105–1113, Feb. 2012.

[237] S. Nemat-Nasser and S. Zamani, “Modeling of electrochemomechanical response of ionic polymer-metal composites with various solvents,” *Journal of Applied Physics*, vol. 100, no. 6, p. 064310, 2006.

[238] Z. Chen, D. R. Hedgepeth, and X. Tan, “A nonlinear, control-oriented model for ionic polymer-metal composite actuators,” in *Decision and Control, 2008. CDC 2008. 47th IEEE Conference on*. IEEE, 2008, pp. 1851–1856.

[239] G. D. Bufalo, L. Placidi, and M. Porfiri, “A mixture theory framework for modeling the mechanical actuation of ionic polymer metal composites,” *Smart Materials and Structures*, vol. 17, no. 4, p. 045010, Aug. 2008.

[240] T. Wallmersperger, B. Akle, D. Leo, and B. Kröplin, “Electrochemical response in ionic polymer transducers: An experimental and theoretical study,” *Composites Science and Technology*, vol. 68, no. 5, pp. 1173–1180, Apr. 2008.

[241] M. Porfiri, “An electromechanical model for sensing and actuation of ionic polymer metal composites,” *Smart Materials and Structures*, vol. 18, no. 1, p. 015016, Jan. 2009.

[242] B. J. Akle, D. J. Leo, M. A. Hickner, and J. E. McGrath, “Correlation of capacitance and actuation in ionomeric polymer transducers,” *Journal of Materials Science*, vol. 40, no. 14, pp. 3715–3724, 2005.

[243] S. Tadokoro, M. Fukuhara, Y. Maeba, M. Konyo, T. Takamori, and K. Oguro, “A dynamic model of ICPF actuator considering ion-induced lateral strain for molluskan robotics,” in *IEEE/RSJ International Conference on Intelligent Robots and System*, vol. 2. IEEE, Oct. 2002, pp. 2010–2017.

[244] D. J. Leo, K. Farinholt, and T. Wallmersperger, “Computational models of ionic transport and electromechanical transduction in ionomeric polymer transducers (invited paper),” in *Proceedings of SPIE*, Y. Bar-Cohen, Ed., vol. 5759. SPIE, May 2005, p. 170.

[245] T. Wallmersperger, D. J. Leo, and C. S. Kothera, “Transport modeling in ionomeric polymer transducers and its relationship to electromechanical coupling,” *Journal of Applied Physics*, vol. 101, no. 2, p. 024912, 2007.

[246] D. Pugal, H. Kasemägi, K. J. Kim, M. Kruusmaa, and A. Aabloo, “Finite element simulations of the bending of the IPMC sheet,” in *Electroactive Polymer Actuators and Devices (EAPAD)*, Y. Bar-Cohen, Ed., vol. 6524, Apr. 2007, pp. 65 240B–65 240B–9.

[247] D. Pugal, K. J. Kim, A. Punning, H. Kasemägi, M. Kruusmaa, and A. Aabloo, “A self-oscillating ionic polymer-metal composite bending actuator,” *Journal of Applied Physics*, vol. 103, no. 8, p. 084908, 2008.

[248] D. Pugal, H. Kasemägi, M. Kruusmaa, and A. Aabloo, “An advanced finite element model of IPMC,” in *Proceedings of SPIE*, vol. 6927. SPIE, 2008, pp. 692 711–692 711–8.

[249] D. Pugal, A. Aabloo, and K. J. Kim, “Dynamic surface resistance model of IPMC,” in *Proceedings of SPIE*, vol. 7289. SPIE, 2009, pp. 72 891E–72 891E–9.

[250] D. Pugal, K. J. Kim, and A. Aabloo, “Modeling the transduction of IPMC in 3D configurations,” in *Proceedings of SPIE*, vol. 7644, 2010, pp. 76 441T–76 441T–9.

[251] D. Pugal, “hp-FEM model of IPMC deformation,” phD, University of Tartu, 2014.

[252] D. Pugal, P. Solin, K. J. Kim, and a. Aabloo, “Hp-FEM electromechanical transduction model of ionic polymer-metal composites,” *Journal of Computational and Applied Mathematics*, vol. 260, pp. 135–148, 2014.

[253] R. Caponetto, V. De Luca, S. Graziani, F. Sapuppo, and E. Umana, “A multi-physics model of an IPMC actuator in the electrical, chemical, mechanical and thermal domains,” in *2012 International Conference on Synthesis, Modeling, Analysis and Simulation Methods and Applications to Circuit Design (SMACD)*. IEEE, Sep. 2012, pp. 157–160.

[254] R. Caponetto, V. De Luca, and S. Graziani, “A multiphysics model of IPMC actuators dependence on relative humidity,” in *2015 IEEE International Instrumentation and Measurement Technology Conference (I2MTC) Proceedings*. IEEE, May 2015, pp. 1482–1487.

[255] A. P. Sarvazyan, A. R. Skovoroda, S. Y. Emelianov, J. B. Fowlkes, J. G. Pipe, R. S. Adler, R. B. Buxton, and P. L. Carson, *Biophysical Bases of Elasticity Imaging*. Boston, MA: Springer US, 1995, pp. 223–240.

[256] K. Arda, N. Ciledag, E. Aktas, B. K. Aribas, and K. Köse, “Quantitative assessment of normal soft-tissue elasticity using shear-wave ultrasound elastography.” *AJR. American journal of roentgenology*, vol. 197, no. 3, pp. 532–6, Sep. 2011.

[257] J.-L. Gennisson, N. Grenier, R. Hubrecht, L. Couzy, Y. Delmas, M. Derieppe, S. Lepreux, P. Merville, A. Criton, J. Bercoff, and M. Tanter, “Multiwave technology introducing shear wave elastography of the kidney: Pre-clinical study on a kidney fibrosis model and clinical feasibility study on 49 human renal transplants,” in *2010 IEEE International Ultrasonics Symposium*. IEEE, Oct. 2010, pp. 1356–1359.

[258] American Institute of Ultrasound in Medicine and AIUM Standards Committee, *Standard methods for measuring performance of pulse-echo ultrasound imaging equipment*. Rockville, Md.: The Institute, 1991.

[259] American Institute of Ultrasound in Medicine, *Acoustic output measurement and labeling standard for diagnostic ultrasound equipment*. Rockville, Md.: The Institute, 1992.

[260] D. White, F. Duck, A. Fairhead, L. Rothenberg, A. Shaw, J. Zagzebski, and M. Zankl, "Tissue substitutes, phantoms and computational modelling in medical ultrasound," in *ICRU Report*. International Commission on Radiation Units and Measurements, Bethesda, MD, 1998.

[261] S. Emelianov, R. Erkamp, M. Lubinski, A. Skovoroda, and M. O'Donnell, "Non-linear tissue elasticity: adaptive elasticity imaging for large deformations," in *1998 IEEE Ultrasonics Symposium. Proceedings*, vol. 2. IEEE, 1998, pp. 1753–1756.

[262] S. A. Goss, R. L. Johnston, and F. Dunn, "Comprehensive compilation of empirical ultrasonic properties of mammalian tissues." *The Journal of the Acoustical Society of America*, vol. 64, no. 2, pp. 423–57, Aug. 1978.

[263] S. A. Goss, R. L. Johnston, and F. Dunn, "Compilation of empirical ultrasonic properties of mammalian tissues. II." *The Journal of the Acoustical Society of America*, vol. 68, no. 1, pp. 93–108, Jul. 1980.

[264] K. Yasukawa, T. Kunisue, K. Tsuta, Y. Shikinami, and T. Kondo, "An Ultrasound Phantom with Long-Term Stability Using a New Biomimic Soft Gel Material," *2007 IEEE Ultrasonics Symposium Proceedings*, no. C, pp. 2501–2502, Oct. 2007.

[265] T. Hall, M. Bilgen, M. Insana, and T. Krouskop, "Phantom materials for elastography," *IEEE Transactions on Ultrasonics, Ferroelectrics and Frequency Control*, vol. 44, no. 6, pp. 1355–1365, 1997.

[266] E. L. Madsen, J. A. Zagzebski, R. A. Banjavie, and R. E. Jutila, "Tissue mimicking materials for ultrasound phantoms," *Medical Physics*, vol. 5, no. 5, pp. 391–394, Sep. 1978.

[267] M. M. Burlew, E. L. Madsen, J. A. Zagzebski, R. A. Banjavic, and S. W. Sum, "A new ultrasound tissue-equivalent material." *Radiology*, vol. 134, no. 2, pp. 517–20, Feb. 1980.

[268] E. L. Madsen, G. R. Frank, T. a. Krouskop, T. Varghese, F. Kallel, and J. Ophir, "Tissue-mimicking oil-in-gelatin dispersions for use in heterogeneous elastography phantoms." *Ultrasonic imaging*, vol. 25, no. 1, pp. 17–38, Jan. 2003.

[269] E. L. Madsen, M. A. Hobson, G. R. Frank, H. Shi, J. Jiang, T. J. Hall, T. Varghese, M. M. Doyley, and J. B. Weaver, "Anthropomorphic breast phantoms for testing elastography systems." *Ultrasound in medicine & biology*, vol. 32, no. 6, pp. 857–74, Jun. 2006.

[270] E. L. Madsen, G. R. Frank, and F. Dong, "Liquid or Solid Ultrasonically Tissue-Mimicking Materials with Very Low Scatter," *Ultrasound in Medicine & Biology*, vol. 24, no. 4, pp. 535–542, May 1998.

[271] K. Kawabata, Y. Waki, T. Matsumura, and S. Umemura, "Tissue mimicking phantom for ultrasonic elastography with finely adjustable elastic and echographic properties," in *IEEE Ultrasonics Symposium, 2004*, vol. 2, no. C. IEEE, 2004, pp. 1502–1505.

[272] K. Kumar, M. E. Andrews, V. Jayashankar, A. K. Mishra, and S. Suresh, "Measurement of Viscoelastic Properties of Polyacrylamide-Based Tissue-Mimicking Phantoms for Ultrasound Elastography Applications," *IEEE Transactions on Instrumentation and Measurement*, vol. 59, no. 5, pp. 1224–1232, May 2010.

[273] T. Ling, Q. Jin, H. Yao, and H. Zheng, "Design and Characterization of a Tissue-Mimicking Phantom for Ultrasonic Elastography," in *2010 4th International Conference on Bioinformatics and Biomedical Engineering*. IEEE, Jun. 2010, pp. 1–4.

[274] T. Kondo, M. Kitatuji, and H. Kanda, "New tissue mimicking materials for ultrasound phantoms," in *IEEE Ultrasonics Symposium, 2005.*, vol. 3. IEEE, 2005, pp. 1664–1667.

[275] R. A. Lerski, T. C. Duggan, and J. Christie, "A simple tissue-like ultrasound phantom material," *British Journal of Radiology*, vol. 55, no. 650, pp. 156–157, Feb. 1982.

[276] K. Yagi, M. Tokuda, and T. Ueda, "Evaluation of the tensile strength properties by the difference in the degree of polymerization of pva gels," in *Micro-Nanomechatronics and Human Science, 2004 and The Fourth Symposium Micro-Nanomechatronics for Information-Based Society, 2004. Proceedings of the 2004 International Symposium on*. IEEE, 2004, pp. 207–212.

[277] W. Khaled, T. Neumann, H. Ermert, S. Reichling, A. Arnold, and O. T. Bruhns, "Evaluation of material parameters of PVA phantoms for reconstructive ultrasound elastography," in *2007 IEEE Ultrasonics Symposium Proceedings*. IEEE, Oct. 2007, pp. 1329–1332.

[278] K. C. Chu and B. K. Rutt, "Polyvinyl alcohol cryogel: An ideal phantom material for MR studies of arterial flow and elasticity," *Magnetic Resonance in Medicine*, vol. 37, no. 2, pp. 314–319, Feb. 1997.

[279] L. E. Maggi, M. A. von Krüger, W. C. A. Pereira, and E. E. C. Monteiro, "Development of silicon-based materials for ultrasound biological phantoms," in *2009 IEEE International Ultrasonics Symposium*. IEEE, Sep. 2009, pp. 1962–1965.

[280] M. O. Culjat, D. Goldenberg, P. Tewari, and R. S. Singh, "A review of tissue substitutes for ultrasound imaging." *Ultrasound in medicine & biology*, vol. 36, no. 6, pp. 861–73, Jun. 2010.

[281] K. Zell, J. I. Sperl, M. W. Vogel, R. Niessner, and C. Haisch, "Acoustical properties of selected tissue phantom materials for ultrasound imaging." *Physics in medicine and biology*, vol. 52, no. 20, pp. N475–84, Oct. 2007.

[282] M. Anton, M. Kruusmaa, A. Aabloo, and A. Punning, "Validating Usability of Ionomeric Polymer-Metal Composite Actuators for Real World Applications," *2006 IEEE/RSJ International Conference on Intelligent Robots and Systems*, pp. 5441–5446, Oct. 2006.

[283] K. Ogata, *Modern Control Engineering*, 3rd ed. Upper Saddle River, NJ, USA: Prentice-Hall, Inc., 1997, ch. 12–13, p. 803.

[284] A. Hunt, "Inverted pendulum with ipmc actuator in deionized water," [Online]. Available: https://www.youtube.com/watch?v=10PrrR3nZAE, (Last accessed: Nov. 20 2016).

[285] A. Hunt, "IPMC (ioonpolümeer-metall komposiit) sensori ja täituriga manipulaator ja selle juhtimine," Master's thesis, University of Tartu, Faculty of Science and Technology, Tartu, Estonia, 2009.

[286] Environmental Robotics Inc., "Products," [Online]. Available: http://www.environmental-robots.com/products.html, (Last accessed: Dec. 13 2016).

[287] K. Zhou and J. C. Doyle, *Essentials of Robust Control*, ser. Prentice Hall Modular Series for Eng. Prentice Hall, 1998.

[288] J. E. Bibel and D. S. Malyevac, "Guidelines for the selection of weighting functions for h-infinity control," DTIC Document, Tech. Rep., 1992.

[289] R. Öpik, "Seadmed kirurgiliste fantoomimaterjalide arendamiseks," Master's thesis, Tallinn University of Technology, Faculty of Mechanical Engineering, Tallinn, Estonia, 2011.

ACKNOWLEDGEMENTS

I would need to thank my supervisor professor Kruusmaa for this opportunity and challenge to conduct my doctoral studies under her guidance.

Additionally, I thank Andres Punning and Urmas Johanson (IMS lab, University of Tartu) for providing materials and advice whenever needed, professors Tan and Chen for receiving me in Smart Microsystems Lab in Michigan State University, and my former colleagues at the TUT Centre for Biorobotics for the productive daily meetings. I am most grateful to professor Boyer (Robotics group, IRCCyN) for the opportunity to stay in their group, and for the valuable lessons and discussions during my stay in Nantes.

This work and participation in related activities has been funded by U.S. CRDF Grant No. 16059, Estonian Science Foundation (ESF) Grant No. 6765, Estonian Research Council Projects SF0140018s12 and IUT33-9, European Union FP7 ICT-2009.5.2 project SAFROS and ICT-2009.2.1 project I-SUR, and Archimedes Foundation DoRa T8 and Kristjan Jaak mobility programmes.

ABSTRACT
Application-Oriented Performance Characterization of the Ionic Polymer Transducers (IPTs)

IPMC (Ionic Polymer-Metal Composite) and IPCMC (Ionic Polymer-Carbon-Metal Composite) materials, commonly addressed as IPTs (Ionic Polymer Transducers) are ”smart” materials that bend when voltage is applied between their electrodes and generate voltage when they are bent. Their attractive novel properties have been hypothesized to spark major technological advances, revolutionizing many fields, e. g. medicine, robotics and energetics. Since their discovery over two decades ago many reports have proposed potential implementations in various fields, but adapting these into practical use relies on improvements in material performance, and has been delayed due to slow advances in material development. Since IPTs possess both sensing and actuation capabilities it is natural to explore combining a sensor and an actuator of the same material for closed-loop operation. So far, very few preliminary studies look into this opportunity.

This thesis concentrates on investigating the performance of the IPT materials and the feasibility of their applications. First the performance of the IPMCs is studied at their limits as they are used for the first time in a real-time task, by balancing an inverted pendulum system. Next, a novel integrated IPCMC sensor-actuator design is proposed and realized, combining the actuation and sensing functionalities into a compact design with minimum impact on actuation performance. Then, an improved design of the integrated IPT sensor-actuator is proposed and built, and its performance is thoroughly characterized in a series of closed-loop experiments, providing significant amount of qualitative and quantitative information on the sensor-actuator concept, actuation and sensing capabilities of different IPMC and IPCMC materials and their potential limitations. Finally, soft tissue phantom[2] manufacturing techniques are introduced and validated in order to produce a test-bed for evaluating medical applications of IPTs in realistic conditions.

Balancing an inverted pendulum system is a very challenging task for IPTs considering their actuation properties, and it serves as an abstract application

[2]Phantoms in the context of this thesis are specially designed objects that substitute humans or animals in the processes of experiments, training etc., realistically mimicking some relevant aspects of their tissue properties and/or anatomy.

study with straight-forward evaluation criteria of pass or fail. To the best of author's knowledge it is the first attempt to utilize IPTs in real-time application. This study is expected to provide valuable information on the behaviour of the materials at their capability limits, and identify potential material-related limitations. IPMC-actuated inverted pendulum assembly consists of a short and wide IPMC sample that actuates a rigid extension rod that further moves a mobile cart supporting the inverted pendulum. The whole assembly is submerged in water. A state-space model is used to describe the dynamics of the system, a full-state feedback controller is designed, and experiments are performed to balance the inverted pendulum. The results show that it is possible to balance the system for 30 minutes and longer, but the inertia of the system must be sufficiently small. Unexpectedly significant back-relaxation effect observed in this study required a control system modification before it was possible to stabilize the system, and could significantly limit the utilization of these materials.

Using IPT sensors to provide position feedback to IPT actuators allows to preserve the advantageous properties of the IPT materials in closed-loop actuation systems, making them compact and easier to construct. This study also aims to investigate the feasibility of the integrated IPT sensor-actuator, provide a preliminary evaluation of its closed-loop performance and identify potential limitations of such a concept. The design of the prototype consists of two short mechanically coupled IPCMC samples that are fixed to a clamp with electrical terminals in one end, and to a rigid extension in the other end. Its sensing and actuation dynamics are captured using black-box models, PI controller is designed and closed-loop experiments are performed to evaluate the design. The results of this study capture the closed-loop behaviour of the IPT sensor-actuator following sinusoidal references (0.1 Hz, 0.5 Hz and 1 Hz), and provide a comparison with the same experiments using camera-based feedback. In the short term (few seconds) the IPTs perform very well, providing better precision than the vision-based position feedback. Longer experiments (up to 1 minute) suffer from a low-frequency noise in the IPT sensor signal (short-circuit current) that causes the error accumulation in position estimation and the respective control voltage saturation. While the sensor-actuator concept is demonstrated to be qualitatively feasible, a more thorough study is required to quantitatively characterize its performance and suppress the sensing noise that is suspected to originate from the sensing signal amplifier.

The work on the integrated IPT sensor-actuator is resumed in a greater depth on an improved design. This study aims to thoroughly characterize the proposed design, the alternative materials and their performance. The improved design is similar to the original sensor-actuator, using two actuator samples that are symmetrically positioned on both sides of a narrow sensor sample. The actuation and sensing dynamics of the device are captured using physics-based models that characterize the assembly and materials in terms of their fundamental parameters. Closed-loop experiments are conducted using three different materials, PI and $\mathtt{H}_\infty$ controllers, a multitude of different reference signals (unit step, 4 sinusoids, 3 random signals and a long duration sinusoid), using both IPT and laser distance meter as the feedback source. Besides characterization this allows to evaluate the significance of the control method, as well as compare the results material-wise and against an external feedback. The results show an improved performance, achieving up to 30 min long 1 Hz sinusoidal reference following with IPT feedback, 90 times longer than ever reported before. Low-frequency noise in IPT sensing signal reduces when using an improved amplifier, but still causes error accumulation in position estimation, limiting experiment durations from a few seconds up to several minutes, varying with material and input signals. While physics-based models are very laborious and cannot be recommended for applications, the significantly better performance of the $\mathtt{H}_{\infty}$ controller suggests that advanced control methods should be preferred over simplistic ones when possible. Novel properties of the IPTs provide an alternative to the bulky conventional sensors and actuators, but while their performance and reliability remain substantially inferior they cannot be considered mature for applications.

Current IPT actuation capabilities are insufficient for many of the proposed applications, but this limitation along with the material's mechanical compliance may prove to be a beneficial attribute in medical applications, providing an intrinsic safety measure. So far, the proposed invasive medical applications of IPTs have only passed preliminary proof-of-concept validation. This study aims to produce an easy to manufacture ultrasound compatible test-bed with realistic elasticity and desired (potentially patient-specific) anatomy for exploitation in investigating feasibility of the IPTs in invasive medical applications. First, the available phantom materials[3] are reviewed and gelatin gels are identified to best meet the set criteria. Experiments are conducted to relate the material composition to its properties, phantom manufacturing techniques are introduced and renal biopsy phantoms are manufactured for qualitative validation by interventional radiology residents. Evaluation results show that the phantoms have realistic anatomy and they appear realistic in ultrasound imaging. Based on the established phantom manufacturing procedure a soft tissue mimicking test-bed design is proposed for validating feasibility of IPTs in medical applications as an active guidewire in a catheter system. Thus the procedure for manufacture realistic test-beds for validating invasive medical applications of IPTs is established and validated, but validating the applications themselves remains a future work.

[3]Phantom materials mimic the living tissues in terms of one or more of their properties.

KOKKUVÕTE
Ioonpolümeeridest täiturite võimekuse karakteriseerimine rakendusteks

Ioonpolümeer-metall komposiidid (IPMCd) ja ioonpolümeer-süsinik-metall komposiidid (IPCMCd), mida ühiselt kutsutakse ka ioonpolümeer sensoriteks ja täituriteks (IPTd) on ”targad” materjalid, mis painduvad kui nende elektroodidele rakendada pinge, ja tekitavad mõõdetava pinge oma elektroodidele kui neid painutada. Oletatakse, et nende materjalide uudsed ja ebatavalised omadused annavad tõuke olulistele tehnoloogilistele uuendustele valdkondades nagu meditsiin, robootika ja energeerika. Esimest korda esitleti IPT materjale üle kahe kümnendi tagasi ja sellest saati on pakutud nendele materjalidele palju potensiaalseid rakendusi erinevates valdkondades, kuid nende kasutuselevõtt sõltub arengutest materjalide võimekuses ja sisuliselt seisab materjaliarenduse taga. Kuna IPT materjalid funktsioneerivad nii sensorite kui ka täituritena, siis on võimalik nende uudseid omadusi maksimaalselt ära kasutada kombineerides samasse lahendusse kaks materjalitükki, millest üks töötab sensori ja teine täiturina, saavutades integreritud tagasisidega lahenduse. Seni on sellisele konseptsioonile väga vähe tähelepanu pööratud ja see kindlasti väärib põhjalikumat uurimist.

Käesolev väitekiri uurib IPT materjalide sooritusvõimet ja nende sobivust praktiliste rakenduste tarbeks. Töö esimeses osas uuritakse IPMC materjalide käitumist maksimaalse suutlikkuse piiril kasutades neid esmakordselt reaalajakriitilises rakenduses, tasakaalustades pöördpendlit. Järgmisena pakutakse välja ning realiseeritakse uudne integreeritud IPT sensor-täitur, mis kombineerib materjalide uudsed sensorite ja täiturite omadused samasse kompaktsesse lahendusse, ja mõjutab täituri suutlikkust minimaalselt. Seejärel esitletakse täiustatud disainiga versiooni integreeritud IPT sensor-täiturist, mille omadusi uuritakse põhjalikumalt tagasisidega eksperimentides kasutades automaatjuhtimissüsteeme. Tulemused annavad rohkelt kvalitatiivset ja kvantitatiivset informatsiooni IPT sensor-täituri konseptsiooni ja erinevate IPT materjalide võimekuse ning kasutust piiravate omaduste kohta. Viimasena esitatakse ja valideeritakse pehmete kudede

fantoomide[4] valmistamise tehnika, et toota katsekeskkond IPT meditsiinialaste rakenduste hindamiseks realistlikes tingimustes.

Pöördpendli tasakaalustamine on IPT materjalide üldisi omadusi arvestades väga keeruline ülesanne, mida võib käsitleda kui selgete soorituskriteeriumitega abstraktset näidet uurimaks IPT materjalide kasutamist rakendustes. Autori teada on see esimene katse kasutada IPT materjale reaalajakriitilises rakenduses. Oodatavasti annavad antud uurimuse tulemused väärtuslikku infot materjalide käitumise kohta oma suutlikkuse piiridel ja aitavad tuvastada potentsiaalseid omadusi, mis võimad nende rakendamist piirata. Pöördpendli tasakaalustamiseks kasutatakse lühikest ja laia IPMC materjali tükki, mille külge kinnitatud pikendusega liigutatakse käru, mille peale asub pöördpendel. Kogu süsteem on asetatud vette. Süsteemi dünaamika kirjeldamiseks kasutatakse olekuruumi mudelit, mille baasil disainitakse automaatjuhtimissüsteem. Järgnevates eksperimentides on võimalik pöördpendlit tasakaalustada järjest kuni 30 minutiks, kuid süsteemi komponendid tuleb selleks võimalikult kergeks teha. Eksperimentide läbiviimise käigus ilmneb, et kasutatud materjalid käituvad vägagi mittelineaarselt ilmutades olulisel määral vastassunas paindumist (back-relaxation), mis võib teatud rakendustes olla oluline puudus. Selleks, et oleks võimalik pöördpendel tasakaalustada tuleb esialgset automaatjuhtimissüsteemi muuta.

IPT täituritele kombineerimine samast materjalist sensoritega võimaldab teostada lihtsa ehitusega ja kompaktseid tagasisidega süsteeme, millel säilivad IPT materjalide uudsed omadused. Seetõttu pakutakse järgnevalt välja integreeritud IPT sensor-täituri konseptsioon eesmärgiga uurida selle idee teostatavust, hinnata vastava lahenduse käitumist tagasisidega juhtimises ning tuvastada võimalikke praktikas rakendatavust piiravaid asjaolusid. Valmiv prototüüp koosnev kahest lühiksest kõrvutiasetsevast IPCMC materjalitükist, mis on üht otsa pidi kinnitatud elektriliste kontaktidega fikseeritud klambri külge, ja mille teised otsad on mehaaniliselt kokku ühendatud ning nende külge on paigaldatud jäik pikendus. Seadme dünaamika kirjeldamiseks kasutatakse empiirilisi mudeleid, mille järgi disainitakse PI (proportsionaalne-integraalne) automaatjuhtimissüsteem. Seejärel teostatakse prototüübi käitumise uurimiseks tagasisidega juhtimise eksperimendid kasutades sinusoidaalseid sisendsignaale sagedustega 0.1 Hz, 0.5 Hz ja 1 Hz. Tulemuste hindamiseks sooritatakse eksperimendid kasutades positsiooni mõõtmiseks nii IPT sensori kui ka välise tagasisideallika mõõdetud positsiooni. Esialgu (mõne sekundi jooksul eksperimendi algusest) toimib IPT tagasiside väga hästi ning pakub täpsemat positsioonilugemit kui kaamera pildist loetu. Pikemates katsetes (kestusega kuni 1 minut) ilmneb, et IPT sensori signaalis sisaldub ka madalsageduslik müra, mis põhjustab vea kogunemist täituri positsiooni mõõtmistes, mille tagajärjel täituri pinge jõuab küllastusse. Oletatavasti on selle põhjuseks liialt lihtsa ehitusega

[4]Fantoomid käesoleva töö kontekstis on spetsiaalselt kavandatud ja valmistatud objektid, mis asendavad eksperimentides, väljaõppel jne. inimesi või loomi, jäljendades realistlikult mingeid olulisi aspekte vastavates koeomadustes ja/või anatoomias.

sensori lühisvoolu võimendi. Seega antud töös näidatakse, et integreeritud IPT sensor-täituri konseptsioon on teostatav, kuid selle võimekuse ja piirangute kvantitatiivseks hindamiseks on tarvis teostada põhjalikum uuring.

Integreeritud IPT sensor-täituri konseptsiooni uurimist jätkatakse põhjalikumalt uue konstruktsiooniga prototüübi peal. Töö eesmärgiks on põhjalikult karakteriseerida prototüübi ehitus, kasutatud materjalid ning käitumine. Täiustatud prototüüp on konseptsiooni poolest väga sarnane esialgsele, kuid kasutab kaht laia IPT täiturit, mis on paigutatud sümmeetriliselt kummalegi poole kitsast sensorit. Süsteemi dünaamika kirjeldamiseks kasutatakse füüsikalisi mudeleid, mis kirjeldavad seadme ja materjalide dünaamikat kasutades füüsikaliselt tähenduslikke parameetreid. Prototüübi käitumist tagasisidega eksperimentides uuritakse kasutades kolme erinevat IPT materjali, PI ja $\mathtt{H}_\infty$ automaatjuhtimissüsteeme, nii IPT sensori kui laserkaugusmõõdiku tagasisidet, ja mitmeid erinevaid sisendsignaale (ühikaste, 4 erineva sagedusega siinust, 3 erinevat juhuslikku signaali ja pika kestusega siinust). See võimaldab peale prototüübi ja materjalide võimekuse iseloomustamise ka hinnata juhtimissüsteemi mõju, võrrelda tulemusi erinevate materjalide ning IPT ja laserkaugusmõõdiku vahel. Tulemused näitavad edasiminekut võrreldes esialgse prototüübiga omadega ning IPT tagasisidet kasutades saavutatakse lausa 30 min kestusega 1 Hz siinuse järgimine, mis on 90 korda pikem kui kunagi varem. Madalsageduslik müra IPT sensori signaalis küll väheneb kasutades teistsuguse ehitusega võimendit, kuid jätkuvalt põhjustab positsiooni mõõtmistes viga ja piirab eksperimentide kestust mõne sekundi ja mõne minuti vahele, olenevalt sisendsignaalist ja kasutatavast materjalist. Füüsikaliste mudelite kasutamisega kaasnev parameetrituvastus on väga töömahukas ning praktikas on mõistlikum kasutada empiirilisi mudeleid süsteemi kirjeldamiseks. PI ja $\mathtt{H}_\infty$ kontrollerite tulemuste võrdluse baasil maksab võimalusel kasutada pigem arenenumaid meetodeid. Uudsed IPT materjalide omadused pakuvad huvitavaid alternatiive tänapäeval levinud sensoritele ja täituritele, kuid kuni nende suutlikkus ja usaldusväärsus on oluliselt kehvemad ei saa neid veel pidada piisavalt küpseteks.

IPT täiturite praegune võimekus on paljude väljapakutud rakenduste jaoks ebapiisav, kuid see puudus võib osutuda kasulikuks omaduseks meditsiinialastes rakendustes, kus (koos paindlikkusega) see toimib materjalisisese ohutusmeetmena. Seni väljapakutud invasiivsed meditsiinialased IPT rakendused on läbinud vaid esialgsed katsed, mis kinnitavad ideede toimimist. Antud töö eesmärk on luua metoodika lihtsastivalmistatavate ultraheli all kasutatavate katsevahendite valmistamiseks, mis lubaks saavutada soovitud (potentsiaalselt patsiendispetsiifilise anatoomiaga) ehituse ja inimkudedele sarnase elastsuse, et uurida IPT materjalide kasutatavust invasiivsetes meditsiinialastes rakendustes. Esmalt vaadeldakse erinevaid fantoomimaterjale[5], millest kõige sobilikumaks osutuvad zelatiini geelid. Edasi selgitatakse katseliselt välja materjalide omadusete ja kompositsiooni vahelised seosed, tutvustatakse fantoomide valmistamise prot-

[5]Fantoomimaterjalid jäljendavad üht või mitut eluskudede omadust.

sesse, ning toodetakse treeningfantoomid neeru biopsia protseduuri harjutamiseks radioloogiaresidentidele, kes kvalitatiivselt hindavad saavutatavate fantoomide omadusi. Tulemused näitavad, et fantoomide anatoomia ja väljanägemine ultraheli all on realistlikud. Baseerudes kirjeldatud fantoomide tootmise metoodikal pakutakse järgmisena välja katsevahendi disain, mis võimaldaks realistlikes tingimustes uurida IPT materjalide kasutatavust meditsiinirakendustes, näiteks aktiivse juhttraadina õõnessondi ehituses. Seega IPT invasiivsete meditsiinialaste rakenduste valideerimiseks sobilike realistlike katsevahendite tootmise protsess on kirjeldatud ja valideeritud, kuid rakenduste endi uurimine jääb praeguse seisuga tuleviku tööks.

APPENDIX A

Hunt, A., Chen, Z., Tan, X., and Kruusmaa, M. (2010). Control of an inverted pendulum using an Ionic Polymer-Metal Composite actuator. In 2010 IEEE/ASME International Conference on Advanced Intelligent Mechatronics Proceedings, pp. 163–168.

2010 IEEE/ASME International Conference on
Advanced Intelligent Mechatronics
Montréal, Canada, July 6-9, 2010

Control of an Inverted Pendulum Using an Ionic Polymer-Metal Composite Actuator

Andres Hunt, Zheng Chen, Xiaobo Tan, Maarja Kruusmaa

Abstract—**Ionic polymer-metal composites (IPMCs) are electroactive materials that bend under an applied electric field. Existing work has typically dealt with the control of IPMC actuators themselves. In this paper we investigate the stabilization of an inverted pendulum on a cart using an IPMC actuator. Different from the traditional setting of cart-pendulum systems, we require that the voltage on the IPMC actuator stay close to zero, to prolong the actuator life and reduce power consumption. A state-space model is developed for the system, based on which an LQR controller together with an observer is designed. The proposed control scheme is able to stabilize the inverted pendulum for the entire duration of the experiment (five minutes). These results indicate that IPMC actuators hold potential for more sophisticated control applications.**

I. Introduction

IPMCs (Ionic Polymer Metal Composite) are a class of electroactive polymers (EAP) with intrinsic actuation and sensing properties. In particular, they bend when a voltage is applied across their electrodes, and conversely, they generate a voltage between its electrodes when subject to a mechanical stimulus [1]. IPMCs are amenable to miniaturization and can be easily cut into different shapes. They require low voltages for actuation and exhibit large displacements with respect to their dimensions. These properties are advantageous compared to conventional actuation devices such as DC motors. IPMCs have been proposed for various robotic applications, examples of which include a tadpole robot [2], snake-like actuators [3], a prototype walking robot [4], a ray-like underwater robot [5], a micromanipulator [6], a jellyfish-like robot [7], and a robotic fish [8]. The material has also been proposed for medical applications, e.g., for an active catheter system [9].

Modeling and control of IPMC actuators have been investigated by several authors. The control of IPMC manipulators is usually addressed in the cantilever beam configuration, where one end of a thin IPMC strip is fixed between electric contacts and the tip displacement or blocking force is controlled [10,11]. Typically these methods are accurate only at small deformations, for example, when measuring the output force of a cantilevered IPMC actuator against a fixed load cell. Furthermore, most IPMC-related control studies have been focused on the control of IPMC actuators themselves [4,12-15].

In this paper we examine the control of an IPMC-actuated system where potentiallly large deformation is required. In particular, we would like to stablize an inverted pendulum on a cart that is actuated by an IPMC manipulator. With large deformation, a number of nonlinearities, such as hysteresis, [16,17], become pronounced, and often demand sophisticated control strategies for IPMC actuators [16-18]. To prolong the actuator life and reduce the power consumption (important for many real applications), we require that the actuation voltage on IPMC be low for most of the time, which is different from traditional settings in control of cart-pendulum systems. In addition, the complexity of the IPMC-cart-pendulum system and the relatively low force output of IPMCs present significant challenges in achieving the goal of stablization.

The inverted pendulum problem with an IPMC actuator was previously studied in [19], where a simple empirical model was used. The approach in [19] permitted the balancing of the pendulum for only 10 s. In this paper, using a physical model for the IPMC-cart-pendulum system, we construct an LQR controller together with an observer. The proposed method is shown to stabilize the pendulum repeatedly for the entire duration of the experiments (5 min). We believe that this proof-of-concept control problem demonstrates that IPMC materials hold potential for real-world control applications. The remainder of the paper is organized as follows. IPMC materials are described in more details in Section II. The pendulum control problem is presented in Section III, followed by the modeling and control design in Section IV. Experimental setup is described in Section V, and experimental results are presented in Section VI. Finally, concluding remarks are provided in Section VII.

II. IPMC Materials

A. *IPMC Working Principles*

IPMCs consist of ion-conductive polymer backbone immersed with a solution of ions and solvent. The thickness of the polymer sheet varies among different materials and remains in the order of several hundred micrometers. Both sides of the polymer sheet are covered with conductive

This work was supported by the U.S. CRDF-ETF joint grant ESM1-2901-TL-07/GUS16059 and ETF grant 6765.

A. Hunt and M. Kruusmaa are with the Centre for Biorobotics, Tallinn University of Technology, Akadeemia tee 15A–111, 12618 Tallinn, Estonia (e-mail: andres.hunt@biorobotics.ttu.ee, maarja@biorobotics.ttu.ee).
Z. Chen is with Mechanical & Aerospace Engineering Department, University of Virginia, 122 Engineer's Way, Charlottesville, VA 22904-4746 USA (e-mail: zc7u@eservices.virginia.edu).
X. Tan is with the Department of Electrical & Computer Engineering, Michigan State University, 2120 Engineering Building, East Lansing, MI 48824 USA (e-mail: xbtan@egr.msu.edu).

surface electrodes, and usually noble metals are used for these electrodes.

When a voltage is applied to the surface electrodes, the resulting electric field causes the uniformly distributed ions to move towards one electrode. In the case of mobile cations, these ions will migrate towards the cathode side while carrying some solvent molecules along. This causes one side of the polymer to swell and the other side to shrink, resulting in material bending (Figures 1 and 2) [1].

IPMCs require low voltages for actuation, with the maximum values depending on the material at hand. Usually the maximum ratings are about 4 V. For dry samples, the critical voltage that may damage the material structure is lower. For wet samples, the electrolysis taking place above 2.5 V decreases the material performance, because the material starts losing solvent [1]. The output force at the tip of an IPMC beam is at the order of 1 mN (rating for IPMC size 10 mm by 10 mm).

The main drawbacks of IPMC materials include their time-varying performance and mechanical hysteresis. With the research over the past decade, the materials have become more stable but these problems are not completely resolved.

B. *Mechanical Hysteresis*

IPMCs exhibit shape hysteresis, especially when actuated at high voltages (and thus large deformations). Here we give one possible explanation to this phenomenon.

When a voltage is applied to an IPMC sheet, the ions move towards one electrode taking some solvent along. After the ion migration has stopped the solvent diffuses back as the result of mechanical stress and the osmosis effect. It can be observed as a slow decrease in IPMC deformation (Figure 3 A). Now when a zero voltage is applied, the ions are forced rapidly to redistribute. They return to oppositely charged ions fixed in the polymer backbone while the solvent is still unequally distributed. That results in the deformation of the material (Figure 3 B) in the opposite direction. After some time the mechanical stress has forced the solvent to distribute uniformly and IPMC deformation disappears (Figure 3 C).

C. *Materials*

In our task it was necessary to use IPMCs with a relatively high output force. We chose platinum-coated IPMCs

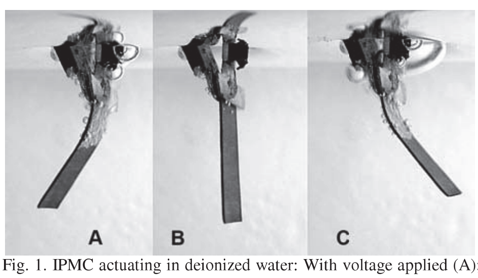

Fig. 1. IPMC actuating in deionized water: With voltage applied (A); at rest (B); and voltage applied with opposite polarization (C).

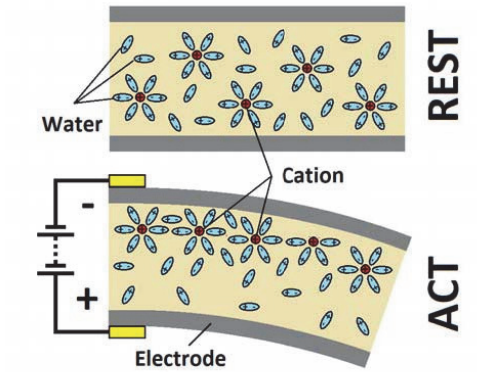

Fig. 2. Illustration of IPMC actuation mechanism. In rest ions are uniformly distributed inside the polymer (above); When voltage is applied ions move in electric field and take solvent with them – material bends (below).

provided by Environmental Robotics Inc. These IPMCs are 360 μm thick including electrodes. Chen *et al.* measured their Young's modulus [20] to be $Y=5.71\cdot10^8$ Pa. These materials need to be hydrated for long-time operation. The experiments reported in this paper were carried out in a small water tank.

III. Inverted Pendulum

A. *The Classical Inverted Pendulum on a Cart*

An inverted pendulum system consists of a cart carrying a rotary joint that supports the pendulum (Figure 4). The system is controlled through a force applied to the cart and its movement is constrained to a single plane.

Without proper control, the upright position of the pendulum is not stable. The typical control objective is to keep the pendulum upright and keep the cart at a specified position. System behavior can be described with a state-space model, based on which full state feedback (block diagram shown in Figure 4) or output feedback control can be designed.

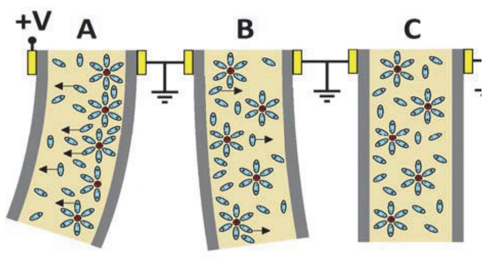

Fig. 3. IPMC hysteresis: Voltage is applied and ions have moved to one electrode. Solvent is slowly migrating due to mechanical stress and osmosis, and deformation slowly decreases (A); Zero voltage and ions have distributed uniformly. Due to non-uniform solvent distribution a slowly decreasing opposite deformation can be observed (B); IPMC has reached the initial state (C).

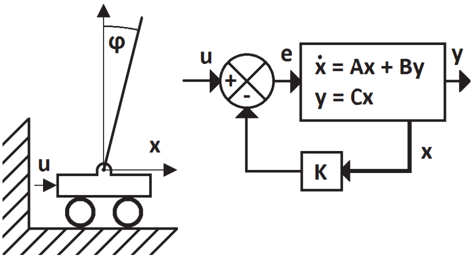

Fig. 4. Classical inverted pendulum with cart (left) and its typical control system (right).

B. IPMC-driven Inverted Pendulum

The inverted pendulum constructed for our task consists of a lightweight cart carrying low-friction hinge mechanism that supports a carbon fiber pendulum rod. The cart is made of steel wires and carbon fiber sticks and is operated on stainless steel rails.

The cart is moved with an IPMC actuator mechanism, which consists of a short IPMC strip placed between electrodes and a rigid extension added to the other end. The IPMC used in our experiments was 30 mm wide and 10 mm high. The extension length is a trade-off between the output force and the displacement at the cart level. The actuator – cart coupling mechanism has very low friction. The design principle and the photo of the system are shown in Figures 5 and 6, respectively.

The total length of the IPMC manipulator, from the clamp to the cart level, is 67 mm. The cart weighs 0.5 g. The pendulum rod is 68 mm long and it weighs 19 mg.

The system is immersed in a glass tank filled with deionized water. This increases the damping effect and the buoyancy compensates 12 mg of pendulum rod mass. The impact of turbulence is relatively small and is neglected as the speeds are low and object dimensions are small. Tank dimensions are much larger than the setup (tank: 130 mm (length) by 290 mm (width) by 210 mm (height)) reducing the turbulence and actuation impact on the environment.

C. Task Modification and Formulation

For the IPMC-driven inverted pendulum, because of IPMC mechanical hysteresis, we cannot keep the cart at a given position without providing an actuation voltage. The IPMC's rest position changes after an actuation voltage has been applied and then removed. Therefore, we have modified the original inverted pendulum problem and changed the control objective. To prolong the life of an IPMC actuator, we ask that the actuation voltage is kept low and desirably close to zero. By doing this, we also guarantee that the cart location will not be too far away from its original location when the IPMC was initially at rest. Reducing the actuation voltage also leads to reduction in power consumption, which is important in many real applications.

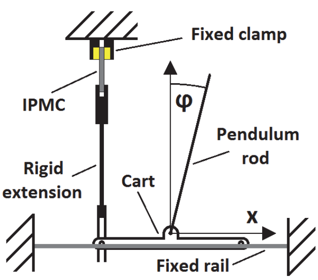

Fig. 5. Schematic of the IPMC-driven inverted pendulum-cart system.

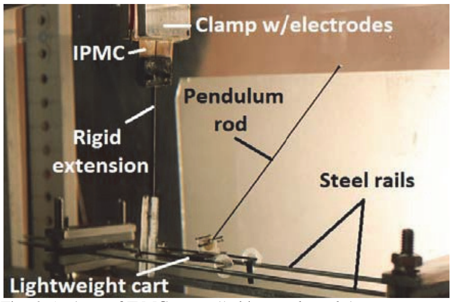

Fig. 6. A photo of IPMC-controlled inverted pendulum.

IV. System Model and Control Design

A. System Model

The system has three coupled subsystems: the IPMC manipulator, the cart, and the inverted pendulum. The input to the overall system is the IPMC actuation voltage. Through reduction of a physics-based model [11], we obtain a first-order model describing the relationship between the moment output M of the IPMC manipulator and the actuation voltage U:

$$\frac{M(s)}{U(s)} = \frac{a}{s+b} \quad (1)$$

Here a and b are constants and s is the Laplace variable. With the cart position, the pendulum angle, and their time-derivatives, the system has a total of five state variables. Some of the system parameters are directly measurable; others are obtained by fitting models to frequency response measurements. Parameters a and b in (1) are not directly measurable. They are determined by curve-fitting the IPMC actuator frequency response. Sinusoidal voltages logarithmically distributed over the frequency range from 0.1 Hz to 30 Hz were applied to the IPMC and the actuator tip moment was measured using a load cell. The measurements were done at 10 different frequencies with amplitude of 1.5 V. The experimental setup is described later in Section V.

One can further measure the frequency response for the combined IPMC/cart system, by taking the actuation voltage as input and the cart position X as output. This can be taken as a cascade of the moment dynamics (1) and the effective mechanical dynamics:

$$\frac{X(s)}{U(s)} = \frac{ac}{(s+b)(Is^2+rs+k)} \quad (2)$$

Here I is the effective moment of inertia of the IPMC/cart system, r is the effective damping constant, k is the effective stiffness, and c is some constant related to the DC gain of the system. Note that, since the angle of the IPMC manipulator will be relatively small, we take the cart displacement to be proportional to the angular position of the IPMC manipulator. Since parameters a and b are already identified through the procedure described earlier, the rest of parameters can be found by fitting the measured frequency response of (2). In our experiments, measurements were taken at 20 frequencies within the interval from 0.1 Hz to 10 Hz, with voltage amplitude of 2.5 V. The obtained model will also be used to get the virtual position signal in the feedback control experiments, which has proven effective in keeping the IPMC voltage near zero.

The model-fitting results are shown in Figure 7. With the identified parameters, the overall model can be expressed in the state space:

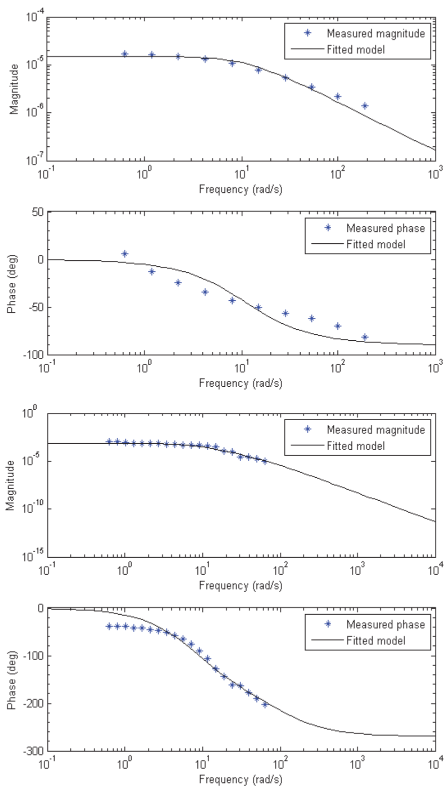

Fig. 7. The measured frequency response for IPMC moment and its fit (two upper charts) and the measured cart position frequency response and its fit (two lower charts)

$$\dot{x} = Ax + Bu;$$
$$y = Cx;$$
$$A = \begin{pmatrix} 0 & 1 & 0 & 0 & 0 \\ 86 & 0 & 1.84\cdot10^4 & 3.18\cdot10^3 & 9\cdot10^5 \\ 0 & 0 & 0 & 1 & 0 \\ 0.063 & 0 & -614 & -106 & -3\cdot10^4 \\ 0 & 0 & 0 & 0 & -10.9 \end{pmatrix}; \quad (3)$$
$$B = \begin{pmatrix} 0 \\ 0 \\ 0 \\ 0 \\ -1.64\cdot10^{-4} \end{pmatrix}; C = \begin{pmatrix} 1 & 0 & 0 & 0 & 0 \\ 0 & 0 & 1 & 0 & 0 \end{pmatrix};$$

B. Controller

Using the system model we designed a full-state linear quadratic optimal controller. Since the state of the IPMC moment is not directly measurable and the velocity measurements for the cart and the pendulum are noisy, we also designed a full-state observer using the pole placement technique.

In the experiments we use the cart model from equation (2) to estimate the virtual cart position, which is subject to the material hysteresis-induced uncertainty. It turns out that using the virtual position in feedback outperforms using the measured cart position, and a likely reason will be provided in Section VI when we discuss the experimental results.

The control system's block diagram is shown in Figure 8. For the previously described system, our controller and observer gains were:

$K = (-10^6 \;\; -4.8\cdot10^3 \;\; -1.2\cdot10^5 \;\; -5.11\cdot10^4 \;\; -5.8\cdot10^6)$;

$$L = \begin{pmatrix} 582 & 1138 \\ 9.4\cdot10^4 & 4.3\cdot10^5 \\ -4.71 & 402 \\ -1.5\cdot10^3 & 3.4\cdot10^4 \\ 6.8 & -97 \end{pmatrix}$$

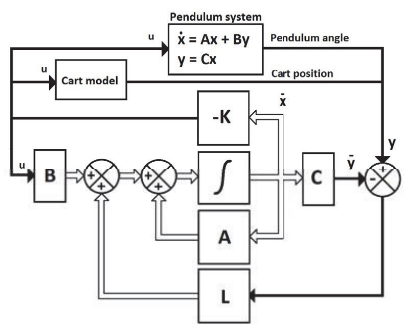

Fig. 8. Control system block diagram.

V. EXPERIMENTAL SETUP

We used two setups in the experiments – one to measure the IPMC moment response, and the other to measure the cart position response and to conduct the inverted pendulum control experiments.

In the inverted pendulum experiments and in the cart position frequency response measurements we used Dragonfly Express IEEE1394b camera to measure the cart's position and the pendulum's angle (at 120 Hz and 130 Hz frame rate). Experiments were controlled with a PC running LabView 8.6. Data acquisition board NI PCI-6703 was used to drive the IPMC through a unity gain amplifier based on LM675. For the frequency response measurements the pendulum was dismounted from the cart. The block diagram is shown in Figure 9 (A).

For measuring the IPMC moment response the actuator tip was fixed to MLT0202 load cell from ADInstruments Ltd and voltages were applied to the actuator. The measurements were controlled from a PC in NI LabView 8.6 environment. We used data acquisition cards NI PCI-6703 and PCI-6034E to apply the output voltage and to acquire the load cell measurements respectively. Again, the IPMC was driven through the unity gain amplifier. The block diagram for these experiments is shown in Figure 9 (B).

VI. EXPERIMENTAL RESULTS AND DISCUSSION

We simulated the cart model during experiments making it easy to switch between the actual position and the virtual position in the feedback in inverted pendulum experiments. The results showed that, when using the actual position in feedback, the system could not be stabilized for more than 10 seconds. However, when using the virtual cart position feedback, the pendulum could be stabilized repeatedly for the entire duration of 5-minutate experiments. The same controller and observer gains were used and some of these experiments were also recorded [21]. One explanation for this is that, because of mechanical hysteresis, the actual position of the cart drifts over time even if the actuation voltage is relatively symmetric. The latter could result in saturation for the IPMC voltage output (limited to 3.5 V) and the loss of controller effectiveness. Figure 10 shows one segment of trajectory for the pendulum angle, cart position and its estimation during one of the experiments, where the virtual cart position was used in the control. Also the actuator angle, applied voltage and IPMC estimated output momentum are shown.

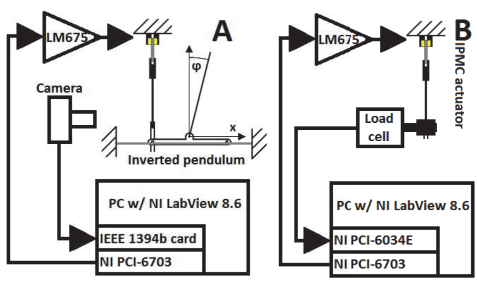

Fig. 9. Experimental setup for measuring the cart position's frequency response and to control the inverted pendulum (A); The setup for measuring the momentum response (B).

In the experiments both the cart position and the pendulum angle had moderate fluctuations. This can be addressed to remaining static friction that cancels out small corrections.

High voltages needed for the actuation also caused electrolysis inside the IPMC (3.5 V saturated). Because of this the IPMC lost ions and could not be continuously reused. With the same material we managed to balance the pendulum in total for up to 30 minutes and then the IPMC was not sufficiently capable to actuate any more. The materials were refurbished by re-immersing them with ions.

Overall the task of stabilizing the pendulum with an IPMC actuator was successfully completed. Total possible balancing period was surprisingly long given the moderate stability of the IPMC materials.

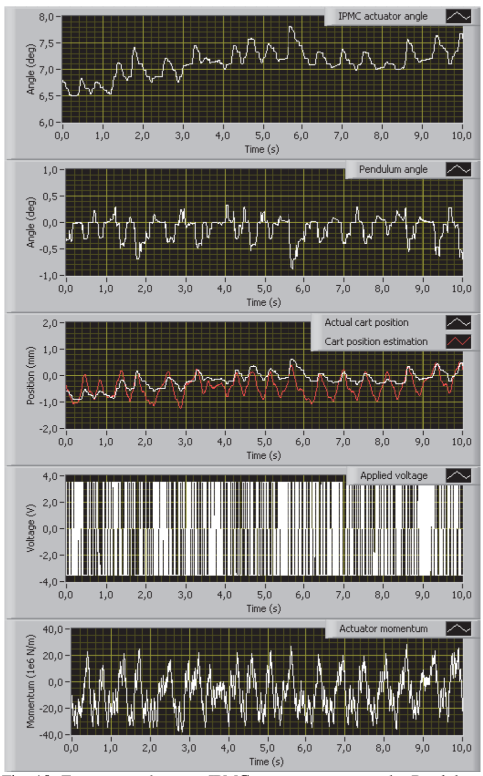

Fig. 10. From top to bottom: IPMC actuator output angle; Pendulum angle; Cart position estimation and actual position; Applied voltage; IPMC output momentum to actuator.

VII. CONCLUSION

In this work we have demonstrated the stabilization of an inverted pendulum using an IPMC actuator. The aim was to validate the feasibility of IPMC material for more complicated applications where the actuator undergoes large deformations. We developed the system model incorporating the physical IPMC model by introducing IPMC moment as one of the state variables. An LQR controller and a full-state observer were designed for this system. In the implementation, both the actual cart position and the virtual position estimated by the cart model were explored for feedback. The latter allows us to consider IPMC's mechanical hysteresis as an uncertainty and to keep the pendulum upright with the cart staying near the initial position.

For future work, we will examine a more challenging scenario where the pendulum and cart are operated in air environment. We will further analyze the effects of nonlinearities (including mechanical hysteresis) and investigate efficient control algorithms to mitigate such effects.

REFERENCES

[1] M. Shahinpoor and K. J. Kim, "Ionic polymer–metal composites—I. Fundamentals," *Smart Mater. Struct.,* vol. 10, no. 4, pp. 819–833, 2001.

[2] J. Jung, B. Kim, Y. Tak, and J.-O. Park, "Undulatory tadpole robot (TadRob) using ionic polymer metal composite (IPMC) actuator," in *Proc. of the IEEE/RSJ Int. Conf. on Intelligent Robots and Systems*, Las Vegas, Nevada, Oct. 2003, pp. 2133 – 2138.

[3] K. Ogawa, Y. Nakabo, T. Mukai, K. Asaka, and N. Ohnishi, "A snake-like swimming artificial muscle," in *Proceedings of The 2nd Conf. on Artificial Muscles*, Osaka, 2004.

[4] M. Yamakita, N. Kamamichi, T. Kozuki, K. Asaka, and Z.-W. Luo, "Control of biped walking robot with IPMC linear actuator,". In *the Proc. of the IEEE/ASME International Conference on Advanced Intelligent Mechatronics*, 2005, pp. 48 – 53.

[5] M. Anton, A. Punning, A. Aabloo, M. Listak, and M. Kruusmaa, "Towards a biomimetic EAP robot", in *Proc. of TAROS 2004, "Towards Autonomous Systems*", University of Essex, 6.-8. Sept. 2004.

[6] M. Kruusmaa, A. Hunt, A.Punning, M.Anton, and A.Aabloo, "A linked manipulator with ion-polymer metal composite (IPMC) joints for soft- and micromanipulation," in *Proceedings of IEEE International Conference on Robotics and Automation*, Pasadena, CA, 2008, pp.3588 – 3593.

[7] S.-W. Yeom and I.-K. Oh, "A biomimetic jellyfish robot based on ionic polymer metal composite actuators," *Smart Mater. Struct.*, vol. 18, 2009.

[8] 21AZ. Chen, S. Shatara, and X. Tan, "Modeling of biomimetic robotic fish propelled by an ionic polymer-metal composite caudal fin," *IEEE/ASME Transactions on Mechatronics*, 2009, to appear. doi:10.1109/TMECH.2009.2027812.

[9] H.-H. Lin, B.-K. Fang, M.-S. Ju, and C.-C. K. Lin, "Control of ionic polymer-metal composites for active catheter systems via linear parameter-varying approach", *Journal of Intelligent Material Systems and Structures*, vol. 20, no. 3, pp. 273-282, 2009.

[10] K. Mallavarapu, K. Newbury, and D. Leo, "Feedback control of the bending response of ionic polymer-metal composite actuators," in *Proc. of Smart Structures and Materials 2001 – Electroactive Polymer Actuators and Devices*, vol. 4329, pp. 301–310, 2001.

[11] Z. Chen, X. Tan, "A control-oriented and physics-based model for ionic polymer-metal composite actuators," *IEEE/ASME Transactions on Mechatronics*, vol. 13, no. 5, pp. 519-529, 2008.

[12] J. S. Lee, S. Gutta, and W. Yim, "Open-loop control of ionic polymer metal composite (IPMC) based underwater actuator using a network of neural oscillator," in *Proceedings of the 2007 IEEE/RSJ International Conference on Intelligent Robots and Systems*, San Diego, CA, 2007, pp 2132-2137.

[13] R. Richardson, M. Levesley, M. Brown, J. Hawkes, K. Watterson, and P. Walker, "Control of ionic polymer metal composites", *IEEE/ASME Transactions on Mechatronics*, vol. 8, no. 2, pp. 245-253, 2003.

[14] N. Bhat, and W.-J. Kim, "Precision force and position control of an ionic polymer metal composite," in *Proceedings of the Institution of Mechanical Engineers, Part I: Journal of Systems and Control Engineering*, vol. 218, no. 6, pp. 421-432, 2004.

[15] S. Kang, J. Shin, S. J. Kim, H. J. Kim, and Y. H. Kim, "Robust control of ionic polymer-metal composites", *Smart Mater. Struct.*, vol. 16, pp. 2457-2463, 2007.

[16] Z. Chen, X. Tan, and M. Shahinpoor, "Quasi-static positioning of ionic polymer-metal composite (IPMC) actuators," in *Proc. of the IEEE/ASME International Conference on Advanced Intelligent Mechatronics*, Monterey, CA, 2005, pp. 60-65.

[17] L. Hao and Z. Li, "Modeling and adaptive inverse control of hysteresis and creep in ionic polymer–metal composite actuators", *Smart Mater. Struct*. vol. 19, pp. 025014, 2010.

[18] N. T. Thinh, Y.-S. Yang, and I.-K. Oh, "Adaptive neuro-fuzzy control of ionic polymer metal composite actuators," *Smart Mater. Struct.*, vol. 18, pp. 065016, 2009.

[19] M. Anton, A. Punning, A. Aabloo, and M. Kruusmaa, "Validating usability of ionomeric polymer-metal composite actuators for real Life applications," in *Proceedings of the 2006 IEEE/RSJ International Conference on Intelligent Robots and Systems*, Beijing, China, 2006.

[20] Z. Chen, Y. Shen, N. Xi, and X. Tan, "Integrated sensing for ionic polymer-metal composite actuators using PVDF thin films," *Smart Materials and Structures*, vol. 16, 2007, pp. S262–S271.

[21] A. Hunt. (2010, February). Experiment video file. Available: http://www.youtube.com/BioroboticsTTU.

APPENDIX B

Hunt, A., Chen, Z., Tan, X., and Kruusmaa, M. (2009). Feedback Control of a Coupled IPMC (Ionic Polymer-Metal Composite) Sensor-Actuator. In ASME 2009 Dynamic Systems and Control Conference Proceedings, Volume 1, pp. 485–491.

Proceedings of the ASME 2009 Dynamic Systems and Control Conference
DSCC2009
October 12-14, 2009, Hollywood, California, USA

DSCC2009-2700

FEEDBACK CONTROL OF A COUPLED IPMC (IONIC POLYMER-METAL COMPOSITE) SENSOR-ACTUATOR

Andres Hunt
Intelligent Materials and Systems Laboratory
Institute of Technology
Tartu University
Nooruse 1, Tartu 50411
ahunt@ut.ee

Zheng Chen
Xiaobo Tan
Smart Microsystems Laboratory
Dept. of Electrical and Computer Engineering
Michigan State University
East Lansing, MI 48824 USA
chenzhe1@egr.msu.edu
xbtan@egr.msu.edu

Maarja Kruusmaa
Center for Biorobotics
Tallinn University of Technology
Akadeemia tee 15A-111, 12618 Tallinn Estonia
Maarja@biorobotics.ttu.ee

ABSTRACT

An ionic polymer-metal composite (IPMC) is an electroactive material that bends when electrically stimulated and generates electric current when bent. In this paper we investigate a coupled IPMC sensor-actuator using both the sensing and actuation properties of these electroactive materials. We describe the design of a coupled IPMC sensor-actuator, the feedback controller and the experimental evaluation of the system. Experimental results show the feasibility of closed-loop control of IPMC actuator with a mechanically coupled IPMC sensor.

INTRODUCTION

Electroactive polymers are materials that change their shape and size when electrically stimulated. This paper is concerned with a certain type of electroactive polymer materials, ionic polymer-metal composite (IPMC) [1]. The typical behavior of an IPMC actuator is shown in Fig. 1. In Fig. 1 (B) a strip of IPMC is clamped between the electrical contacts at the top. When a low voltage is applied to the electrodes, the material bends in response to the stimulation, as shown in Fig. 1 (A) and Fig. 1 (C). The driving voltage of these materials is usually around 2 V – 5 V. The direction of bending depends on the polarity of the applied voltage. The displacement of the tip depends on the amplitude of input.

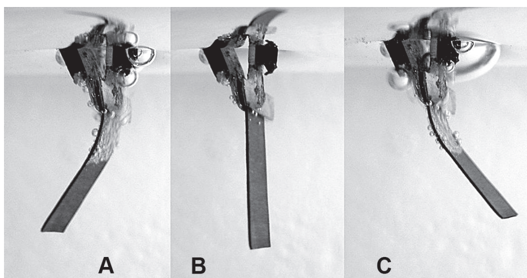

FIGURE 1. THE IPMC MATERIAL UNDER ELECTRIC STIMULATION

An IPMC actuator is made of a thin ion-exchange polymer membrane filled with ionic liquid and coated with a thin metal layer from both sides. With electrical activation, an electric field through the polymer membrane is generated, which in turn causes ion migration. The non-uniform concentration of ions is responsible for that the polymer matrix swells on one side and shrinks on the other side, resulting in the bending motion.

The polymer backbone is usually around 0.2 – 0.5 mm thick and the metal layer is around 20 µm. These materials thus permit designing actuators on a miniature scale driven at low voltages. At the same time they are mechanically simple and this makes them especially suitable for miniaturization.

IPMC materials are also reported to have a reverse effect to actuation. Mechanical bending of the IPMC material contracts one side of the membrane while expands the other. This forces the mobile ions to move against the pressure gradient. The expanded side therefore contains an excess of ions. This phenomenon produces a voltage at the surface electrodes of the IPMC [2].

The sensor properties could considerably expand the possible application areas of IPMC materials. The feedback signal for controlling an IPMC actuator is usually gained via external sensors, such as a load cell or a camera [3, 5, 6, 7]. Obviously, this configuration poses limitations for applications of IPMC actuators. In particular, a bulky external sensor would limit the mobility, miniaturization, and autonomy of an IPMC actuated device.

There have been some attempts in using soft smart materials as a compact means to provide feedback signals for IPMC actuators. For example, several groups have explored the use of two mechanically coupled IPMC stripes for simultaneous sensing and actuation [3, 4], but few details of successful implementation have been reported. The change of IPMC surface resistance with the bending curvature has been proposed as a potential means to provide feedback for an IPMC actuator [8, 9], but the feedback signal tends to be noisy and no feedback control has been experimentally demonstrated. Chen and coworkers [12, 13] have investigated the use of a PVDF film for providing sensory feedback for IPMC actuators. However, it is well known that PVDF is sensitive to temperature variations and special precaution has to be taken to deal with that [13].

In this paper we present detailed study on using a pair of mechanically coupled but electrically decoupled IPMCs for feedback control. In particular, an IPMC is used as an active joint for moving an elongated beam. We first present the construction of the IPMC sensor-actuator. Then we discuss the characterization and empirical modeling of the actuator and sensor dynamics. The empirical models are used for controller design. As an example, a PI controller is designed and applied to the sensor-actuator pair. Experimental results show that it is feasible to close the control loop with an integrated IPMC sensor.

IPMC SENSOR-ACTUATOR

As illustrated in Fig. 2, the IPMC manipulator consists of an IPMC actuator, a sensor and a rigid extension. The actuator and the sensor are mechanically coupled on both ends. The upper clamps, which are fixed, also provide electrical access/readout for the actuator and the sensor.

Dimensions of the manipulator are small to keep the device lightweight. The clamp at the fixed end has a width of 16 rmm , while the clamp at the other end has approximately the same width and a height of 9 mm. The distance between the two clamps is the active length of the actuator/sensor pair. It varies in experiments between 3 mm and 7 mm. The IPMC actuator width is 10 mm, while the IPMC sensor is much narrower. The latter has a width of 1.5 mm to 2 mm, to minimize its mechanical influence on the system. The manipulator extension has a length of 55 mm.

IPMC Materials used in the experiments were developed by the Intelligent Materials and Systems Lab at Tartu University. They differ by the fabricatiom method of the first layer of surface electrodes. The polymer membrane of the IPMCs is made of Nafion™ 117 treated with $LiClO_4$ solution and immersed in neat ionic liquid Emi-Tf. The first electrode layer for different samples was either TiC derived carbon, coconut shell based activated carbon, anhydrous RuO_2 or hydrous RuO_2. Next the first layer of surface electrode was covered with a layer of gold to increase the surface conductivity. All these materials are suitable for working in dry air and their properties do not change much in this environment. Best experiment results were achieved with the IPMC with the first electrode layer of coconut shell based activated carbon and the experimental results presented in this paper are from experiments with these materials.

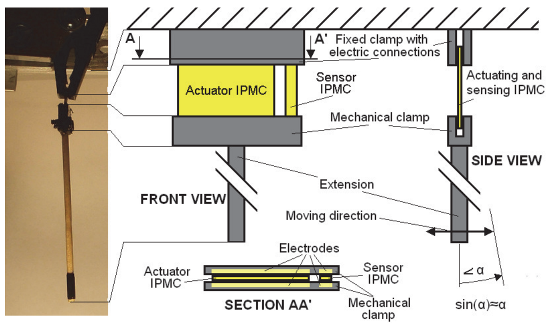

FIGURE 2. THE IPMC MANIPULATOR CONSTRUCTION (RIGHT) AND PHOTO (LEFT)

We assume that the IPMC sensor-actuator pair behaves linearly for the following reasons. First, from our previous work [11], it follows that a short IPMC with an extension has a very linear relation between the applied voltage and the consequent manipulator bending angle. The IPMC actuator tends to have the largest curvature close to the fixed clamp. Thus the IPMC can be viewed as a rotating joint. Next, since in our work the actuation angles are relatively small, the sine of the manipulator angle is approximately the same as the angle itself. Therefore, the manipulator tip position has a linear relation to the voltage applied to the actuating IPMC.

SYSTEM SETUPS

In the experiments two system setups were used. The first was for measuring the frequency response of the IPMC actuator and for feedback control of the IPMC sensor-actuator device. Also in several cases measurements of the sensor frequency responses were conducted with this setup. The second experimental setup was used only to measure the frequency response of the sensor. The signal sampling frequency in all experiments was 120 Hz, which is sufficient for our frequency range. This is also the camera's maximum frame rate at the maximum resolution.

Setup 1

In this setup the tip position of the manipulator (Fig. 2) is measured with a Dragonfly Express IEEE 1394b camera from Point Grey Research Inc. We drive the IPMC actuator with an operational amplifier (LM675T) working as a voltage follower. The device is controlled through a National Instruments data acquisition card (NI PCI-6703).The IPMC sensor signal is amplified with OP275G operational amplifiers and read through NI PCI6034E data acquisition card when needed. The experiments are conducted on a PC computer running LabView 8.5. The setup schematic is shown in Fig. 3

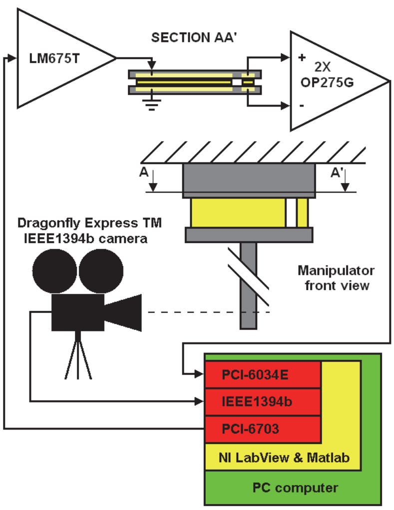

FIGURE 3. EXPERIMENT SETUP ONE

Setup 2

In the second setup the manipulator position was measured with the previously mentioned IEEE1494b camera. We used OP275G operational amplifiers connected to NI PCI6034E for measuring the IPMC sensor signal and NI PCI6703 card with LM675T operational amplifier to drive a hard disk drive (HDD) head actuating the manipulator. The part of HDD head containing magnet was fixed to the same construction as the manipulator and its moving tip had mechanical coupling (stiff strings) to IPMC manipulator tip. The IPMC actuator was disconnected in this setup. This experiment again was conducted in the LabView environment. The drawing of the setup is shown in Fig. 4.

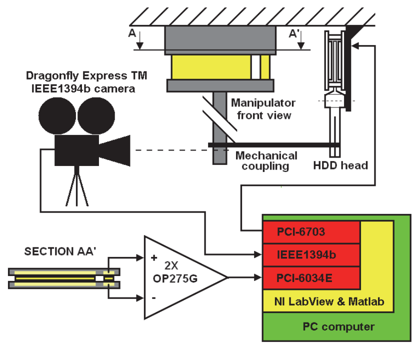

FIGURE 4. EXPERIMENT SETUP TWO

CHARACTERIZING THE IPMC ACTUATOR

The IPMC actuator frequency response was measured using Setup 1 as described above (Fig. 3). The driving voltage was applied to the IPMC manipulator and the position of the actuator was measured simultaneously. For the driving signal we used sinusoidal waves at different frequencies. The frequencies were applied one after another for fixed periods of time. For each driving signal frequency, the magnitude and phase data for the output were extracted, and the empirical Bode plots were constructed. Based on the measured frequency response, we seek a finite-dimensional rational transfer function to fit the data. We used a Labview program running a Matlab node for this purpose. The main function used was “invfreqs”, and the error weights, polynomial orders and other variables were manipulated in the program while pole-zero map and Bode plots were observed simultaneously to achieve the best fit.

Results

The frequency range used was from 0.1 Hz to 15 Hz. At higher frequencies the actuation amplitude was negligible. Within this range, experiments were conducted with 20 frequencies in a logarithmic distribution. The actuation voltage amplitude was 2 V. The measured magnitude and phase points along with the computed fit for the actuator IPMC are shown in Fig. 5. The identified transfer function is

$$\frac{5.53\times10^{6} s+6.63\times10^{7}}{s^{5}+1.17\times10^{2} s^{4}+4.571\times10^{3} s^{3}+1.97\times10^{5} s^{2}+4.26\times10^{6} s+3.27\times10^{6}} \tag{1}$$

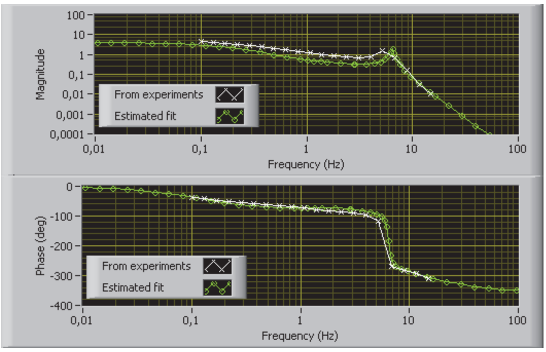

FIGURE 5. ACTUATOR IPMC EXPERIMENTAL BODE PLOTS WITH FITTED TRANSFER FUNCTION BODE PLOTS

CHARACTERIZING IPMC SENSOR

We used both setups described earlier for the IPMC sensor characterization, because we used two different ways to stimulate the sensor: 1) the IPMC actuator and 2) a HDD head. First, Setup 2 was used. The manipulator was actuated with a HDD head and an amplified IPMC sensor signal was measured simultaneously..

When actuated with the HDD head, the frequency response had a poor consistency at low frequencies (below 1 Hz). This is due to the mechanical friction that distorts the sinusoidal position output. Using an IPMC to actuate manipulator when measuring IPMC sensor frequency response gave better results at low frequencies. At frequencies over 10 Hz, however, the magnitude of the actuator response was very small, resulting in poor estimation of the sensor transfer function. Since our control experiments were conducted at relatively low frequencies (determined by the bandwidth of the actuator), we mainly used the IPMC actuator to obtain the sensor frequency response.

Similarly as in the characterization of the actuator, we fitted a transfer function to the measured Bode plots for the sensor response. Since later on we will use the inverse of sensor dynamics to compute the manipulator tip position, we enforce in identification the condition that the sensor dynamics be stable and minimum-phase, so its inverse will be stable. In fitting process the error weights of the estimation in the experimental magnitude and phase points and the polynomial maximum orders were manipulated until best result was achieved.

Results

When characterizing the IPMC sensor actuated with a HDD head , we used the frequency range of 0.1 Hz to 15 Hz. When using an IPMC actuator for sensor characterization, we used the frequency range of 0.1 Hz to 8 Hz. In both cases 20 frequencies were used at logarithmic intervals . Typically the sinusoidal signal was applied for 30s with a current frequency. The driving voltage amplitude of the IPMC was again 2 V and that of the HDD head was 0.2 V since it was much more sensitive.

Fig. 6 shows the measured inverse frequency response of the sensor, actuated with the IPMC actuator, and the Bode plots of the estimated transfer function for the sensor

$$\frac{71.24s+137.3}{s+0.0436} \tag{2}$$

We note that although the phase plots show poor match close to and below 0.1 Hz, it is not a problem for us since that is outside of the frequency range of interest in this paper.

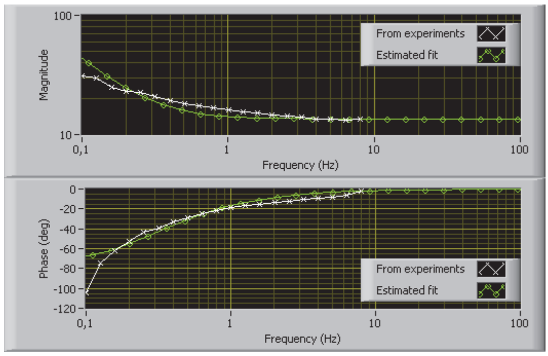

FIGURE 6. SENSOR IPMC EXPERIMENTAL BODE PLOTS WITH FITTED TRANSFER FUNCTION BODE PLOTS

CONTROLLER DESIGN

Since the main objective of this study is to demonstrate the feedback control of IPMC actuator with an IPMC sensor, the emphasis is not on the optimal choice of controller design. Instead, we have chosen to use a PI controller due to its simplicity.

We first used computer simulations to design the gains for the PI controller. Unity feedback was applied to the actuator IPMC model, assuming that the proper position information is gained using the inverse of the transfer function for the IPMC sensor. The parameters for the PI controller are obtained by accommodating the step response and the responses to sinusoidal inputs at different frequencies.

Simulation results

Fig. 7 shows the simulation results of tracking signals of three different frequencies. The PI controller used is

$$T(s) = \frac{0{,}0059\ s + 13.8}{s} \tag{3}$$

In order to limit the actuation voltage, it is not desirable to use very high gains for the controller. As a result, there is an appreciable tracking error for frequencies of 1 Hz and higher. This is not a big concern since our interest is in validating the simulation results with experimental ones. Both in simulations and experiments the frequencies of 0.1Hz, 0.5 Hz and 1 Hz were chosen for testing.

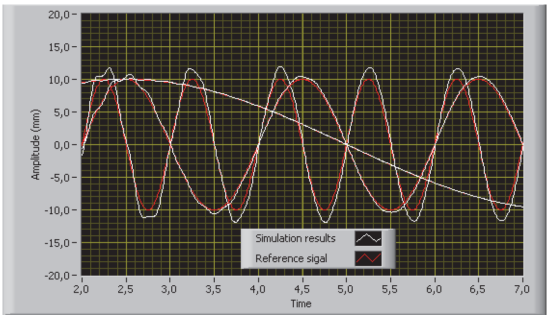

FIGURE 7. SIMULATION RESULTS ON DESIRED AND ACHIEVED OUTPUT AT 0.1 HZ, 0.5 HZ, AND 1 HZ

CAMERA-BASED FEEDBACK CONTROL EXPERIMENTS

The purpose of camera-based feedback control experiments was to check the model and controller validity and let us fine-tune the controller gains for better performance. Also, this would provide reference data for comparing with our IPMC sensor-based feedback control experiments.

With the feedback from camera the output position error remained within one pixel length (0.19 mm), making the manipulator precision acceptable. As we use same camera as an observer afterwards it will be also the observation precision. In current experiments, we also monitor the estimated position from the IPMC sensor.

Results

The experimental results of position tracking with camera feedback is shown in Fig. 8. It can be seen that the model errors cause the IPMC estimated position to have small error, while, based on the camera, the manipulator is following the reference signal at 0.1Hz (upper chart).

At 0.5 Hz and 1 Hz (middle and lower charts) all the reference signals, camera measured positions and the IPMC estimations overlap reasonably well. The small errors in IPMC sensor position estimation are mainly caused by the transfer function fit errors.

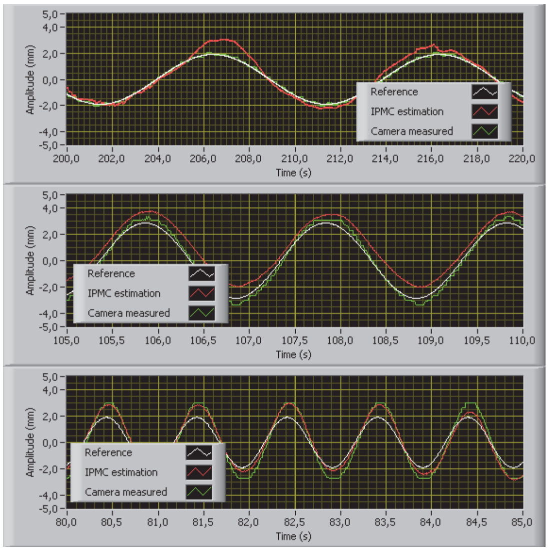

FIGURE 8. CAMERA FEEDBACK EXPERIMENTS AT 0.1HZ (UP), 0.5HZ (IN THE MIDDLE) AND 1HZ (DOWN)

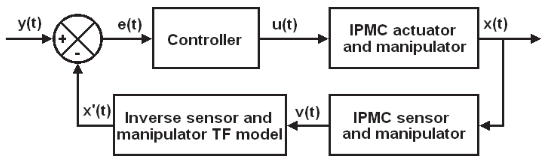

FIGURE 9. BLOCK DIAGRAM OF THE SYSTEM WITH IPMC SENSOR FEEDBACK

IPMC SENSOR FEEDBACK EXPERIMENTS

In these experiments the position information was obtained from the IPMC sensor, as illustrated in Fig. 9. We used the camera as an observer to gain the actual manipulator tip position. In these experiments the fine-tuned controller from the camera feedback control experiments was applied.

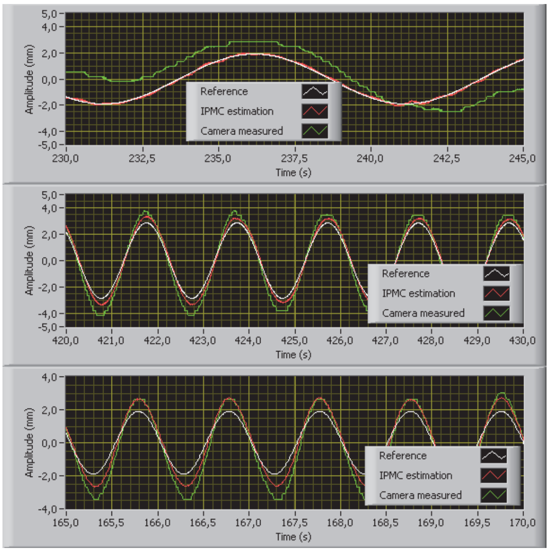

FIGURE 10. IPMC SENSOR FEEDBACK EXPERIMENTS AT 0.1HZ (UP), 0.5HZ (IN THE MIDDLE) AND 1HZ (DOWN)

Results

Fig. 10 shows the experimental results on feedback control using the position information extracted from the IPMC sensor. Three different frequencies were used. It can be seen that reasonable tracking performance, which is comparable to both the simulation results and the camera-based feedback control results, is achieved. In these experiments the manipulation at 0.5Hz showed the best results with the system being stable for up to 2 minutes. During the experiments at 0.1 Hz the system remained stable for up to 45 seconds and at 1 Hz for 60 seconds.

We comment, however, that the cause for system becoming instable was some low-frequency drift observed for the IPMC sensor output, which presented a challenge in tracking for relatively long time (several minutes). In a series of experiments we eliminated periodically the offset error and then the system remained stable for entire experiment durations (approximately 5 minutes). From the drift spectrum it was seen that largest magnitudes remained in the range of up to 0.2 Hz. While the exact cause of the drift is still under investigation, possible sources could include amplifier drift, temperature variation, IPMC sensor transfer function error at low frequencies and IPMC material properties. It is known that the IPMCs are a relatively immature technology, especially in long-term stability. We expect further improvement of the feedback control performance as the material matures.

The main advantage of using IPMC sensor with a predicted sensor inverse transfer function is the high short-term precision in position prediction. It should be lined out that the angles of the manipulator within the experiments were so small that they are considered the same as their sines. Also even when comparing to the camera that measured the manipulator tip position in the very end of it (Fig. 11) the IPMC estimation gives higher resolution of the position than the camera. The offset in the figure is set to view both curves in parallel.

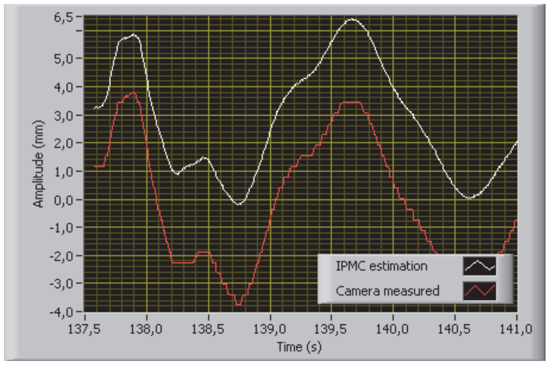

FIGURE11. IPMC POSITION ESTIMATION HAS HIGHER PRECISION THAN CAMERA ESTIMATION

Thus we consider our proposed IPMC sensor-actuator setup to be relatively successful and usable with some improvements. In our future work we will use physical IPMC models for estimating position from the IPMC sensor.

CONCLUSIONS

In this paper we have represented the feedback control of an IPMC sensor-actuator. The sensor and actuator were mechanically connected but electrically isolated. Experiments were performed to identify the actuator and sensor dynamics, which were then used for the design of feedback controller. With a PI controller, the IPMC sensor-based feedback delivers comparable performance as that based on a camera. Future work includes refinement of the conditioning and processing IPMC sensor signal to obtain better consistency. We will also examine more advanced control designs with physics-based, control oriented IPMC sensor and actuator models [14, 15].

ACKNOWLEDGMENTS

This work was supported by U.S. CRDF (Grant No. 16059) and Estonian Science Foundation (Grant No. 6765).

REFERENCES

[1] K. Oguro, Y. Kawami, and H. Takenak,. “Bending of an ion-conducting polymer film-electrode composite by an electric stimulus at low voltage,” Journal of Micromachine Society, vol. 5, 27–30, 1992.

[2] K. Sadeghipour, R. Salomon, S. Neogi, “Development of a novel electrochemically active membrane and ‘smart’ material based vibration sensor/damper,” Smart Materials and Structures, vol. 1, 172-179, 1992.

[3] K. Mallavarapu, K. Newbury, and D. Leo, “Feedback control of the bending response of ionic polymer-metal composite actuators,” Proc. of Smart Structures and Materials 2001 – Electroactive Polymer Actuators and Devices, Vol. 4329, pp. 301–310.

[4] M.Yamakita, A.Sera, N.Kamamichi, K.Asaka, Z.W.Luo, “Integrated Design of IPMC Actuator/Sensor,” Proceedings of the 2006 IEEE International Conference on Robotics and Automation, pp.1834-1839, 2006.

[5] Y. Nakabo, T. Mukai, K. Asaka, “Kinematic modeling and visual sensing of multi-DOF robot manipulator with patterned artificial muscle,” Proc. IEEE Int. Conf. Robotics and Automation (ICRA 2005), Barcelona, pp.4326-4331, 2005.

[6] M. Anton, A. Punning, A. Aabloo, M. Kruusmaa, “Validating usability of ionomeric polymer-metal composite actuators for real life applications,” IEEE/RSJ International Conference on Intelligent Robots and Systems; Beijing, China, 2006.

[7] M. Yamakita, N. Kamamichi, T. Kozuki, K. Asaka, Z.-W. Luo, ” Control of biped walking robot with IPMC linear actuator,” Proceedings of the 2005 IEEE/ASME International Conference on Advanced Intelligent Mechatronics, pp. 48-53, 2005

[8] A. Punning, M. Kruusmaa, A. Aabloo, “Self-sensing actuator and method of controlling thereof,” PCT patent application, PCT/EE2007/000004, 8.03.2007.

[9] A. Punning, M. Kruusmaa, A. Aabloo, “A self-sensing ionomeric polymer metal composite (IPMC) actuator, ” Sensors and Actuators A: Physical, vol. 136, no. 2, pp. 656–664, 2007.

[10] E. Mbemmo, Z. Chen, S. Shatara, X. Tan, “Modeling of biomimetic robotic fish propelled by an ionic polymer-metal composite actuator,” in Proceedings of the 2008 IEEE International Conference on Robotics and Automation, Pasadena, CA, pp.689-694, 2008.

[11] M. Kruusmaa, A. Hunt, A.Punning, M.Anton,A.Aabloo, “A linked manipulator with ion-polymer metal composite (IPMC) joints for soft- and micromanipulation,” Proceedings of IEEE International Conference on Robotics and Automation, Pasadena, CA, pp.3588 – 3593, 2008.

[12] Z. Chen, Y. Shen, N. Xi, X. Tan, “Integrated sensing for ionic polymer-metal composite actuators using PVDF thin films,” Smart Materials and Structures, vol. 16, no. 2, pp. S262-S271, 2007

[13] Z. Chen, K. Kwon, X. Tan, “Integrated IPMC/PVDF sensory actuator and its validation in feedback control,” Sensors and Actuators A: Physical, vol. 144, no. 2, pp 231-241, 2007

[14] Z. Chen, X. Tan, “A control-oriented and physics-based model for ionic polymer-metal composite actuators,” IEEE/ASME Transactions on Mechatronics, vol. 13, no. 5, pp. 519-529, 2008.

[15] Z. Chen, X. Tan, A. Will, C. Ziel, “A dynamic model for ionic polymer-metal composite sensors,” Smart Materials and Structures, vol. 16, pp. 1477-1488, 2007.

APPENDIX C

Hunt, A., Chen, Z., Tan, X., and Kruusmaa, M. (2016). An integrated electroactive polymer sensor–actuator: design, model-based control, and performance characterization. Smart Materials and Structures, 25(3), pp. 035016.

IOP Publishing — Smart Materials and Structures
Smart Mater. Struct. 25 (2016) 035016 (16pp) doi:10.1088/0964-1726/25/3/035016

An integrated electroactive polymer sensor–actuator: design, model-based control, and performance characterization

A Hunt[1], Z Chen[2], X Tan[3] and M Kruusmaa[1]

[1] Centre for Biorobotics, Department of Information Technology, Tallinn University of Technology, Akadeemia tee 15A-111, 12618 Tallinn, Estonia
[2] Department of Electrical Engineering and Computer Science, Wichita State University, 252 Jabara Hall, 1845 Fairmount St. Wichita, KS 67260, USA
[3] Department of Electrical & Computer Engineering, Michigan State University, 428 S. Shaw Lane, 2120 Engineering Building, East Lansing, MI 4882 USA

E-mail: Andres.Hunt@ttu.ee

Received 11 August 2015, revised 24 January 2016
Accepted for publication 29 January 2016
Published 22 February 2016

Abstract

Ionic electroactive polymers (IEAPs), particularly ionic polymer-metal composites (IPMCs) and carbon-polymer composites (CPCs), bend when a voltage is applied on their electrodes, and conversely, they generate an electrical signal when subjected to a mechanical bending. In this work we study and compare the capabilities of IPMC and CPC actuators and sensors in closed-loop control applications. We propose and realize an integrated IEAP sensor–actuator design, characterize its performance using three different materials, and compare the results. The design consists of two short IEAP actuators and one sensor mechanically coupled together in a parallel configuration, and an attached rigid extension significantly longer than the IEAPs. This allows the device to be compliant, simple to construct, lightweight, easy to miniaturize, and functionally similar to a one-degree-of-freedom rotational joint. For control design and accurate position sensing in feedback experiments, we adapt physics-based and control-oriented models of actuation and sensing dynamics, and perform experiments to identify their parameters. In performance characterization, both model-based H_∞ control and proportional-integral control are explored. System responses to step inputs, sinusoids, and random references are measured, and long-duration sinusoidal tracking experiments are performed. The results show that, while IEAP position sensing is stable for only a limited time-span, H_∞ control significantly improves the performance of the device.

Keywords: IPMC, CPC, EAP, actuator, sensor, control, feedback

(Some figures may appear in colour only in the online journal)

1. Introduction

The rapidly advancing field of materials science has introduced many ‘smart’ materials with novel sensing and actuation capabilities. The ability of electroactive polymer (EAP) materials to change their shapes or sizes under electrical excitation is offering appealing alternatives to conventional sensors and actuators [1]. Two functionally similar classes of such materials are ionic polymer-metal composites (IPMCs) [2] and carbon-polymer-composites (CPCs) [3]. Both are ionic electroactive polymers (IEAPs) that change their curvature when a voltage is applied across their electrodes and conversely, generate an electrical signal when they are bent. Since their first introduction over two decades ago [4], their properties have been greatly improved, e.g., both the power consumption and surface resistance have been significantly reduced [5].

IEAP materials have been proposed for various applications in the field of robotics [6] due to their technological potential and advantages over conventional actuators, including easy scalability, light weight, and low actuation voltage, to name a few. Robotic fish propulsion [7–9], heart rate monitoring [10], embryo injection [11], linked manipulator [12], seismic sensor [13] and artificial lateral line [14] are some examples of reported studies on exploiting IEAPs. Thorough overviews on the materials and their proposed applications can be found in [15–17].

In some applications (e.g. robotic fish propulsion) the actuator performs well in the open-loop configuration. However, feedback is often desirable to further improve the performance. In this regard, IEAP self-sensing actuation schemes appear attractive, the implementation of which includes measuring actuator's surface resistance [18], and patterning actuator's electrodes to create resistive sensor areas on its edges [19], among others. Unfortunately, these solutions typically have not been demonstrated to function in feedback configurations. The feedback in IEAP actuator control is most often accomplished using an external sensor, e.g., a camera [20, 21] or a laser distance meter [22–26]. However, such solutions greatly increase the overall size of the system. Some authors have overcome this issue by mechanically integrating various sensors with IEAP actuators. For example, Chen *et al* combined a PVDF sensor with an IPMC actuator [27], and Leang *et al* added a strain gauge on an IPMC actuator's surface [28]. Since these approaches involve bonding of other materials on the IEAP surface, they also add significantly to the stiffness and thus result in reduction in the actuation capabilities.

In addition to the aforementioned reports, there are many other works that implement feedback control on IEAP actuators (e. g. [23, 29–34]), but only a few studies utilize the same materials for providing the feedback signal. For example, Newbury implemented a compensator for controlling oscillations of a rotary device using one IPMC sensor and four IPMC actuators [35]. He reported 1 s long feedback experiment fragments to demonstrate improved performance (over the open-loop configuration) in a narrow frequency interval. Bonomo *et al* [36] attached two identical IPMCs side-by-side to a plastic sheet and fed the amplified voltage signal generated by one IPMC to the other, in order to either suppress (negative feedback) or sustain (positive feedback) the oscillations initiated by an external stimulus. A maximum of 5 s long experiments were reported and the feasibility of the design was qualitatively concluded, based on the IPMC sensor's output voltage in combination with visual observations, while the actual deformations were not measured. Later, Yamakita *et al* [37] presented preliminary results on using IPMCs in parallel for actuation and sensing in precision feedback control. They were able to conduct two experiments using an unspecified setup—tracking a step input and a 0.2 Hz sinusoidal signal, each for 10 s. More recently, Gonzalez *et al* [38] used an IPMC sensor to provide feedback in their work on an IPMC microgripper. They used empirical models and PID control to track step inputs of magnitude from 0.1 to 1 mm, for a maximum of 20 s. The results showed that reaching the reference level takes at least 5 s and for some of the larger amplitudes, it is not possible to reach the reference level. These works did not quantitatively characterize the control precision.

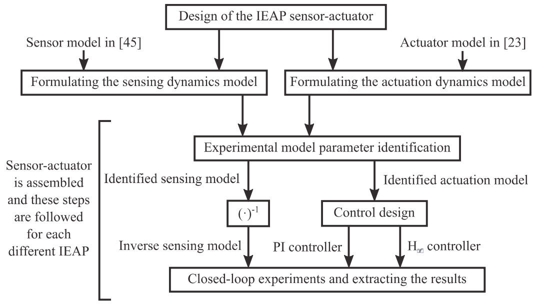

Figure 1. General structure of this work and dependencies between its parts.

In our preliminary work [39] we presented the feedback control of a coupled IPMC sensor–actuator. Empirical models of actuation and sensing dynamics were experimentally identified, a PI controller was designed, and experiments on tracking sinusoidal references were conducted. With IPMC feedback the maximum experiment duration of 120 s was achieved.

In this paper we (1) improve the pivot-like IEAP sensor–actuator design enhancing its actuation capabilities and reducing undesirable twisting motions; (2) model the dynamics of the prototype utilizing physics-based models for IEAP sensing and actuation dynamics; (3) validate the proposed design and quantitatively characterize its performance in model-based feedback control experiments with three different input signals (step, sine, and random references), and an extended (up to 2 h) sine following; (4) compare the results for integrated sensing against external sensing, and PI against H_∞ control, on three identical sensor–actuator prototypes, each constructed utilizing different type of IEAP. An Au-plated IPMC, a Pt-plated IPMC and a CPC material with carbon electrodes are used to obtain a broader comparison between materials similar in construction and function. The general structure of the presented work is illustrated in figure 1. To the best of authors' knowledge this is the first report to achieve up to 30 min long tracking in IEAP sensing feedback configuration (being 90 times longer than reported by other groups), and 2 h long tracking in case of external feedback. Also, the presented quantitative results provide a qualitative 'sense' about the maturity of the IEAP materials for applications.

The rest of this paper is organized as follows. In section 2 we introduce the concept and the prototype of the IEAP sensor–actuator, the IEAP materials, their modelling and control, experimental setup, experimental procedures and evaluation metrics. Section 3 presents the results of model identification and feedback experiments. The results are analysed in section 4 and the conclusions are presented in section 5.

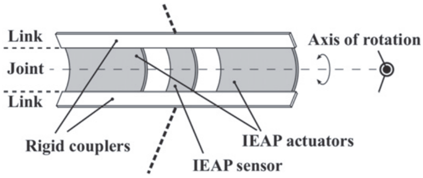

Figure 2. Concept of the proposed IEAP sensor–actuator. The device can be approximated as a rotational joint when the attached rigid links are significantly longer than the IEAPs.

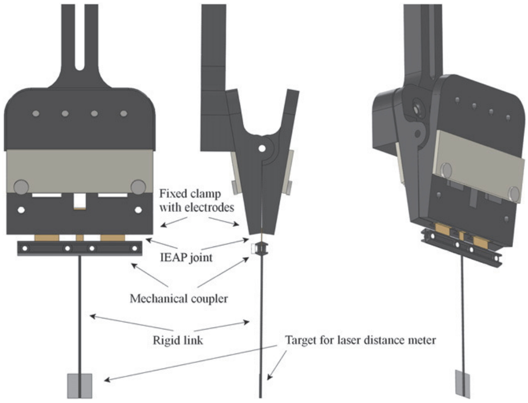

Figure 3. Construction of the proof-of-concept IEAP sensor–actuator prototype used in the experiments.

2. Materials and methods

2.1. The design of the IEAP sensor–actuator

The device consists of IEAPs that are connected in parallel for simultaneous actuation and sensing, with mechanical couplers at both ends, as shown in figure 2. One of the couplers also accommodates terminals connected to IEAP electrodes.

A practical solution for the integrated sensor–actuator used in the experiments in this paper is shown in figure 3. Three IEAP samples are used in parallel—a narrow one in the middle for sensing and two wide ones symmetrically on both sides for actuation. This prevents any potential undesirable twisting during actuation. Short IEAPs are used in the design as they are more efficient than long ones [12, 40], and they allow the sensor to closely follow the shape of the actuator. The resulting behaviour functionally resembles a one-degree-of-freedom rotary joint. On one end the IEAPs are mechanically coupled together using lightweight plastic plates and screws. A carbon fibre rod with a plate on the other end is attached to this coupler so that the motion of its tip can be observed using a laser distance meter. The other end of the IEAP samples is clamped by a spring-loaded plastic clamp with gold-plated silver electrodes. The clamp thus couples the IEAPs mechanically, connects them electrically to sensing or actuation circuits, and fixes that end to the Earth frame during the experiments. Its construction allows one to easily change the sample sets.

The clamp in the fixed end is oriented so that the rotational axis is horizontal and the motion of the extension rod takes place in a vertical plane. In this configuration the IEAPs do not strain due to gravity. The components of the setup such as the clamp are intentionally not miniaturized, as it is not essential for the experiments in this paper. The backbone components of both the clamp and the mechanical coupler are made of ABS plastic using a rapid prototyping machine 3D Touch (3D Systems Inc). All the components of the setup are chemically resistant to water, making it possible to experiment with both wet and dry IEAP materials.

2.2. IPMC and CPC materials

The IPMC and CPC materials consist of a thin membrane sheet (Nafion or Flemion) that is coated with conductive electrodes [2, 3]. Mobile counter-ions are loosely coupled to the ionomer backbone. When a voltage is applied between the electrodes, these counter-ions start migrating in the electric field towards one surface. In the case of Nafion polymer with Li^+ counter-ions, they migrate towards the anode. Actuation voltages vary among materials, but usually are up to 5 V.

IPMCs and CPCs also exhibit sensing properties [41, 42]. Bending an IEAP sheet causes the counter-ion migration within the material due to the pressure gradient across the material thickness. This results in electric potential difference between the surface electrodes; however, the sensing voltages are orders of magnitude smaller than the voltages required for actuation. Typical sensing approaches include measuring the voltage between the electrodes [41, 43] and measuring the sensor charge or current [44–46]. Some IEAPs show a significant change in their surface resistance when bending, which can be used for position sensing, as shown in [18, 19]. We choose to use the IEAP short-circuit current for estimating the material deformation due to its reported high accuracy [45].

In the experiments we use three different IEAP materials that are labelled as material #1, #2 and #3, and respectively we label the sample sets cut from these materials as sample set #1, #2 and #3. Material #1 is made of Nafion™117 membrane that is coated with coconut shell-derived active carbon electrodes using direct assembly procedure [3]. To enhance the surface conductivity the material is further covered with gold foil and hot-pressed, and immersed in EMI-Tf ionic liquid. The detailed manufacturing procedure is described in [3]. These materials have low surface resistance that varies insignificantly while bending, and they can work well in dry environments due to low vapour pressure of the ionic liquid.

Material #2 is a typical platinum-coated IPMC provided by Environmental Robotics Inc. It is made of Nafion™117 polymer that is deposited with Pt electrodes using an electroless plating procedure. The loosely coupled hydrogen ions in the polymer are exchanged with larger Li ions.

Material #3 is produced 5 years earlier, similarly as #2, except that the electrodes are made of gold instead of platinum. The functionality of materials #2 and #3 highly depends on their water concentration and they need to be kept hydrated. The experiments with these materials are conducted in water to prevent water evaporation and guarantee consistent conditions throughout the experiments.

2.3. Model-based feedback control

The interactions among the polymer backbone, ions, and solvent (or ionic liquid) make the IEAP sensing and actuation dynamics complex and the overall behaviour poorly predictable. To a large extent these issues can be overcome with proper modelling and control of the materials. The aim of modelling the IEAP sensing and actuation dynamics in this work is threefold: describing the used materials in terms of their fundamental physical parameters; providing the actuation models for control design; and providing inverse sensing models that relate the IEAP sensor short-circuit current to the actual position of the tip of the sensor–actuator in the closed-loop experiments. Regardless of that many reports have been published on modelling the IEAP sensors and actuators, the actuation and sensing phenomena is yet not fully understood. Multiple potential dominant processes have been proposed, and overviews on modelling can be found in the review papers [16, 17, 47].

In this work we model the sensing and actuation dynamics of the IEAP materials using the Laplace domain models developed by Chen *et al* in [23, 45]. These were originally derived to describe the IPMCs, but are also valid for the functionally identical CPC materials. In particular, it is presumed in the derivation process in [23, 45] that the mechanism behind the actuation and sensing phenomenon is the proportional coupling between the accumulated charge and mechanical stress, while the solvent effects are negligible (see chapter 2 in [45] and chapter II in [23]). Thus, the ionic liquid in CPCs functions both as solvent and counter-ions in IPMCs. Furthermore, the polymer backbone of all IEAPs used in this work is Nafion$^{\mathrm{TM}}$117, and the CPC electrodes (nanoporous carbon covered with gold foil) are equivalent to the coatings of the IPMCs (Pt or Au electrodes, with dendritic structure in the surface layers of the polymer backbone).

Both these models were derived based on the PDEs of the governing physical processes within the sensor and actuator while taking into account the surface resistance effects. The resulting infinite-dimensional Laplace domain models were further reduced to lower-order models in the form of rational transfer functions usable for real-time computation and control design. In the following we introduce the adaption of these models to describe sensing and actuation dynamics of our IEAP sensor–actuator, and their use for control design. Construction of the resulting models is illustrated in figure 4. For clarity, the notations are adapted from [23, 45] where possible.

2.3.1. Modelling the sensor dynamics. The model of IEAP sensing adapted from equation (55) in [45] relates the out-of-plane displacement of the tip of the IEAP beam $w(s)$ to the short-circuit current between the material electrodes $i(s)$, s being the Laplace variable. Assuming small deformations and sensor bending in the first cantilever shape mode (using the

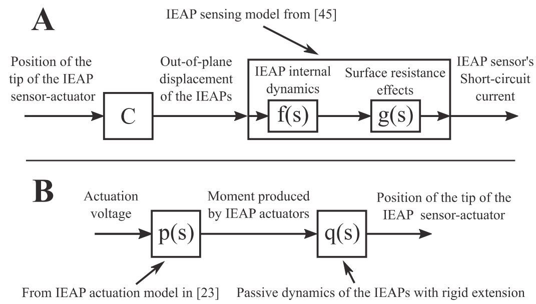

Figure 4. Block diagrams describing the construction of the IEAP (A) sensing and (B) actuation models.

spatial derivative of the 1st cantilever shape mode in the tip of the beam), the relation between $w(s)$ and the manipulator tip position $x(s)$ can be expressed as a constant $C = L/(1.3765L_{\mathrm{e}} + L)$, where L is the length of the IEAP and L_{e} is the length of the elongation from the IEAP to the measuring plane. The sensing model can be written as:

$$\hat{H}(s) = \frac{i(s)}{x(s)} = C \cdot f(s) \cdot g(s), \tag{1}$$

with $f(s)$ describing the sensing dynamics and $g(s)$ incorporating the surface resistance effects (see figure 4(A)). These parts can be re-written in a practical form for application:

$$f(s) = \frac{\lambda_1 s^3 + \lambda_2 s^2 + \lambda_3 s}{s + K}, \tag{2}$$

$$g(s) = \frac{\mu_1 s^2 + \mu_2 s + \mu_3}{s^2 + \mu_4 s + \mu_5}, \tag{3}$$

with the terms in $f(s)$:

$$K \approx \frac{F^2 d C^-}{\kappa_{\mathrm{e}} RT}, \tag{4}$$

$$\lambda_1 = -\frac{3YW_{\mathrm{s}}h\sqrt{Kd}}{8\alpha_0 L^3 K^2}; \qquad \lambda_2 = -4K\lambda_1,$$
$$\lambda_3 = 8K^2\left(\sqrt{\frac{d}{h^2 K}} - 1\right)\lambda_1, \tag{5}$$

and in $g(s)$:

$$\mu_1 = \frac{L^2}{6}, \qquad \mu_2 = \frac{3h}{\kappa_{\mathrm{e}} r_0}, \qquad \mu_3 = \frac{12h^2}{\kappa_{\mathrm{e}}^2 r_0^2 L^2},$$
$$\mu_4 = \frac{12h}{\kappa_{\mathrm{e}} r_0 L^2}, \qquad \mu_5 = \frac{24h^2}{\kappa_{\mathrm{e}}^2 r_0^2 L^4}. \tag{6}$$

As in [23, 45], the terms are: Y is the Young's modulus, W_{s} is the width of the IEAP sensor, d is the ion diffusivity, h is the half the material thickness, α_0 is the charge–stress coupling constant, κ_{e} is the dielectric permittivity, r_0 is the surface resistance per material length and width, F is the Faraday constant, C^- is the anion concentration, R is the universal gas constant, and T is the absolute temperature. For more details about the model, refer to [45].

The resulting model is improper as its numerator is of higher order than the denominator; however, in the experiments we use its proper inverse.

2.3.2. Modelling the actuation dynamics. The model for actuation dynamics is adapted from the work of Chen *et al* [23]. They linked the bending dynamics of a long flexible IPMC beam to the input voltage by deriving the model for voltage-induced bending and cascading it with the second-order vibration dynamics of a flexible beam. In this work we model the actuation dynamics of the IEAP sensor–actuator considering the system as a rigid beam with non-uniform cross-section that is connected to the Earth frame by a pivot joint (IEAPs) with torsional stiffness. The joint is actuated by torques generated by the IEAP actuators, where the model relating the IEAP input voltage to the bending moment is adapted from the intermediate results of Chen *et al* [23]. Naturally, we split the actuation dynamics into two parts—the actuation model $p(s)$ relating the produced moment $M(s)$ to the applied voltage $V(s)$, and the mechanical model of the device's passive dynamics $q(s)$ relating the input moment $M(s)$ to the position $X(s)$ of the tip of the rigid link attached in the mobile end of the IEAP sensor–actuator (see figure 4(B)):

$$G(s) = \frac{X(s)}{V(s)} = p(s) \cdot q(s). \tag{7}$$

We assume that the surface resistance along the IEAP actuator's electrodes is zero ($r_1' = 0$) as the actuator is very short, and the surface resistances of the materials in hand are low. With some manipulations one can extract the expression for $p(s)$ from the intermediate results (particularly, equations (20), (29) and (46)) in [23]:

$$p(s) = \frac{M(s)}{V(s)} = \frac{\alpha_0 \kappa_e K W_a h(1-\gamma)}{\gamma \kappa_e r_2' s^2 + \gamma(h + \kappa_e K r_2')s + Kh}, \tag{8}$$

where K is given in equation (4) and γ is defined as:

$$\gamma = h\sqrt{\frac{K}{d}}, \tag{9}$$

r_2' is the resistance through the IEAP per length and W_a denotes the width of the actuator. It must be noted that when neglecting the surface resistance, the actuation moment does not depend on the IEAP length.

The passive dynamics of the rigid mobile link attached to the IEAPs can be captured with a second-order system

$$q(s) = \frac{X(s)}{M(s)} = \frac{\mathcal{L}}{I} \cdot \frac{1}{s^2 + 2\xi\omega_n s + w_n^2}, \tag{10}$$

which is valid for the frequency range of interest. Here I is the moment of inertia with respect to the clamping axis, ξ accommodates the damping of the environment and internal friction in IEAPs, ω_n is the natural frequency of the system and $\mathcal{L}$ is the distance from the IEAP clamping level to the position-measuring height on the mobile link.

2.3.3. Control. Based on the model for actuation dynamics we design two controllers, a PI controller and an H_∞ controller. The PI controller is manually tuned to achieve shortest settling time in tracking a step input.

The H_∞ controller is designed according to the procedures given in [48]. The sensitivity weight on output error W_e (low-pass) and the weight on control effort W_u (high-pass) were used in the design procedure according to [48, 49]. First- and second-order weights are used to design the controller that is later reduced to the fifth order for implementation purposes.

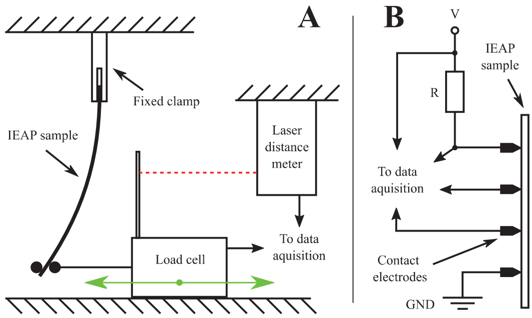

Figure 5. Experimental setups for measuring the material's (A) Young's modulus and (B) dimension-normalized surface resistance.

2.4. Experimental setups

The experimental setup used to measure Young's modulus is illustrated in figure 5. The material sample is suspended in air using a fixed clamp. The tip of the sample is held between a fork attached to a force gauge Panlab TRI202P and its position is measured using a laser distance meter SICK OD2-P250W150U0. The force and position readings are recorded using a PC computer with NI PCIe-6343 data acquisition board and NI Labview 2010 environment. The force gauge position is changed manually and its position is fixed at the instances of recording the readings.

The four-point resistance measurement setup used to determine the material's surface resistance is illustrated in figure 5. The material sample is pressed against the electrodes and a constant voltage of 0.1 V is applied. The voltages on the resistor and on the inner electrodes are measured and the surface resistance per length and width r_0 is calculated using the same PC computer with NI PCIe-6343 and NI Labview 2010.

The diagram of the setup used in the rest of the experiments is shown in figure 6 and a photo of the actual setup is in figure 7. The spring-loaded clamp is fixed such that the mobile link of the IEAP sensor–actuator is hanging down, since in such a configuration the gravity does not cause any lateral strains in the IEAPs in the rest position. In the spring-loaded clamp, the actuators are electrically connected in parallel to each other. They are driven from a PC through the amplifier of a Kepco BOP 20-10MC bipolar power supply that is optimized for capacitive loads. The sensor's short-circuit current is measured using a two-stage amplifier (based on OPA111BM operational amplifiers), that converts the

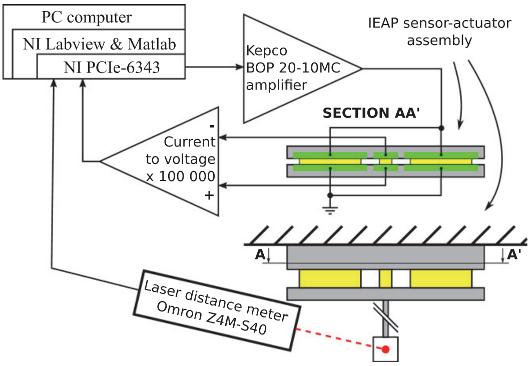

Figure 6. Experimental setup that is used to measure the damping ratio, natural frequency and frequency responses in the model identification phase, and to perform the feedback experiments.

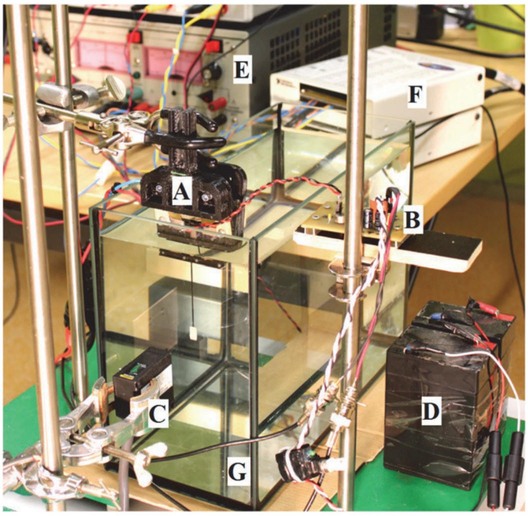

Figure 7. A photo of the final experimental setup used in feedback experiments and in some system identification experiments. (A) The proof-of-concept IEAP sensor–actuator; (B) short-circuit current-to-voltage converter and amplifier; (C) laser distance meter; (D) amplifier's battery pack; (E) power supply unit Kepco; (F) data acquisition board's terminal boxes; (G) water tank (only used with the samples that must be kept hydrated, currently set #3).

current to voltage and amplifies the signal (by factor of 100 000). The amplifier's power is supplied from a battery pack to eliminate noise propagation from the power grid. The position of the tip of the mobile link is measured using an Omron Z4M-S40 laser distance meter with resolution of 40 μm. The experiments are controlled from a PC computer with NI Labview 2010 SP1 software through NI PCIe-6343 data acquisition board. Program loops in frequency response measurements and feedback control experiments are implemented with a sampling frequency of 10 kHz.

2.5. Parameter identification

The terms in the sensing and actuation models (sections 2.3.1 and 2.3.2) include known constants (universal gas constant R and Faraday's constant F) and parameters that must be identified for each material prior to the control design and closed-loop control experiments.

First, the average material thickness $2h$ and the surface density of the material sheet are determined. Young's modulus Y of the sheet is identified from the bending experiments of the material beam, i.e. deformations are applied and the corresponding forces are measured at the tip of the vertically suspended material sample (see the setup in figure 5(A)). The ratio between the applied forces P and the resulting deformations σ is determined using linear regression, and Young's modulus is obtained according to [50]:

$$Y = \frac{Pl^3}{3\sigma I_y}, \quad I_y = \frac{(2h)^3 w}{12}, \tag{11}$$

where l is the length of the material sheet, I_y is the area moment of inertia, and w is the width of the material sample. The dimension-normalized surface resistance r_0 is obtained using a four-point resistance measuring scheme (0.1 V applied, measurements taken in steady state) shown in figure 5(B).

Next, the sample sets (two actuators, one sensor) are cut from the respective material sheet targeting widths of 3 mm and 10 mm for the sensor and actuators respectively. The sensor–actuator prototype is assembled and the width of the sensor W_s, widths of the actuators W_a and the length of the IEAPs L are measured. The moment of inertia for the assembly of the IEAPs and the mobile link is calculated (with respect to the outer clamping edge of the fixing clamp) from their geometry and the densities of their parts. The sensor–actuator device assembly is suspended vertically and the laser distance meter is set to point the tip of the extension rod. The effective length of the actuating portion L_e (from the clamp to the laser distance meter level) is measured.

Once the setup is complete, the natural frequency w_n and the damping ratio ξ are determined from free oscillations (due to external stimulus) of the mobile link. Next, the frequency responses are measured for actuation and sensing dynamics. Sinusoidal voltage inputs of 2 V amplitude are sequentially applied on the actuators, with frequencies logarithmically spaced in the 0.2–15 Hz, or wider interval (aiming to capture the characteristic phase transitions), for the duration of at least two full periods, but no less than 30 s. Simultaneously, the position of the tip of the link and the IEAP short-circuit current are measured using a laser distance meter and a current amplifier, respectively. The magnitude and phase information is extracted, and transfer function models for actuation and sensing dynamics are then identified through curve-fitting the remaining model parameters that cannot be determined individually (i.e., ion-diffusivity d, charge–stress coupling constant α_0, dielectric permittivity κ_e, anion concentration C^-, and resistance trough the polymer r_2').

While curve-fitting cannot uniquely define all these parameters, the structure of the models (in chapters 2.3.1 and

Table 1. Identified model parameters for each IEAP sensor–actuator assembly.

Measured or calculated parameter	Symbol	# 1	# 2	# 3	Unit
Material thickness	$2h$	277	353	282	μm
Young's modulus	Y	140	154	658	MPa
Surface resistance	r_0	0.543	64.0	0.144	Ω
Total width of the actuators	W_a	18.9	20.8	20.8	mm
Sensor width	W_s	1.95	3.72	2.96	mm
Operational material length	L	3.03	2.53	2.22	mm
Effective length of elongation	L_e	61.0	59.64	58.60	mm
Moment of inertia about clamp	I_{xx}	1.79×10^{-7}	1.71×10^{-7}	1.66×10^{-7}	kg m^2
Material surface density	ρ	0.460	0.650	0.570	kg m^{-2}
Natural frequency	ω_0	15.9	8.70	10.0	Hz
Damping ratio	ξ	0.0611	0.100	0.135	—
Room temperature	t	22.4	22.9	21.6	°C
Fitted parameter					
Ionic diffusivity	d	3.44×10^{-12}	3.48×10^{-11}	3.32×10^{-11}	m^2 s^{-1}
Anion concentration	C^-	1064	1068	1089	mol m^{-3}
Resistance trough material	r_2'	9.98×10^{-6}	9.99×10^{-6}	1.00×10^{-5}	Ω m
Dielectric permittivity for sensor	κ_{e_s}	3.76×10^{-3}	1.52×10^{-3}	1.38×10^{-3}	F m^{-1}
Dielectric permittivity for actuator	κ_{e_a}	2.99×10^{-6}	5.07×10^{-7}	1.41×10^{-7}	F m^{-1}
Charge–stress coupling constant for sensor	α_{0_s}	1.39×10^5	3.35×10^5	3.18×10^5	J C^{-1}
Charge–stress coupling constant for actuator	α_{0_a}	−0.213	−0.0220	−0.0828	J C^{-1}

2.3.2) offers certain constraints, and when approximate numbers for initial values are chosen according to the literature [23, 44, 45, 51], the fitting process converges to real-valued physically realistic parameters. Initial values for anion concentration C^- and ion diffusivity d are chosen according to [44] (except for d in case of material #1, that is taken from [51]), while the rest of the parameters are taken from the results in [23, 45]. Curve-fitting these parameters is performed in Matlab environment, where we apply unconstrained non-linear optimization (*fminsearch* function) in order to minimize the cost function that accounts for the errors between the measured frequency responses and the model predictions, both in sensing and actuation dynamics.

After the models for both the actuation and sensing dynamics are identified, we proceed with the experiments to characterize the performance of the closed-loop system.

2.6. Performance characterization

The performance is characterized in the following four types of experiments: step response, sinusoidal reference following at four different frequencies, random reference following at three different spectra, and finally long-duration sinusoidal reference following for testing of the stability.

The results are compared to determine the dependency of performance on material type and control scheme (particularly whether robust control is essential), and to investigate the differences between the IEAP sensor feedback performance against the laser distance sensor-based external feedback.

3. Experimental results

The material and system parameters were measured or curve-fitted as described in section 2.5 and the resulting parameters for all sample sets are summarized in table 1. The measured and fitted frequency responses for sensing and actuation dynamics are shown in figures 8 and 9 respectively.

Based on the actuator models, an H_∞ and a PI controller are designed, as described in section 2.3.3. Next, the step responses of the closed-loop systems are measured using the reference signal $u(t) = U(t - 0.5s)$ mm, where $U(\cdot)$ is the Heaviside step function. Each of the experiments' duration is 15 s. Tracking errors (i.e. difference between the reference and the actual position) measured by the laser distance sensor are shown in figure 10 and the step responses are characterized quantitatively (delay time t_d to reach 50% of the reference, rise time t_r from 10% to 90%, peak time t_p, percent overshoot PO and settling time t_s for 5% bound) in table 2.

The dry sample set (#1) exhibits strong high-frequency noise (up to 20% of the reference position) in the position estimation (caused by high gain in the high frequency range in the sensor's inverse model). Thus, before extracting the figures from the experimental results for this sample set in IEAP feedback configuration, we apply down-sampling by ten times.

Sample set #3 shows strong nonlinear behaviour both in sensing and actuation. Out of all used materials, it exhibits the strongest low-frequency drift in short-circuit sensing current, causing erroneous position estimation. Also, the actuator is unable to keep reference position for the duration of the experiment even in the laser feedback configuration (voltage remains in saturation after 5.627 s for PI/laser, 2.354 s for PI/

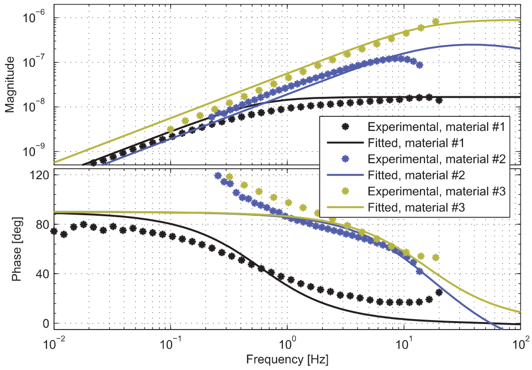

Figure 8. Measured and fitted frequency responses relating the short-circuit current of the IEAP sensor to the position of the tip of the rigid link. Measured frequency interval is varied to capture the phase transition in sensing dynamics.

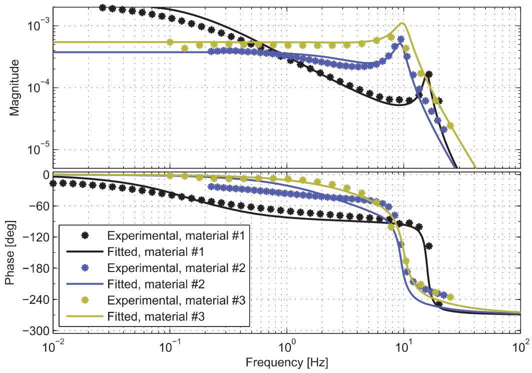

Figure 9. Measured and fitted frequency responses relating the position of the tip of the rigid link to the voltage applied to the IEAP actuators.

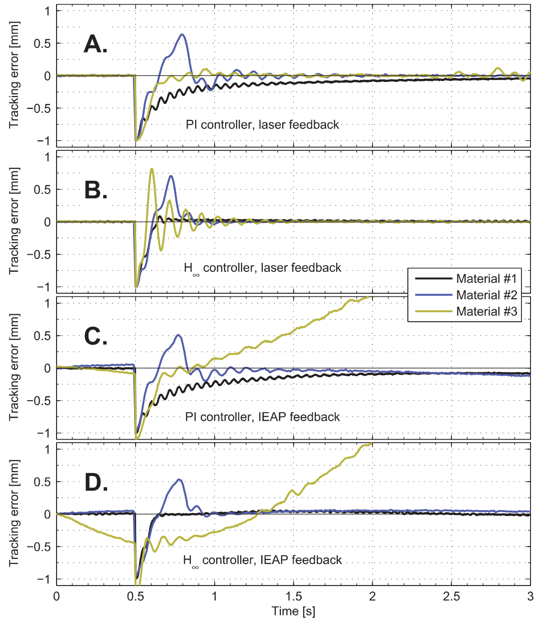

Figure 10. Tracking errors for the experimentally measured step responses. First 3 s of the experiments are shown.

IPMC, 11.291 s for H_∞/laser and 1.550 s for H_∞/IPMC feedback configurations). The control voltage reaches saturation at the 3.5 V limit, reference is not followed and eventually material bends backwards beyond its resting position. Experiment is halted to protect the actuators. In PI/laser configuration the sample set #3 fails to stabilize to 5% bound and its settling time is shown for 10% bound.

For comparison, the step responses of the identified actuation models in closed-loop configuration with the designed PI and H_∞ controllers are simulated using Matlab R2015b software. The results are shown in figure 11, and characterized in table 3.

Sinusoid tracking experiments are performed at four frequencies, i.e., 0.5, 1, 2, and 3 Hz. Each experiment duration is 30 s unless the control voltage saturates and it has to be aborted to prevent damaging the materials. One way to characterize these results is through the difference in the magnitude and phase between the reference and laser distance meter readings (at the reference signal frequency), and through the RMS error over the course of the experiment. These results are given in table 4. The magnitude and phase differences are extracted using Fourier transform while the RMS error is calculated in the time domain. The evolution of the RMS errors over each period during the experiments is shown in figure 12. The reference and the laser distance meter readings during the experiments over a single period are shown in figure 13 for illustrative purposes. The displayed period begins at 2 s after the start of the experiment.

In the random reference tracking experiments the same set of input signals is applied to all the sample sets. The signals are generated using sequences of random numbers passed trough a fourth-order Bessel bandpass filter (at 10 kHz sampling rate). Three frequency intervals are used, with lower frequency 0.1 Hz and the upper frequency of either 2, 3 or 4 Hz. The duration of the experiments is 30 s. The results for various configurations are characterized by the RMS tracking error over the whole experiment duration in table 5. Some experiments (marked in the table) are halted before they reached 30 s to prevent damaging the materials. As these numbers alone give too little details, we further plot the RMS error over each 0.5 s of the experiment in figure 14, and the first 2 s of the experiment course in figure 15.

The extended sine tracking experiments are conducted using only the H_∞ controller, first with IEAP feedback and then with the laser feedback. The reference signal is a 1 Hz sine wave with 1 mm amplitude that is applied for 30 min and 2 h for the IEAP and laser feedback, respectively, unless the

Table 2. Characterization of the experimentally measured step responses.

Feedback		#	$t_d(s)$	t_r (s)	$t_p(s)$	PO (%)	$t_s(s)$
PI	Laser	# 1	0.096	1.066	4.762[a]	1.52%	2.440
		# 2	0.060	0.120	0.290	63.4%	0.800
		# 3	0.087	0.132	0.221	12.4%	2.500[b]
	IEAP	# 1	0.144	1.164	—[a]	—	—
		# 2	0.060	0.120	0.270	51.1%	—
		# 3	0.114	0.127	0.280	216%	—[b]
H_∞	Laser	# 1	0.074	0.096	0.154	8.82%	0.212
		# 2	0.080	0.080	0.220	70.2%	0.350
		# 3	0.054	0.052	0.099	83.3%	0.768[b]
	IEAP	# 1	0.072	0.088	0.192	5.79%	0.781
		# 2	0.080	0.110	0.270	53.0%	0.914^2
		# 3	0.057	0.667	0.990	195%	—[b]

[a] Overdamped system.
[b] Following the reference failed before intended end.

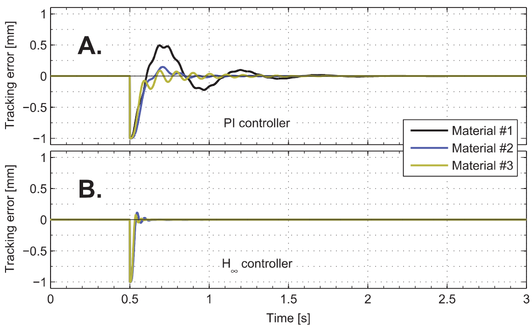

Figure 11. Tracking errors in the simulated step responses for the identified actuation models in closed-loop configuration with the respective (A) PI and (B) H_∞ controllers.

Table 3. Characterization of the simulated step responses for the identified actuation models in closed-loop configuration with the designed PI and H_∞ controllers.

Feedback	#	$t_d(s)$	$t_r(s)$	$t_p(s)$	PO(%)	$t_s(s)$
PI	# 1	0.053	0.074	0.188	49.4%	0.781
	# 2	0.070	0.073	0.201	14.7%	0.252
	# 3	0.054	0.055	0.190	8.74%	0.404
H_∞	# 1	0.023	0.021	0.045	3.07%	0.036
	# 2	0.026	0.019	0.047	11.5%	0.071
	# 3	0.021	0.016	0.037	7.59%	0.042

control voltage saturates for an entire reference signal period. The results are characterized by the RMS error over each reference signal period shown in figure 16. In table 6 the duration of each experiment is given. For sample set #2 in laser feedback configuration the experiment is halted due to external disturbance. During these experiments we also measure the actuation current and calculate the period-averaged power consumption that is given in figure 17.

4. Discussion

A prototype of the IEAP sensor–actuator utilizing the same type of materials for sensing and actuation within the same device is built and characterized in this work.

When designing the experiments we intended to obtain consistent fits between the sensing and actuation dynamics in terms of parameters describing the material properties. Naturally, the charge–stress coupling constant α_0 remains different as it results from distinct processes in sensing and actuation context. The only parameter that does not match is the dielectric permittivity κ_e while the rest are the same for sensing and actuation dynamics. We speculate that there exist unidentified processes in sensing and/or actuation mechanisms of the CPCs and IPMCs that have not been accounted for.

While comparing the experimentally measured frequency responses to the identified models in figures 8 and 9, the discrepancies clearly indicate that both for actuation and sensing there exist some unmodeled dynamics. This does not disturb remarkably the control design and feedback experiments, and in fact, is completely expected, considering the relatively complex derivation process of the physics-based control-oriented models in [23, 45]. Feedback configuration well compensates for the inaccuracies in the actuation model while the discrepancies in the sensing model cause small systematic errors both in phase and magnitude in the IEAP feedback experiments. One possibility to improve the modelling accuracy is to further extend the modelling scope of the used physics-based models. Another, less laborious alternative is replacing the physics-based models with some 'grey-box' or 'black-box' models. In this work we avoided this approach as it gives only little or no information about the IEAP fundamental physical parameters.

The resulting sensors' unrealistic dielectric permittivities (under realistic constraints fitting does not converge) seem to suggest that it is not correct to presume that the entire thickness of the IEAP behaves as a dielectric medium. Thus, the resulting dielectric permittivities actually describe effective parameters of a parallel-plate capacitor with the

Table 4. Characterization of the experimental results of the closed-loop sinusoidal reference tracking.

	Control configuration	PI						H_∞					
		Laser			IEAP			Laser			IEAP		
	Material #	# 1	# 2	# 3	# 1	# 2	# 3	# 1	# 2	# 3	# 1	# 2	# 3
0.5 Hz	Amplitude (% of ref)	74.8	105	102	66.9	94.9	200	98.5	103	100	89.5	90.5	112
	Phase wrt ref (deg)	−22.8	−1.90	−13.6	−23.1	−0.986	−75.2	−3.75	−1.46	−2.94	−6.29	−0.881	−10.4
	RMS error (%)	30.5	4.64	15.4	35.3	106	380	4.87	2.94	4.51	29.3	99.3	143
1 Hz	Amplitude (% of ref)	64.5	113	101	58.7	106	22.7	98.0	108	101	89.9	103	72.8
	Phase wrt ref (deg)	−35.6	−4.70	−22.2	−33.5	−3.48	−92.0	−6.20	−4.45	−7.13	−8.07	−3.92	−3.89
	RMS error (%)	42.7	12.3	26.9	43.9	15.3	226	7.71	8.57	8.81	84.7	39.9	212
2 Hz	Amplitude (% of ref)	49.3	166	80.6	48.6	124	80.0	99.4	115	98.9	83.9	114	108
	Phase wrt ref (deg)	−51.2	−105	−47.8	−51.8	−84.7	−35.8	−10.7	−12.3	−13.2	−13.4	−14.9	−33.8
	RMS error (%)	55.4	155	52.8	95.9	211	112	13.5	19.6	18.3	226	59.8	59.8
3 Hz	Amplitude (% of ref)	37.8	125	61.9	36.4	121	66.6	87.4	117	97.4	67.3	112	64.0
	Phase wrt ref (deg)	−58.3	−120	−65.9	−57.0	−110	−88.7	−14.1	−27.6	−24.6	−33.1	−45.8	−76.6
	RMS error (%)	61.5	141	66.2	134	136	162	26.6	41.1	30.4	386	67.3	191

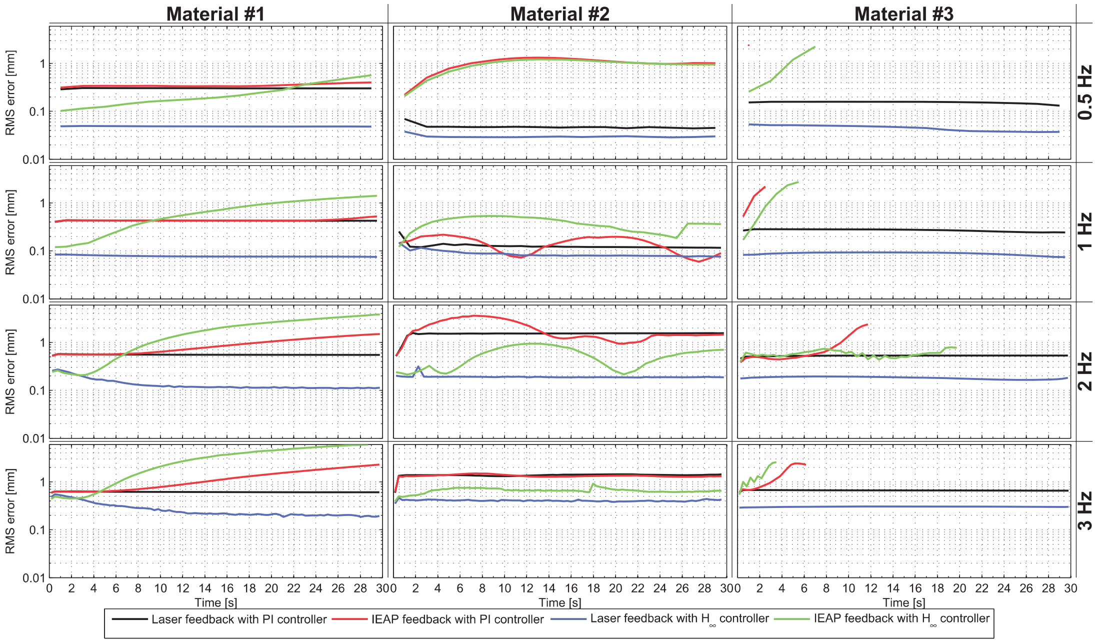

Figure 12. RMS errors in experimentally measured sinusoidal reference tracking. Calculated over each period of the sinusoidal reference signal.

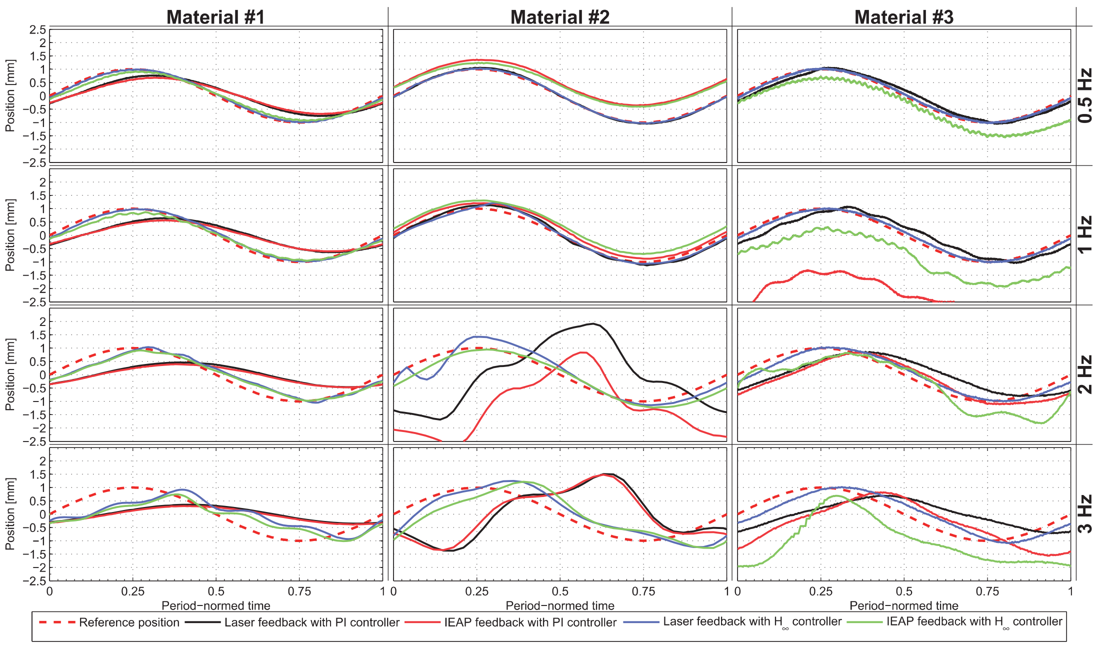

Figure 13. Reference signals and experimentally measured positions in sinusoidal reference tracking experiments. Single period is plotted for each experiment, starting at 2 s from the beginning of the experiment.

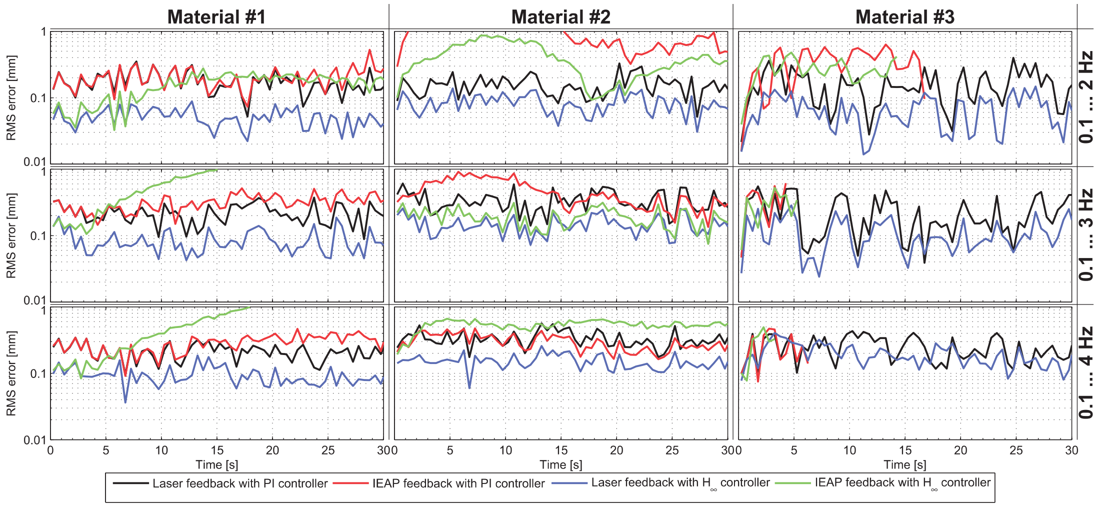

Figure 14. RMS error in random reference following experiments. Calculated over each 0.5 s interval.

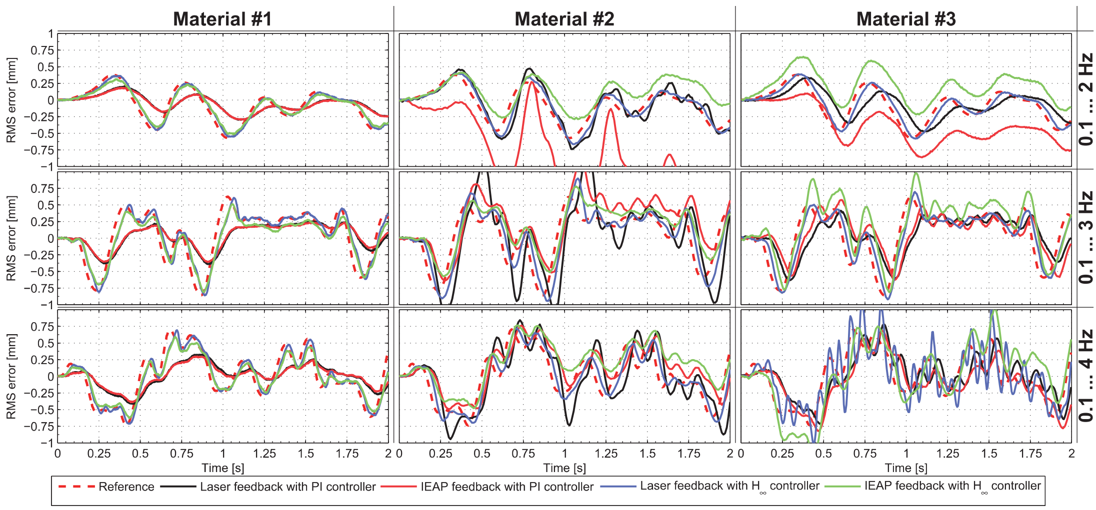

Figure 15. Reference signal and measured position in the random reference following experiments. First 2 s of the experiments are plotted.

Table 5. RMS errors (mm) in random reference following experiments.

Control config.	PI						H_∞					
	Laser			IEAP			Laser			IEAP		
Material #	# 1	# 2	# 3	# 1	# 2	# 3	# 1	# 2	# 3	# 1	# 2	# 3
0.1–2 Hz interval	0.190	0.167	0.189	0.219	1.32	0.637[1]	0.0541	0.0884	0.0793	0.170	0.470	1.08[2]
0.1–3 Hz interval	0.233	0.363	0.257	0.327	0.507	1.06[3]	0.0930	0.156	0.127	1.19	0.201	1.78[4]
0.1–4 Hz interval	0.223	0.348	0.251	0.297	0.309	1.90[5]	0.0986	0.156	0.165	0.989	0.543	1.46[6]

Note: Marked experiments were aborted at [1]17.0*s*, [2] 14.7*s*, [3]4.56*s*, [4]5.82*s*, [5]6.88*s* and [6]3.90*s* to prevent harming materials with saturated driving voltage.

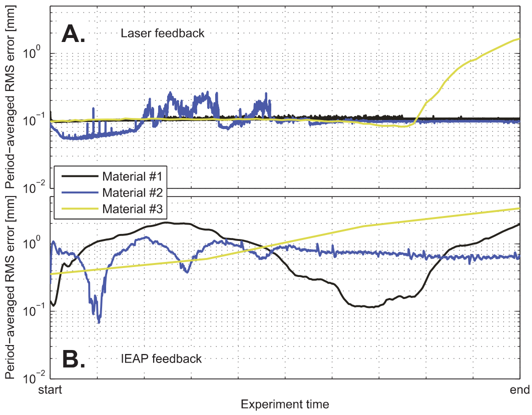

Figure 16. RMS error over each period in the long-term sinusoidal reference following. (A) Laser feedback; (B) IEAP feedback. Time is normalized to the experiments' durations for plotting purposes. Durations are given in table 6.

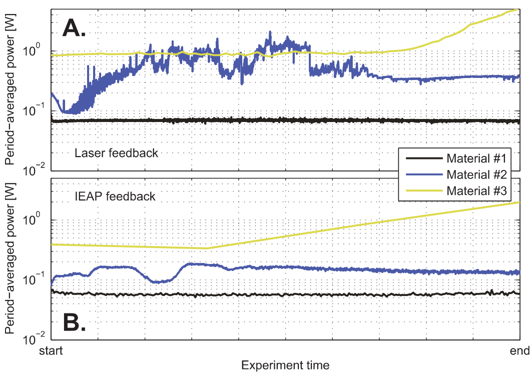

Figure 17. Power consumption of the IEAP actuators in long-term sinusoidal reference following experiments. (A) shows the results for laser feedback, (B) for IEAP feedback. Time is normalized to the experiments' durations for plotting purposes. Durations are shown in table 6.

dimensions of the IEAP. In fact, the effective thickness of a parallel-plate capacitor with the surface area of the IEAP has later been shown to be (approximately) equal to the depth of the counter-ion boundary layers near the IEAP electrodes (see [52]). Despite the described inaccuracies, the models in hand are the best set of control-oriented physics-based models available at the time and they well approximate the measured frequency responses of the sensing and actuation dynamics.

Comparing the closed-loop step response simulation predictions (figure 11 and table 3) to the experimental results (figure 10 and table 2) shows that the actual performance of the sensor–actuator device is inferior to the predictions. Resulting settling times and other figures are in experimental results multiple times larger (except the overshoot for the material #1 in laser feedback configuration with PI controller). That is because our simulation results characterize best scenario performances, i.e. when voltage saturation, external disturbances, model perturbations, noises of various origins, etc are not present. Properly addressing these processes is very laborious.

Examining the results reported in tables 2–6 and figures 10–16 allows to compare the IEAP feedback performance material-wise, controller-wise, and against external feedback. The main limiting factor in IEAP feedback concept appears to be the low-frequency drifting in the sensors' short-circuit current, that varies material-wise in magnitude, and respectively in impact on the performance. Its potential causes include interactions between the amplifier and the material, environmental influences, potential material degradation (see [53]) and internal dynamics effects, and needs further investigation.

Performance in closed-loop experiments with IEAP sensing remained inferior to the laser distance meter feedback due to the aforementioned low-frequency sensing noise. It degrades the system's long-term performance while in the short run (few seconds) they do not differ significantly (see figures 10, 12 and 14).

It is also seen in the experiments (see tables 2, 4 and 5) that the H_∞ controller performs better and should be preferred over the PI controller (including the step response which the PI is tuned for). This suggests that the complexity of the IEAP actuation dynamics can be compensated with proper model-based control, either using the physics-based 'white box' models that we use in this work, or some less complex 'grey-box' or 'black-box' models, e.g. fully empirical models used in our previous work [39].

While sample sets #1 and #2 perform similarly in all experiments, the set #3 performs much worse than the others. Its actuator's 'zero' position changes even under sinusoidal reference following (see laser feedback duration experiment in figure 16), eventually saturating the input voltage and failing to follow the reference. Also, its position sensing is very noisy, causing most of the experiments to be aborted soon after they begin. It is not clear what processes cause or dominate these unwanted effects. In terms of actuation, the shorter operational length of the sample set #3 does not seem to influence the actuation magnitude remarkably (see figure 9). Instead, we speculate that the nonlinear actuation behaviour is caused by the significantly higher material stiffness (table 1). According to [54], when the pressure within the cathode boundary layer clusters within the polymer backbone increases (stronger effect in stiffer materials), the additional cations near the cathode start extensive restructuring and redistribution, that is responsible for back-relaxation, and possibly also for our observations. In terms of sensing, sample set #3 has significantly larger charge–stress coupling constant than the other materials, and it exhibits stronger short-circuit current (see table 1 and figure 8), that the sensing model in chapter 2.3.1 also explains with higher Young's modulus. We hypothesize that mechanical stress in IEAPs drives some additional nonlinear ion and solvent dynamics that is responsible for the low-frequency sensing noise, and thus the noise is stronger in materials with higher Young's modulus.

Table 6. Experiment durations for long-term sinusoidal reference following.

Feedback		Laser			IPMC	
Material	#1	#2	#3	#1	#2	#3
Duration	7200 s	4513.3 s	76.82 s	300 s	1800 s	4.295 s

In long-term actuation experiments with IEAP feedback the sensing signal of the sample set #1 is less stable than in case of the set #2 (figure 16). This experiment is halted at 300 s to avoid damage to the actuators while the material #2 runs the entire 30 min experiment. Comparing to the longest IEAP feedback control experiments reported so far (20 s, [38]), it is 15 and 90 times longer respectively. In other experiments the drifting in the sensors' short-circuit sensing current varies material-wise, but between materials #1 and #2 clear superiority cannot be seen.

The actuation performances of these materials are also similar, but cannot be directly compared due to the difference in the environments. The external influences acting on the sample set #1 in the air are insignificant, while the set #2 in the water experiences also the added mass effects in addition to greater damping. In the long-term laser feedback experiments both materials work reliably for the entire experiment durations, i.e., over 1 h. The higher power consumption of the sample set #2 can be explained with the damping effects (figure 17), but the causes of its fluctuations are unclear (potentially a poor actuator contact). Among these two IEAPs (#1 and #2), it is primarily the working environment that should dictate which one to prefer.

In the feedback experiments our IEAP sensor–actuator performed well over 7500 and 4900 cycles with material #1 and #2 respectively, without noticeable signs of performance degradation. Thus, considering the typical properties and degradation [53] of the IEAP materials and feedback results presented in previous studies (see section 1), the proposed design is shown to work very well. The factors that could limit its applications are primarily associated with the material properties. Actuation-wise, larger achievable deformations could be desirable, and sensing-wise, the reason for low-frequency sensing noise should be identified and suppressed. The large amount of experiments conducted in this paper well address the strengths and weaknesses of the IEAPs and hopefully will aid in material selection for applications.

5. Conclusions

In this work we propose and test an IEAP sensor–actuator device with integrated actuation and sensing capability. The proposed pivot-like design allows to combine the benefits of both the 'smart' IEAP materials and the matured tools of conventional robotics. We describe the design concept and the prototype, introduce the physics-based control-oriented models of sensing and actuation dynamics, their identification procedures, the experiment courses and the performance evaluation metrics. Closed-loop experiments with the IEAP sensor–actuator prototype are performed, and the results are presented for three different IEAP materials, two controllers and two feedback sources.

The proposed design is proven to work well considering the rather nonlinear and unstable properties of the IEAP materials. The H_∞ control is shown to offer significant improvements over PI controller. Thus identifying the system using physics-based models as in this work, or with some less involved black- or grey-box models and designing a model-based controller is recommended. Position feedback from the laser distance meter expectedly results in more stable performance while the low-frequency noise in the sensors' short-circuit current limits the timespan of reliable position feedback from the IEAP sensing scheme. The cause of this noise is unknown and we intend to further investigate it in our future work.

Sample sets #1 and #2 perform similarly and a particular material should be preferred depending on the work environment (air or water, respectively). The different environment is also the reason why these materials cannot be compared in more detail. Sample set #3 performs significantly worse than the others, exhibiting strong nonlinear relation between input voltage and output position for the actuators and very strong low-frequency noise in short-circuit current for the sensor.

In feedback experiments the sample sets #1 and #2 performed in total well over 7500 and 4900 sinusoidal cycles respectively, material #3 was able to perform less than 450 cycles. In laser distance meter feedback configuration we did not see signs of performance degradation even at the end of 2 h long experiment, and in IEAP sensor feedback configuration we were able to conduct 30 min long sinusoidal reference following without saturating the actuation voltage. In IEAP feedback configuration this is 90 times longer experiment than achieved in previous reports.

With all the presented results the proposed sensor–actuator realization is thoroughly characterized, making it also a good basis for choosing the control and feedback scheme, and the materials to work with in the applications for those not familiar with the IEAP materials.

Acknowledgments

Authors thank Andres Punning and Urmas Johanson (IMS Lab, University of Tartu) for providing materials and their constructive support during this work. This work was supported by US CRDF Grant No. 16059 and Estonian Research Council Projects SF0140018s12 and IUT33-9.

References

[1] Bar-Cohen Y 2004 Turning heads *IEEE Spectr.* **41** 28–33

[2] Shahinpoor M and Kwang J K 2001 Ionic polymer-metal composites: I. Fundamentals *Smart Mater. Struct.* **10** 819–33

[3] Palmre V, Brandell D, Mäeorg U, Torop J, Volobujeva O, Punning A, Johanson U, Kruusmaa M and Aabloo A 2009 Nanoporous carbon-based electrodes for high strain ionomeric bending actuators *Smart Mater. Struct.* **18** 095028

[4] Oguro K, Kawami Y and Takenaka H 1992 Bending of an ion-conducting polymer film-electrode composite by an electric stimulus at low voltage *J. Micromachine Soc.* **5** 27–30

[5] Palmre V, Brandell D, Mäeorg U, Torop J, Volobujeva O, Punning A, Johanson U and Aabloo A 2010 Ionic polymer metal composites with nanoporous carbon electrodes *Proc. SPIE* **7642** 76421D

[6] Shahinpoor M 1994 Continuum electromechanics of ionic polymeric gels as artificial muscles for robotic applications *Smart Mater. Struct.* **3** 367

[7] Guo S, Fukuda T and Asaka K 2003 A new type of fish-like underwater microrobot *IEEE/ASME Trans. Mechatronics* **8** 136–41

[8] Chen Z, Shatara S and Tan X 2010 Modeling of biomimetic robotic fish propelled by an ionic polymer-metal composite caudal fin *IEEE/ASME Trans. Mechatronics* **15** 448–59

[9] Punning A, Anton M, Kruusmaa M and Aabloo A 2004 A biologically inspired ray-like underwater robot with electroactive polymer pectoral fins *IEEE International Conference on Mechatronics and Robotics* **2004** 241–5

[10] Keshavarzi A, Shahinpoor M, Kwang J K and Lantz J 1999 Blood pressure, pulse rate, and rhythm measurement using ionic polymer-metal composite sensors *Proc. SPIE* **3669** 369–76

[11] Chen Z, Shen Y, Xi N and Tan X 2007 Integrated sensing for ionic polymer-metal composite actuators using PVDF thin films *Smart Mater. Struct.* **16** S262–71

[12] Kruusmaa M, Hunt A, Punning A, Anton M and Aabloo A 2008 A linked manipulator with ion-polymer metal composite (IPMC) joints for soft- and micromanipulation *IEEE Int. Conf. on Robotics and Automation* (Piscataway, NJ: IEEE) pp 3588–3593

[13] Ando B, Baglio S, Beninato A, Graziani S, Pagano F and Umana E 2012 A seismic sensor based on IPMC combined with ferrofluids *IEEE International Conference on Instrumentation and Measurement Technology (I2MTC)* pp 1829–32

[14] Abdulsadda A T and Tan X 2013 Nonlinear estimation-based dipole source localization for artificial lateral line systems *Bioinspiration Biomimetics* **8** 026005

[15] Shahinpoor M 2003 Ionic polymer-conductor composites as biomimetic sensors, robotic actuators and artificial muscles—a review *Electrochim. Acta* **48** 2343–53

[16] Pugal D, Jung K, Aabloo A and Kim K J 2010 Ionic polymer-metal composite mechanoelectrical transduction: review and perspectives *Polym. Int.* **59** 279–89

[17] Bhandari B, Lee G Y and Ahn S H 2012 A review on IPMC material as actuators and sensors: fabrications, characteristics and applications *Int. J. Precis. Eng. Manuf.* **13** 141–63

[18] Punning A, Kruusmaa M and Aabloo A 2007 A self-sensing ion conducting polymer metal composite (IPMC) actuator *Sensor Actuators* A **136** 656–64

[19] Kruusamäe K, Brunetto P, Punning A, Kodu M, Jaaniso R, Graziani S, Fortuna L and Aabloo A 2011 Electromechanical model for a self-sensing ionic polymer metal composite actuating device with patterned surface electrodes *Smart Mater. Struct.* **20** 124001

[20] Anton M, Kruusmaa M, Aabloo A and Punning A 2006 Validating usability of ionomeric polymer-metal composite actuators for real world applications *2006 IEEE/RSJ Int. Conf. on Intelligent Robots and Systems* (Piscataway, NJ: IEEE) pp 5441–5446

[21] Hunt A, Chen Z, Tan X and Kruusmaa M 2010 Control of an inverted pendulum using an ionic polymer-metal composite actuator *2010 IEEE/ASME Int. Conf. on Advanced Intelligent Mechatronics* (Piscataway, NJ: IEEE) pp 163–168

[22] Bhat N D 2004 Modeling and precision control of ionic polymer metal composite *Master's Thesis* Texas A&M University

[23] Chen Z and Tan X 2008 A control-oriented and physics-based model for ionic polymer-metal composite actuators *IEEE/ASME Trans. Mechatronics* **13** 519–29

[24] Mallavarapu K, Newbury K M and Leo D J 2001 Feedback control of the bending response of ionic polymer-metal composite actuators *SPIE's 8th Annual Int. Symp. on Smart Structures and Materials* vol 4329 pp 301–310

[25] Xing H L, Jeon J H, Park K C and Oh I K 2013 Active disturbance rejection control for precise position tracking of ionic polymer-metal composite actuators *IEEE/ASME Trans. Mechatronics* **18** 86–95

[26] Thinh N T, Yang Y-S and Oh I-K 2009 Adaptive neuro-fuzzy control of ionic polymer metal composite actuators *Smart Mater. Struct.* **18** 065016

[27] Chen Z, Kwon K-Y and Tan X 2008 Integrated IPMC/PVDF sensory actuator and its validation in feedback control *Sensors Actuators* A **144** 231–41

[28] Leang K K, Shan Y, Song S and Kim K J 2012 Integrated sensing for IPMC actuators using strain gages for underwater applications *IEEE/ASME Trans. Mechatronics* **17** 345–55

[29] Richardson R C, Levesley M C, Brown M D, Hawkes J A, Watterson K and Walker P G 2003 Control of ionic polymer metal composites *IEEE/ASME Trans. Mechatronics* **8** 245–53

[30] Kaneda Y, Kamamichi N, Yamakita M, Asaka K and Luo Z 2003 Control of linear artificial muscle actuator using IPMC *SICE 2003 Annual Conf.* vol 2 pp 1650–1655

[31] Kang S, Shin J, Kim S J, Kim H J and Kim Y H 2007 Robust control of ionic polymer-metal composites *Smart Mater. Struct.* **16** 2457–63

[32] Fang B-K, Ju M-S and Lin C-C K 2007 A new approach to develop ionic polymer-metal composites (IPMC) actuator: fabrication and control for active catheter systems *Sensors Actuators* A **137** 321–9

[33] Hao L, Sun Z, Li Z, Su Y and Gao J 2012 A novel adaptive force control method for IPMC manipulation *Smart Mater. Struct.* **21** 075016

[34] Lee G-Y, Choi J-O, Kim M and Ahn S-H 2011 Fabrication and reliable implementation of an ionic polymer-metal composite (IPMC) biaxial bending actuator *Smart Mater. Struct.* **20** 105026

[35] Newbury K M 2002 Characterization, modeling and control of ionic polymer transducers *PhD Thesis* Virginia Polytechnic Institute and State University

[36] Bonomo C, Fortuna L, Giannone P and Graziani S 2004 A sensor–actuator integrated system based on IPMCs *Sensors 2004. Proc. IEEE* (Piscataway, NJ: IEEE) pp 489–492

[37] Yamakita M, Sera A, Kamamichi N, Asaka K and Luo Z-W 2006 Integrated design of IPMC actuator/sensor *Proc. 2006 IEEE Int. Conf. on Robotics and Automation* (Piscataway, NJ: IEEE) pp 1834–1839

[38] Gonzalez C and Lumia R 2015 An IPMC microgripper with integrated actuator and sensing for constant finger-tip displacement *Smart Mater. Struct.* **24** 055011
[39] Hunt A, Chen Z, Tan X and Kruusmaa M 2009 Feedback control of a coupled IPMC (ionic polymer-metal composite) sensor–actuator *ASME 2009 Dynamic Systems and Control Conf.* pp 485–491
[40] Anton M, Aabloo A, Punning A and Kruusmaa M 2008 A mechanical model of a non-uniform ionomeric polymer metal composite actuator *Smart Mater. Struct.* **17** 025004
[41] Sadeghipour K, Salomon R and Neogi S 1992 Development of a novel electrochemically active membrane and 'smart' material based vibration sensor/damper *Smart Mater. Struct.* **1** 172–9
[42] Shahinpoor M and New A 1995 A new effect in ionic polymeric gels: the ionic flexofelectric effect *Smart Structures & Materials '95* (San Diego, CA) vol 2441 pp 42–53
[43] Konyo M, Konishi Y, Tadokoro S and Kishima T 2004 Development of velocity sensor using ionic polymer-metal composites *Proc. SPIE* **5385** pp 307–318 SPIE
[44] Farinholt K and Leo D J 2004 Modeling of electromechanical charge sensing in ionic polymer transducers *Mech. Mater.* **36** 421–33
[45] Chen Z, Tan X, Will A and Ziel C 2007 A dynamic model for ionic polymer-metal composite sensors *Smart Mater. Struct.* **16** 1477–88
[46] Bonomo C, Fortuna L, Giannone P, Graziani S and Strazzeri S 2006 A model for ionic polymer metal composites as sensors *Smart Mater. Struct.* **15** 749–58
[47] Shahinpoor M and Kim K J 2004 Ionic polymer-metal composites: III. Modeling and simulation as biomimetic sensors, actuators, transducers, and artificial muscles *Smart Mater. Struct.* **13** 1362–88
[48] Zhou K and Doyle J C 1998 *Essentials of Robust Control* (*Prentice Hall Modular Series for Eng*) (Englewood Cliffs, NJ: Prentice-Hall)
[49] Bibel J E and Malyevac D S 1992 *Guidelines for the Selection of Weighting Functions for H-Infinity Control* (Dahlgren, VA: Dahlgren Division of the Naval Surface Warfare Center)
[50] Timoshenko S 1940 *Strength of Materials: I. Elementary Theory and Problems* 2nd edn (New York: D. Van Nostrand Company, Inc.) pp 147–153 ch 35
[51] Li J, Wilmsmeyer K G, Hou J and Madsen L A 2009 The role of water in transport of ionic liquids in polymeric artificial muscle actuators *Soft Matter* **5** 2596–602
[52] Porfiri M 2009 An electromechanical model for sensing and actuation of ionic polymer metal composites *Smart Mater. Struct.* **18** 015016
[53] Punning A *et al* 2014 Lifetime measurements of ionic electroactive polymer actuators *J. Intell. Mater. Syst. Struct.* **25** 2267–75
[54] Nemat-Nasser S and Zamani S 2006 Modeling of electrochemomechanical response of ionic polymer-metal composites with various solvents *J. Appl. Phys.* **100** 064310

APPENDIX D

Hunt, A., Ristolainen, A., Ross, P., Öpik, R., Krumme, A., and Kruusmaa, M. (2013). Low cost anatomically realistic renal biopsy phantoms for interventional radiology trainees. European Journal of Radiology, 82(4), pp. 594–600.

European Journal of Radiology 82 (2013) 594–600

Contents lists available at SciVerse ScienceDirect

European Journal of Radiology

journal homepage: www.elsevier.com/locate/ejrad

Low cost anatomically realistic renal biopsy phantoms for interventional radiology trainees

Andres Hunt [a,*], Asko Ristolainen [a,1], Peeter Ross [c,d,2], Rivo Öpik [a,3], Andres Krumme [b,4], Maarja Kruusmaa [a,5]

[a] Centre for Biorobotics, Faculty of Information Technology, Tallinn University of Technology, Akadeemia tee 15A-111, 12618 Tallinn, Estonia[6]
[b] Department of Polymer Materials, Faculty of Chemical and Materials Technology, Tallinn University of Technology, Ehitajate tee 4A, 19086 Tallinn, Estonia[7]
[c] Clinic of Diagnostic, Center of Radiology, East Tallinn Central Hospital, Ravi 18, 10138 Tallinn, Estonia[8]
[d] Institute of Clinical Medicine, Technomedicum, Tallinn University of Technology, Akadeemia tee 15A, 12618 Tallinn, Estonia

ARTICLE INFO

Article history:
Received 23 May 2012
Received in revised form 8 December 2012
Accepted 10 December 2012

Keywords:
Phantom
Ultrasound
Biopsy
Patient-specific
Anatomy
Training

ABSTRACT

This paper describes manufacturing of economically affordable renal biopsy phantoms for radiology residents and practicing radiologists. We reconstructed a realistic 3-dimensional patient-specific kidney model from CT data, manufactured an organ mould and casted the kidney phantoms. Using gelatin gel materials with calibrated parameters allowed making phantoms with realistic mechanical, ultrasound and CT properties including various pathologies. The organ phantoms with cysts included were further casted into gelatin gel medium. They were validated by radiology residents in biopsy training and compared against self-made phantoms traditionally used in the curriculum of interventional radiology. The realism, durability, price and suitability for training were evaluated. The results showed that our phantoms are more realistic and easier to use than the traditional ones. Our proposed technology allows creating a low-cost (50 $/kg) alternative to the pricy commercial training phantoms available today.

1. Introduction

Minimally invasive (MI) methods of treatment, including interventional radiology, are becoming more preferable in medicine because of lower risk of infection, reduced hospital stay, reduced patient stress and discomfort and lower total treatment cost [1]. In the field of radiology, this approach is increasingly common both in diagnostics and treatment. Rapidly advancing methods and equipment for the procedures used in interventional radiology cause frequent introduction of new products requiring fast adapting from doctors. Practising is important for maintaining and improving the skills [2], it yields in faster performance, reduces the number of missed lesions [2], significantly reduces operating room time [3] and improves the success rate in biopsy [4]. The studies show that even experienced radiologists start over with the learning curve when changes are made in equipment [4] whereas practising on phantoms has been shown useful in training and skill development [5]. For ethical, clinical quality and safety reasons the doctors need to become familiar with the properties of new equipment or procedures prior to applying them on patients. This is why the phantoms that realistically mimic anatomy and tissue properties are useful not only for the residents in their training, but also for practising radiologists in their every-day work.

For interventional procedures (e.g. biopsy, drainage, etc.) in radiology and other fields the high pricing of the abdominal training phantoms and biopsy phantom organs may result in dismissal of practising a new procedure or lack of training on phantoms that realistically represents anatomy, mechanical and ultrasound properties of human tissue. There are several providers of models and practicing equipment for educational purposes in medicine; however the variety of training phantoms is small. A (potentially not exhaustive) list of abdominal phantoms and separate kidney phantoms suitable for training of minimally invasive renal interventions using ultrasound (US) imaging is given in Table 1. These relatively expensive phantoms have many imperfections in anatomy, can

* Corresponding author. Tel.: +372 5196 1764.
E-mail addresses: Andres.Hunt@ttu.ee (A. Hunt), Asko.Ristolainen@ttu.ee (A. Ristolainen), Peeter.Ross@itk.ee (P. Ross), Rivo.Opik@ttu.ee (R. Öpik), Andres.Krumme@ttu.ee (A. Krumme), Maarja.Kruusmaa@ttu.ee (M. Kruusmaa).
1 Tel.: +372 526 8094.
2 Tel.: +372 620 4460.
3 Tel.: +372 5566 4739.
4 Tel.: +372 620 2907.
5 Tel.: +372 518 3074.
6 URL: http://www.biorobotics.ttu.ee/tikiwiki_eng/tiki-index.php.
7 URL: http://www.kk.ttu.ee/km/in_english.html.
8 URL: http://itk.ee/kliinikud/diagnostikakliinik.

0720-048X/$ – see front matter © 2013 Elsevier Ireland Ltd. All rights reserved.
http://dx.doi.org/10.1016/j.ejrad.2012.12.020

Table 1
A list of commercially available phantoms suitable for renal biopsy training.

Company	Phantom product description	Price[a]
CIRS	Abdominal phantom model 057 with partial kidneys, suitable for biopsy training.	$2363.00
	Kidney training phantom, simulates resistance to needle insertion, no internal structure.	$375.25
Kyoto Kagaku	Abdominal intraoperative and laparoscopic phantom IOUSFAN, organs in water bath. Suitability for biopsy unclear.	$4940.00
	Ultrasound examination training model ABDFAN. Suitability for biopsy unclear.	$9500.00
Blue Phantom	Renal biopsy training model; representing renal cortex, medulla, major and minor calyx.	$3499.00
	Replacement kidneys for renal biopsy phantom. Represents cortex, medulla; major and minor calyx. Sold in a pair.	$399.00

[a] As marked on manufacturer or retailer websites on 3 May 2012.

stand a limited amount of work cycles and rarely represent pathologies.

There are many phantom materials available for mimicking soft human tissues. They can be classified as hydrogels, organogels and flexible elastomer materials. Gelatin gels are simple to manufacture and have easily controllable US and mechanical properties [6,7]. More non-linear and wider range of elasticity can be achieved by combining gelatin with oil resulting oil-in-gelatin dispersions [8]. The Young's modulus of the gelatin gels can be varied from 2.5 kPa to 500 kPa [7], their US broadband attenuations are 0.2–1.5 dB/(cm MHz) and the US propagation speed of 1550–1650 m/s has been reported [6]. Similarly to human tissue, gelatin has linear attenuation increase with respect to the ultrasound frequency [6]. The drawbacks of the gelatin gels include susceptibility to bacteria (can be overcome with additives, e.g. thimerosal, p-methyl benzoic acid, p-propyl benzoic acid, etc.) and the long settling time of the mechanical properties (up to 100 days from manufacturing) [7]. Agar gels are similar to gelatin both in terms of properties and the manufacturing process, but offer higher non-linearity of elasticity and have a naturally higher melting temperature [7,9]. The US propagation speed is close to 1540 m/s and the broadband US attenuation of 0.1–0.7 dB/(cm MHz) has been reported [9].

Chemical gels have both advantages and disadvantages in comparison with the described physical gels (agar, gelatin). The elasticity and echographic properties of the polyacrylamide gels are finely adjustable, very stable [10] and these materials are not a suitable environment for bacteria because of several very toxic ingredients (acrylamide, etc.). The manufacturing process and properties are well described [10], the naturally low US broadband attenuation can be risen with additives. Polyurethane tissue substitutes are also stable and permit achieving a very low Young's modulus. A recently reported US compatible swollen segmented polyurethane gel (S-SPUG) [11] exhibits good long-term stability and appears to also have desired mechanical properties. However, as it is typical for polyurethane gels, very little details are reported on the manufacturing process. Other phantom materials include (1) oil gels, e.g. propylene glycol with gelatinizer that reportedly have stable properties; (2) open cell foams that can be filled with various mediums such as gelatin [12]; (3) PVAs (polyvinyl alcohol) that require long freeze–thaw cycles to influence the cross-linking; however they are economically affordable and need only few ingredients [13]; (4) silicon-based rubbers that have unsuitable mechanical characteristics, too low US propagation speed and too high attenuation [14]; etc. More thorough overview of the phantom material technologies can be found in Ref. [15].

This work describes material manufacturing and calibration processes using gelatin gels and development of renal biopsy phantoms with (1) realistic, potentially patient-specific anatomy; (2) realistic mechanical, ultrasound and computed tomography (CT) properties; (3) pathologies (cysts or tumours) with desired shapes, sizes and locations; and (4) affordable price. We test our phantoms in renal biopsy training where the radiology residents evaluate the results of our work after a hands-on workshop.

2. Materials and methods

2.1. Properties of human kidneys

To build renal biopsy phantoms with realistic human tissue properties, the respective figures (US propagation speed, broadband US attenuation, Young's modulus and radiodensity) were obtained from the literature and used as guidelines in phantom development. General requirements for the soft tissue substitutes can be found in ICRU (International Commission on Radiation Units & Measurements) and AIUM (American Institute of Ultrasound Medicine) reports that specify the US broadband attenuation of 0.3–0.7 dB/(cm MHz) and the US propagation speed of 1540 ± 15 m/s [16]. US broadband attenuation of a human kidney varies from 0.533 to 0.8 dB/(cm MHz) with mean value of 0.73 dB/(cm MHz) measured in the interval of 1.5–3.5 MHz [17]. The US propagation speed has been reported to vary from 1540 m/s to 1570 m/s [18] and these numbers also overlap with the respective figures for horses, pigs and dogs [17]. The tissue elasticity has been reported to behave very non-linearly and the measured Young's modulus highly depends on the extent of the applied strain. In Ref. [19], shear wave elastography was used to measure the elasticity of human kidneys and the patients also underwent a biopsy to validate the results. The elasticity of the kidney's cortex and the medulla were reported respectively 10.7 ± 2.1 kPa and 5.1 ± 2.5 kPa for healthy kidneys while the diseased kidneys were stiffer with respective figures of 32.7 ± 2.4 kPa and 23.1 ± 5.6 kPa. From the results it was concluded that the stiffness of the human kidney varies from 5 to 50 kPa. The radiodensity of the human kidney varies between 30 HU (Hounsfield units) and 50 HU [20] and was stoichiometrically calculated to be 43 HU.

2.2. Manufacturing and calibration of gelatin gel

We used gelatin gels (foodstuff derived from the collagen in animal bones and skin) as the tissue-mimicking material as they are self-supportive solids with a proper range of achievable elasticity, US characteristics and a relatively simple manufacturing process. The gel typically consists of (1) food gelatin and distilled water forming the material's backbone; (2) formaldehyde that rises the gel's melting temperature (desirable) and makes the gel stiffer (usually undesirable) by inducing cross-linking; (3) alcohol to increase the sound propagation speed of the medium (typically n-propanol for lower vapor pressure); (4) graphite flakes and glass-beads to increase the ultrasound attenuation and backscatter; and (5) various substances to prevent bacterial invasion (e.g. Germall® Plus). The material fabrication has been well reported in numerous works, e.g. [6,7]. In the preparation process the heating durations are kept short and temperatures low to prevent protein denaturation. Gelatin gels stiffen for up to 100 days from manufacturing [7], thus the expected time of exploitation had to be taken into account.

The material manufacturing procedure is not very sensitive to variations and differs across reports. Based on the literature and

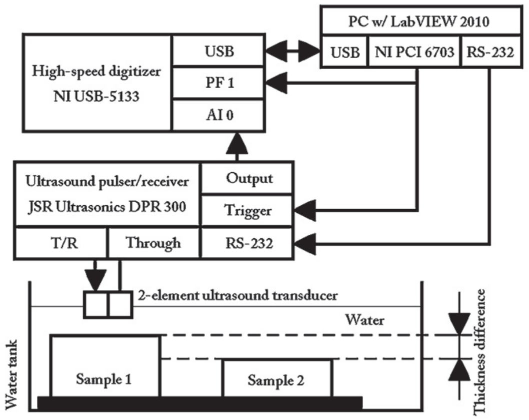

Fig. 1. Setup to measure US attenuation.

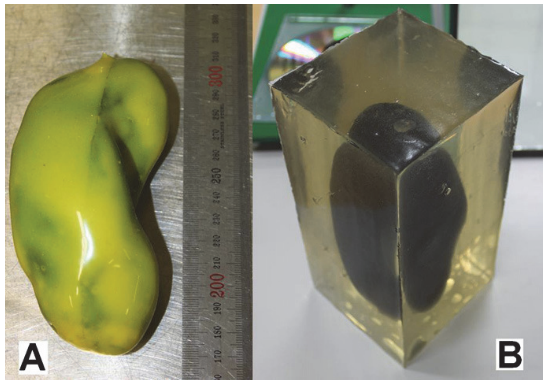

Fig. 2. Kidney phantom with a protective silicon skin (A) and a complete renal biopsy training phantom (B).

our experience, we manufactured the gels according to following steps:

- Gelatin (SG 720, Gelita Sweden AB) and graphite flakes (product 332461, Sigma–Aldrich) were added to water and allowed to hydrate for 10 min (weighed using KERN PCB250-3 and PCB10000-1).
- The hydrated mixture was placed in a hot water bath (60–70 °C) and stirred constantly until the mixture cleared and its temperature rose to 32. . .40 °C.
- The mixture was placed in vacuum chamber for 10 min (approx. 10 kPa) to degas the solution. The solution cleared and bubbles surfaced.
- Formaldehyde (37 wt% solution, product 252549, Sigma–Aldrich) was added while slowly stirring the solution.

The prepared gel was casted into a mould, rotated until it congealed to prevent the graphite from settling and placed in a refrigerator for further hardening and storage (5 °C). We did not add alcohol and preservatives in the gels as the US propagation speed was already realistic and the phantoms were intended to be used within a week from manufacturing. In case longer preservation is needed we consider adding food preservatives E214 (ethyl 4-hydroxybenzoate) and E210 (benzoic acid). In order to prevent dehydration the material has to be sealed from air.

The properties of gelatin gels were mapped to their composition by measuring the properties of test samples that were manufactured according to the previously described steps. With each composition two cylindrical samples (46 mm diameter) with different thickness (12 mm and 17 mm) were casted. The material properties change within days and therefore for each property we manufactured a new set of samples and measured them one day post manufacturing.

We measured the Young's modulus in compression experiments using a custom-built DMA (Dynamic Mechanical Analysis) machine. The radiodensity measurements of the phantom materials were performed using a multidetector CT scanner (Brilliance 64, Philips Healthcare). US properties were measured in pulse-echo configuration (setup shown in Fig. 1) using a US pulser/receiver (DPR 300 from JSR Ultrasonics) and a 5 MHz transducer (SAUTER GmbH). US broadband attenuation was found by comparing the attenuation difference between two samples of the same material with different thickness (in water), and subtracting the attenuation of water. The number and the properties of medium interfaces remained the same (their effects can be neglected) and only thickness of mediums varied (the total thickness remains constant), allowing to calculate the attenuation. US propagation speed was found from time-of-flight experiments.

2.3. Phantom development

To produce a kidney phantom with realistic (patient-specific) anatomy we created a kidney mould from a human abdominal CT scan. The right kidney was segmented (length 13 cm) using 3D Slicer software and from the volumetric data the organ mould was designed. The mould was made of polyamide PA12 in two parts using rapid prototyping (Formiga P100, EOS GmbH).

According to the calibration results (see Section 3) we manufactured the training phantoms with 100 g/l of gelatin, 0.1 wt% of formaldehyde and 0.9 wt% of graphite powder concentrations. This composition represents well diseased kidney tissue (approx. 40 kPa, 0.60 dB/(cm MHz)).

Prior to casting a phantom the biopsy targets representing spherical cysts were made of gelatin gel (90 g/l of gelatin and 0.05 wt% of formaldehyde). The gel was dyed red to validate biopsy results and no graphite was added in order to gain low US broadband attenuation, similar to liquid. In order to make the phantoms appear realistic also in CT imaging we further adjusted the compositions of the cysts (60 g/l of gelatin and 2 wt% of formaldehyde) and the surrounding medium (80 g/l of gelatin, 2 wt% of formaldehyde). The composition of the kidney medium was kept the same.

Cysts were fixed inside the mould, close to the surface using thin needles that were removed after the gel had nearly congealed. In each phantom, three 5 mm diameter cysts were distributed over the kidney and two 10 mm diameter cysts were placed in the upper and lower pole of the kidney phantom.

With cysts in place the kidney was casted and left to solidify. Further, it was fixed in the middle of a rectangular box (165 mm × 80 mm × 80 mm) and a solid gelatin gel medium was casted around it to represent the surrounding tissue that is penetrated during the biopsy. For the biopsy study, the phantoms were covered with a thin layer of opaque plastic to prevent the trainees from seeing into the phantom and visually guiding the biopsy tools. A moulded kidney used in phantoms is shown in Fig. 2A and a complete training phantom in Fig. 2B.

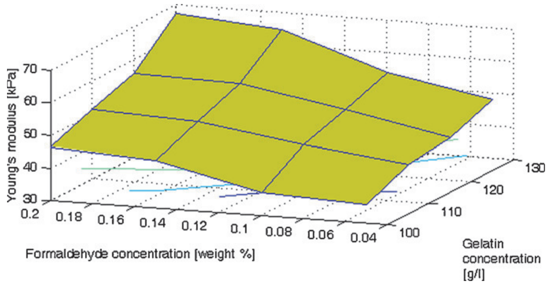

Fig. 3. Gelatin gel's Young's modulus plotted against gelatin and formaldehyde concentrations.

2.4. Phantom evaluation

The phantoms were evaluated for four criteria – suitability for training of US guided interventions, realism in medical imaging (US and CT modalities), durability and price of the phantom material. The suitability of human kidney phantoms for training of US guided interventions was evaluated and compared against a traditional homemade phantom during a usual 5 days interventional radiology training practice of the second year radiology residents. The training took place in the radiology department performing approximately 200,000 radiology exams annually (including interventional radiology) and all together, 7 residents were involved.

The traditional approach to train the skills of US guided interventions of radiology residents in our hospital is practising on self-made phantoms made of gelatin gel with sugar and various fruits, berries or vegetables. These objects represent areas of interest and allow verifying the correctness of the procedure by investigating the substance of the biopsy material. The prepared biopsy material is placed in a plastic case and covered with an opaque plastic.

During the biopsy training each resident practised in parallel on a traditional phantom and on our new one. Training included fine needle aspirations (19–21G needle), true-cut biopsies (14–18G), and insertion of drainage catheters under the US guidance. Both linear (8–12 MHz) and convex (1.5–4 MHz) clinical US probes were available. After the practical work all residents were asked to fill a questionnaire to evaluate both phantoms for their overall importance in biopsy training, suitability for different biopsy tasks, anatomical correctness and structures.

3. Results

3.1. Material calibration

To determine the impact of gelatin and formaldehyde on the Young's modulus a set of material samples were manufactured with gelatin concentrations from 100 g/l to 130 g/l with 10 g/l increments and formaldehyde concentrations from 0.05 wt% to 0.2 wt% with 0.05 wt% increments. The results (plotted in Fig. 3) show that both of the substances make the gel stiffer and have a linear impact on the Young's modulus. Further experiments showed that adding graphite makes the material stiffer; however the effect is insignificant at concentrations used in our phantoms (up to 1 wt%).

A set of samples with 0.1 wt% formaldehyde and no graphite were prepared to determine the impact of gelatin concentration on the US broadband attenuation. Gelatin concentrations from 100 g/l to 140 g/l with 10 g/l increments were used and the results are shown in Fig. 4. Varying formaldehyde concentration has negligible effect on attenuation. We further determined the relation between graphite concentration and US broadband attenuation.

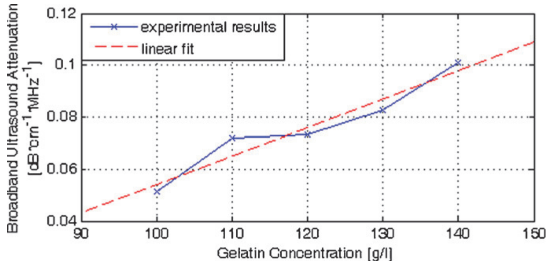

Fig. 4. Broadband US attenuation with respect to gelatin concentration.

A set of samples with graphite concentrations of 0–0.75 wt% with 0.25 wt% increments and gelatin concentrations of 95 g/l, 105 g/l and 115 g/l was prepared. From the results shown in Figs. 4 and 5 it is evident that gelatin increases the attenuation, however its impact is insignificant compared to the effect of graphite and therefore can be neglected.

US propagation speed was measured along with the US broadband attenuation and the average speed over all the samples was 1495 m/s with 32.7 m/s standard deviation. No significant dependence on gelatin, formaldehyde or graphite concentration was found at these compositions.

The cylindrical samples used in previous experiments were too small to gain accurate results for material's radiodensity and therefore larger (250 ml) samples were prepared. Formaldehyde concentration (from 0 wt% to 2 wt% with 100 g/l gelatin) had no distinguishable effect on radiodensity while the increased graphite concentration (0–1 wt% with 100 g/l gelatin and 0.1 wt% formaldehyde) only increased the standard deviation of the radiodensity (from approximately 3 HU to 8 HU). At the compositions of interest only gelatin concentration (samples with no graphite, 0.1 wt% of formaldehyde and 60–140 g/l of gelatin with 20 g/l increments) had a significant effect on the gel's radiodensity as it is shown in Fig. 6.

3.2. Phantom evaluation

The results from the questionnaire filled in by residents after the training (summarized in Tables 2 and 3) showed that the preparation before procedures and practising on phantoms in general is considered to be very important for understanding the complexity of manual coordination of the needle on the US image plane. All residents agreed or strongly agreed (mean 4.86 out of 5) that phantoms are useful in interventional radiology training and understood the importance of knowing the properties of equipment and appearance of needle's course in the US image.

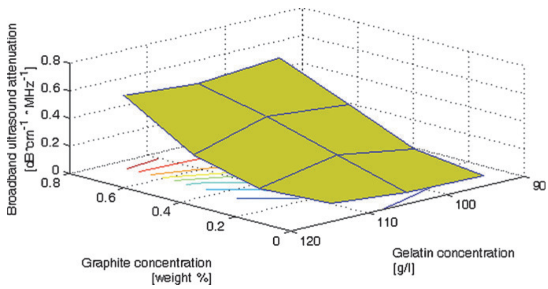

Fig. 5. Broadband US attenuation with respect to graphite and gelatin concentration.

Table 2
General evaluation of interventional radiology training.

#	Evaluation question	Score[a,b]
1	Practicing on a phantom is an essential part of the interventional radiology course	4.86 (0.38)
2	Practicing on a phantom improves manual coordination of the needle in the US plane	4.86 (0.38)
3	Practicing on a phantoms helps understanding the essential procedures to prepare puncturing (transducer, needle, positioning)	4.00 (0.58)
4	Phantom is useful for understanding the properties of the US device for intervention	4.14 (0.58)
5	Phantom helps to understand the path of the puncturing needle during the intervention	4.57 (0.53)

[a] Rated in the scale from 1 (strongly disagree) to 5 (strongly agree) points.
[b] Standard deviations shown in brackets.

Table 3
Comparison of traditional self-made phantoms (SMP) to our renal biopsy phantoms (RBP).

#	Evaluation question	Score[a,b]		p-Values[c]
		SMP	RBP	
1	The size of the phantom is suitable for practicing	4.14 (0.69)	4.43 (0.53)	0.79
2	Phantom's consistency is suitable for practicing	4.43 (0.53)	4.29 (0.49)	0.30
3	Structures inside the phantom are similar to anatomical/pathological structures	2.43 (1.13)	4.17 (0.75)	0.99
4	The sizes of structures inside the phantom are suitable for puncturing	4.43 (0.53)	4.50 (0.55)	0.59
5	When puncturing structures inside the phantom it is easy to understand that the puncturing was done in correct location	3.57 (1.51)	3.00 (1.41)	0.23
6	The phantom should be available in everyday training over a longer period in addition to teaching practice only	2.50 (1.38)	4.71 (0.49)	0.99
7	Echographic properties of the phantom significantly vary while practicing	3.33 (1.03)	3.57 (1.27)	0.64
8	The phantom is suitable for practicing thin needle biopsy	4.29 (0.49)	3.57 (1.13)	0.08
9	The phantom is suitable for thick needle biopsy	4.14 (1.07)	4.67 (0.52)	0.85

[a] Rated in the scale from 1 (strongly disagree) to 5 (strongly agree) points.
[b] Standard deviations shown in brackets.
[c] For hypothesis that new phantoms score higher than traditional ones.

Comparison of the results about different phantoms (summarized in Table 3) revealed that phantoms manufactured by us are considered to be more realistic than the self-made ones in terms of US anatomy and pathology (4.5 vs. 2.43). Residents also were in favour of that this type of phantoms should be available for daily practice (4.71 vs. 2.5). In other terms, no remarkable preference for either of the phantom was seen.

US images and a CT image of a renal biopsy phantom are shown in Figs. 7 and 8 respectively. The radiodensities of the phantom medium and cyst material were in average 33 HU and 19 HU, respectively. With current complexity the cost of phantoms, including labour, was approximately 50 $/kg or 60 $ per single phantom.

4. Discussion

As a result of the phantom material calibration experiments the composition of the gelatin gel was mapped to the material properties. Each of the investigated gel's properties can be separately tuned as they significantly depend only on the concentration of one or two ingredients. Even though it appeared that the softer range of a healthy human kidneys is difficult to mimic as gelatin gels with Young's modulus below 10 kPa are very fragile, the Young's modulus of stiffer healthy kidneys and of all the diseased kidneys is possible to reproduce. Realistic US broadband attenuation for human kidneys is achieved approximately at 1 wt% concentration of graphite and the US propagation speed matches the actual speed in a kidney with less than 5% error. The resulting distortion is insignificant and can be corrected by adding alcohol. According to these results it is possible to manufacture gels that realistically mimic human kidneys and a variety of other soft tissues. The material keeps hardening for up to 100 days, however according to the hardening curves in Ref. [7] it is possible to manufacture phantoms with a Young's modulus that stabilizes at a realistic value for human tissues.

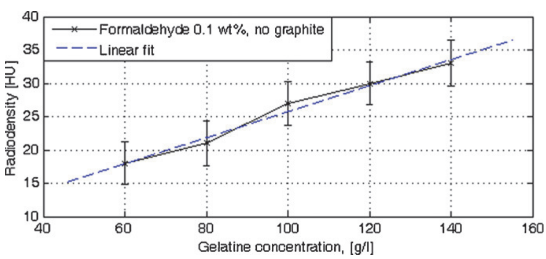

Fig. 6. Radiodensity of gelatin gel with respect to gelatin concentration plotted with standard deviations.

The ultrasound images of a kidney phantom taken in our hospital (Fig. 7) show that the kidney medium appears realistic, however it somewhat lacks the internal structure. The cysts also have a realistic appearance of a liquid-like medium. Comparing images of our phantom and a human volunteer (Fig. 7) the kidney medium does not appear similar as different gains were used. This is because the surrounding tissue of the human kidney has higher attenuation than the kidney itself and vice versa in case of the phantom. In future work we intend to cast the kidney in a medium with higher US attenuation to also realistically mimic the surrounding tissue.

According to the questionnaire results (Tables 2 and 3) our phantoms were well-received, the residents considered them realistic and found that they should be available for everyday training.

The radiodensity of the prepared phantoms (average 33 HU) very well matched the radiodensity of human kidneys (Section 2.1). The density of the cyst material (16–22 HU) was still slightly over the average density of simple cysts; however, the difference in the densities of renal and cyst material was sufficient to distinguish between these structures in CT scans (see Fig. 8).

Despite that the phantoms were made to be used within one week post manufacturing, they did not show signs of deterioration three months later. Isolating them from air (e.g. in a food wrap to prevent dehydration) in a refrigerator (5 °C) allows preservation for several months. Preservation time can be further extended using previously described additives.

A significant advantage of our renal biopsy training phantoms is that they are economically affordable. Low (50 $/kg including labour) price and disposability after using make our phantoms an appealing training platform and an alternative to pricy commercial

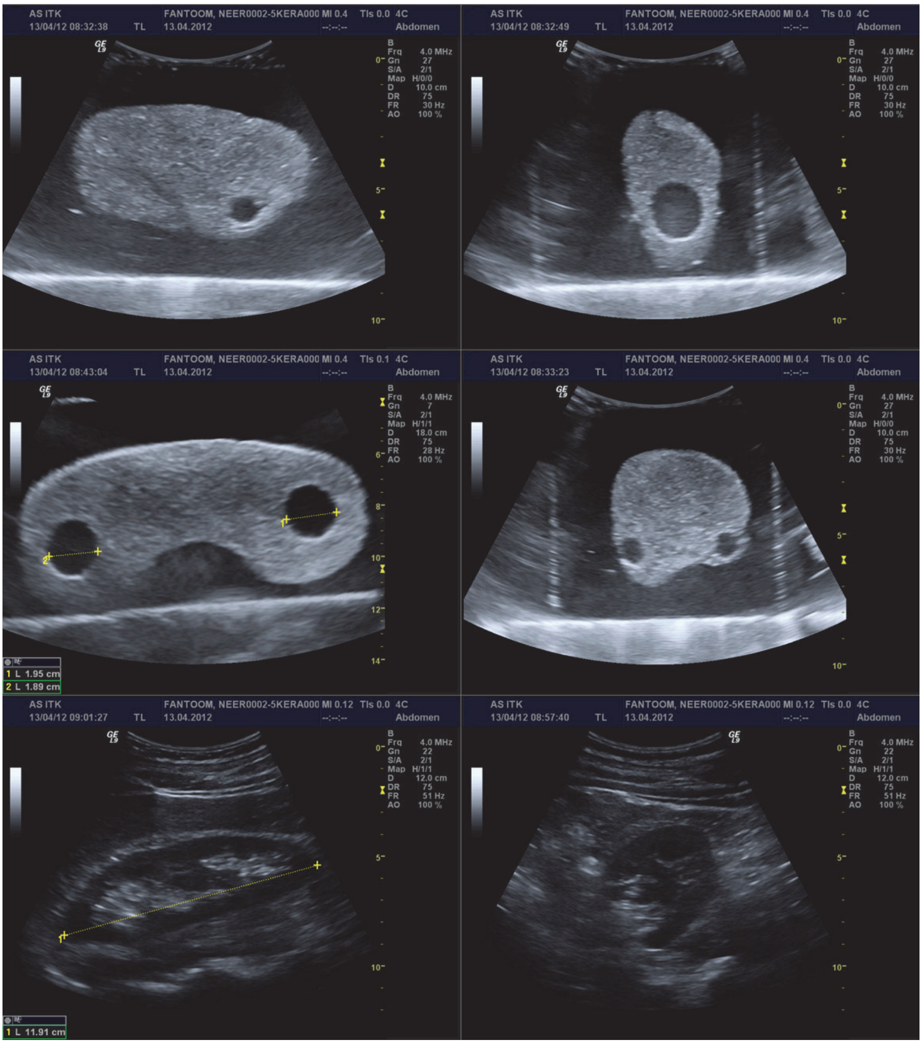

Fig. 7. Ultrasound images of a kidney phantom (four upper images) and a real human kidney (two images below).

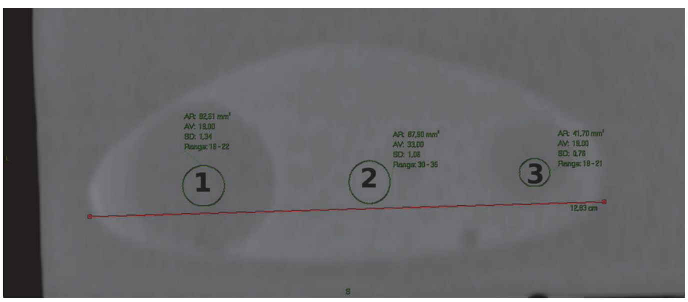

Fig. 8. CT scan of a biopsy phantom. Region properties: (1) area 82.51 mm^2, average radiodensity 19.00 HU, standard deviation 1.34 HU, range 16–22 HU; (2) area 87.90 mm^2, average radiodensity 33.00 HU, standard deviation 1.06 HU, range 30–35 HU; (3) area 41.70 mm^2, average radiodensity 19.00 HU, standard deviation 0.76 HU, range 18–21 HU. The length of the red line is 12.83 mm.

phantoms. The main limitation of this work is modelling the kidney as a homogeneous tissue representing no other internal structure than pathologies. Also, the phantom's resistance to the needle insertion and US backscatter properties of the phantom materials were not investigated for their complexity. We intend to overcome these shortcomings in our future work and also incorporate blood vessels with pulsating flow.

5. Conclusions

In this work we introduced economically affordable renal biopsy phantoms that represent patient-specific anatomy with desired pathologies, look realistic in US and CT imaging and have a realistic elasticity. We calibrated the properties (US, elasticity, radiodensity) of gelatin gels against their ingredient concentrations and identified the composition to mimic the human kidney tissue. Phantoms were casted in a mould that was manufactured from a human kidney model segmented from a CT scan. Further, we investigated the suitability of these phantoms for US and CT imaging and evaluated their viability for interventional radiology training on seven radiology residents during their training of US-guided interventions.

The new phantoms were well-received and preferred over the traditional biopsy phantoms that are used in our hospital. The results showed that they look realistic in US and CT imaging and can be preserved for several months without specific additives. The cost of 60 $ per phantom or 50 $/kg (including labour) makes our disposable and anatomically realistic phantoms an economically affordable alternative to pricey commercial phantoms.

The biopsy training results gave us useful feedback for future improvements. In the future work we are going to surround the kidney phantom with a medium that has similar US attenuation to the surrounding tissues in humans. Also, we intend to add the internal structure to represent blood vessels and distinguish between parenchyma and hilum of the kidney.

Conflict of interest

The authors declare that they have no conflicts of interest.

Acknowledgements

This work was supported by European Union FP7 ICT-2009.5.2 project SAFROS and ICT-2009.2.1 project I-SUR. The authors want to thank East Tallinn Central Hospital for their assistance and their permission to access their medical imaging equipment, and the radiology residents for their willingness to participate in validation.

References

[1] Bragg K, Vanbalen N, Cook N. Future trends in minimally invasive surgery. AORN Journal 2005;82(December (6)):1006–14, 1016–8; quiz 1019–22.

[2] Nicotra JJ, Gay SB, Wallace KK, McNulty BC, Dameron RD. Evaluation of a breast biopsy phantom for learning freehand ultrasound-guided biopsy of the liver. Academic Radiology 1994;1(December (4)):385–7.

[3] Peters MB, Camacho D, Ojeda H, et al. Defining the learning curve for laparoscopic splenectomy for immune thrombocytopenia purpura. American Journal of Surgery 2004;188(November (5)):522–5.

[4] Liberman L, Benton CL, Dershaw DD, Abramson FA, LaTrenta LR, Morris EA. Learning curve for stereotactic breast biopsy: how many cases are enough? American Journal of Roentgenology 2001;176(March (3)):721–7.

[5] Harvey JA, Moran RE, Hamer MM, DeAngelis GA, Omary RA. Evaluation of a turkey-breast phantom for teaching freehand, US-guided core-needle breast biopsy. Academic Radiology 1997;4(July (8)):565–9.

[6] Madsen EL. Tissue mimicking materials for ultrasound phantoms. Medical Physics 1978;5:391.

[7] Hall TJ, Bilgen M, Insana MF, Krouskop TA. Phantom materials for elastography. IEEE Transactions on Ultrasonics, Ferroelectrics and Frequency Control 1997;44(6):1355–65.

[8] Madsen EL, Frank GR, Krouskop TA, Varghese T, Kallel F, Ophir J. Tissue-mimicking oil-in-gelatin dispersions for use in heterogeneous elastography phantoms. Ultrasonic Imaging 2003;25(January):17–38.

[9] Madsen E. Liquid or solid ultrasonically tissue-mimicking materials with very low scatter. Ultrasound in Medicine & Biology 1998;24(May (4)):535–42.

[10] Kawabata K, Waki Y, Matsumura T, Umemura S. Tissue mimicking phantom for ultrasonic elastography with finely adjustable elastic and echographic properties. In: Proceedings of IEEE ultrasonics symposium. 2004. p. 1502–5.

[11] Yasukawa K, Kunisue T, Tsuta K, Shikinami Y, Kondo T. An ultrasound phantom with long-term stability using a new biomimic soft gel material. In: 2007 IEEE ultrasonics symposium proceedings. October 2007. p. 2501–2.

[12] Lerski RA, Duggan TC, Christie J. A simple tissue-like ultrasound phantom material. British Journal of Radiology 1982;55(February (650)):156–7.

[13] Khaled W, Neumann T, Ermert H, Reichling S, Arnold A, Bruhns OT. Evaluation of material parameters of PVA phantoms for reconstructive ultrasound elastography. In: 2007 IEEE ultrasonics symposium proceedings. 2007. p. 1329–32.

[14] Maggi LE, von Kruger MA, Pereira WCA, Monteiro EEC. Development of silicon-based materials for ultrasound biological phantoms. In: 2009 IEEE international ultrasonics symposium. 2009. p. 1962–5.

[15] Culjat MO, Goldenberg D, Tewari P, Singh RS. A review of tissue substitutes for ultrasound imaging. Ultrasound in Medicine & Biology 2010;36(June): 861–73.

[16] International Commission on Radiation Units and Measurements. Tissue substitutes, phantoms, and computational modelling in medical ultrasound. Bethesda, MD: Oxford University Press; 1998.

[17] Goss SA, Johnston RL, Dunn F. Comprehensive compilation of empirical ultrasonic properties of mammalian tissues. The Journal of the Acoustical Society of America 1978;64(August (2)):423–57.

[18] Duck FA. Physical properties of tissue – a comprehensive reference book. London, UK: Academic Press; 1990.

[19] Gennisson J, Grenier N, Hubrecht R, et al. Multiwave technology introducing shear wave elastography of the kidney: pre-clinical study on a kidney fibrosis model and clinical feasibility study on 49 human renal transplants. In: IEEE international ultrasonics symposium. 2010. p. 1356–9.

[20] Preim B, Bartz D. Visualization in medicine: theory, algorithms, and applications. San Francisco, USA: Morgan Kaufmann; July 2007. p. 47.

CURRICULUM VITAE

Personal data

Name:	Andres Hunt
Date of birth:	November 20, 1984
City of birth:	Pärnu, Estonia
Citizenship:	Estonian

Contact data

Address:	Akadeemia tee 7A – 17, 12611 Tallinn, Estonia
Phone:	+372 5196 1764
E-mail:	Andres.Hunt@ttu.ee

Education

2009 – 2017:	Tallinn University of Technology	PhD studies
2007 – 2009:	University of Tartu	MSc in Applicational Physics
2004 – 2007:	University of Tartu	BSc in Applicational Physics

Language competence

Estonian:	Native speaker
English:	Very good both spoken and written
Russian:	Basic level both spoken and written

Professional employment

2009 – 2010:	Centre for Biorobotics, Tallinn University of Technology	Engineer
2010 – 2013:	Centre for Biorobotics, Tallinn University of Technology	Researcher
2013 – 2017:	Centre for Biorobotics, Tallinn University of Technology	Junior Researcher

Supervised thesis

2010:	MSc	Gert Toming	Development and characterization of a hydrodynamic test bench and digital particle image velocimetry system
2011:	MSc	Rivo Öpik	Apparatus for developing surgical phantom materials
2011:	MSc	Richard Villenberg	Developing ultrasound surgical phantom materials

ELULOOKIRJELDUS

Isikuandmed

Nimi:	Andres Hunt
Sünniaeg:	20 november 1984
Sünnikoht:	Pärnu, Eesti
Kodakondsus:	Eestlane

Kontaktandmed

Aadress:	Akadeemia tee 7A – 17, 12611 Tallinn, Eesti
Telefon:	+372 5196 1764
E-post:	Andres.Hunt@ttu.ee

Hariduskäik

2009 – 2017:	Tallinna Tehnikaülikool	Doktorantuur
2007 – 2009:	Tartu Ülikool	MSc Rakendusfüüsikas
2004 – 2007:	Tartu Ülikool	BSc Rakendusfüüsikas

Keelteoskus

Eesti keel:	Emakeel
Inglise keel:	Kõrgtase kõnes ja kirjas
Vene keel:	Algtase kõnes ja kirjas

Teenistuskäik

2009 – 2010:	Biorobootika Keskus, Tallinna Tehnikaülikool	Insener
2010 – 2013:	Biorobootika Keskus, Tallinna Tehnikaülikool	Teadur
2013 – 2017:	Biorobootika Keskus, Tallinna Tehnikaülikool	Nooremteadur

Juhendatud lõputööd

2010:	MSc	Gert Toming	Voolu visualiseerimise ja hüdrodünaamilise katseseadmestiku ehitamine ja karakteriseerimine
2011:	MSc	Rivo Öpik	Seadmed kirurgiliste fantoomimaterjalide arendamiseks
2011:	MSc	Richard Villenberg	Kirurgiliste ultrahelifantoomide materjalide arendamine robotkirurgias

DISSERTATIONS DEFENDED AT TALLINN UNIVERSITY OF TECHNOLOGY ON *INFORMATICS AND SYSTEM ENGINEERING*

1. **Lea Elmik**. Informational Modelling of a Communication Office. 1992.

2. **Kalle Tammemäe**. Control Intensive Digital System Synthesis. 1997.

3. **Eerik Lossmann**. Complex Signal Classification Algorithms, Based on the Third-Order Statistical Models. 1999.

4. **Kaido Kikkas**. Using the Internet in Rehabilitation of People with Mobility Impairments – Case Studies and Views from Estonia. 1999.

5. **Nazmun Nahar**. Global Electronic Commerce Process: Business-to-Business. 1999.

6. **Jevgeni Riipulk**. Microwave Radiometry for Medical Applications. 2000.

7. **Alar Kuusik**. Compact Smart Home Systems: Design and Verification of Cost Effective Hardware Solutions. 2001.

8. **Jaan Raik**. Hierarchical Test Generation for Digital Circuits Represented by Decision Diagrams. 2001.

9. **Andri Riid**. Transparent Fuzzy Systems: Model and Control. 2002.

10. **Marina Brik**. Investigation and Development of Test Generation Methods for Control Part of Digital Systems. 2002.

11. **Raul Land**. Synchronous Approximation and Processing of Sampled Data Signals. 2002.

12. **Ants Ronk**. An Extended Block-Adaptive Fourier Analyser for Analysis and Reproduction of Periodic Components of Band-Limited Discrete-Time Signals. 2002.

13. **Toivo Paavle**. System Level Modeling of the Phase Locked Loops: Behavioral Analysis and Parameterization. 2003.

14. **Irina Astrova**. On Integration of Object-Oriented Applications with Relational Databases. 2003.

15. **Kuldar Taveter**. A Multi-Perspective Methodology for Agent-Oriented Business Modelling and Simulation. 2004.

16. **Taivo Kangilaski**. Eesti Energia käiduhaldussüsteem. 2004.

17. **Artur Jutman**. Selected Issues of Modeling, Verification and Testing of Digital Systems. 2004.

18. **Ander Tenno**. Simulation and Estimation of Electro-Chemical Processes in Maintenance-Free Batteries with Fixed Electrolyte. 2004.

19. **Oleg Korolkov**. Formation of Diffusion Welded Al Contacts to Semiconductor Silicon. 2004.

20. **Risto Vaarandi**. Tools and Techniques for Event Log Analysis. 2005.

21. **Marko Koort**. Transmitter Power Control in Wireless Communication Systems. 2005.

22. **Raul Savimaa**. Modelling Emergent Behaviour of Organizations. Time-Aware, UML and Agent Based Approach. 2005.

23. **Raido Kurel**. Investigation of Electrical Characteristics of SiC Based Complementary JBS Structures. 2005.

24. **Rainer Taniloo**. Ökonoomsete negatiivse diferentsiaaltakistusega astmete ja elementide disainimine ja optimeerimine. 2005.

25. **Pauli Lallo**. Adaptive Secure Data Transmission Method for OSI Level I. 2005.

26. **Deniss Kumlander**. Some Practical Algorithms to Solve the Maximum Clique Problem. 2005.

27. **Tarmo Veskioja**. Stable Marriage Problem and College Admission. 2005.

28. **Elena Fomina**. Low Power Finite State Machine Synthesis. 2005.

29. **Eero Ivask**. Digital Test in WEB-Based Environment 2006.

30. **Виктор Войтович**. Разработка технологий выращивания из жидкой фазы эпитаксиальных структур арсенида галлия с высоковольтным p-n переходом и изготовления диодов на их основе. 2006.

31. **Tanel Alumäe**. Methods for Estonian Large Vocabulary Speech Recognition. 2006.

32. **Erki Eessaar**. Relational and Object-Relational Database Management Systems as Platforms for Managing Softwareengineering Artefacts. 2006.

33. **Rauno Gordon**. Modelling of Cardiac Dynamics and Intracardiac Bio-impedance. 2007.

34. **Madis Listak**. A Task-Oriented Design of a Biologically Inspired Underwater Robot. 2007.

35. **Elmet Orasson**. Hybrid Built-in Self-Test. Methods and Tools for Analysis and Optimization of BIST. 2007.

36. **Eduard Petlenkov**. Neural Networks Based Identification and Control of Nonlinear Systems: ANARX Model Based Approach. 2007.

37. **Toomas Kirt**. Concept Formation in Exploratory Data Analysis: Case Studies of Linguistic and Banking Data. 2007.

38. **Juhan-Peep Ernits**. Two State Space Reduction Techniques for Explicit State Model Checking. 2007.

39. **Innar Liiv**. Pattern Discovery Using Seriation and Matrix Reordering: A Unified View, Extensions and an Application to Inventory Management. 2008.

40. **Andrei Pokatilov**. Development of National Standard for Voltage Unit Based on Solid-State References. 2008.

41. **Karin Lindroos**. Mapping Social Structures by Formal Non-Linear Information Processing Methods: Case Studies of Estonian Islands Environments. 2008.

42. **Maksim Jenihhin**. Simulation-Based Hardware Verification with High-Level Decision Diagrams. 2008.

43. **Ando Saabas**. Logics for Low-Level Code and Proof-Preserving Program Transformations. 2008.

44. **Ilja Tšahhirov**. Security Protocols Analysis in the Computational Model – Dependency Flow Graphs-Based Approach. 2008.

45. **Toomas Ruuben**. Wideband Digital Beamforming in Sonar Systems. 2009.

46. **Sergei Devadze**. Fault Simulation of Digital Systems. 2009.

47. **Andrei Krivošei**. Model Based Method for Adaptive Decomposition of the Thoracic Bio-Impedance Variations into Cardiac and Respiratory Components. 2009.

48. **Vineeth Govind**. DfT-Based External Test and Diagnosis of Mesh-like Networks on Chips. 2009.

49. **Andres Kull**. Model-Based Testing of Reactive Systems. 2009.

50. **Ants Torim**. Formal Concepts in the Theory of Monotone Systems. 2009.

51. **Erika Matsak**. Discovering Logical Constructs from Estonian Children Language. 2009.

52. **Paul Annus**. Multichannel Bioimpedance Spectroscopy: Instrumentation Methods and Design Principles. 2009.

53. **Maris Tõnso**. Computer Algebra Tools for Modelling, Analysis and Synthesis for Nonlinear Control Systems. 2010.

54. **Aivo Jürgenson**. Efficient Semantics of Parallel and Serial Models of Attack Trees. 2010.

55. **Erkki Joasoon**. The Tactile Feedback Device for Multi-Touch User Interfaces. 2010.

56. **Jürgo-Sören Preden**. Enhancing Situation – Awareness Cognition and Reasoning of Ad-Hoc Network Agents. 2010.

57. **Pavel Grigorenko**. Higher-Order Attribute Semantics of Flat Languages. 2010.

58. **Anna Rannaste**. Hierarcical Test Pattern Generation and Untestability Identification Techniques for Synchronous Sequential Circuits. 2010.

59. **Sergei Strik**. Battery Charging and Full-Featured Battery Charger Integrated Circuit for Portable Applications. 2011.

60. **Rain Ottis**. A Systematic Approach to Offensive Volunteer Cyber Militia. 2011.

61. **Natalja Sleptšuk**. Investigation of the Intermediate Layer in the Metal-Silicon Carbide Contact Obtained by Diffusion Welding. 2011.

62. **Martin Jaanus**. The Interactive Learning Environment for Mobile Laboratories. 2011.

63. **Argo Kasemaa**. Analog Front End Components for Bio-Impedance Measurement: Current Source Design and Implementation. 2011.

64. **Kenneth Geers**. Strategic Cyber Security: Evaluating Nation-State Cyber Attack Mitigation Strategies. 2011.

65. **Riina Maigre**. Composition of Web Services on Large Service Models. 2011.

66. **Helena Kruus**. Optimization of Built-in Self-Test in Digital Systems. 2011.

67. **Gunnar Piho**. Archetypes Based Techniques for Development of Domains, Requirements and Sofware. 2011.

68. **Juri Gavšin**. Intrinsic Robot Safety Through Reversibility of Actions. 2011.

69. **Dmitri Mihhailov**. Hardware Implementation of Recursive Sorting Algorithms Using Tree-like Structures and HFSM Models. 2012.

70. **Anton Tšertov**. System Modeling for Processor-Centric Test Automation. 2012.

71. **Sergei Kostin**. Self-Diagnosis in Digital Systems. 2012.

72. **Mihkel Tagel**. System-Level Design of Timing-Sensitive Network-on-Chip Based Dependable Systems. 2012.

73. **Juri Belikov**. Polynomial Methods for Nonlinear Control Systems. 2012.

74. **Kristina Vassiljeva**. Restricted Connectivity Neural Networks based Identification for Control. 2012.

75. **Tarmo Robal**. Towards Adaptive Web – Analysing and Recommending Web Users` Behaviour. 2012.

76. **Anton Karputkin**. Formal Verification and Error Correction on High-Level Decision Diagrams. 2012.

77. **Vadim Kimlaychuk**. Simulations in Multi-Agent Communication System. 2012.

78. **Taavi Viilukas**. Constraints Solving Based Hierarchical Test Generation for Synchronous Sequential Circuits. 2012.

79. **Marko Kääramees**. A Symbolic Approach to Model-based Online Testing. 2012.

80. **Enar Reilent**. Whiteboard Architecture for the Multi-agent Sensor Systems. 2012.

81. **Jaan Ojarand**. Wideband Excitation Signals for Fast Impedance Spectroscopy of Biological Objects. 2012.

82. **Igor Aleksejev**. FPGA-based Embedded Virtual Instrumentation. 2013.

83. **Juri Mihhailov**. Accurate Flexible Current Measurement Method and its Realization in Power and Battery Management Integrated Circuits for Portable Applications. 2013.

84. **Tõnis Saar**. The Piezo-Electric Impedance Spectroscopy: Solutions and Applications. 2013.

85. **Ermo Täks**. An Automated Legal Content Capture and Visualisation Method. 2013.

86. **Uljana Reinsalu**. Fault Simulation and Code Coverage Analysis of RTL Designs Using High-Level Decision Diagrams. 2013.

87. **Anton Tšepurov**. Hardware Modeling for Design Verification and Debug. 2013.

88. **Ivo Müürsepp**. Robust Detectors for Cognitive Radio. 2013.

89. **Jaas Ježov**. Pressure sensitive lateral line for underwater robot. 2013.

90. **Vadim Kaparin**. Transformation of Nonlinear State Equations into Observer Form. 2013.

92. **Reeno Reeder**. Development and Optimisation of Modelling Methods and Algorithms for Terahertz Range Radiation Sources Based on Quantum Well Heterostructures. 2014.

93. **Ants Koel**. GaAs and SiC Semiconductor Materials Based Power Structures: Static and Dynamic Behavior Analysis. 2014.

94. **Jaan Übi**. Methods for Coopetition and Retention Analysis: An Application to University Management. 2014.

95. **Innokenti Sobolev**. Hyperspectral Data Processing and Interpretation in Remote Sensing Based on Laser-Induced Fluorescence Method. 2014.

96. **Jana Toompuu**. Investigation of the Specific Deep Levels in *p*-, *i*- and *n*-Regions of GaAs p^+-pin-n^+ Structures. 2014.

97. **Taavi Salumäe**. Flow-Sensitive Robotic Fish: From Concept to Experiments. 2015.

98. **Yar Muhammad**. A Parametric Framework for Modelling of Bioelectrical Signals. 2015.

99. **Ago Mõlder**. Image Processing Solutions for Precise Road Profile Measurement Systems. 2015.

100. **Kairit Sirts**. Non-Parametric Bayesian Models for Computational Morphology. 2015.

101. **Alina Gavrijaševa**. Coin Validation by Electromagnetic, Acoustic and Visual Features. 2015.

102. **Emiliano Pastorelli**. Analysis and 3D Visualisation of Microstructured Materials on Custom-Built Virtual Reality Environment. 2015.

103. **Asko Ristolainen**. Phantom Organs and their Applications in Robotic Surgery and Radiology Training. 2015.

104. **Aleksei Tepljakov**. Fractional-order Modeling and Control of Dynamic Systems. 2015.

105. **Ahti Lohk**. A System of Test Patterns to Check and Validate the Semantic Hierarchies of Wordnet-type Dictionaries. 2015.

106. **Hanno Hantson**. Mutation-Based Verification and Error Correction in High-Level Designs. 2015.

107. **Lin Li**. Statistical Methods for Ultrasound Image Segmentation. 2015.

108. **Aleksandr Lenin**. Reliable and Efficient Determination of the Likelihood of Rational Attacks. 2015.

109. **Maksim Gorev**. At-Speed Testing and Test Quality Evaluation for High-Performance Pipelined Systems. 2016.

110. **Mari-Anne Meister**. Electromagnetic Environment and Propagation Factors of Short-Wave Range in Estonia. 2016.

111. **Syed Saif Abrar**. Comprehensive Abstraction of VHDL RTL Cores to ESL SystemC. 2016.

112. **Arvo Kaldmäe**. Advanced Design of Nonlinear Discrete-time and Delayed Systems. 2016.

113. **Mairo Leier**. Scalable Open Platform for Reliable Medical Sensorics. 2016.

114. **Georgios Giannoukos**. Mathematical and Physical Modelling of Dynamic Electrical Impedance. 2016.

115. **Aivo Anier**. Model Based Framework for Distributed Control and Testing of Cyber-Physical Systems. 2016.

116. **Denis Firsov**. Certification of Context-Free Grammar Algorithms. 2016.

117. **Sergei Astatpov**. Distributed Signal Processing for Situation Assessment in Cyber-Physical Systems. 2016.

118. **Erkki Moorits**. Embedded Software Solutions for Development of Marine Navigation Light Systems. 2016.

119. **Andres Ojamaa**. Software Technology for Cyber Security Simulations. 2016.

120. **Gert Toming**. Fluid Body Interaction of Biomimetic Underwater Robots. 2016.